UNIVERSITY OF CALIFORNIA SAN DIEGO

Low-Valent Materials Enabled by *m*-terphenyl Isocyanide Ligands

A Dissertation submitted in partial satisfaction of the requirements
for the degree Doctor of Philosophy

in

Chemistry

by

Krista P. Balto

Committee in charge:

Professor Joshua S. Figueroa, Chair
Professor Guy Bertrand
Professor Seth M. Cohen
Professor Nathan Romero
Professor Andrea R. Tao

2024

The Dissertation of Krista P. Balto is approved, and it is acceptable in quality and form for publication on microfilm and electronically.

University of California San Diego

2024

DEDICATION

To my sister, Marissa.

I hope this shows we are capable of extraordinary things.

EPIGRAPH

"Though she be but little, she is fierce!"

William Shakespeare

TABLE OF CONTENTS

LIST OF FIGURES

LIST OF TABLES

LIST OF ABBREVIATIONS

Symbol	**Meaning**
δ	Integration of ^{1}H NMR signal
Å	Angstrom (10^{-10} m)
a	Unit cell axis a
ATR	Attenuated total reflectance
α	unit cell angle α
B	Unit cell axis b
β	unit cell angle β
br	broad
C_{iso}	terminal isocyanide carbon
CNR	Isocyanide
CO	Carbon monoxide, carbonyl
COD	1,5–cyclooctadiene (C_8H_{12})
Cp	cyclopentadienyl (C_5H_5)
c	Unit cell axis c
Calcd.	calculated
cm^{-1}	wavenumber
°C	Degrees ceslius
Dipp	2,6,–diisopropylphenyl (2,6–i $Pr_2C_6H_3$)
e^-	electron

equiv.	equivalents
EPR	Electron paramagnetic resonance
FTIR	Fourier Transform Infrared Spectroscopy
GoF	Goodness of Fit
g	grams
γ	Unit cell angle γ
IR	infrared
^{i}Pr	Isopropyl ($CH(CH_3)_2$)
J	NMR coupling constant
K	Degrees Kelvin
L	Ligand (neutral), liters
M	Transition-metal, molar (mol/L)
Me	Methyl (CH_3)
MeCN	acetonitrile
Mes	Mesityl, 2,4,6–trimethylphenyl (2,4,6–$Me_3C_6H_2$)
m	*meta* position
Min	minutes
Mol	moles
n	Moles, mmol
NMR	Nuclear Magnetic Resonance
ν	Infrared stretching frequency
ν_{CN}	Isocyanide stretching frequency (cm^{-1})
OTf	Triflate, trifluoromethylsulfonate ([OSO_2CF_3])

o	*Ortho* position
Ph	Phenyl (C_6H_5)
p	*Para* position
Ppm	Parts per million
π	pi
R	Organic group, alkyl group
R	Residual value (X-ray crystallography)
RT	Room temperature
S	Electronic spin
SOF	Site occupancy factor
s	Singlet, seconds
σ	sigma
T	temperature
TGA	Thermogravimetric analysis
THF	tetrahydrofuran
t	triplet
Tol	Toluene, tolyl (C_7H_8)
^{t}Bu	Tertiary-butyl ($C(CH_3)_3$)
Tripp	Triisopropylphenyl (2,4,6–i $Pr_3C_6H_2$)
V	Volume, mL
V	Unit cell volume
VT	Variable temperature
X	Halide or pseudo halide

x	Molar fraction
Xyl	xylyl
Z	Number of molecules in unit cell

ACKNOWLEDGEMENTS

I came into UCSD's graduate program under the impression I would solely work on materials chemistry. In fact, I was set on working with Prof. Seth Cohen, however my rotations proved my interests expanded further into the realm of organometallic chemistry than I previously imagined. While the Cohen lab was productive and filled with excellent chemists and mentors, the Figs always had a little "spice" in their lab. The Schimpf's said everyone turned to the Figs when they needed help, and, well, I knew I wanted to be one of the Figs. When I say "spice", I mean it in terms of pure chaos, where Neville would be blasting music while working up his ligand, there was always someone in lab no matter what hour of the day, and it was evident the lab had a very close sense of camaraderie, despite the different personalities and walks of life in it. I believe Josh's enthusiasm and the conversation I first had with him was what sealed the deal for me. Josh is unique and believes in his students and their capabilities, he believed in me and my abilities when I was just rotating. For me, it was this faith, along with his unwavering passion for science and discovery that convinced me to join the lab.

I had thought my undergraduate experience would be difficult to top in terms of opportunities, however I was once again wrong. My graduate experience is one filled with personal and professional self-discovery, and I hope those who join the lab have their own experience with this. Josh put me on several collaborative projects, and one turned me into a semi-capable nano scientist (against my will, at first). The countless awards, opportunities and knowledge accumulated are all due to the intensity and passion Josh has towards chemistry and his students. TLDR; I owe him a lot.

I think the best way to approach the acknowledgement section is to mention those who I met in chronological order, beginning with Michael Neville. I was thrown to the wolves my first

day of rotation and Neville was there to laugh at me (though *slightly* guiding me) while I fell. This consisted of him telling me "you're doing great!!" (accompanied with a hand clap, finger guns and disappearing to the fifth floor to work on his carpentry skills) as I spilled precious ligand everywhere in his glove box, trying to set up my first coupling. Michael's teaching style was more of a "hands-off" approach, however his knowledge of chemistry, wood-working and literally everything was impressive. I strived to be as knowledgeable as him, and he was always someone to look up to in the group. If you have a problem, Michael had (still has) a solution, just not during his mountain biking time on Wednesdays. He was also crucial in passing down the "box yoga" technique.

The second person encountered was Alejandra, who I genuinely feared the first time I met her. Her intensity and concentration regarding her projects were inspiring and intimidating. Josh told me she was protective of her chemistry and to at least try to befriend her since she was the best person to mentor me in the lab. I think this took me approximately 6 months to do, with me pestering her (every five minutes) about ditopic ligand synthesis. Eventually though, she took me under her wing and showed me how the Figs do MOF chemistry.

To Vincent, you were so quiet the first time I met you, but I knew you were extremely skilled and dedicated. You were literally always in the glove box. Did you ever leave? I didn't know. Maybe to get Subway or to go lift. This, again, was inspiring and I wanted to be like you. I have you to thank for the countless conversations about MOFs and the countless ideas you always threw at me. I will never forget the transformation of your diet from yams, boiled chicken and unseasoned oatmeal to Chipotle, Hot Pot, Art of Espresso and Blue Pepper. I have you to thank for showing me all the good hot pot spots in San Diego. I hear you're coming back soon and I know everyone is excited for your return.

To Adam, you are literally Michael 2.0, and your knowledge regarding chemistry and handyman things has saved me (and my car) countless times. You made me feel included in the lab and were probably the friendliest member at first, willing to answer any of my questions. I think you and I have struggled through ligand land together more times than I want to remember. I have witnessed the many phases of Adam (Gl-adam, S-adam, B-adam and M-adam and the newest level: D-Adam). My favorite by far is MI-Adam and it has been a pleasure working with every type (even if you do hate koalas).

To Ritchie, despite you making fun of me all the time, I appreciate you and your extensive XRD knowledge. Also, the self-deprecating jokes will never not be hilarious and you make really good food. I appreciate your bluntness and your sarcasm - it is refreshing and much needed in lab. I really hope you make it to Durham or some crystallography facility because you are so talented and knowledgeable. I'm glad you found your passion.

Sweet Sean, my coffee buddy, I hope you persevere and continue to do what you do best. It has truly been a pleasure watching you develop into a brilliant chemist, and I know you have what it takes to become a professor. I already know you will inspire many students to become chemists, you are so patient and kind and that is what they will remember most. I'll never forget when I told Angelica you guys would get along- the beginning of a great friendship. Sean's Sweets must live on forever and same with net veganism.

To my 1/3 wife Angelica, I am so blessed to have met you through Amy (my other wife whom I also love endlessly) and I have you both to thank for my personal self-growth. I've been so fortunate to have you down the hall when I'm about to lose my mind. You have truly been a great friend and you are a brilliant human being. We have so many great memories together and you will always be my best friend. I know I can always count on you to listen to me and give your

honest feedback. Your way of thinking is one-of-a-kind unique, and you encouraged me to expand my mind and consider another perspective on life. Without you, I would have never discovered my softer, more emotional side and for that I am grateful.

To my battle buddy, Nick, you found me at a lower point in life, but you have taken me for what I am and accepted it, all while making me better. I love you endlessly and have you to thank for the countless encouraging conversations, ice cream trips and my new lethal skill set. Thank you for supporting me through thick and thin. Your determination and perseverance are unmatched, and you inspire me to be the best at my job too, just like you.

To my family, even though you are across the US, you have always been there for me, despite me being grossly independent. I appreciate your faith in me and everything you have done to get me into the position I have found myself in today (Dr. Krista Balto). To my sister, Marissa- continue fighting for you, you are one of a kind unique and I will always be here for you. This dissertation is dedicated to you, a testament to what we can become when we never stop fighting for it.

Chapter 1 is adapted from Balto, K.P.; Sikma, R.E.; Figueroa, J.S.; Cohen, S. "Metal Organic Frameworks with Low Valent Metal Nodes" Angew. Chem. Int. Ed. 2022, 61 (33), e202206353. The dissertation author was the co-first author of this paper. Permission to include published material in this dissertation has been obtained from all coauthors.

Chapter 2 is adapted from "Crystalline Hydrogen-Bonding Networks and Mixed-Metal Framework Materials Enabled by an Electronically Differentiated Heteroditopic Isocyanide/Carboxylate Linker Group". The dissertation author was the primary investigator and author of this paper and permission to include this material has been obtained from co-authors.

Chapter 3 is a continuation of the research done in Chapter 2, the dissertation author is the primary researcher of this unpublished work.

Chapter 4 is adapted from a manuscript in preparation by Balto, K.P.; Arroyave, A.; MacMillan, S. M.; Moore, C.E.; Gembicky, M.; Rheingold, A.L.; Lancaster, K.M.; Figueroa, J.S. entitled "A Porous Crystalline Ni(0) Organometallic Framework with Redox Properties". The dissertation author was the primary researcher and author of this paper. Permission to include this has been obtained from all coauthors.

Chapters 5 and 6 feature collaborative work done through the Materials Science Research and Engineering (MRSEC) program at UCSD. This work dominated most of my last year of my PhD research. More specifically, Chapter 5, is in part, a reprint of the material as it appears in *ACS Nano*, Balto, K. P.; Wang, Y.; Chen, A.; Figueroa, J. S.; Pascal, T.; Tao, A. R. "Curvature-Selective Nanocrystal Surface Ligation Using Sterically-Encumbered Metal-Coordinating Ligands" *ACS Nano*, 2022, 16, ASAP. DOI: 10.1021/acsnano.2c04595. Permission to include published material in this dissertation has been obtained from all coauthors.

Chapter 6 is a continuation of the research done in Chapter 5, the dissertation author is the primary researcher of this unpublished work.

VITA

2019 Honors Bachelor of Science in Chemistry, University of Delaware.

2021 Master of Science in Chemistry, University of California San Diego.

2024 Doctor of Philosophy in Chemistry, University of California San Diego.

PUBLICATIONS

Dissertation Related.

Balto, K.P.; Arroyave, A.; MacMillan, S. M.; Moore, C.E.; Gembicky, M.; Rheingold, A.L.; Lancaster, K.M.; Figueroa, J.S. "A Porous Crystalline Ni(0) Organometallic Framework with Redox Properties". *In Preparation.*

Balto, K.P.; **Sikma, R.E**.; Figueroa, J.S.; Cohen, S. "Metal Organic Frameworks with Low Valent Metal Nodes" *Angew. Chem. Int. Ed.* **2022**, *61* (*33),* e202206353. DOI: 10.1002/anie.202206353.

Authors in Bold Contributed Equally.

Balto, K. P.; **Wang, Y.; Chen, A.;** Figueroa, J. S.; Pascal, T.; Tao, A. R. "Curvature-Selective Nanocrystal Surface Ligation Using Sterically-Encumbered Metal-Coordinating Ligands" *ACS Nano*, **2022**, 16, ASAP. DOI: 10.1021/acsnano.2c04595.

Authors in Bold Contributed Equally.

Balto, K.P*.;* Gembicky, M.; Rheingold, A. L.; Figueroa, J. S. "Crystalline Hydrogen-Bonding Networks and Mixed-Metal Framework Materials Enabled by an Electronically Differentiated Heteroditopic Isocyanide/Carboxylate Linker Group" *Inorganic Chemistry.* **2021**, *60 (16),* 12545-12554. DOI: 10.1021/acs.inorgchem.1c01804.

Others.

Bi, L.; Jamnuch, S.; Chen, A.; Do, A.; ***Balto, K.P***.; Wang, Z.; Zhu, Q.; Wang, Y.; Zhang, Y.; Tao, A.R.; Pascal, T.A.; Figueroa, J.S.; Li, S. "Molecular Scale Visualization of Steric Effects of Ligand Binding to Reconstructed Au(111) Surfaces" *J. Am. Chem. Soc.* **2024**, Accepted. DOI: https://doi.org/10.1021/jacs.4c00002.

Lorzing, G. R.; ***Balto, K.P***.; Antonio, A. M.; Trump, B. A.; Brown, C. M.; Bloch, E. D. "Elucidating the Structure of the Metal–Organic Framework Ru-HKUST-1" *Chem. Mater.* **2020**, 32, 18, 7710–7715. DOI: 10.1021/acs.chemmater.0c01944.

Gosselin, A. J.; Rowland, C. A.; ***Balto, K.P.***; Yap, G. P. A.; Bloch, E. D. "Design and Synthesis of Porous Nickel(II) and Cobalt(II) Cages" *Inorg. Chem.* **2018**, 57, 19, 11847–11850. DOI: 10.1021/acs.inorgchem.8b01130.

ABSTRACT OF THE DISSERTATION

Low-Valent Materials Enabled by *m*-terphenyl Isocyanide Ligands

by

Krista P. Balto

Doctor of Philosophy in Chemistry

University of California San Diego, 2024

Professor Joshua S. Figueroa Chair

In coordination chemistry, sterically encumbering ligands are often used to control the coordination number, geometry, and electronic structure of transition-metal complexes. The *m*-terphenyl ligand scaffold is particularly effective in isolating reactive, low-coordinate metal

complexes due to its sterically encumbering nature. In past years, we have employed monotopic *m*-terphenyl isocyanide ligands to isolate low coordinate, highly reactive organometallic complexes. The isolation of these species is possible not only due to the steric pressure of the *m*-terphenyl backbone, but also due to the synergistic bonding occurring between electron-rich metal and isocyanide ligand molecular orbitals. Indeed, isocyanides are isolobal to carbon monoxide (CO), and both ligands function as both σ-donors and π-acceptors with strong π-backbonding interactions. However, unlike CO, isocyanide ligands can be functionalized, allowing for the formation of multitopic *m*-terphenyl isocyanide ligands. By capitalizing on this tunability, we reported the synthesis of multitopic *m*-terphenyl isocyanide ligands for the formation of isocyanide coordination networks (^{ISO}CNs).

While isocyanide ligands have been studied extensively in organometallic chemistry, the study of isocyanide ligands in nano- and materials science remains underdeveloped. This dissertation will be split into two parts, where chapters 1 through 4 will discuss the history of low-valent metal-organic frameworks (MOFs) and the impact the multitopic *m*-terphenyl isocyanide ligands have in the generation of new low-valent materials. In addition, while the isolation of novel *m*-terphenyl-based ^{ISO}CNs will be discussed, their reactivity will also be detailed. In the second portion of this dissertation, collaborative work with University of California, San Diego's department of nanoengineering will be highlighted. The use of monotopic *m*-terphenyl isocyanide ligands as capping reagents on nanomaterial surfaces will be discussed in detail, as well as the synthesis and isolation of new functionalized ligand scaffolds to characterize their binding on gold (Au) and silver (Ag) surfaces.

Chapter 1 Metal Organic Frameworks With Low Valent Metal Nodes

1.1. An Introduction to Low Valent MOFS.

Metal–organic frameworks (MOFs) are self-assembled, crystalline materials with 2- or 3-dimensional framework structures.[1] These materials are traditionally synthesized using anionic linkers (e.g., carboxylates, azolates, etc.) with high-valent metal ions/clusters, referred to as secondary building units (SBUs).[2] Strong, but sufficiently reversible, metal–ligand bonding allows for the formation of robust MOFs using these ligands and metals.[3] However, the formally oxidized nature of these SBUs precludes both the reductive chemistry and substrate binding affinity (via π-backbonding) that are the hallmark of low-valent metals.[4] While many MOFs have been shown to participate in Lewis acid catalysis, those involved in multi-electron catalysis are much more rare.[5] To impart MOFs with the ability to mediate multi-electron catalysis, several strategies have been developed to append low-valent metals to MOFs through ancillary metal binding groups. These have been extensively reviewed and will not be covered in detail here.[6–8] Incorporation of nonstructural low-valent metals can be accomplished before, during, or after formation of the MOF lattice. Most commonly, low-valent metals are incorporated into MOFs by postsynthetic modification (PSM) approaches,[9] specifically post synthetic metalation.[10] This involves the formation of a MOF structure containing free metal-binding groups and subsequent metalation of these sites using low-valent metal precursors. This has been demonstrated using phosphines, bipyridines, and other ligands.[11–14] Generally, incorporation of low-valent metals in MOFs requires the presence of both electronically soft Lewis basic donors and MOF-forming hard Lewis basic donors in a single ligand architecture. While this approach has been successful for the realization of functional MOFs, in these designs the low-valent metals are incorporated as pendant groups and

do not benefit from the stabilization attendant with lattice/network formation. As such, they may degrade or leach into solution when the materials are used for catalysis or other applications,[15] and the incorporation of these complexes as pendant groups can result in pore blockage, hindering substrate access to internal metal sites.[5] In addition, it is difficult to achieve high metal loadings, and structural characterization of the low-valent sites can be challenging, particularly by single-crystal X-ray diffraction (SCXRD) methods.[6–8] To date, there are few examples where low-valent metals are the main structural component in a MOF lattice. These MOFs will be referred to here as low-valent MOFs (LVMOFs). It should be noted that the chemistry of low-valent coordination polymers is well known and predates the emergence of LVMOFs.[16, 17] The definition of a MOF put forth by Matzger in 2017 is used herein, where MOFs are defined as "a class of coordination polymers comprising organic linkers wherein metal–ligand interaction/bonding leads to 2D or 3D crystalline network structures."[18] This requires that MOFs be crystalline, while omitting the qualifier that they must contain "potential voids" as defined by IUPAC.[19] In this dissertation, low-valent metals are defined as metals in the +1 or 0 oxidation state, or otherwise in an unusually low, reactive oxidation state. Additionally, some examples of MOFs containing reactive 4d transition metal nodes/SBUs in the +2/+3 oxidation state will be highlighted. MOF stability is largely dictated by the strength of the metal-ligand bonds that form the extended structure.[3] Low-valent metals typically form the strongest coordination bonds with neutral, π-acidic ligands, such as carbon monoxide (CO), phosphines, and isocyanides.[20–23] Neutral nitrogen donors (e.g., pyridine, nitriles) may also be used,[24, 25] although these ligands are poor π-acceptors,[26] and thus are not ideal

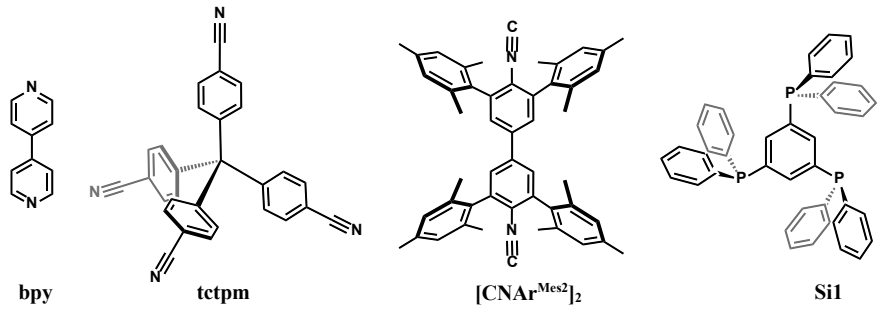

Figure 1.1 Ligands with pyridyl (bpy), nitrile (tctpm), isocyanide ((CNAr^{Mes2}), and phosphine (Si1) metal binding groups that have been used in LVMOF synthesis.

for forming stable LVMOFs. Neutral sulfur donors (e.g., thioethers) are electronically softer than nitrogen donors and have been employed as ligands for transition-metal-based catalyst precursors.[27] However, these ligands are both less effective σ-donors and π-acceptors when compared to phosphines. Neutral sulfur donors also frequently form labile metal-ligand bonds,[28] thereby hindering their use as linkers for LVMOFs.[29–33] The majority of LVMOFs reported to date have utilized linkers with two or more isocyanide, phosphine, or nitrogen donors, with linker structure, rigidity, and symmetry often resembling those of traditional MOF linkers that are used to produce divergent framework structures (Figure 1.1).

1.2. MOFs with Nitrogen Donors.

Some of the earliest coordination networks were synthesized from nitrile- and pyridine-based ligands with CuI nodes.[1] In 1989, Robson and co-workers demonstrated the deliberate design of a diamondoid CuI coordination network featuring a rigid 4,4',4'',4'''-tetracyanotetraphenylmethane (tctpm, Figure 1.1) linker.[34, 35] The resulting crystalline solid, with the formula [Cu(tctpm)](BF_4), has a SCXRD-estimated pore volume of 700 Å^3 and fits most definitions of a MOF. The demonstration of rational material design using a rigid, tetrahedral linker in concert with tetrahedral CuI centers represented an important step toward the emergence

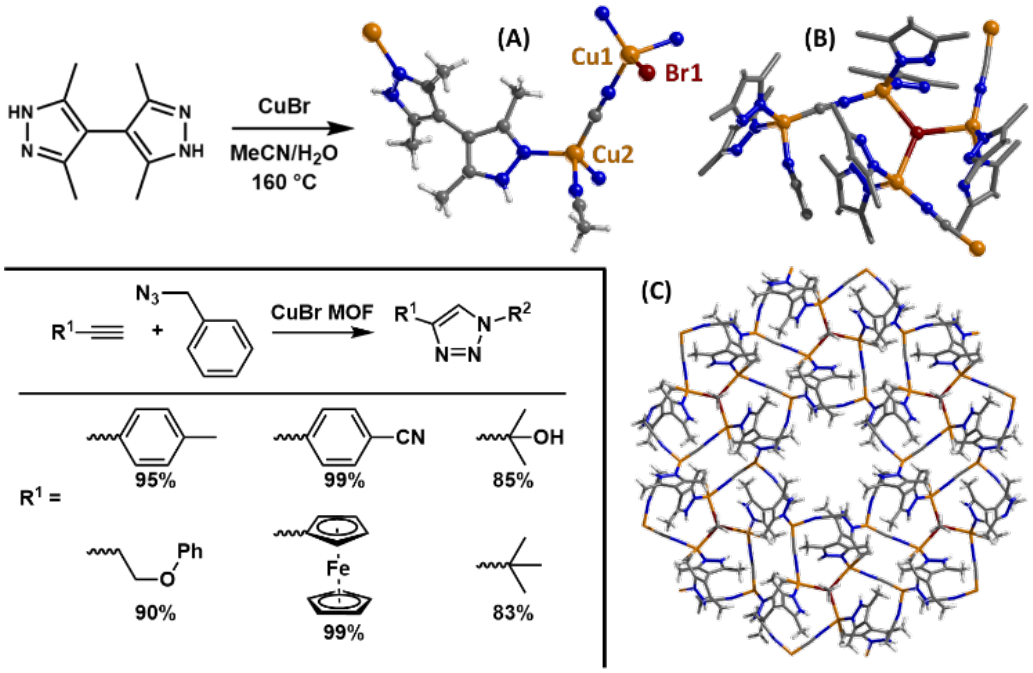

Figure 1.2. Synthesis of and crystal structure of CuBr MOF with images of A) the asymmetric unit, B) the full Cu_3Br trimeric SBU, and C) the extended structure along the crystallographic c-axis. Inset: AAC reaction catalyzed by CuBr MOF with substrate scope and corresponding yields.

of the MOF field. An early example from Yaghi and co-workers, for which the term "metal–organic framework" was coined, was realized by the solvothermal reaction of 4,4'-bipyridine (bpy, Figure 1.2) with CuI to give a 3D, interpenetrated framework.[36] These early examples of CuI coordination networks were instrumental in establishing the design principles for MOF synthesis but did not demonstrate high stability nor reactivity at the CuI centers. Indeed, harnessing the reactivity of low-valent metals in a heterogeneous setting is one of the primary motivations for the synthesis of LVMOFs. Since these early reports, several catalytically active CuI coordination networks have been described.[37, 38] One example is a 2015 report by Sun and co-workers, where the reaction of CuX (X=Cl, Br, I) with 3,3',5,5'-tetramethyl 4,4'-bipyrazole yielded three new coordination materials (Figure 1.2).[39] CuCl gave a 1D coordination polymer, while CuBr and CuI gave 3D LVMOFs. These materials demonstrated the ability to catalyze azide–alkyne "click"

(AAC) reactions in good yields. In addition, several studies have reported on unsaturated CuI sites in MFU-4l (metal–organic framework Ulm University-4large),[40] which have been investigated for

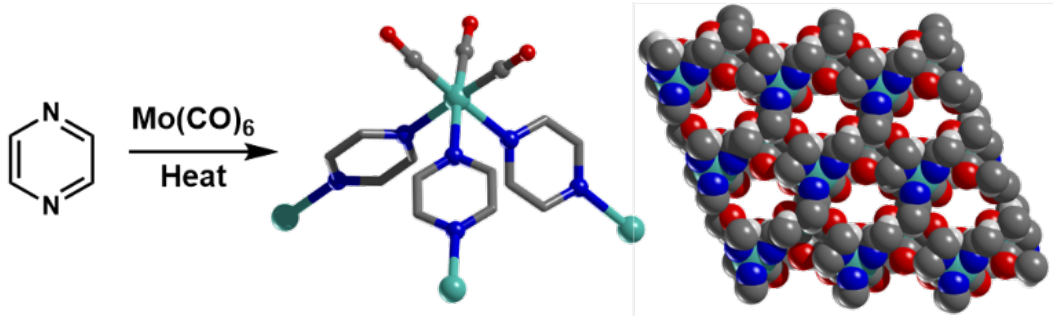

Figure 1.3. Synthesis and structure of fac-$Mo(CO)_3(pz)_{3/2}$ showing close-up of Mo(0) node (center) and space-filling representation of the extended structure along the crystallographic a-axis (right).

binding to CO, C_2H_4, and olefins.[41–43] LVMOFs with AgI nodes have been synthesized using neutral N-donors, with one of the first reported by Lee and co-workers in 1995.[44] Self-assembly of 1,3,5-tricyanobenzene (tcb) and 1,3,5-tris(4-ethynylbenzonitrile)benzene (teb) with $Ag(CF_3SO_3)$ in benzene resulted in the formation of 2D materials with honeycomb sheets. Charged N-donors have also been used to synthesize AgI MOFs, with one example described in a 2004 publication by Yang and Raptis.[45] The LVMOF was formed by the reaction of 3,5- diphenyl-1,2,4-triazole (3,5-Ph2-tz) with AgI salts. SCXRD revealed a 3D cationic framework assembled by the connection of $[Ag_5(\mu^3\text{-}3,5\text{-}Ph_2\text{-}tz)_6]$ clusters through two coordinate AgI ions to give the formula $Ag_3[Ag_5(\mu^3\text{-}3,5\text{-}Ph_2\text{- }tz)_6]^{2+}$, with uncoordinated NO_3^- or BF_4^- balancing the charge.

In 2021, Pedersen and co-workers described a series of LVMOFs, which represented only the second report of well-defined MOFs with zero-valent nodes (Figure 1.3).[46] Reaction of pyrazine (pz) with group 6 metal carbonyls gave 3D MOF structures with Cr(0) , Mo(0) , and W(0) nodes. The three isostructural MOFs have the formula fac-$M(CO)_3(pz)_{3/2}$ (M=Cr, Mo, W) and were characterized by SCXRD, revealing the presence of small open channels. The M(0) nodes are 3-connected through fac-oriented pyrazine donors, with three fac-oriented CO ligands filling

out the octahedral coordination sphere. Although the Cr(0) and W(0) MOFs were observed to decompose in air over a period of days, the Mo(0) material remained crystalline after a year in air and displayed the highest thermal stability of the three. This example demonstrates that, in certain cases, neutral N-donors can be used for LVMOF synthesis outside of monovalent group 11 cations.

1.3. LVMOFS with Organometallic Linkages.

Organometallic ligands forming metal-carbon bonds are an integral part of catalytic chemistry.[22] While some organometallic species exist only as short-lived intermediates in catalytic cycles, many are stable, isolable compounds. The most common are metal carbonyls,[47] although these are not suitable for derivatization as previously mentioned, and thus not viable as LVMOF linkers. Organoisocyanides are isolobal to CO, but can be readily adapted as multitopic ligands for the formation of organometallic coordination polymers and networks.[23] These function as both σ-donors and π-acceptors, with strong π-backbonding interactions allowing them to stabilize low-valent metals.[48, 49] In 1985 and 1986, Efraty and co-workers described the synthesis of mixed-valent $Pd^{0/II}/Pt^{0/II}$ and zero-valent Pd^{0} /Pt^{0} coordination polymers based on 4,4'-diisocyanobiphenyl,[50, 51] demonstrating the ability of isocyanides to stabilize low- and zero-valent metals in solid-state materials.

Some of the first ordered organoisocyanide networks were prepared by Lawrence and co-workers, who reported Cu^{I} coordination polymers connected through either 4,4'-diisocyanobenzene or 4,4'-diisocyanobiphenyl.[52] The polymers were found to be crystalline by PXRD and, although precise atomic structures were not determined, X-ray photoelectron spectroscopy (XPS) confirmed that Cu remained in the +1 oxidation state. Taking inspiration from these Cu^{I} -isocyanide coordination polymers and the ability of isocyanide ligands to stabilize Cu^{I} species with a range of geometries,[53] Figueroa and co-workers generated a series of Cu^{I}

coordination networks using sterically encumbered m-terphenyl isocyanide ligands.[54] Importantly, the atomic structures of these materials were determined by SCXRD. Reaction of the ditopic isocyanide linker $[CNAr^{Mes2}]_2$ (Figure 1.4A) with $[Cu(MeCN)_4](PF_6)$ afforded a 3D coordination material with tetrahedral, 4-connected Cu^I nodes, denoted as Cu^{ISO}CN-1. This 2-fold interpenetrated diamondoid network represented the first example of a structurally characterized 3D MOF constructed from diisocyanide linkers. Additional heating of Cu^{ISO}CN-1 resulted in exfoliation of 25% of the isocyanide linkers, yielding a 2D, interpenetrated coordination network with THF-capped tris isocyanide Cu^I nodes, Cu^{ISO}CN-2. An analogous MOF, Cu^{ISO}CN-3, was obtained directly using a higher reaction temperature under conditions otherwise identical to those used to synthesize Cu^{ISO}CN-1. This 2D material also displayed THF-capped tris-isocyanide Cu^I nodes but was found to be non-interpenetrated. Accordingly, gas sorption analysis of Cu^{ISO}CN-3 using CO_2 gave a Langmuir surface area of 200 m^2/g, demonstrating permanent porosity. The MOF displayed excellent thermal stability (beyond 450 °C) by thermogravimetric analysis (TGA), and as also shown to be stable in both acidic and basic environments, highlighting the ability of

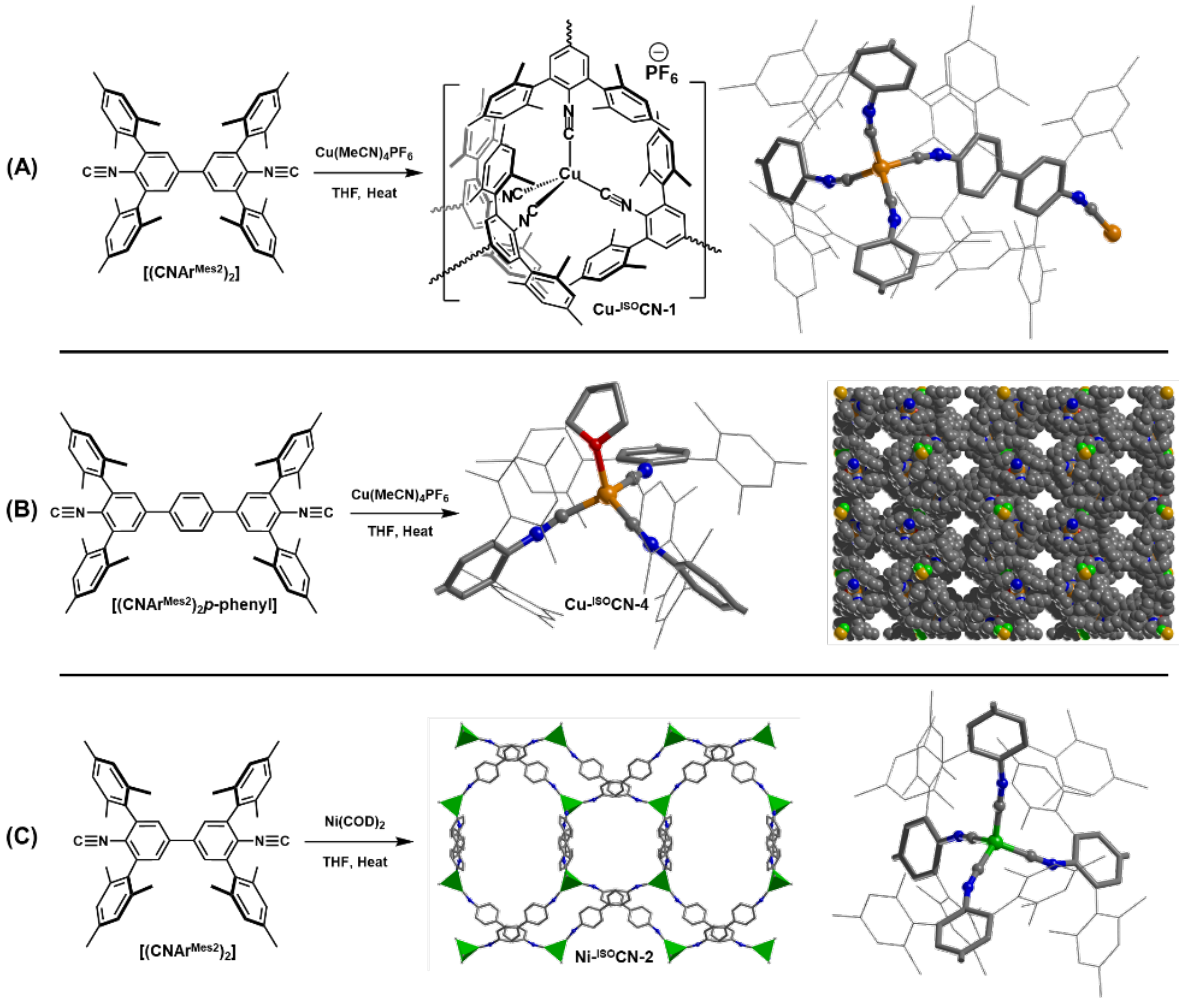

Figure 1.4. A) Synthesis and crystal structure of Cu-^{ISO}CN-1 showing tetrahedral CuI nodes;[51] B) synthesis and crystal structure of Cu-^{ISO}CN-4 highlighting 3-connected Cu^{I} node and extended structure of a single 1D sheet;[52] C) synthesis and crystal structure of Ni-^{ISO}CN-2 with view of extended structure and tetrahedral Ni^{0} nodes.[54] Color scheme: C=gray, N=blue, O=red, Cu=orange, Ni=green.

bulky isocyanide ligands to form highly stable LVMOFs. More recently, an expanded Cu(I) - isocyanide framework was reported featuring an extended ditopic m-terphenyl isocyanide linker, 1,4-$(CNAr^{Mes2})_2C_6H_4$ (Figure 1.4B).[55] The addition of a phenylene spacer between the isocyanide donors resulted in the formation of a MOF structure with large open channels, Cu^{ISO}CN-4. The structure is 4-fold interpenetrated and consists of interwoven 2D sheets, creating channels that measure approximately 28×19 Å. Although the material was not found to be permanently porous

by gas sorption, $Cu^{ISO}CN$-4 displayed thermal stability up to 400 °C and was shown to extract pyridine from aqueous media with 85% efficiency.

Having established that bulky *m*-terphenyl isocyanide linkers could form 2- and 3-dimensional MOF structures with Cu(I) , this approach was then extended to Ni^0 , a much more reactive low-valent metal.[57] Reaction of $Ni(COD)_2$ (COD=1,5-cyclooctadiene) with $[CNAr^{Mes2}]_2$ (Figure 1.4C) in THF yielded a crystalline material, $Ni^{ISO}CN$-2, which was shown by X-ray absorption spectroscopy (XAS) to contain Ni^0 exclusively. A similar procedure gave a single-crystalline material, which was determined by SCXRD to be a 3D MOF with tetrahedral Ni^0 nodes. The structure is a doubly interpenetrated diamondoid framework with 4-connected Ni^0 nodes bridged by the ditopic isocyanide linkers (Figure 1.4C). $Ni^{ISO}CN$-2 was found to be permanently porous by N_2 sorption experiments with a BET surface area of 580 m^2/g. The material displayed stability in a range of organic solvents under inert atmosphere, as well as thermal stability to ca. 300 °C by TGA. This work described the first example of a MOF with zero-valent metal nodes, marking an important milestone in the progression of the LVMOF field.

In 2019, Dong and co-workers reported a 2D Pd(II) LVMOF formed by the solvothermal reaction between a tritopic isocyanide linker and PdI_2.[58] This LVMOF was applied as a heterogeneous catalyst for Suzuki–Miyaura coupling to produce substituted biphenyls. Significantly, in comparison to molecular Pd-isocyanide catalysts, the LVMOF required lower reaction temperatures, shorter times, and lower catalyst loadings while giving much higher yields. N-Heterocyclic carbenes (NHCs) are another popular class of organometallic ligands for low-valent metals.[59, 60] Metal-NHC complexes have been incorporated as pendant groups in MOFs to produce heterogeneous catalysts.[61] Additionally, numerous coordination polymers based on metal-NHC bonds have been reported, including some catalytically active porous coordination

polymers.[62,63] Despite this, no crystalline LVMOFs have been described that are connected through structural metal-NHC bonds. Finally, platinum-acetylide coordination polymers were reported as early as the 1970's,[16] and gold-acetylide polymers are also well known.[17, 29] Acetylide ligands act as good σ-donors and moderate π-acceptors,[64,65] and thus, metal-acetylide linkages can be viable for LVMOF synthesis. Mak and co-workers have reported a plethora of 2D and 3D Ag^{I} -acetylide frameworks employing a mixed donor strategy.[66] A similar strategy was demonstrated in 2017 by Cao and co-workers, where Ag^{I} and (4- ethynylphenyl)diphenylphosphine were used to synthesize four 2D and 3D MOF structures.[67] The LVMOFs consist of high nuclearity Ag^{I} -phosphine clusters linked in two or three dimensions through Ag-acetylide bonds. However, the synthesis of LVMOFs with metal-acetylide linkages remains underdeveloped.

1.4. LVMOFs Based on Metal-Phosphine Bonds.

Organophosphine ligands are among the most widely used ligands in low-valent metal complexes.[68] Their soft, expanded lone pair of electrons (relative to 2p donors) allows for a significant degree of covalent orbital overlap, and π-backbonding can occur by donation from metal orbitals into P-C σ* orbitals.[66] Accordingly, a number of phosphine−metal coordination polymers have been reported,[67-69] and phosphines have been attached to various solid supports to heterogenize phosphine−metal complexes.[70] Humphrey,[71] Lin,[7] Wade,[72] and others[73] have pioneered the incorporation of organophosphine ligands into MOFs and the use of such materials as platforms for low-valent metal complexes. However, there exist only a handful of MOFs in which metal−phosphine bonds serve as primary structural elements.

A significant hurdle in the design and synthesis of phosphine-based LVMOFs is linker design. For example, Lim and Cohen reported a series of di- and tritopic phosphine ligands based on planar, aromatic cores (Figure 1.5).[74-78]

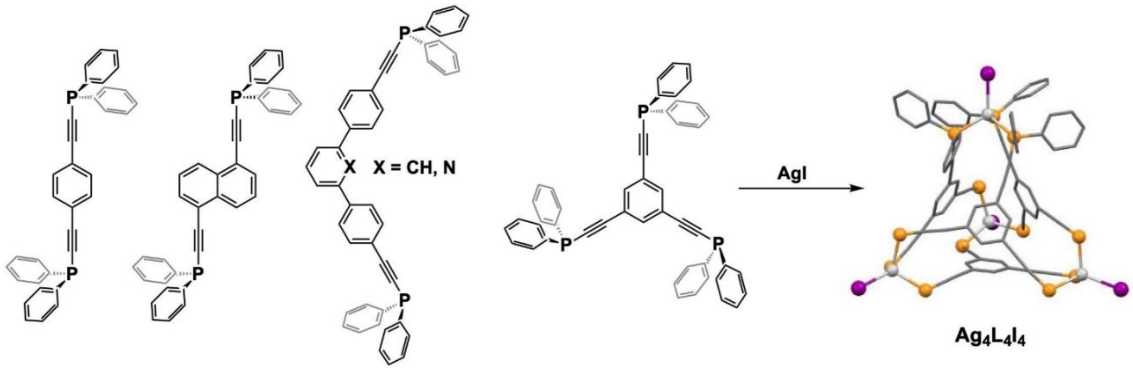

Figure 1.5. Di- and tri-topic phosphine ligands used for synthesis of 1D coordination polymers and 0D clusters. Reaction of tritopic phosphine ligand with Ag^I results in a 0D tetrahedral cluster.[74-75] For clarity, in the crystallographic representation, the phenyl groups have been removed from all phosphine ligands except one. Color scheme: C = gray, P = yellow, Ag = silver, I = purple.

The phosphine groups in these ligands were arranged in geometries analogous to the arrangement of carboxylate groups in common MOF linkers; however, only 0D clusters and 1D coordination polymers were obtained when these ligands were combined with Cu(I), Ag(I), and Au(I). Free rotation of the P−C bonds allows these ligands to adopt a range of geometries, while the trigonal pyramidal geometry of the phosphines and steric factors lead to lower symmetry compared to analogous carboxylate linkers. An additional issue is that many low-valent metals can only accommodate two or three phosphine ligands, meaning the metal sites in phosphine-based coordination polymers generally display lower connectivity compared to typical MOF nodes/SBUs. As early as 2002, James and co-workers prepared a 2D Ag^I -phosphine MOF by the reaction between 1,3,5- tris(diphenylphosphino)benzene and Ag(OTf).[79] The material contains Ag^I nodes in both linear and trigonal planar coordination geometries, forming a material with large open channels (1.60–1.84 nm). Solvent guests in the channels were readily exchanged and

removed by heating under vacuum, but surface areas were not reported. A Cu^{I} LVMOF based on the ligand 4-(3,5- bis(diphenylphosphino)phenyl)pyridine was reported by Su and co-workers in 2012.[80] The use of mixed pyridyl and phosphine donors allowed the formation of a 3D LVMOF structure with homochiral 1D channels. Three isostructural materials were synthesized with Cl^-, Br^- and PF_6^- counterions, CuL-Cl, CuL-Br and CuL- PF_6. The coordination networks are based on 3-connected, tetrahedral Cu^{I} centers bearing two phosphine donors, one pyridyl donor, and one halide (or solvent with weakly coordinating PF_6^-). CuL- Br and CuL-PF_6 were effective catalysts for the ketalization reaction between ethylene glycol and small ketones (e.g., 2- butanone) (Figure 1.6). Little to no conversion was observed for bulkier ketones (e.g., benzophenone), indicating size selectivity, and the LVMOFs were shown to be recyclable without loss of crystallinity.

In 2014, a 3D Ag^{I} MOF structure was reported that was obtained by the solvothermal reaction of the tetratopic phosphine linker 1,1,2,2-tetrakis((4- diphenylphosphino)phenyl)ethylene with $Ag(BF_4)$ in the presence of air.[81] Interestingly, the system was found to fix atmospheric CO_2 as carbonate, forming a 3D MOF structure. The same material was not obtained under an Ar atmosphere, demonstrating that the presence of CO_2 (and thus, the incorporation of carbonate) is essential for formation of the 3D structure. The trigonal planar Ag^{I} nodes of the material are 3-connected through two phosphine linkers and a μ_2-bridging carbonate, where the phosphine linkers are 4-connected to form a (3,4)-connected net. Open channels are visible in the crystal structure, although permanent porosity was not demonstrated.

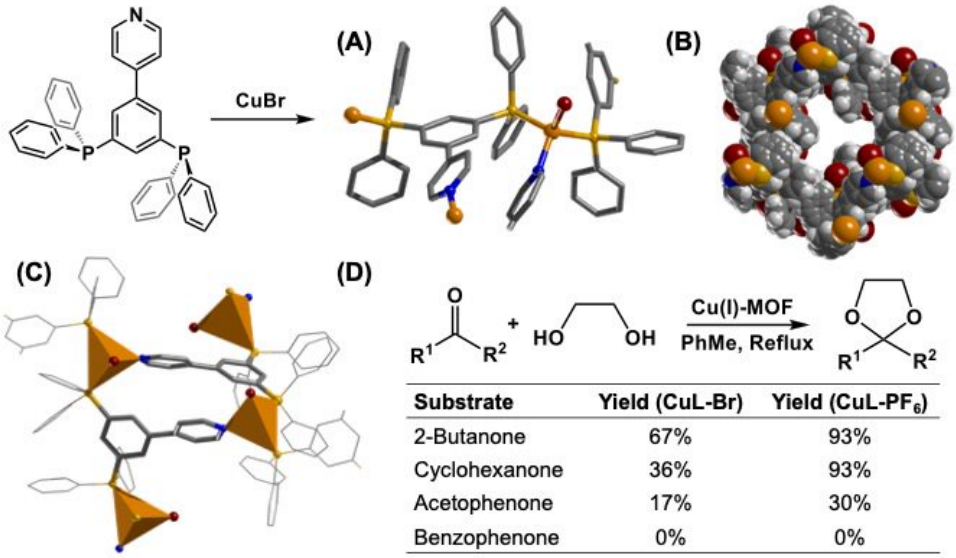

Substrate	Yield (CuL-Br)	Yield (CuL-PF_6)
2-Butanone	67%	93%
Cyclohexanone	36%	93%
Acetophenone	17%	30%
Benzophenone	0%	0%

Figure 1.6. Synthesis of CuL-Br and images of crystal structure showing: A) expanded asymmetric unit with full 3-connected linker and tetrahedral Cu(I) node; B) space-filling representation of open channel along crystallographic c-axis; C) dimeric Cu_2L_2 SBU. (D) Ketalization reaction catalyzed by CuL-Br and CuL-PF_6 with yields for substrates of varying size.[77] Color scheme: C = gray, H = white, N = blue, P = yellow, Cu = orange, Br = red.

In 2021, Humphrey and co-workers published a series of bimetallic MOFs based on a monometallic parent framework, PCM-102, with trimeric Co^{II} SBUs connected through carboxylated phosphine linkers and 4,4'-bipyridine.[82] PCM-102 was found to contain diphosphine pockets in which the approximately trans bis(phosphine) sites could coordinate single low-valent metal ions. This was demonstrated by postsynthetic incorporation of Cu^{I} , Ag^{I} , and Au^{I} , while the Ag^{I} version (Ag-PCM-102) could also be synthesized directly by coordination of the phosphines to Ag^{I} in situ during MOF growth. In this case, the trans-P_2(M) sites (M= Cu^{I}, Ag^{I}, Au^{I}) served as secondary 2-connected metal nodes.

Importantly, the installation of these low-valent nodes drastically improved the gas sorption properties of the bimetallic materials compared to the parent PCM-102. The N_2 BET surface areas of Ag- and Au-PCM-102 are over 1500 m^2/g, while silver-free PCM-102 is essentially non-porous. The increase in surface area for Cu-PCM-102 was more modest (N_2

SBET~ 400 m^2/g demonstrating that the porosity of the materials depends directly on the strength of the phosphine-metal bonds. These MOFs were evaluated for the separation of C2 hydrocarbons, wherein the selectivity for various C2 gases was found to be tunable based on the identity of the low-valent nodes. Although these MOFs contain more traditional SBUs in addition to the low-valent nodes, this work demonstrated that metal-phosphine linkages can serve as robust structural components to produce porous MOFs.

Phosphine-based coordination polymers of $Pd^{0/II}$ and $Pt^{0/ II}$ are known, as are MOFs incorporating Pd^{II} and Pt^{II} sites, but only recently LVMOFs containing persistent Pd^0 or Pt^0 sites have been described. In 2022, Sikma and Cohen detailed the synthesis of LVMOFs with Pd^0 and Pt^0 metal nodes stabilized by tetratopic phosphine linkers.[83] Tetra-phenylsilane/stanne-based ligands bearing diphenylphosphino groups in each of the para positions reacted with $Pd(PPh_3)_4$ or $Pt(PPh_3)_4$ to form (4,4)-connected diamondoid nets (Figure 1.7). Direct reaction between the linkers and $Pd(PPh_3)_4$ yielded poorly crystalline solids, which led the authors to develop triphenylphosphine-modulated syntheses that yielded highly crystalline materials. This circumvented a common issue in the synthesis of coordination polymers, wherein the formation of strong coordination bonds leads to kinetically inert linkages and prevents formation of highly crystalline materials.[84] The MOFs generally displayed air stability and good solvent stability under inert atmosphere and were found to be luminescent in the solid state. These materials represented the first examples of 3D, crystalline MOFs constructed using only metal-phosphine bonds, and the first MOFs with Pd^0 and Pt^0 metal nodes.

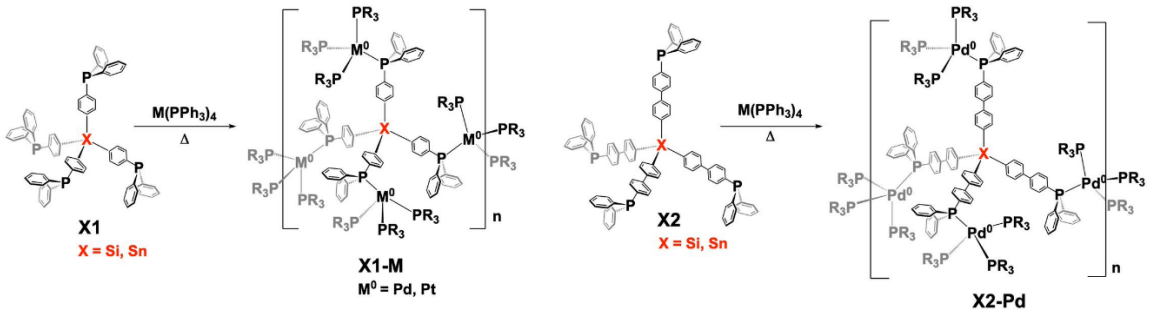

Figure 1.7. Synthetic scheme for M(0) MOFs using X1 and X2 linkers.

In addition to the isolation and characterization of three dimensional Pd(0) and Pt(0) LVMOFs, a one dimensional Rh(I) LVMOF (Sn1-Rh) was also reported by Sikma and Cohen through the use of the tetratopic phosphine linker Sn1. Importantly, inspection of the crystal structure of Sn1-Rh reveals the nodes in the material are coordinatively unsaturated. This provided evidence that tetratopic phosphine linkers enable the formation of LVMOFs with the ability to bind substrates for catalytic applications. Indeed, this was further investigated by Griffin and Cohen, who reported the synthesis of an Ir(I) coordination polymer from the tetratopic phosphine ligand SnX1 coupled with the use of PPh_3 as a modulator (Figure 1.8).[84] Importantly, the nodes in the material, denoted Sn1-Ir, are effectively analogues of Vaska's complex and are capable of reversibly binding O_2. Furthermore, the material displays similar reactivity to Vaska's complex as it can catalyze the reductive formation of enamines from amides. While Vaska's complex outperforms Sn1-Ir in terms of catalytic activity, the material is easily recycled between catalytic reactions. The study of Sn1-Ir provides insight towards future development of heterogeneous analogues of low-valent homogenous catalysts.

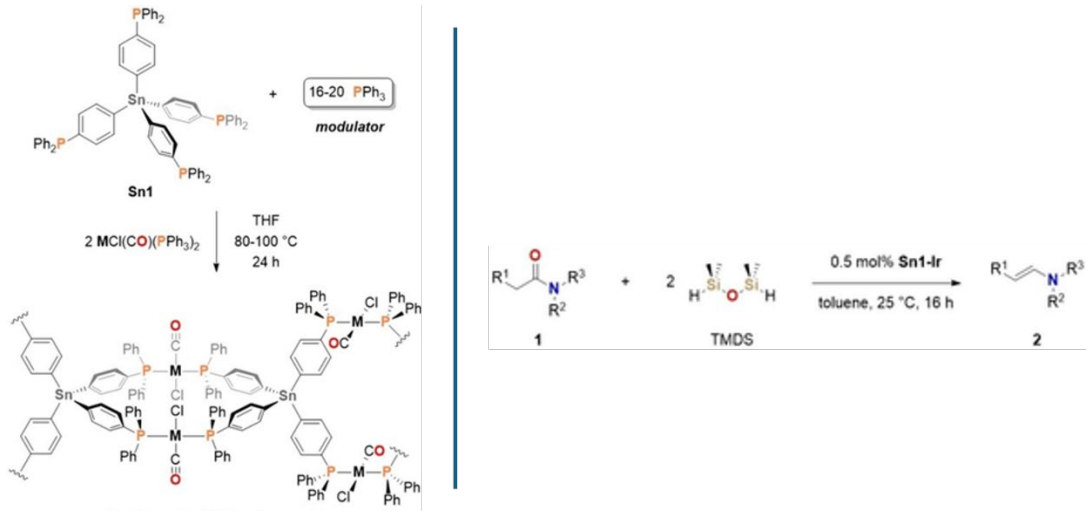

Figure 1.8. (Left) Synthesis of Sn1-Ir.(Right) Reaction scheme for the Sn1-Ir catalyzed reductive formation of enamines.[85]

1.5. Conclusions.

Examples of LVMOFs predate even the use of the term "MOF", with many early LVMOFs incorporating Cu^{I} or Ag^{I} metal nodes. However, other examples of LVMOFs incorporating zero- and other low-valent metal nodes remain largely unexplored. While ligand design and synthesis of these systems may be nontrivial, there remains many opportunities to prepare new LVMOFs. These may be targeted for catalytic applications and expanding the scope of LVMOFs will undoubtedly lead to the discovery of emergent properties that could significantly widen the range of potential applications.

1.6. Acknowledgements.

Chapter 1 is adapted from Balto, K.P.; Sikma, R.E.; Figueroa, J.S.; Cohen, S. "Metal Organic Frameworks with Low Valent Metal Nodes*" Angew. Chem. Int. Ed*. **2022**, 61 (33), e202206353. The dissertation author was the co-first author of this paper. Permission to include published material in this dissertation has been obtained from all coauthors.

1.7. References.

[1] O. M. Yaghi, M. J. Kalmutzki, C. S. Diercks, in *Introduction to Reticular Chemistry* (Eds.: O. M. Yaghi, M. J. Kalmutzki, C. S. Diercks), 2019, pp. 1-27.

[2] C. Gropp, S. Canossa, S. Wuttke, F. Gándara, Q. Li, L. Gagliardi, O. M. Yaghi, *ACS Cent. Sci.* 2020, *6*, 1255-1273.

[3] M. Ding, X. Cai, H.-L. Jiang, *Chem. Sci.* **2019**, 10, 10209-10230.

[4] J. Liu, L. Chen, H. Cui, J. Zhang, L. Zhang, C.-Y. Su, *Chem. Soc. Rev.* 2014, *43*, 6011-6061.

[5] V. Pascanu, G. González Miera, A. K. Inge, B. Martín-Matute, *J. Am. Chem. Soc.* 2019, *141*, 7223-7234.

[6] R. J. Young, M. T. Huxley, E. Pardo, N. R. Champness, C. J. Sumby, C. J. Doonan, *Chem. Sci.* 2020, *11*, 4031-4050.

[7] T. Drake, P. Ji, W. Lin, *Acc. Chem. Res.* 2018, *51*, 2129-2138.

[8] S. Jeoung, S. Kim, M. Kim, H. R. Moon, *Coord. Chem. Rev.* 2020, *420*, 213377.

[9] M. Kalaj, S. M. Cohen, *ACS Cent. Sci.* 2020, *6*, 1046-1057.

[10] J. D. Evans, C. J. Sumby, C. J. Doonan, *Chem. Soc. Rev.* 2014, *43*, 5933-5951.

[11] M. I. Gonzalez, E. D. Bloch, J. A. Mason, S. J. Teat, J. R. Long, *Inorg. Chem.* 2015, *54*, 2995-3005.

[12] R. E. Sikma, P. Kunal, S. G. Dunning, J. E. Reynolds, J. S. Lee, J.-S. Chang, S. M. Humphrey, *J. Am. Chem. Soc.* 2018, *140*, 9806-9809.

[13] A. J. Nuñez, L. N. Shear, N. Dahal, I. A. Ibarra, J. Yoon, Y. K. Hwang, J.-S. Chang, S. M. Humphrey, *Chem. Commun.* 2011, *47*, 11855-11857.

[14] T. Sawano, N. C. Thacker, Z. Lin, A. R. McIsaac, W. Lin, *J. Am. Chem. Soc.* 2015, *137*, 12241-12248.

[15] A. Dhakshinamoorthy, H. Garcia, *Chem. Soc. Rev.* 2014, *43*, 5750-5765.

[16] K. A. Williams, A. J. Boydston, C. W. Bielawski, *Chem. Soc. Rev.* 2007, *36*, 729-744.

[17] R. J. Puddephatt, *Chem. Commun.* 1998, 1055-1062.

[18] S. Seth, A. J. Matzger, *Cryst. Growth. Des.* 2017, *17*, 4043-4048.

[19] S. R. Batten, N. R. Champness, X.-M. Chen, J. Garcia-Martinez, S. Kitagawa, L. Öhrström, M. O'Keeffe, M. Paik Suh, J. Reedijk, *Pure Appl. Chem.* 2013, *85*, 1715-1724.

[20] J. Chatt, *J. Inorg. Nucl. Chem.* 1958, *8*, 515-531.

[21] D. J. Durand, N. Fey, *Chem. Rev.* 2019, *119*, 6561-6594.

[22] R. H. Crabtree, in *The Organometallic Chemistry of the Transition Metals*, 6th ed. (Ed.: R. H. Crabtree), John Wiley & Sons Inc., 2014, pp. 1-39.

[23] M. Knorn, E. Lutsker, O. Reiser, *Chem. Soc. Rev.* 2020, *49*, 7730-7752.

[24] S. Kitagawa, R. Kitaura, S.-i. Noro, *Angew. Chem., Int. Ed.* 2004, *43*, 2334-2375.

[25] J. R. Farrell, G. J. Kerins, K. L. Niederhoffer, L. A. Crandall, C. Ziegler, *J. Organomet. Chem.* 2016, *813*, 41-45.

[26] L. Palacios, A. Di Giuseppe, R. Castarlenas, F. J. Lahoz, J. J. Pérez-Torrente, L. A. Oro, *Dalton Trans.* 2015, *44*, 5777-5789.

[27] J. C. Bayón, C. Claver, A. M. Masdeu-Bultó, *Coord. Chem. Rev.* 1999, *193-195*, 73-145.

[28] M. Mellah, A. Voituriez, E. Schulz, *Chem. Rev.* 2007, *107*, 5133-5209.

[29] R. J. Puddephatt, *Chem. Soc. Rev.* 2008, *37*, 2012-2027.

[30] J. R. Black, N. R. Champness, W. Levason, G. Reid, *J. Chem. Soc., Chem. Commun.* 1995, 1277-1278.

[31] J. He, C. Yang, Z. Xu, M. Zeller, A. D. Hunter, J. Lin, *J. Solid State Chem.* 2009, *182*, 1821-1826.

[32] X.-Q. Liang, R. K. Gupta, Y.-W. Li, H.-Y. Ma, L.-N. Gao, C.-H. Tung, D. Sun, *Inorg. Chem.* 2020, *59*, 2680-2688.

[33] X. Huang, H. Li, Z. Tu, L. Liu, X. Wu, J. Chen, Y. Liang, Y. Zou, Y. Yi, J. Sun, W. Xu, D. Zhu, *J. Am. Chem. Soc.* 2018, *140*, 15153-15156.

[34] B. F. Hoskins, R. Robson, *J. Am. Chem. Soc.* 1989, *111*, 5962-5964.

[35] B. F. Hoskins, R. Robson, *J. Am. Chem. Soc.* 1990, *112*, 1546-1554.

[36] O. M. Yaghi, H. Li, *J. Am. Chem. Soc.* 1995, *117*, 10401-10402.

[37] X. Wang, M. Liu, Y. Wang, H. Fan, J. Wu, C. Huang, H. Hou, *Inorg. Chem.* 2017, *56*, 13329-13336.

[38] H. Fei, D. L. Rogow, S. R. J. Oliver, *J. Am. Chem. Soc.* 2010, *132*, 7202-7209.

[39] Z. Xu, L. L. Han, G. L. Zhuang, J. Bai, D. Sun, *Inorg. Chem.* 2015, *54*, 4737-4743.

[40] G. B. Gardner, D. Venkataraman, J. S. Moore, S. Lee, *Nature.* 1995, *374*, 792-795.

[41] G. Yang, R. G. Raptis, *Chem. Commun.* 2004, 2058-2059.

[42] L. Voigt, R. Wugt Larsen, M. Kubus, K. S. Pedersen, *Chem. Commun.* 2021, *57*, 3861-3864.

[43] in *The Organometallic Chemistry of the Transition Metals*, 2014, pp. 1-39.

[44] M. Wrighton, *Chem. Rev.* 1974, *74*, 401-430.

[45] A. E. Carpenter, C. C. Mokhtarzadeh, D. S. Ripatti, I. Havrylyuk, R. Kamezawa, C. E. Moore, A. L. Rheingold, J. S. Figueroa, *Inorg. Chem.* 2015, *54*, 2936-2944.

[46] Y. Yamamoto, *Coord. Chem. Rev.* 1980, *32*, 193-233.

[47] I. Jaffe, M. Segal, A. Efraty, *J. Organomet. Chem.* 1985, *294.*

[48] I. Feinstein-Jaffe, A. Efraty, *J. Mol. Catal.* 1986, *35*, 285–302.

[49] I. Feinstein-Jaffe, I. Biran, D. Mahalu, S. Cohen, S. A. Lawrence, *Inorganica Chim. Acta* 1988, *154*, 129-131.

[50] B. J. Fox, Q. Y. Sun, A. G. DiPasquale, A. R. Fox, A. L. Rheingold, J. S. Figueroa, *Inorg. Chem.* 2008, *47*, 9010-9020.

[51] D. W. Agnew, M. Gembicky, C. E. Moore, A. L. Rheingold, J. S. Figueroa, *J. Am. Chem. Soc.* 2016, *138*, 15138-15141.

[52] A. Arroyave, M. Gembicky, A. L. Rheingold, J. S. Figueroa, *Inorg. Chem.* 2020, *59*, 11868-11878.

[53] K. P. Balto, M. Gembicky, A. L. Rheingold, J. S. Figueroa, *Inorg. Chem.* 2021, *60*, 12545-12554.

[54] D. W. Agnew, I. M. DiMucci, A. Arroyave, M. Gembicky, C. E. Moore, S. N. MacMillan, A. L. Rheingold, K. M. Lancaster, J. S. Figueroa, *J. Am. Chem. Soc.* 2017, *139*, 17257-17260.

[55] Y. Dong, J.-J. Jv, X.-W. Wu, J.-L. Kan, T. Lin, Y.-B. Dong, *Chem. Commun.* 2019, *55*, 14414-14417.

[56] D. Bourissou, O. Guerret, F. P. Gabbaï, G. Bertrand, *Chem. Rev.* 2000, *100*, 39-92.

[57] W. A. Herrmann, *Angew. Chem., Int. Ed.* 2002, *41*, 1290-1309.

[58] C. I. Ezugwu, N. A. Kabir, M. Yusubov, F. Verpoort, *Coord. Chem. Rev.* 2016, *307*, 188-210.

[59] C. Zhang, J.-J. Wang, Y. Liu, H. Ma, X.-L. Yang, H.-B. Xu, *Chem. Eur. J.* 2013, *19*, 5004-5008.

[60] S. Gonell, M. Poyatos, E. Peris, *Chem. Eur. J.* 2014, *20*, 5746-5751.

[61] J. E. McGrady, T. Lovell, R. Stranger, M. G. Humphrey, *Organometallics.* 1997, *16*, 4004-4011.

[62] D. L. Lichtenberger, S. K. Renshaw, R. M. Bullock, *J. Am. Chem. Soc.* 1993, *115*, 3276-3285.

[63] Y.-P. Xie, T. C. W. Mak, *J. Clust. Sci.* 2014, *25*, 189-204.

[64] S. Zhang, Z. Zhang, R. Cao, *Inorganica Chim. Acta* 2017, *461*, 57-63.

[65] W. Levason, in *Organophosphorus Compounds (1990)*, 1990, pp. 567-641.

[66] A. Vogler, H. Kunkely, *Coord. Chem. Rev.* 2002, *230*, 243-251.

[67] M.-C. Brandys, R. J. Puddephatt, *J. Am. Chem. Soc.* 2002, *124*, 3946-3950.

[68] M.-C. Brandys, R. J. Puddephatt, *J. Am. Chem. Soc.* 2001, *123*, 4839-4840.

[69] G. K. Kole, C. K. Chin, G. K. Tan, J. J. Vittal, *Polyhedron.* 2013, *52*, 1440-1448.

[70] G. R. F. Orton, B. S. Pilgrim, N. R. Champness, *Chem. Soc. Rev.* 2021, *50*, 4411-4431.

[71] S. G. Dunning, G. Nandra, A. D. Conn, W. Chai, R. E. Sikma, J. S. Lee, P. Kunal, J. E. Reynolds Iii, J.-S. Chang, A. Steiner, G. Henkelman, S. M. Humphrey, *Angew. Chem., Int. Ed.* 2018, *57*, 9295-9299.

[72] S. A. Burgess, A. Kassie, S. A. Baranowski, K. J. Fritzsching, K. Schmidt-Rohr, C. M. Brown, C. R. Wade, *J. Am. Chem. Soc.* 2016, *138*, 1780-1783.

[73] A. Beloqui Redondo, F. L. Morel, M. Ranocchiari, J. A. van Bokhoven, *ACS Catal.* 2015, *5*, 7099-7103.

[74] S. H. Lim, Y. Su, S. M. Cohen, *Angew. Chem., Int. Ed.* 2012, *51*, 5106-5109.

[75] S. H. Lim, S. M. Cohen, *Inorg. Chem.* 2013, *52*, 7862-7872.

[76] X. Xu, M. Nieuwenhuyzen, S. L. James, *Angew. Chem., Int. Ed.* 2002, *41*, 764-767.

[77] X. Tan, L. Li, J. Zhang, X. Han, L. Jiang, F. Li, C.-Y. Su, *Chem. Mater.* 2012, *24*, 480-485.

[78] J. Zhang, Q. Yang, Y. Zhu, H. Liu, Z. Chi, C.-Y. Su, *Dalton Trans.* 2014, *43*, 15785-15790.

[79] R. E. Sikma, N. Katyal, S.-K. Lee, J. W. Fryer, C. G. Romero, S. K. Emslie, E. L. Taylor, V. M. Lynch, J.-S. Chang, G. Henkelman, S. M. Humphrey, *J. Am. Chem. Soc.* 2021, *143*, 13710-13720.

[80] R. E. Sikma, S. M. Cohen, *Angew. Chem., Int. Ed.* 2022, *61*, e202115454.

[81] R. S. Forgan, *Chem. Sci.* 2020, *11*, 4546-4562.

[82] M. García-Melchor, A. A. C. Braga, A. Lledós, G. Ujaque, F. Maseras, *Acc. Chem. Res.* 2013, *46*, 2626-2634.

[83] J. A. R. Navarro, E. Barea, J. M. Salas, N. Masciocchi, S. Galli, A. Sironi, C. O. Ania, J. B. Parra, *Inorg. Chem.* 2006, *45*, 2397-2399.

[84] F. X. Llabrés i Xamena, A. Abad, A. Corma, H. Garcia, *J. Catal.* 2007, *250*, 294-298.

[85] S.E. Griffin, G.P. Domescus, C. E. Flores, R.E. Sikma, L. Benz, S.M. Cohen, *Angew. Chem., Int. Ed.*2023, *62, 23,* e202301611.

Chapter 2 Crystalline Hydrogen-Bonding Networks and Mixed-Metal Framework Materials Enabled by an Electronically Differentiated Heteroditopic Isocyanide/Carboxylate Linker Group.

2.1. Introduction.

Metal-organic frameworks (MOFs) are traditionally designed by capitalizing on hard/soft Lewis acid-base theory, where formally oxidized, hard Lewis-acidic metal centers are combined with anionic, hard Lewis-basic linkers to form strong ionic bonds.[7-10] These ionic metal-ligand interactions can lead to extremely robust frameworks that often possess permanent porosity and high internal surface areas.[4–6,11] However, the reliance on oxidized metal centers for the construction of structural nodes (*i.e.* secondary building units; SBUs) in these network materials often precludes their direct participation in multi-electron redox processes. Such redox behavior is exemplified by low-valent metal centers, which are electronically mismatched with hard, anionic ligands for the purpose of network formation.[12-13] Accordingly, there have been increasing efforts aimed at the preparation of mixed-metal MOFs, where hard Lewis-acidic metal centers comprise the structural portion of the network, while "softer", more electron-rich metal centers are appended as reactive sites.[14] As such materials find increasing applications in multi-electron or tandem/cooperative catalysis,[4, 14-15] the development of strategies and methods for their reliable preparation remains desirable.

Several approaches have been reported for the formation of mixed-metal MOFs where low-valent metal centers are a component. Notable among these include post-synthetic metal-ion incorporation into multi-functional linkers,[16-17] metal deposition onto high-valent SBUs[18-21] and the use of either metalloligands[22-25] or heteroditopic linker groups. Of these strategies, heteroditopic linkers offer unique advantages for the reliable formation of mixed-metal framework materials, as two different binding groups can be tuned to match the electronic requirements attendant between "hard" and "soft" metal centers. Recently, we introduced

ditopic *m*-terphenyl isocyanides, $[CNAr^{Mes2}]_2$ and 1,4-$(CNAr^{Mes2})_2C_6H_4$ (Ar^{Mes2} = 2,6-(2,4,6-$Me_3C_6H_2)_2C_6H_2$) as linkers for metal-organic framework materials.[26-28] Isocyanides are electronically "soft" neutral ligands that function as good σ -donors and effective π-acids in a manner similar to that of carbon monoxide (CO).[29-30] While neutral in charge, isocyanides form robust M-L linkages on account of strong π-backing bonding interactions and are therefore adept at stabilizing low-valent metal centers.[13, 31-35] As we have previously reported, ditopic *m*-terphenyl isocyanides can be employed for the formation of thermally robust and crystalline organometallic network materials featuring electron-rich metal centers (e.g. Cu(I) and Ni(0)) as structural nodes.[26-28] However, isocyanides are particularly poor ligands for hard metals (e.g. Mg^{2+}, Zn^{2+}) or metals in high formal oxidation states (e.g. Zr^{4+}). Seeking to exploit this disparate coordination behavior, we reasoned that heteroditopic ligands based on an isocyanide and an anionic binding group could offer a uniquely differentiated electronic environment for the formation of mixed-metal network materials. Accordingly, here we report the preparation and use of a heteroditopic isocyanide/carboxylate linker for the formation of robust mixed-metal network materials. In addition, we show this rigid linker system can also provide hydrogen-bonding networks[36-41] that bridge between molecular and extended-network systems with low-valent metals.

2.2. Results and Discussion.

To retain the encumbering steric properties of the *m*-terphenyl isocyanide framework, while also introducing a carboxylate group in a rigid, linear topology, we targeted the heteroditopic ligand, 1- $CNAr^{Mes2}$-4-$C_6H_4COH_2$ (TIB^{Mes2}; TIB = terphenyl isocyanide benzoate). This linker features a benzoic acid group appended to the *para*-position of the monodentate $CNAr^{Mes2}$ ligand, which has been well utilized for the preparation of low-coordinate, low-valent transition- metal complexes.[42-52] The synthesis of this heterotopic ligand was straightforward and was accomplished

by Suzuki coupling of the *para*-bromo *m*-terphenyl formamide, HC(O)NH(*p*-BrAr^{Mes2}), with 4-methoxycarbonylphenylboronic acid to provide the methyl-ester-protected heterotopic *m*-terphenyl formamide ligand, 1-HC(O)N(H)Ar^{Mes2}-4-$C_6H_4CO_2CH_3$ (Figure 3.1). Subsequent dehydration of this formamide afforded the protected isocyanide 1,4-(CNAr^{Mes2})$C_6H_4CO_2CH_3$, as an off-white solid. The latter was readily deprotected with aqueous

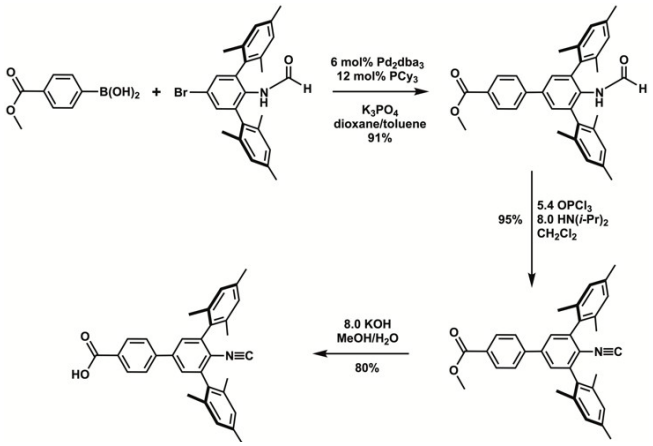

Figure 2.1. Synthesis of the heteroditopic isocyanide/Carboxylate Ligand TIB^{Mes2}H.

KOH to provide the target carboxylic acid, TIB^{Mes2} in 80% yield after an acidic work up (Scheme 1). The isocyano-carboxylic acid TIB^{Mes2} is isolated as colorless microcrystalline solid and gives rise to a ν_{CN} stretching band of 2117 cm^{-1} (ATR-IR) and $^{13}C\{^1H$ NMR chemical shift of 170.9 ppm for the isocyanide carbon. These spectroscopic features agree well with previously reported mono- and di-topic *m*-terphenyl isocyanides.[26, 28, 30] Crystallographic structural determination of 1,4-(CNAr^{Mes2})$C_6H_4CO_2H$ revealed that it is indeed an asymmetric rigid linear organoisocyanide containing a benzoic acid group. In the solid state, the benzoic acid group is canted ~33˚ relative to Ar^{Mes2} unit (Figure 3.33). This torsion angle is similar to that found between the CNAr^{Mes2} groups and the phenylene spacer in the ditopic isocyanide 1,4-(CNAr^{Mes2})$_2C_6H_4$,[28] but differs substantially from the solid-structure of the directly fused ditopic isocyanide, [CNAr^{Mes2}], which adopts a nearly co-planar arrangement of its central biphenyl unit.[26]

However, it is important to note that 1,4-($CNAr^{Mes2}$)$C_6H_4CO_2H$ packs distinct herringbone arrangement in the solid state on account of significant hydrogen bonding between the carboxylic acid groups (Figure 3.34).

To explore the ligation properties of 1,4- ($CNAr^{Mes2}$)$C_6H_4CO_2H$ and determine whether the isocyanide unit can bind selectively to low-valent metals, we surveyed its coordination behavior toward Cu(I) centers. There is a long-standing coordination chemistry of Cu(I) isocyanide complexes,[53-55] and they have been utilized by us and others to assess the relative binding abilities of derivatized isocyanide ligands.[42, 56-58] While Cu(I) centers are not the most effective π-bases, the relatively low +1 formal oxidation state does not lead to an energetically contracted d-orbital manifold. This feature allows Cu(I) centers to bind electronically "softer" ligands such as isocyanides, phosphines and thiols readily, which contrasts with formally Zn(II) centers despite being isoelectronic. However, Cu(I) carboxylates are also a well-known class of molecular and network materials,[59-62] thereby providing an ideal test for the ability of a heteroditopic isocyanide/carboxylate ligand for binding selectivity on the basis of electronic differentiation. The isocyanide unit of TIB^{Mes2} can selectively bind to Cu(I) centers and extent of ligation in the resulting complexes can be controlled by steric pressures of the *m*- terphenyl group. For example, treatment of TIB^{Mes2} with $[Cu(NCMe)_4]PF_6$ in a 3:1 ratio within THF solution generates a single new product as assayed by ^1H NMR spectroscopy. Importantly, this ^1H NMR spectrum featured a broad resonance at +13.1 ppm which is indicative of a preserved carboxylic acid unit. FTIR analysis revealed a sharp ν_{CN} band centered at 2152 cm^{-1}. As we have shown previously for both molecular Cu(I) trisisocyanide complexes,[42] as well as isocyanide networks featuring Cu(I) trisisocyanide SBUs,[26, 28] such a high-energy ν_{CN} band is diagnostic of a cationic $[(L)Cu(CNR)_3]^+$

coordination environment where the fourth L-type ligand is a weak σ-donor. In the presence of stronger σ-donors, a distinctive shift of the ν_{CN} to lower energy is observed due to greater Cu p-orbital participation in bonding.[28] Unfortunately, despite multiple attempts, single crystals suitable for structural determination from this 3:1 TIB^{Mes2}/$[Cu(NCMe)_4]PF_6$

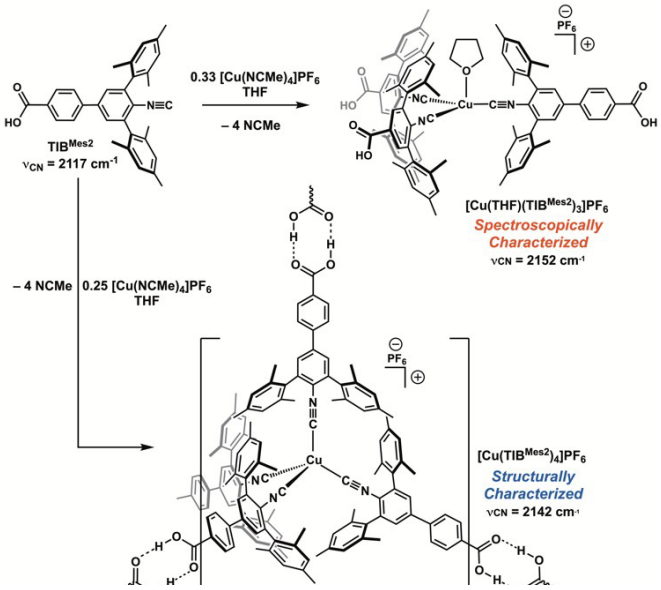

Figure 2.2. Coordination studies of TIB^{Mes2} with Cu(I) centers.

reaction could not be obtained. However, circumstantial evidence for the formation of tris-isocyanide $[Cu(TIB^{Mes2})_3]PF_6$ complex comes from the reaction of TIB^{Mes2} and $[Cu(NCMe)_4]PF_6$ in a 4:1 ratio (Scheme 2.2). Analysis of this latter reaction mixture by solution-phase IR spectroscopy resulted in the same 2152 cm^{-1} ν_{CN} band as the reaction employing a 3:1 TIB^{Mes2}/Cu ratio. However, this band was also accompanied by less intense band at 2118 cm^{-1} indicative of free TIB^{Mes2}. Previously, we have shown that the molecular salt $[(THF)Cu(CNAr^{Mes2})_3]OTf$, which features the same *m*-terphenyl unit as that found in TIB^{Mes2}, resists the binding of a fourth isocyanide ligand in solution.[42] Instead, 1:1 $[(THF)Cu(CNAr^{Mes2})3]OTf/CNAr^{Mes2}$ mixtures establish a

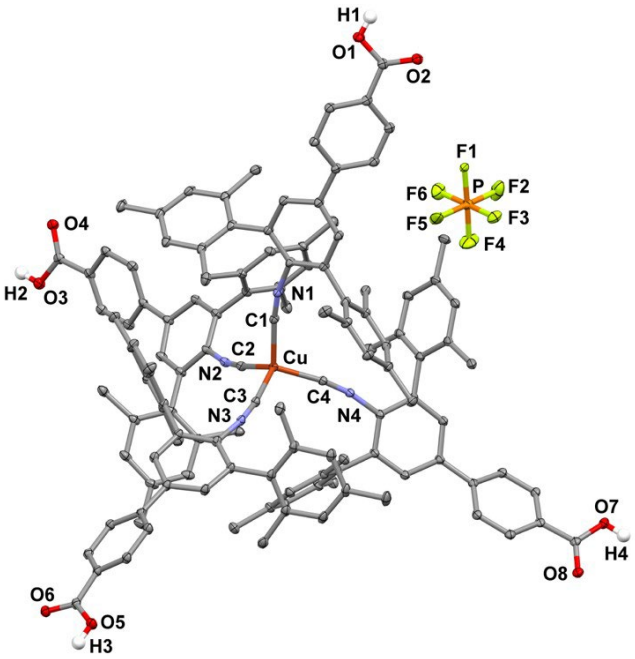

Figure 2.3. Molecular structure of the molecular core of the hydrogen-bonded network $[Cu(TIB^{Mes2})_4]PF_6$. Hydrogen atoms other than those on the carboxylate groups and solvent molecules of co-crystallization have been omitted for clarity.

rapid isocyanide-exchange equilibrium where the putative tetra-isocyanide species$[(THF)Cu(CNAr^{Mes2})_3]OTf$ does not build up to an observable extent by either FTIR or ^1H NMR spectroscopy. On account of the similar steric profile between TIB^{Mes2} and $CNAr^{Mes2}$, we contend that a similar exchange process is likely established in solution and that the 2152 cm^{-1} ν_{CN} band arises from the tris-isocyanide complex, $[(THF)Cu(TIB^{Mes2})_3]PF_6$. Adding further credence to this suggestion, is the fact that crystallization of the 4:1 $TIB^{Mes2}/[Cu(NCMe)_4]PF_6$ mixture from CH_2Cl_2 solution resulted in colorless single crystals, which were determined to be the tetra-isocyanide complex $[Cu(TIB^{Mes2})_4]PF_6$ by X-ray crystallography (Figure 2.3). Most importantly, ATR-IR analysis of single crystals of $[Cu(TIB^{Mes2})_4]PF_6$, which possesses a Cu enter bound by four reasonably strong sigma donating ligands, resulted in a ν_{CN} band of 2142 cm^{-1}. Accordingly, we believe that the 2152 cm^{-1} obtained in the 3:1 $TIB^{Mes2}/[Cu(NCMe)_4]PF_6$

reaction reasonably arises from a tris-isocyanide species.

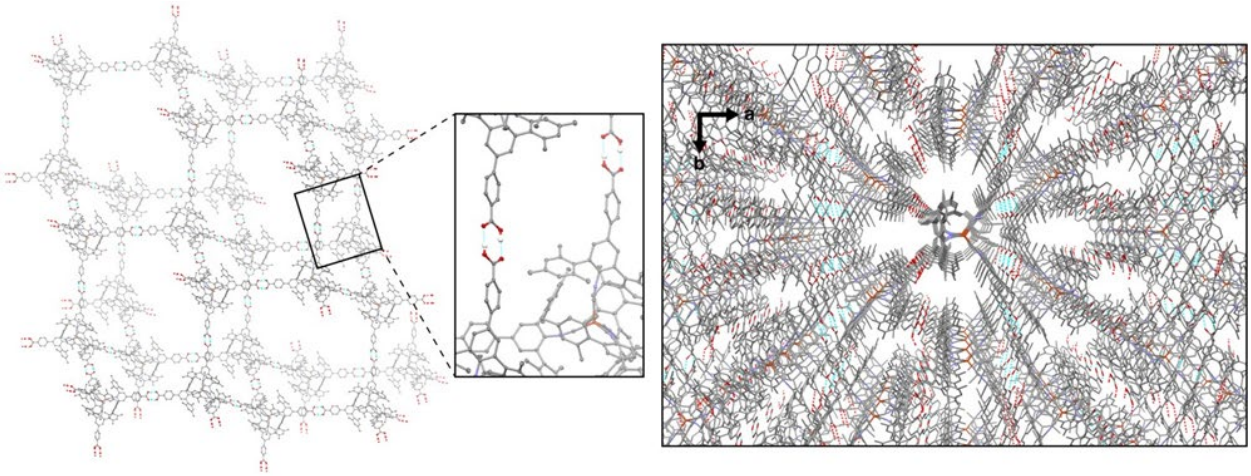

Figure 2.4. (Left) Perspective view of diamondoid net of $[Cu(TIB^{Mes2})_4]PF_6$ with 4-fold interpenetration removed for clarity. Inset depicts zoomed view of $R_2^2(8)$ hydrogen bonds that assemble the hydrogen-bond network. (right) Full interpenetrated view of $[Cu(TIB^{Mes2})_4]PF_6$ down the crystallographic b axis showing internal channel structure. Solvent molecules of co- crystallization and $[PF_6]^-$ ions present within the channels have been omitted for clarity.

Whereas the structure of $[Cu(TIB^{Mes2})_4]PF_6$ confirms that the isocyanide unit selectively binds to the Cu(I) center, it also provides a rationalization for the isolation of a tetra-isocyanide complex in the solid state. Inspection of the extended structure of $[Cu(TIB^{Mes2})_4]PF_6$reveals that is organized into a seven-fold interpenetrated diamondoid (**dia**) hydrogen-bonding network (Figure 2.4). As shown in Figure 3.4, the free carboxylic acid groups of the coordinated TIB^{Mes2} ligand form $R_2^2(8)$ hydrogen bonds[63] to nearest neighbor $[Cu(TIB^{Mes2})_4]^+$ units. This extended lattice structure reasonably stabilizes the coordination of a fourth isocyanide ligand in a manner that overcomes the attendant steric pressures between the *m*-terphenyl groups. Notably, we have observed this effect previously in the isocyanide coordination network Cu-^{ISO}CN-1, which features the ditopic isocyanide $[CNAr^{Mes2}]_2$.[26] In Cu-^{ISO}CN-1, the formation of an extended lattice similarly stabilizes tetrahedral $[Cu(CNAr^{Mes2})_4]^+$ cores by inhibiting ligand dissociation. For the hydrogen-bonding network formed by $[Cu(TIB^{Mes2})_4]PF_6$, the seven-fold interpenetrated **dia** net results in a densely-packed lattice lacking significant voids. Close inspection of the lattice reveals the presence

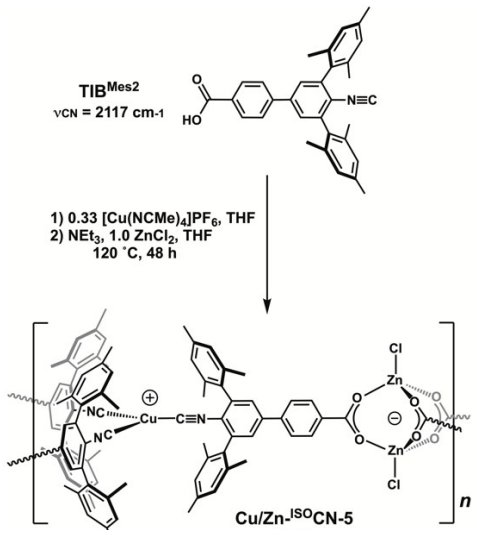

Figure 2.5. Synthesis of the mixed-metal framework Cu/Zn-^{ISO}CN-5.

of ca. 16.5 x 16.1 Å rectangular channels along the crystallographic *b* axis, which is occupied by the $[PF_6]^-$ ions as well as CH_2Cl_2 molecules of co-crystallization (Figure 2.3). Notably, this dense packing of hydrophobic *m*-terphenyl units results in good stability toward liquid H_2O. Indeed, $[Cu(TIB^{Mes2})_4]PF_6$ can be suspended in water for 24 h without appreciable degradation as assayed by ATR-IR spectroscopy (Figure 2.27). This dense packing also protects the Cu(I) centers within $[Cu(TIB^{Mes2})_4]PF_6$ from oxidation, as it has been found to be indefinitely as a solid on the benchtop. However, the hydrogen bonding network is readily disrupted by non- polar organic solvents such as CH_2Cl_2 and THF, in which dissolution rapid and an equilibrium between a tris-isocyanide Cu(I) complex and free TIB^{Mes2} is quickly reestablished. Thermogravimetric analysis (TGA) on crystalline $[Cu(TIB^{Mes2})_4]PF_6$ revealed a persistent multi- stage decomposition between 150 ˚C to 500 ˚C (Figure 2.30), rather than a well-defined process indicative of desolvation followed by single-step decomposition. Hydrogen-bonding networks, especially those utilizing T_d-symmetric building blocks, are known to display robust thermal behavior as solids.[40] In contrast, the ill-defined thermal behavior of $[Cu(TIB^{Mes2})_4]PF_6$ likely reflects an inherent steric instability posed by the *m*- terphenyl groups that is not overcome by the totality of hydrogen bonding at elevated temperatures.

With the selectivity of the TIB^{Mes2} isocyanide unit for Cu(I) centers established, the ability of the carboxylate group to bind a second metal center was assessed for the purpose mixed-metal MOF formation. To ensure that electronic differentiation could be achieved, hard Lewis acidic Zn(II) centers were investigated for preferential binding with the TIB^{Mes2} carboxylate unit. Most notably, pre-ligation of the TIB^{Mes2} isocyanide group to Cu(I), followed by deprotonation of the free carboxylic acid group prior to the introduction of a Zn(II) source served as a reliable strategy for the formation of mixed-metal frameworks (Scheme 2.3). For example, stirring of a 3:1 mixture of TIB^{Mes2} and $[Cu(NCMe)_4]PF_6$ for 30 min in THF solution, followed by the addition of NEt_3 (3.0 equiv.) results in ^1H NMR and FTIR spectra consistent with carboxylate deprotonation, but retention of a tris- isocyanide Cu(I) core (Figure 2.17). Treatment of this THF mixture with $ZnCl_2$ prior to solvothermal heating at 120 ˚C for 48 h resulted in the deposition of large, colorless cubic-shape single crystals. Crystallographic structural determination revealed these crystals to be a mixed-metal Cu(I)/Zn(II) framework (denoted Cu/Zn– ^{ISO}CN-5) that possesses a highly unusual zwitterionic repeat unit. As shown in Figure 2.3, the carboxylate unit of TIB^{Mes2} is competent for the binding of Zn(II) and three ligands assembly into a dimeric $[Cl_2Zn(O_2CR)_3]$ paddlewheel that possesses terminal chloride ligands and an overall negative charge. This Zn_2-based SBU is charge balanced by an unsolvated $[Cu(CNR)_3]^+$ cation that adopts a perfect trigonal planar coordination geometry (∠(∠(C-Cu-C) = 359.99(1)˚). Importantly, residuals within the electron density map of Cu/Zn^{ISO}-CN-5 do not indicate the presence of either $[PF_6]^-$ anions or triethyl ammonium cations, thereby providing additional evidence for a zwitterionic formulation between the Cu and Zn based SBUs. It is important to note that the synthesis of Cu/Zn–^{ISO}CN-5 can be viewed as a variant of

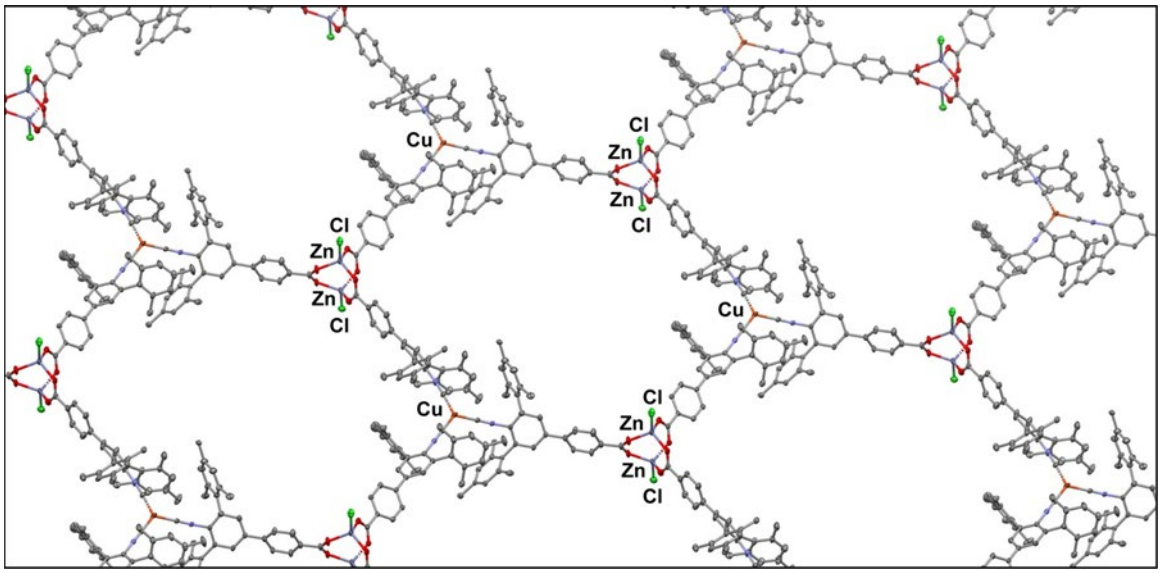

Figure 2.6. Solid-state structure of one hexagonal (6,3) hbc net layer of Cu/Zn-^{ISO}CN-5 showing cationic $[Cu(CNR)_3]^+$ and anionic $[Cl_2Zn_2(O_2CR)_3]^-$ SBUs.

the metalloligand approach for accessing mixed-metal MOFs.[22-24] Whereas the vast majority of metalloligands contain a multidentate chelate unit to sequester the first metal, and a free carboxylate to bind a second metal, pre- ligation of three monodentate TIB^{Mes2} ligands to Cu(I) achieves the same effect on account of electronic differentiation between isocyanide and carboxylate donor groups. This latter approach is further validated by ICP- MS analysis on digested Cu/Zn–^{ISO}CN-5, which resulted in an observed ^{63}Cu/^{66}Zn concentration ratio of 1:2 and is fully consistent with both the structural motifs present in the solid state and their specific charge-balancing requirements. Furthermore, the ATR-IR spectrum of crystalline Cu/Zn–^{ISO}CN-5 revealed a sharp ν_{CN} band at 2156 cm^{-1}, which provides additional evidence for the presence of a non-pyramidalized $[Cu(CNR)_3]^+$ node within Cu/Zn–^{ISO}CN-5.[28] It is also important to note that the ν_{CN} band of Cu/Zn–^{ISO}CN-5 contextualizes the 2152 cm^{-1} ν_{CN} stretch obtained from treatment of 3.0 equiv of TIB^{Mes2} with $[Cu(NCMe)_4]PF_6$ and suggests that the trisisocyanide, $[(THF)Cu(CNR)_3]^+$ fragments are the reactive species in the network formation process. To this end, dissolution of the hydrogen-bonding network $[Cu(TIB^{Mes2})_4]PF_6$ in THF followed by

the addition of NEt_3 and $ZnCl_2$ also produces Cu/Zn-^{ISO}CN-5 after solvothermal heating as assayed by both single crystal and powder X-ray diffraction. As suggested from the solution phase FTIR data of $[Cu(TIB^{Mes2})_4]PF_6$, dissociation of a TIB^{Mes2} ligand more than likely generates a tris-isocyanide core that can engage with other metal centers through carboxylate units.

Inspection of the extended solid-state structure of Cu/Zn–^{ISO}CN-5 revealed that the Cu(I)/Zn(II) dual SBUs organize into an AB stacked-layer, two- dimensional (6,3) honeycomb (**hcb**) network in the *Fdd2* space group (Figure 2.7). Despite possessing a *ca.* 32 Å hexagonal

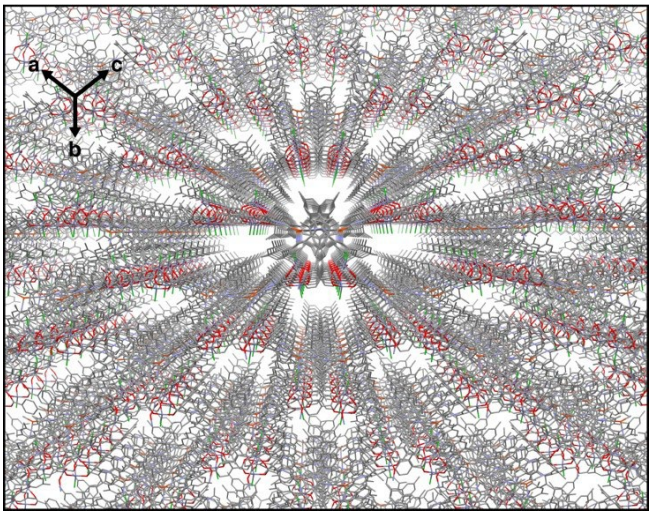

Figure 2.7. Channel structure of Cu/Zn-^{ISO}CN-5 along the diagonal between the crystallographic a and c axes. Chloride ligands of the Zn_2 SBU are colored in green and are found to line the channels.

apertures, the layers are not interpenetrated. However, close stacking of the 2D layers, which is fostered by van der Walls contacts between the *m*- terphenyl groups, creates an overall densely-packed material that exhibits good thermal stability. Thermogravimetric analysis (TGA) on a single crystalline sample of Cu/Zn–^{ISO}CN-5 resulted in a well- behaved, single-step decomposition onset temperature of 390˚ C. This thermal behavior contrasts significantly with that of the hydrogen bonding network $[Cu(TIB^{Mes2})_4]PF_6$ and indicates that increased thermal stability can be

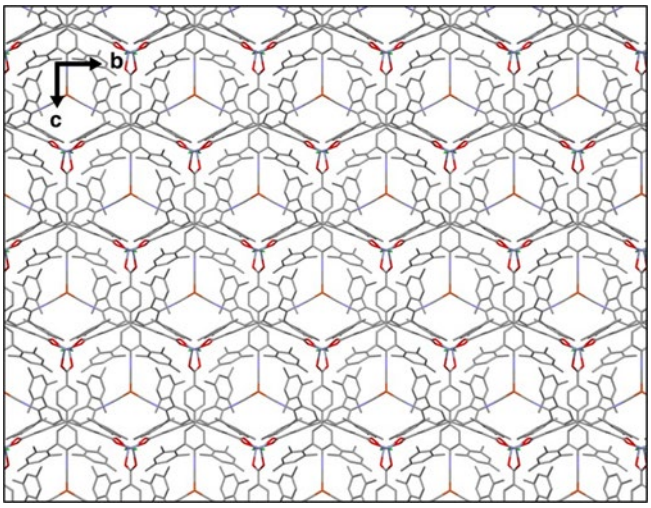

Figure 2.8. View of Cu/Zn-^{ISO}CN-5 along the crystallographic a axis depicting a non-interpenetrated AB stacked-layer arrangement of two-dimensional (6,3) hbc nets.

achieved for metal-isocyanide nodes by SBU formation at the carboxylate groups.

Whereas Cu/Zn–^{ISO}CN-5 exists in the solid state as a densely-packed layered material, there are narrow (19 Å x 17 Å)-wide channels that transverse the diagonal between the crystallographic *a* and *c* axes (Figure 2.5). Notably, the trigonal planar $[Cu(CNR)]^+$ SBUs run parallel to these channels, as does one terminal chloride ligand of the Zn paddlewheel nodes. While this lattice arrangement suggests that exogenous substrates can potentially access the coordinatively unsaturated Cu(I) centers, the small diameter of these channels, coupled with the relatively large van der Walls radii of chlorine atoms, is likely to present significant steric restrictions on substrate penetration. Indeed, this notion was confirmed by gas sorption measurements Cu/Zn– ^{ISO}CN-5 samples activated at 115 ˚C. Attempted measurement of N_2 sorption isotherms showed negligible uptake and corresponding surface area. However, CO_2 sorption runs resulted in modest uptake and derived BET and Langmuir surface area values 141 m^2/g and 191 m^2/g, respectively. Accordingly, we presume that the increased polarizability of CO_2 enables access to the narrow hydrophobic channels present in Cu/Zn–^{ISO}CN-5. To this end, O_2 sorption measurements on Cu/Zn–^{ISO}CN-5 also resulted in negligible uptake, despite the presence

of low- valent and coordinatively-unsaturated $[Cu(CNAr)_3]^+$ sites along the channel walls. This was corroborated by ATR- IR spectroscopic analysis, which showed no change in the ν_{CN} band after dosing single-crystalline Cu/Zn–^{ISO}CN-5 with 1 atm of O_2 for 24 h. While this latter observation may indicate a resistance of the Cu centers to either oxidation or O_2 binding that is electronic in origin, we currently favor the presence of an inaccessible channel structure within Cu/Zn–^{ISO}CN-5 as an explanation for this lack of reactivity.

As indicated from its chemical resistance to O_2, Cu-^{ISO}CN-5 displays excellent air stability. Crystalline samples of the material were subject to drying under vacuum for 15 minutes and are indefinitely stable to ambient atmospheric conditions on the benchtop. Over the course of two weeks, intermittent ATR-IR spectroscopic analysis showed no change in the ν_{CN} or the ν_{CO} bands of Cu-^{ISO}CN-5, and no indication of free TIB^{Mes2} was observed that would indicate decomposition of the Cu(I) center. PXRD analysis of the sample also showed no loss in crystallinity over the course of two weeks, indicating good stability of the framework to atmospheric conditions (Figure 2.39). However, while Cu-^{ISO}CN-5 displays excellent stability in air, addition of the material to deionized water resulted in a loss in crystallinity over the course of 24 hours (Figure 2.40). ATR-IR spectroscopic analysis revealed a broadening of the isocyanide stretch, in addition to a distinct red shift of the carboxylate ν_{CO} stretch to 1608 cm^{-1} from 1629 cm^{-1} (Figure 2.24). Accordingly, this loss in crystallinity is likely due to hydrolysis of the metal-carboxylate SBU, which is not uncommon for Zn/carboxylate paddlewheel- based MOFs.[64-65]

2.3. Conclusions.

The development of synthetic methods that can reliably incorporate low-valent metals into network materials remains attractive as a means of enhancing the physical and chemical properties of porous solids. In addition, the preparation of mixed-metal networks, where the electronic attributes of two or more metals are complementary, are finding increased utilization in the area

of catalysis and separations chemistry.[14-15] Here, we demonstrate that two different donor groups within an electronically-differentiated heteroditopic ligand can be used to assemble a mixed-metal MOF that incorporates low-valent metal sites in a predictable and selective fashion. Specifically, the heteroditopic isocyanide/carboxylic acid ligand, TIB^{Mes2}, can selectively bind low-valent Cu(I) centers through the isocyanide unit, while leaving the carboxylic acid group unperturbed. Without further elaboration, the free carboxylic acid in Cu(I)/TIB^{Mes2} complexes allow for the formation of solid-state hydrogen-bonding networks. However, upon deprotonation, the resulting carboxylate can bind to a "hard" Zn(II) center and enable the formation of a mixed-metal framework material. Whereas the encumbering steric properties of the *m*- terphenyl group of the TIB^{Mes2} linker enables the incorporation of coordinatively-unsaturated $[CuL_3]^+$ sites within this Cu(I)/Zn(II) framework, its densely-packed AB layer structure does not result in significant porosity or surface area. However, given the wide range of carboxylate-based SBUs that give rise to permanently- porous 3D framework materials,[7-8] we believe this approach can be effective for reliable incorporation of low-valent, as well as coordinatively unsaturated, metal centers. Accordingly, synthetic investigations seeking to expand the use of TIB^{Mes2} and related heteroditopic linkers for this purpose are in progress.

2.4. Experimental Section.

Synthesis of HC(O)NH(*p*-$BrAr^{Mes2}$): Formic acid (3.41g, 74 mmol, 10 equiv) was added dropwise via syringe to stirring acetic anhydride (6.04 g, 59.2 mmol, 8.0 equiv). The mixture was warmed to 50 ˚C for 1 h to generate formyl acetic anhydride. This mixture was allowed to cool, then transferred to a stirring THF solution of H_2NAr^{Mes2}-*p*-Br (3.0 g, 7.4 mmol). This mixture was stirred for 24 h, after which all volatiles were removed by dynamic vacuum at 50 ˚C to yield HC(O)NH(*p*-$BrAr^{Mes2}$) as a colorless solid that was used without further purification. Yield: 3.05

g, 7.4 mmol, 95%. ^{1}H NMR (300.02 MHz, $CDCl_3$, 20 ˚C) d = 7.60 (d, 1H, *J* = 9Hz, NHC(O)*H*), 7.29 (s, 2H, *m*-Ar), 6.94 (s, 4H, *m*-Mes), 6.53 (d, 1H, *J* = 9 Hz, N*H*C(O)H), 2.30 (s, 6 H, (Mes-*p*-C*H*$_3$)), 2.02 (s, 12H, (Mes-*o*-C*H*$_3$)). ^{13}C{^{1}H} NMR (125.7 MHz, $CDCl_3$, 20˚C) d = 162.5 (H*C*(O)N), 138.5, 135.7, 135.3, 133.2, 132.9, 131.8, 129.1, 118.8, 21.2 (*p*-Mes-*C*H$_3$), 20.5 (*o*-Mes-*C*H$_3$) ppm. FTIR-ATR (diamond surface, 20 ˚C): ν_{CO} = 1690 cm^{-1} (s), ν_{NH} = 3189 (w), also 2917 (m), 1660 (s), 1521 (s), 1380 (w), 1027 (m), 839(s), 694 (w) cm^{-1}. HR-MS (ESI-TOFMS): Predicted *m*/*z* for $C_{25}H_{26}BrNO$ = 436.1217. Found *m*/*z* = 436.1266 [M]$^{+}$.

Synthesis of 1-HC(O)N(H)Ar^{Mes2}-4-$C_6H_4CO_2CH_3$: A resealable ampoule was charged with the formamide HC(O)NH(*p*-BrAr^{Mes2}) (0.480 g, 1.10 mmol), Pd_2dba_3 (0.030 g, 0.032 mmol, 3 mol%), PCy_3 (0.0186 g, 0.064 mmol, 6 mol%), K_3PO_4 (0.933 g, 4.39 mmol, 4.0 equiv) and 4-methoxycarbonylphenylboronic acid (0.198 g, 1.10 mmol, 1.0 equiv). 1,4-Dioxane (25 mL) and toluene (8 mL) were used to dissolve the solids. The reaction mixture was stirred at 75 ˚C for 24 h under an atmosphere of dinitrogen. The mixture was cooled, filtered through a medium porosity fritted funnel packed with silica, and the filter cake was washed with CH_2Cl_2 (3 × 15 mL). The filtered crude mixture was stripped of all volatiles, washed and sonicated with cold hexanes, and then filtered. The resulting colorless solid, 1-HC(O)N(H)Ar^{Mes2}-4-$C_6H_4CO_2CH_3$, was used without further purification. Yield: 0.495 g, 1.01 mmol, 91%.^{1}H NMR (300.02 MHz, $CDCl_3$, 20 ˚C) d = 8.09 (d, 2H, *J* = 8.4Hz), 7.70 (d, 1H, *J* = 9.4 Hz, NHC(O)*H*), 7.69 (d, 2H, *J* = 9Hz), 7.45 (s, 2H, *m*-Ar), 6.99 (s, 4H, m-Mes), 6.67 (d, 1H, *J* = 9.1Hz N*H*C(O)H), 3.93 (s, 3H, C(O)OC*H*$_3$), 2.34 (s, 6 H, Mes-*p*-C*H*$_3$), 2.07 (s, 12H, Mes-*o*-CH$_3$). ^{13}C{^{1}H} NMR (125.7 MHz, $CDCl_3$, 20 ˚C) d = 167.0 (H*C*(O)N), 162.5 (*C*(O)OCH$_3$), 144.03, 138.4, 137.2, 135.9, 134.2, 133.7, 132.5, 130.3, 129.2, 128.9, 126.8, 53.3 (COOCH3), 21.2 (Mes-*p*-*C*H$_3$), 20.5 (Mes-*o*-*C*H$_3$) ppm. FTIR-ATR (diamond surface, 20 ˚C): $\nu_{CO(ester)}$ = 1720, $\nu_{CO(formamide)}$ = 1685 cm^{-1} (s), ν_{NH} = 3368 cm^{-1} (w), also 2913 (m),

1606 (s), 1271 (s), 1098 (s), 962 (w), 851(s), 752 (w) cm^{-1} . HR-MS (ESI-TOFMS): Predicted *m*/*z* for $[M+H]^+$ $C_{33}H_{33}NO_3$ = 492.2533. Found *m*/*z* = 492.2533 .

Synthesis of 1,4-(CNAr^{Mes2})$C_6H_4CO_2CH_3$: To a stirring CH_2Cl_2 solution of 1-HC(O)N(H)Ar^{Mes2}-4-$C_6H_4CO_2CH_3$ (0.500 g, 1.02 mmol) was added diisopropylamine (0.82 g, 8.14 mmol, 8 equiv) via syringe. After stirring for 5 minutes, $POCl_3$ (0.84 g, 5.49 mmol, 5.4 equiv) was added dropwise via syringe and the solution was stirred for 24 h. Aqueous Na_2CO_3 (1.5 M, 50 mL) was added and the resulting mixture was stirred for 5 h. The organic and aqueous layers were then separated and the organic layer was washed with deionized water. The aqueous layers were combined and extracted with 3 x 25 mL CH_2Cl_2. The organic extracts were combined, dried over $MgSO_4$, filtered and volatiles were removed under reduced pressure. The resultant solid was washed with cold hexanes, collected by filtration and dried under reduced pressure. Yield: 0.460 g, 0.970 mmol, 95%. ^{1}H NMR (300.02 MHz, $CDCl_3$, 20 ˚C): d = 8.11 (d, 2H, *J* = 8.4 Hz, C_6H_4), 7.68 (d, 2H, *J* = 8.5Hz, C_6H_4), 7.51 (s, 2H, *m*-Ar), 7.00 (s, 4H, *m*-Mes), 3.94 (s, 3H, COOCH_3), 2.34 (s, 6 H, Mes-*p*-CH_3), 2.08 (s, 12H, Mes-*o*-CH_3). ^{13}C{^{1}H} NMR (125.7 MHz, $CDCl_3$, 20 ˚C) d = 168.2 (*C*N), 167.1 (*C*(O)OMe), 143.8, 141.2, 140.4, 138.4, 135.9, 134.2, 130.7, 130.1, 128.9, 128.2, 127.5, 52.7 (C(O)O*C*H$_3$), 21.6 (Mes-*p*-*C*H$_3$), 20.6 (Mes-*o*-*C*H$_3$) ppm. FTIR-ATR (diamond surface, 20 ˚C): ν_{CN} = 2117 cm^{-1} (s), ν_{CO} = 1723 (s), also, 2920 (m), 1611 (s), 1434 (m), 1277 (s), 1105 (s), 852(s), 774 (s) cm^{-1}. HR-MS (ESI-TOFMS): Predicted *m*/*z* for $[M+H]^+$ $C_{33}H_{31}NO_2$ = 474.2428. Found *m*/*z* = 474.2424.

Synthesis of 1,4-(CNAr^{Mes2})$C_6H_4CO_2H$ (TIB^{Mes2}): Potassium hydroxide **(**KOH; 0.152 g, 2.71 mmol, 8.0 equiv) was dissolved in a 1:1 mixture of MeOH and deionized water. The mixture was degassed and transferred to a stirring THF solution of 1,4-(CNAr^{Mes2})$C_6H_4CO_2CH_3$ (0.160 g, 0.338 mmol). This mixture was stirred at 50 ˚C for 15 h under an atmosphere of nitrogen. Upon

cooling, all volatiles were removed under dynamic vacuum to yield a solid product. The resulting solid was washed with 1.0 M HCl (3 x10mL), followed by a rinse with cold hexanes and drying under reduced pressure. Yield: 0.125g, 0.272 mmol, 80 %. ^{1}H NMR (500.16 MHz, $CDCl_3$, 20 ˚C): d = 8.18 (d, 2H, *J* = 8.1 Hz, C_6H_4), 7.72 (d, 2H, *J* = 8.1 Hz, C_6H_4), 7.53 (s, 2H, *m*-Ar), 7.00 (s, 4H, *m*-Mes), 2.34 (s, 6 H, Mes-*p*-CH_3), 2.08 (s, 12H, Mes-*o*-CH_3) ppm. $^{13}C\{^{1}H\}$ NMR (125.8 MHz, $CDCl_3$, 20 ˚C): d = 170.9 (CN), 144.2 (COOH), 140.6, 140.1, 138.0, 135.5, 133.7, 130.8, 128.7, 128.4, 127.9, 127.1, 125.5, 21.3 (Mes-*p*-CH_3), 20.4 (Mes-*o*-CH_3) ppm. ATR-IR (diamond surface, 20 ˚C): ν_{CN} = 2117 cm^{-1} (s), ν_{CO} = 1692 (s), also 2917 (m), 1609 (s), 1438 (m), 1277(s), 1017 (m), 907 (w), 849 (s), 770 (s) cm^{-1}. HR-MS (ESI-TOFMS): Predicted *m*/*z* for $[M-H]^-$ $C_{32}H_{29}NO_2$ = 458.2126, Found *m*/*z* = 458.2137.

Synthesis of $[Cu(TIB^{Mes2})_4]PF_6$: A THF solution containing TIB^{Mes2} (0.050 g, 0.110 mmol, 4.0 equiv) was added to a stirring THF solution containing $[Cu(MeCN)_4]PF_6$ (0.010 g, 0.025 mmol, 1.0 equiv). The reaction mixture was allowed to stir for 15 minutes, after which all volatiles were removed under reduced pressure. Dissolution of the resulting colorless powder in CH_2Cl_2, followed by filtration and storage at room temperature for 24 h resulted in colorless crystals which were collected and dried in vacuo. Yield: 0.010 g, 0.015 mmol, 59%. FTIR-ATR (diamond surface, 20 ˚C, crystalline sample): ν_{CN} = 2142 cm^{-1} (s), also ν_{CO} = 1718 (s), 1984 (s) and 1610 (s), 1244 (m), 852(s), 776 (s), 494 (s) cm^{-1} .

Synthesis of $[Cu(TIB^{Mes2})_3(THF)]PF_6$: A THF solution containing TIB^{Mes2} (0.040 g, 0.087 mmol, 3.0 equiv) was added to a stirring THF solution containing $[Cu(MeCN)_4]PF_6$ (0.011 g, 0.030 mmol, 1.0 equiv). The reaction mixture was allowed to stir for 15 minutes, after which all volatiles were removed under reduced pressure. The colorless powder was then washed in pentane (3x2mL) and volatiles removed under reduced pressure. Dissolution of the resulting colorless

powder in difluorobenzene, followed by filtration and storage at room temperature for 24 h resulted in colorless crystals which were collected and dried in vacuo. Yield: 0.031 g, 0.019 mmol, 60% ^{1}H NMR (499.83 MHz, CD_2Cl_2, 20 ˚C): d = 8.21 (d, 2H, *J* = 8.3Hz), 7.79 (d, 2H, *J* = 8.5Hz), 7.59 (s, 2H, *m*-Ar), 6.93 (s, 4H, *m*-Mes), 2.29 (s, 6H, Mes-*p*-C*H*$_3$), 2.00 (s, 12H, Mes-*o*-C*H*$_3$) ppm. ^{13}C{^{1}H} NMR (125.7 MHz, CD_2Cl_2, 20 ˚C): δ = 171.0 (*C*N), 149.8, 141.8, 139.9, 137.0, 132.3, 130.1, 129.3, 128.11, 68.6 (THF), 27.0 (Mes-*p*-*C*H$_3$), 22.4 (THF), 20.7 (Mes-*o*-*C*H$_3$) ppm. ^{19}F NMR (376.3 MHz, CD_2Cl_2, 20 ˚C): δ = –73.5 ppm (d, $^{1}J_{F\text{-}P}$=710.7 Hz). FTIR-ATR (diamond surface, 20 ˚C, powder sample): ν_{CN} = 2155 cm^{-1} (s), also ν_{CO} = 1720 (s) and 1689 (s), 1610 (s), 1419 (m), 1244 (m), 835 (s), 555 (s) cm^{-1} .

Synthesis of Cu/Zn-^{ISO}CN-5. A THF solution containing TIB^{Mes2} (0.015 g, 0.033 mmol, 3.0 equiv) was added to a stirring THF solution containing $[Cu(MeCN)_4]PF_6$ (0.004 g, 0.011 mmol, 1.1 equiv). Triethylamine (6.0 mL, 0.044 mmol, 4.0 equiv) was then added and allowed to stir for 10 min. $ZnCl_2$ (0.0044 g, 0.011mmol, 4.0 equiv) was dissolved in 1.5 mL of THF and added to the Cu/TIB^{Mes2} solution. Upon addition a white solid formed and was transferred to a 15 mL pressure tube. The solid was heated at 120 ˚C for 12 h and cooled to 40 ˚C over the course of 48 h. Colorless single crystals formed on the bottom of the pressure tube, which were washed with 3 x 5 mL THF and then collected. Yield: 0.008 g, 0.009 mmol (based on the Cu-based repeat unit), 80 %. FTIR-ATR (diamond surface, 20 ˚C) ν_{CN} = 2156 cm^{-1} (s) , also ν_{CO} = 1716 (s) and 1610 (s), 1244 (m), 778 (s), 557 (s) cm^{-1}.

^{1}H NMR and IR Spectroscopic Data for TIB^{Mes2} and Precursors

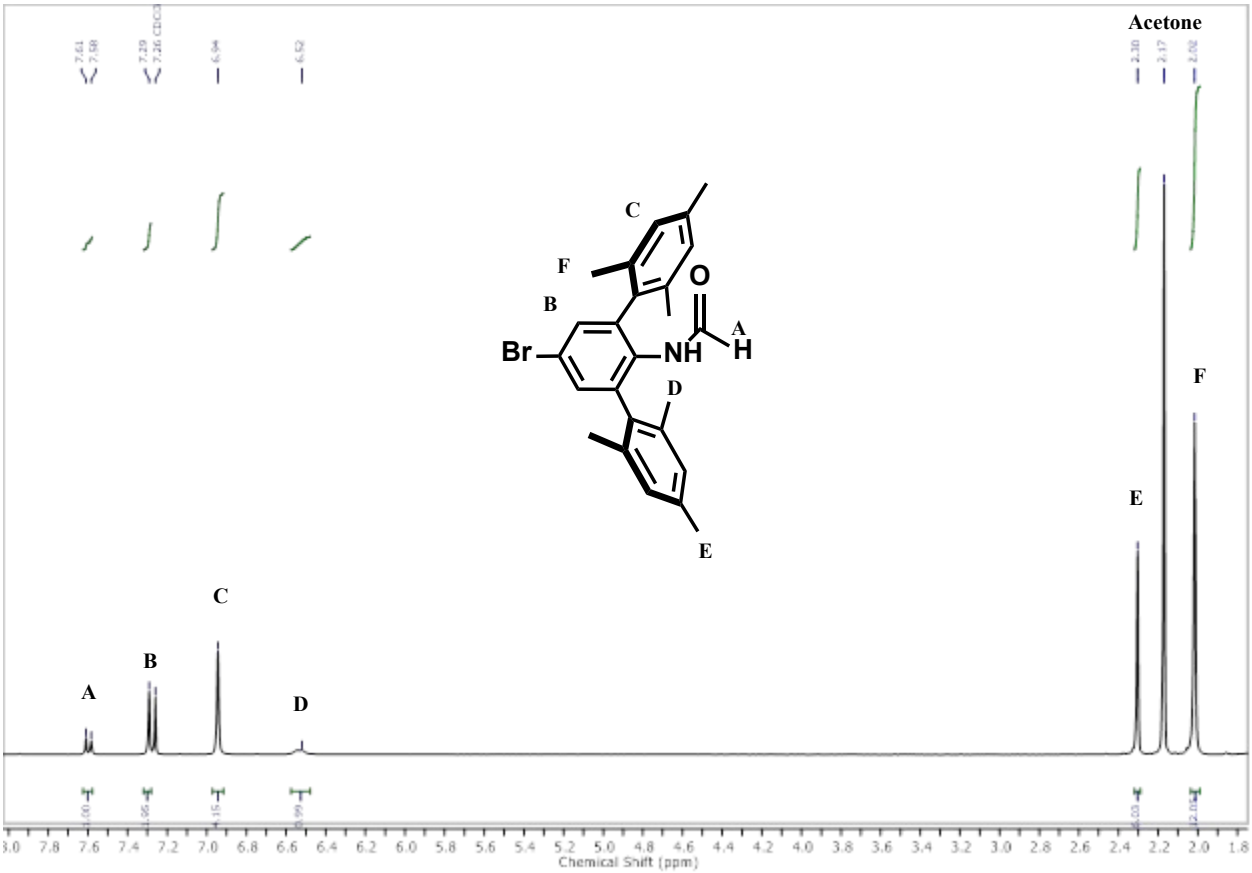

Figure 2.9. ^{1}H NMR spectrum ($CDCl_3$, 300 MHz, 20 ˚C) of HC(O)NH(*p*-BrAr^{Mes2}).

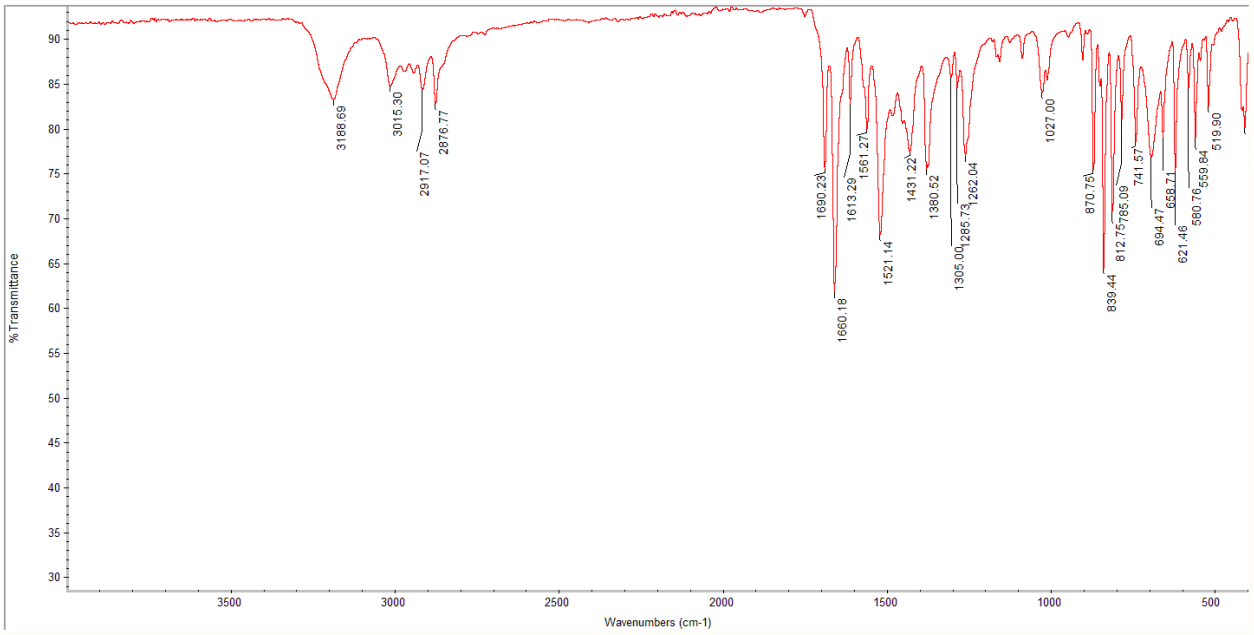

Figure 2.10. ATR-IR spectrum (20 ˚C) of HC(O)NH(*p*-BrAr^{Mes2}).

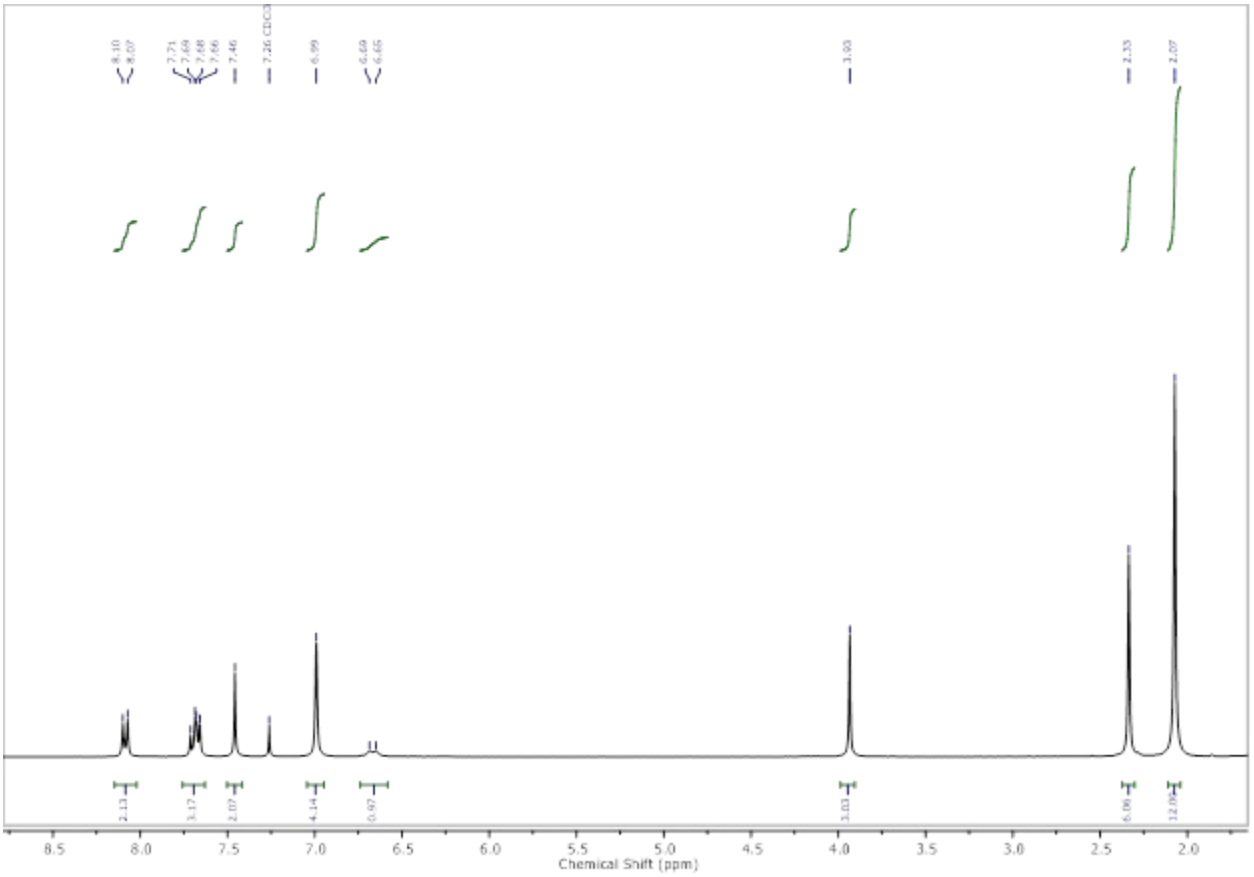

Figure 2.11. ^{1}H NMR spectrum ($CDCl_3$, 300 MHz, 20 ˚C) of 1-HC(O)N(H)Ar^{Mes2}-4-$C_6H_4CO_2CH_3$.

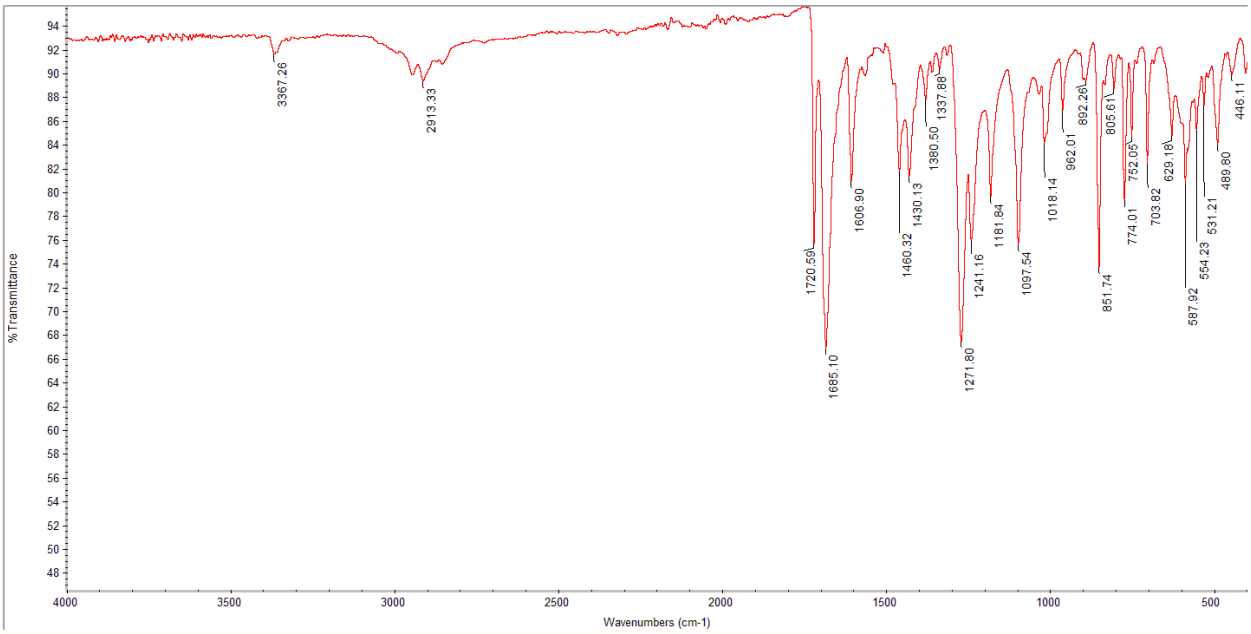

Figure 2.12. ATR-IR spectrum (20 ˚C) of 1-HC(O)N(H)Ar^{Mes2}-4-$C_6H_4CO_2CH_3$.

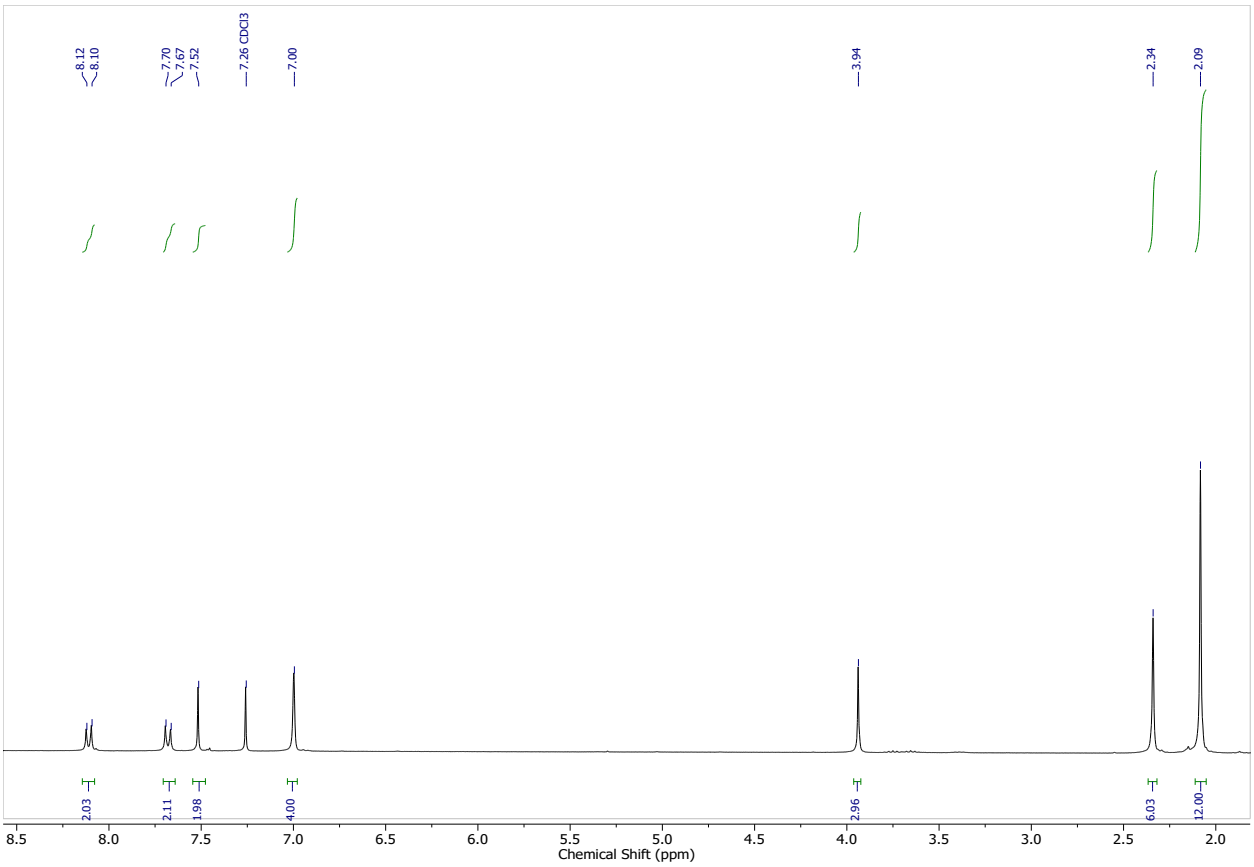

Figure 2.13. ^{1}H NMR spectrum (CDCl3, 300 MHz, 20 ˚C) of 1,4-(CNAr^{Mes2})$C_6H_4CO_2CH_3$.

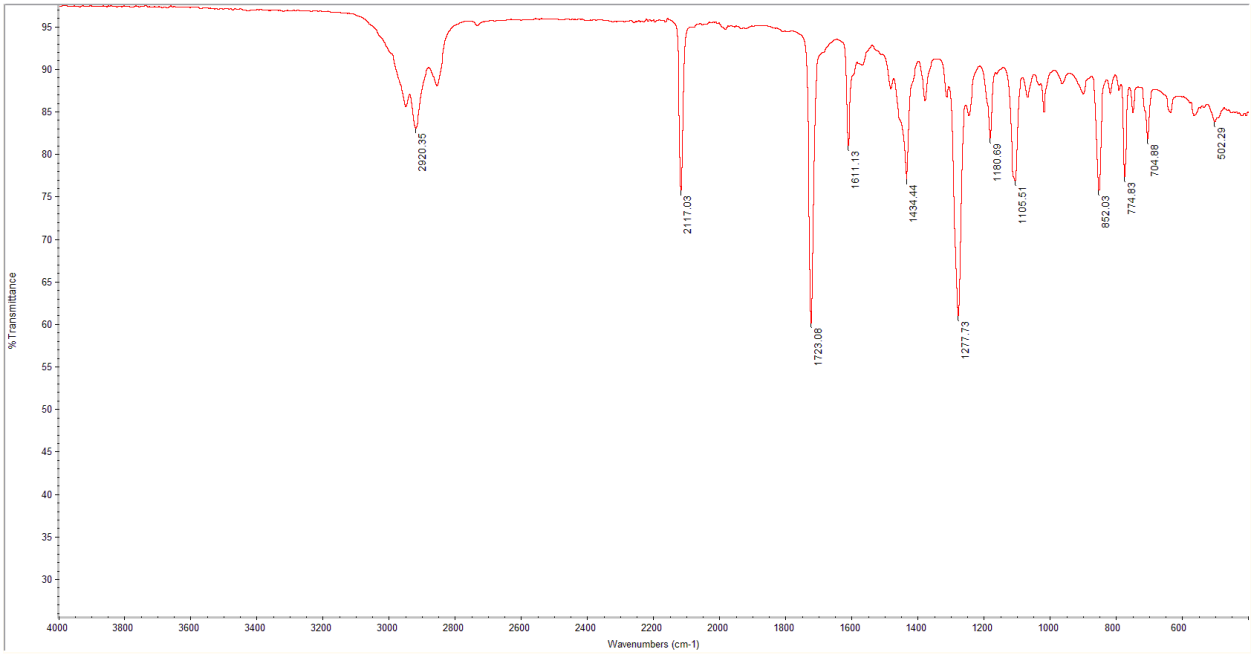

Figure 2.14. ATR-IR spectrum (20 ˚C) of 1,4-(CNAr^{Mes2})$C_6H_4CO_2CH_3$.

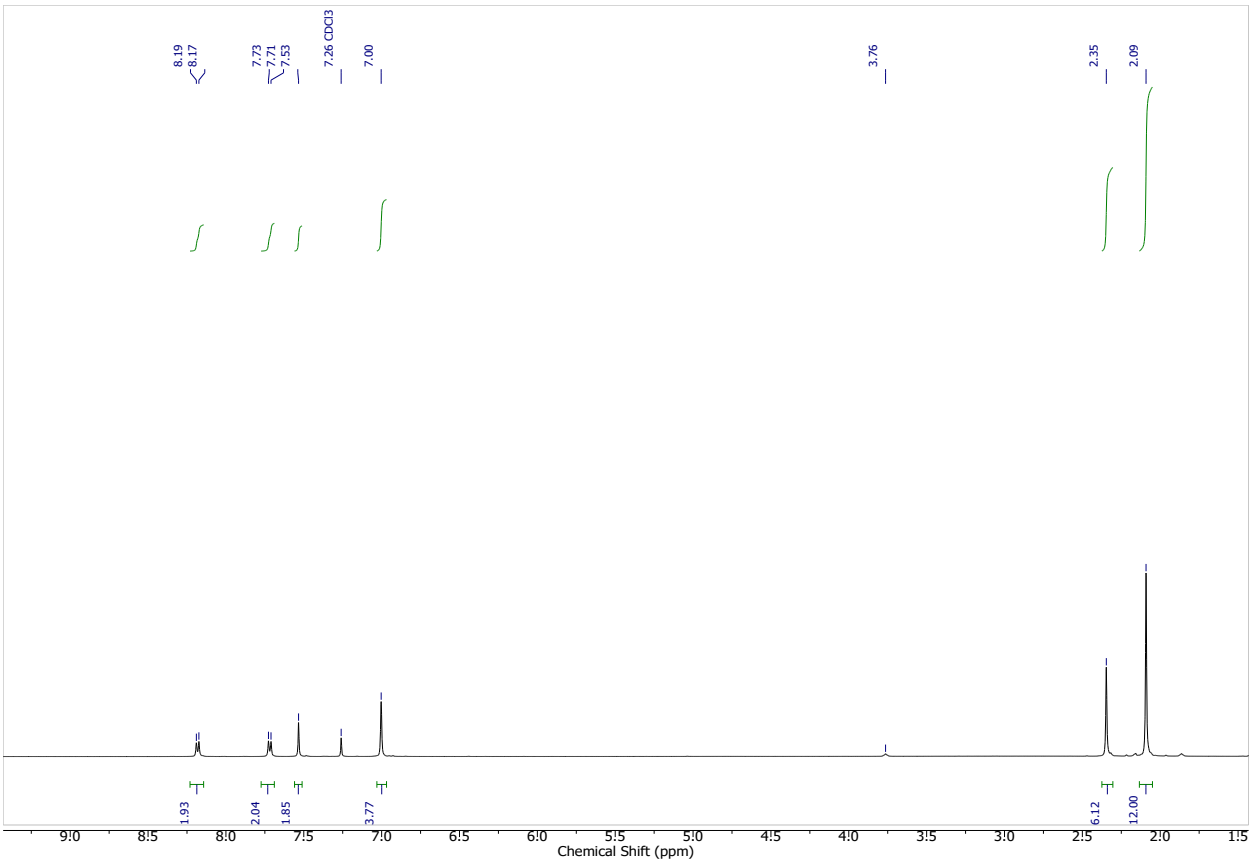

Figure 2.15. ^{1}H NMR spectrum ($CDCl_3$, 500 MHz, 20 ˚C) of 1,4-(CNAr^{Mes2})$C_6H_4CO_2H$ (TIB^{Mes2}H).

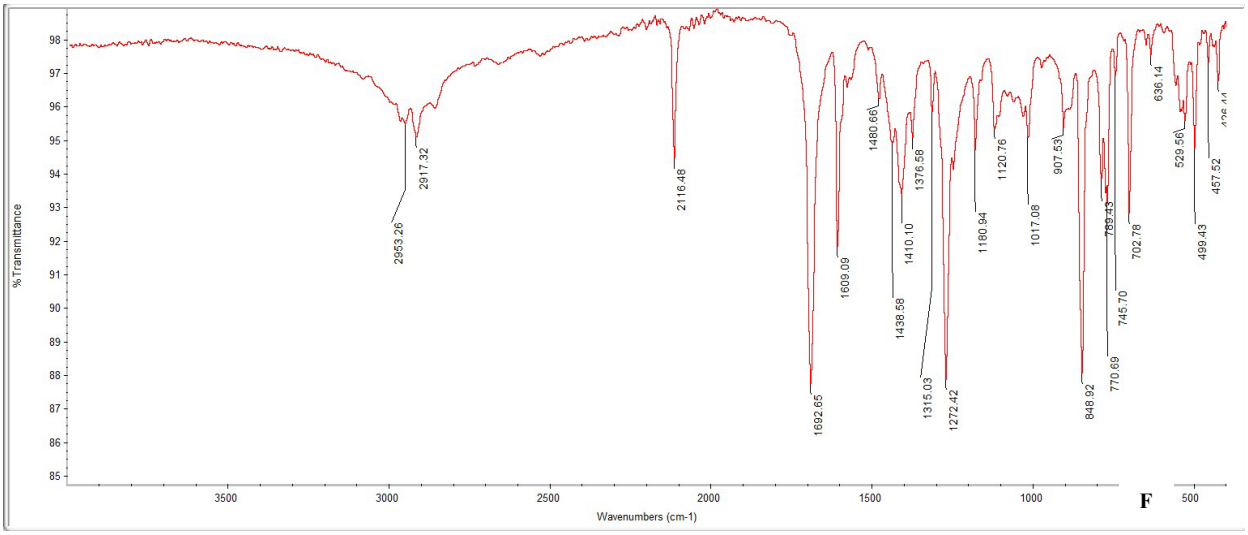

Figure 2.16. ATR-IR spectrum (20 ˚C) of 1,4-(CNAr^{Mes2})$C_6H_4CO_2H$ (TIB^{Mes2}).

Spectroscopic Data for Cu(I) Hydrogen Bonding Networks and Cu/Zn-^{ISO}CN-5.

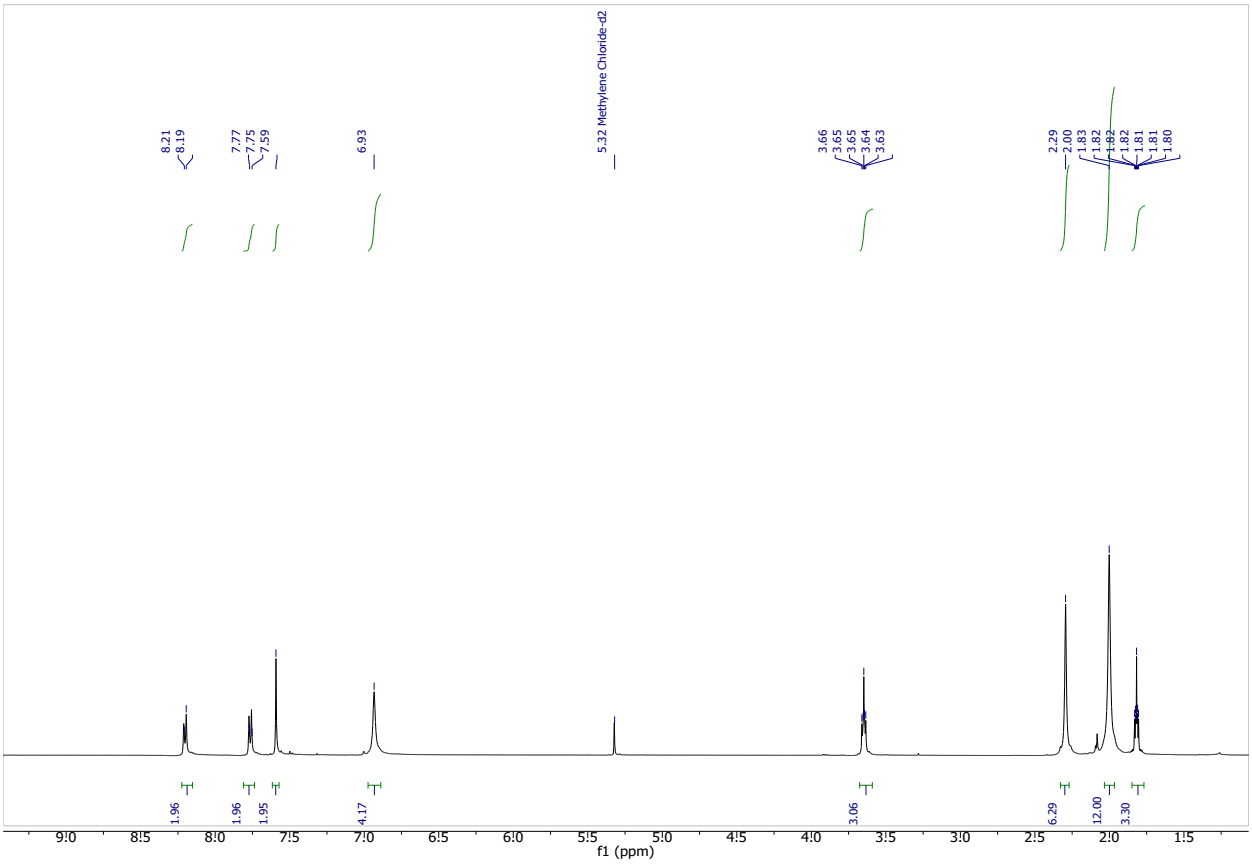

Figure 2.17. ^{1}H NMR Spectrum (500 MHz, CD_2Cl_2, 20 ˚C) from reaction of 3.0 equiv TIB^{Mes2} and $[Cu(NCMe)_4]PF_6$. THF present is suggestive of $[Cu(TIB^{Mes2})_3(THF)]PF_6$ environment in solution.

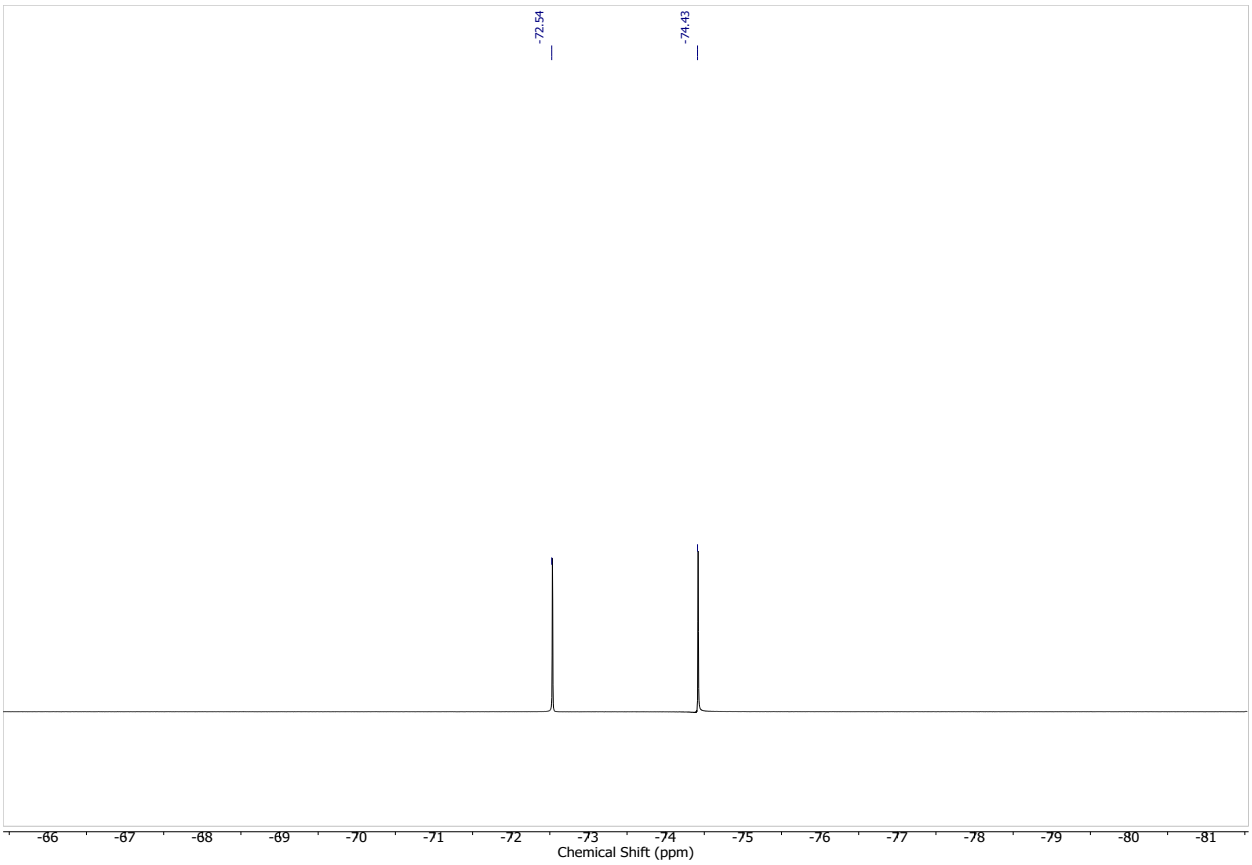

Figure 2.18. ^{19}F NMR Spectrum (282.3 MHz, CD_2Cl_2, 20 ˚C) from reaction of 3.0 equiv TIB^{Mes2} and $Cu(NCMe)_4]PF_6$.

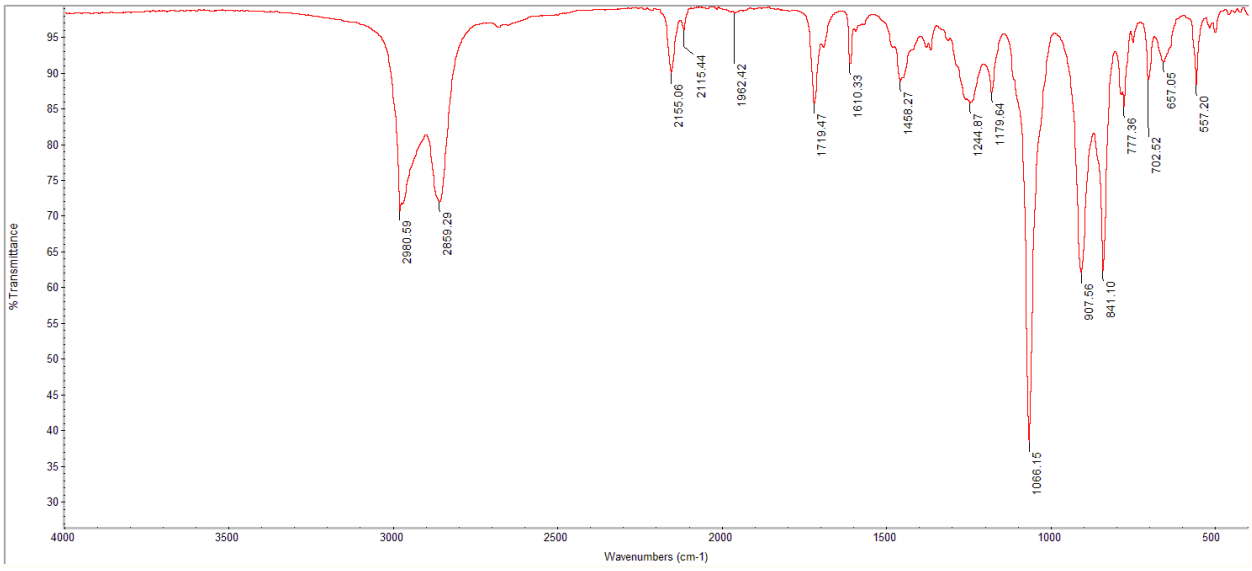

Figure 2.19. Solution IR Spectra of 4.0 equiv TIB^{Mes2} and $[Cu(NCMe)_4]PF_6$ in THF.

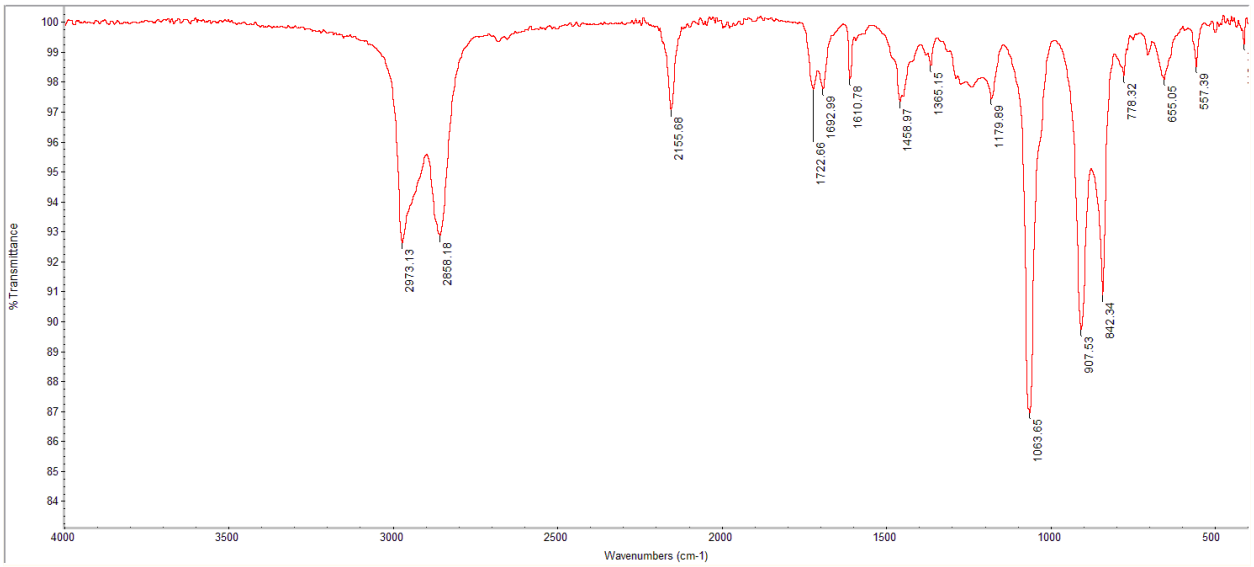

Figure 2.20. Solution IR Spectra of 3.0 equiv TIB^{Mes2} and $[Cu(NCMe)_4]PF_6$ in THF.

Figure 2.21. Solid State ATR-IR spectrum of 4.0 equiv TIB^{Mes2} and $[Cu(NCMe)_4]PF_6$ showing presence of free TIB^{Mes2}.

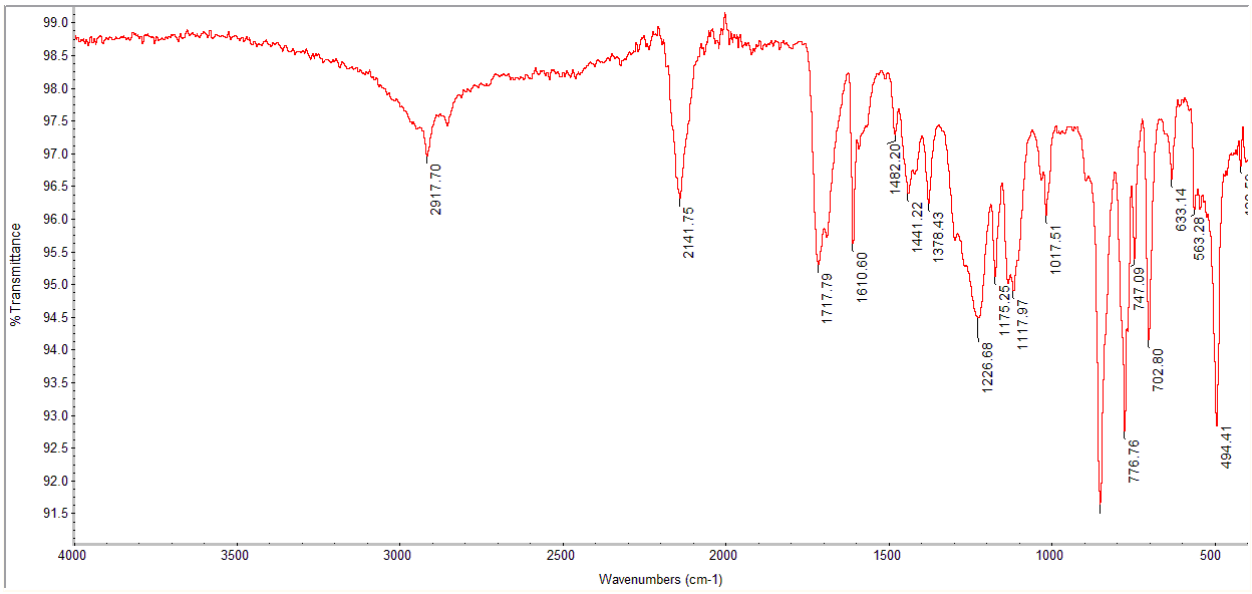

Figure 2.22. Solid State ATR-IR spectrum of the single-crystalline hydrogen-bonding network $[Cu(TIB)_4]PF_6$.

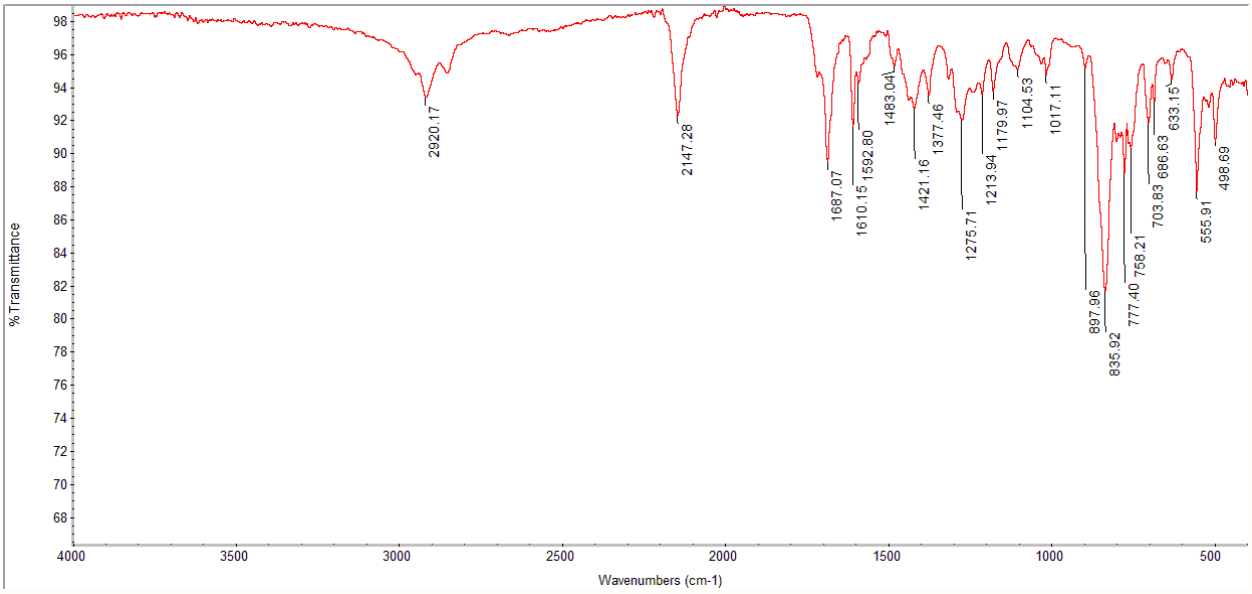

Figure 2.23. ATR-IR spectrum of single-crystalline $[Cu(TIB)_4]PF_6$ after exposure to deionized water for 24 h.

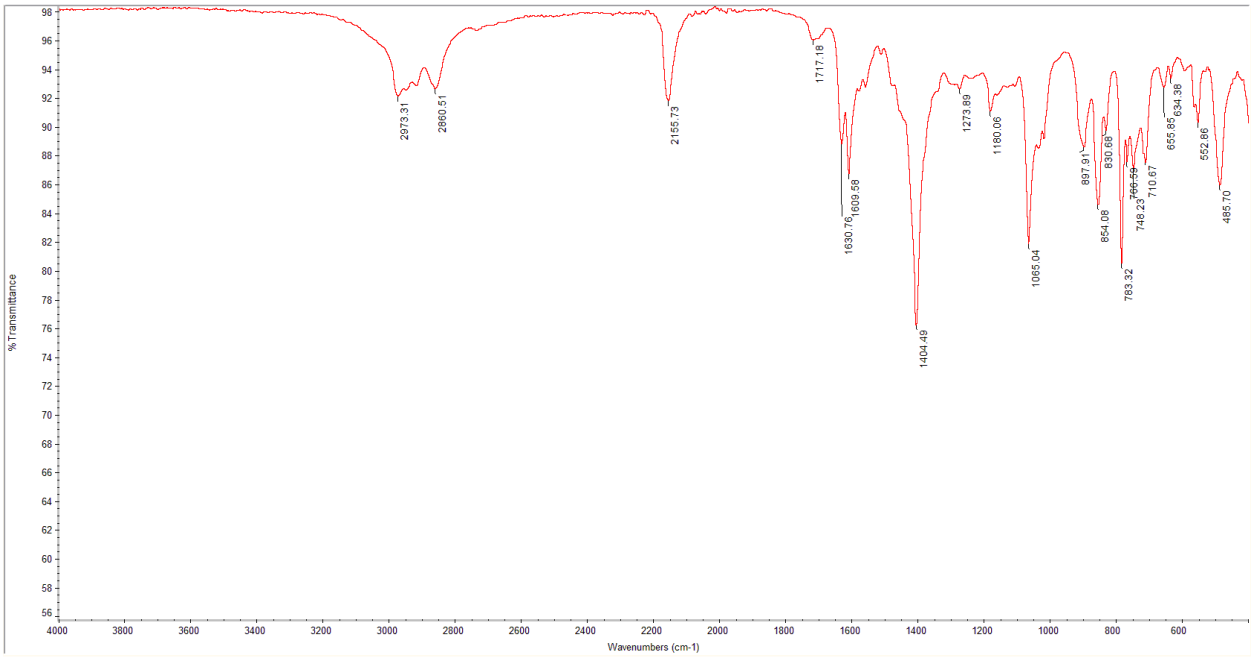

Figure 2.24. ATR-IR spectra of single-crystalline Cu/Zn-Cu-^{ISO}CN-5 using 4.0 equiv of TIB^{Mes2}.

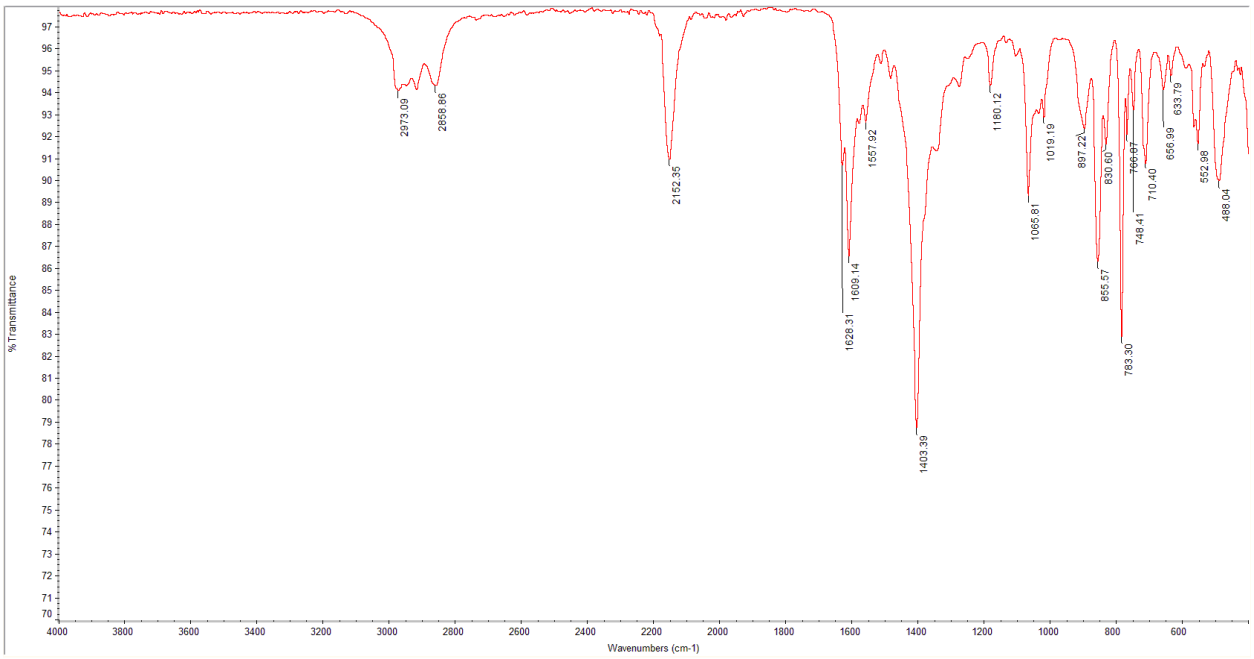

Figure 2.25. ATR-IR spectrum of Cu/Zn-^{ISO}CN-5 using 3.0 equiv of TIB^{Mes2}.

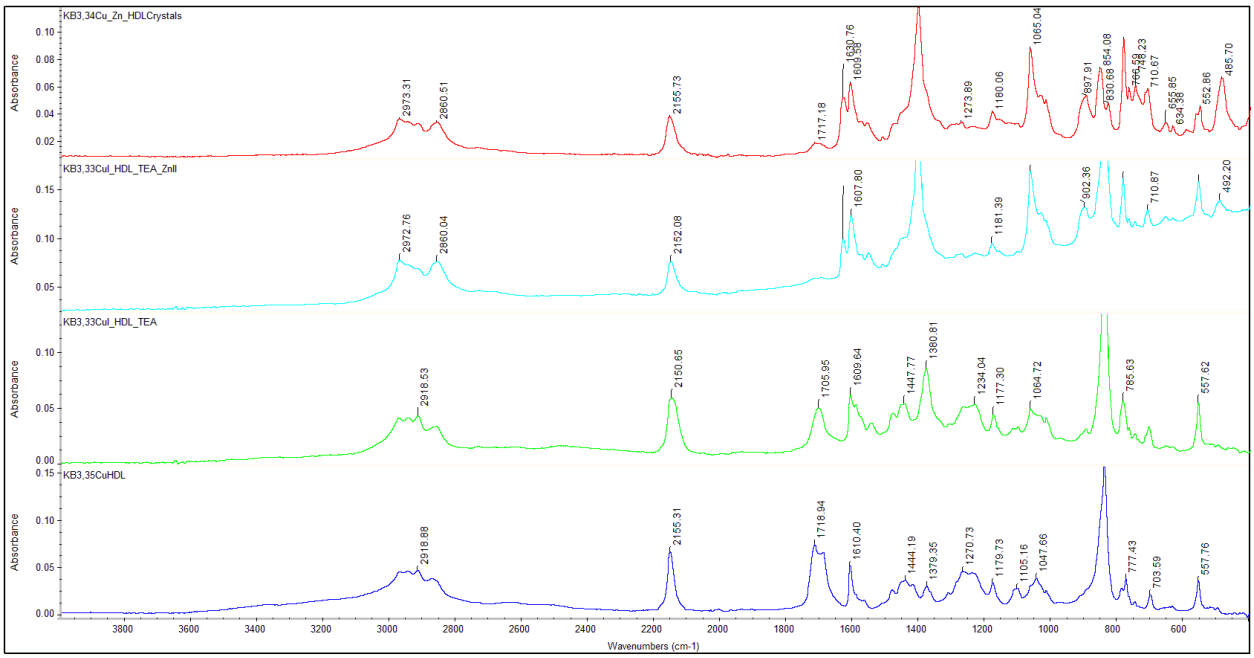

Figure 2.26. Stacked ATR-IR spectra of step-wise synthesis of Cu/Zn^{ISO}CN-5 employing 3.0 equivalents of TIB^{Mes2}. (dark blue, bottom) initial formation of 3:1 Cu(I)/TIB^{Mes2} complex. (green) Deprotonation of 3:1 Cu(I)/TIB^{Mes2} complex with NEt_3. (light blue) After addition of $ZnCl_2$ prior to heating. (red, top) Cu/Zn-^{ISO}CN-5 after solvothermal heating/cooling cycles.

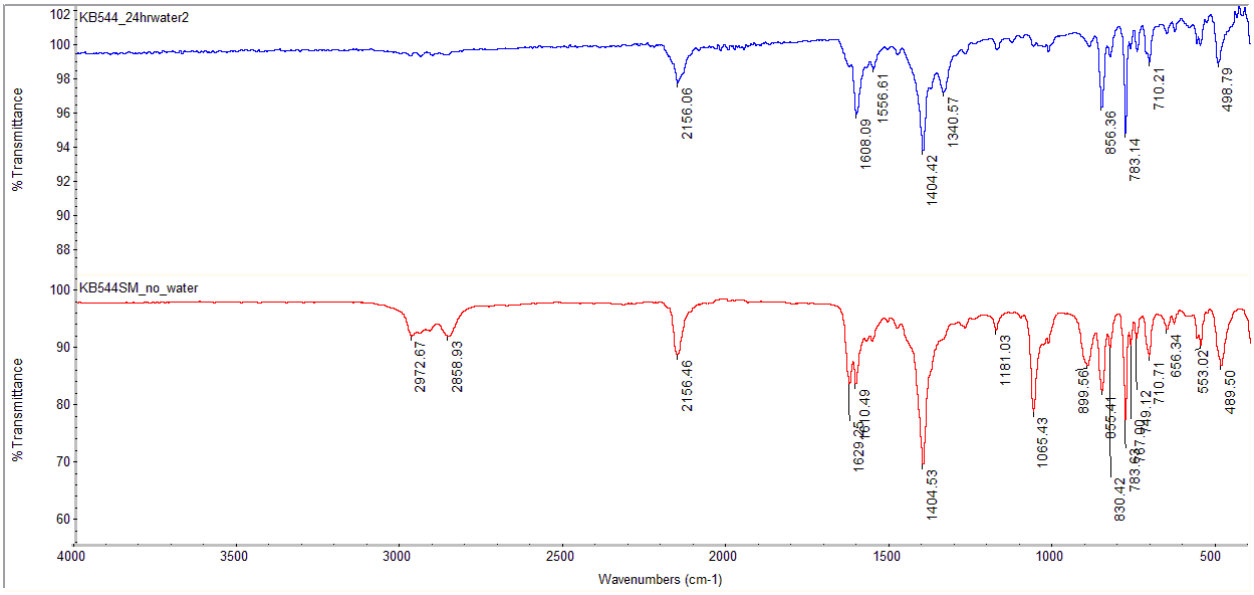

Figure 2.27. ATR-IR spectra of single-crystalline Cu/Zn-^{ISO}CN-5 after exposure to deionized water for 24 h. Note that spectra changes are apparent in carboxylate n_{CO} stretching region.

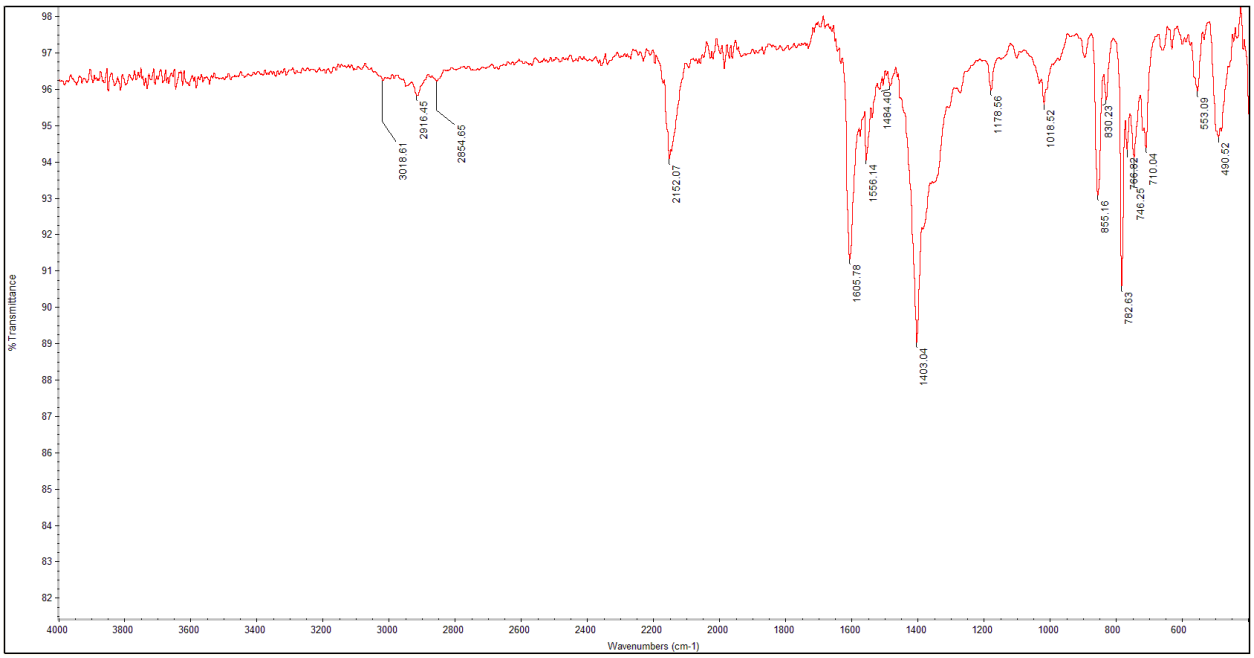

Figure 2.28. ATR-IR spectrum of Cu/Zn-^{ISO}CN-5 after exposure to air for 20 d.

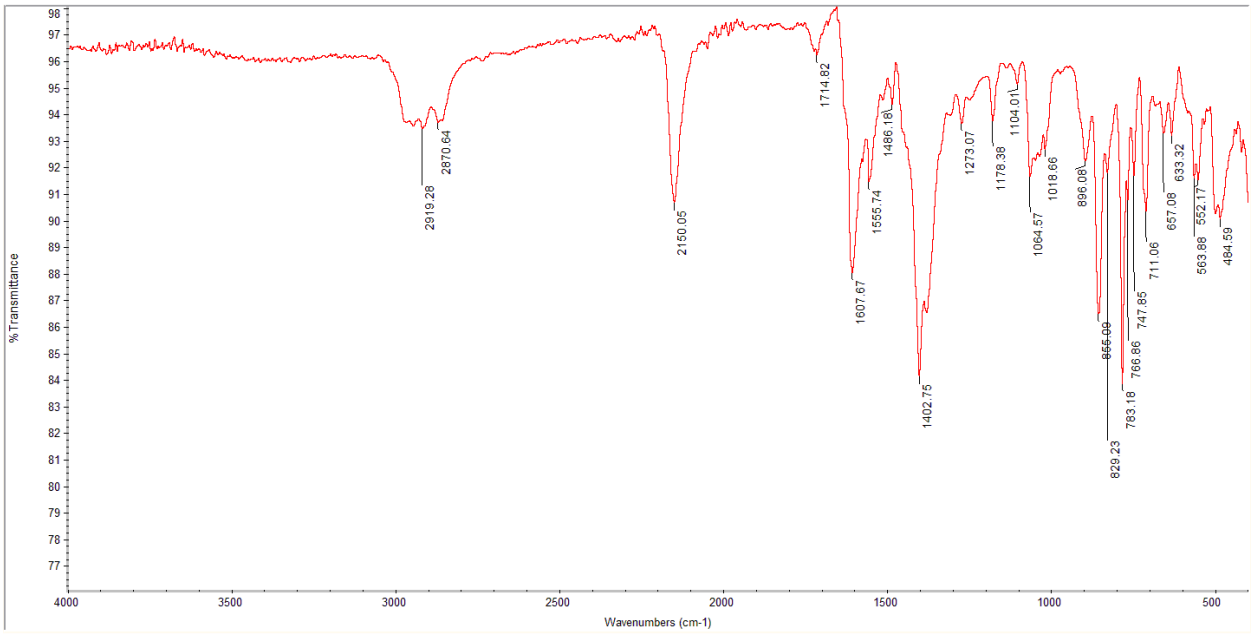

Figure 2.29. ATR-IR spectrum of Cu/Zn-^{ISO}CN-5 after exposure to 1 atm O_2 for 24 hours.

TGA and Gas Sorption Analysis.

Thermal Analysis. Thermogravimetric analysis was performed on ~5–15 mg of material that had been dried under dynamic vacuum for 30 minutes. Analysis was conducted under a stream of dry

dinitrogen gas (80 mL/min) using a Mettler Toledo TGA/DSC 1 STARe System running from 30 ˚C to 800 ˚C with a ramping rate of 5 ˚C/min.

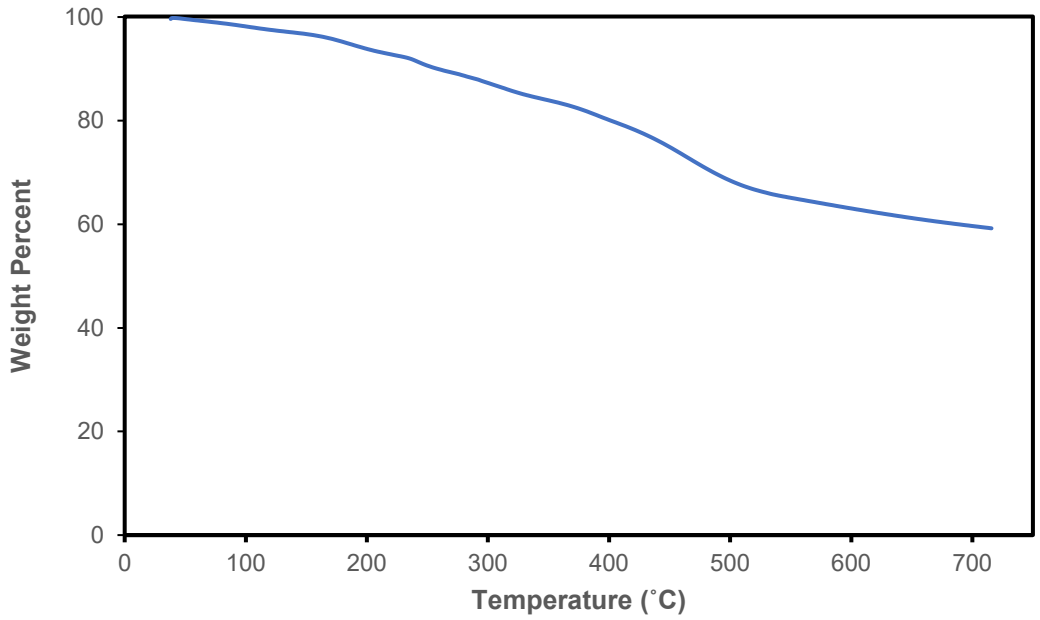

Figure 2.30. Thermogravimetric Analysis of $[Cu(TIB^{Mes2})_4]PF_6$ indicating a multi-step mass loss as a function of temperature.

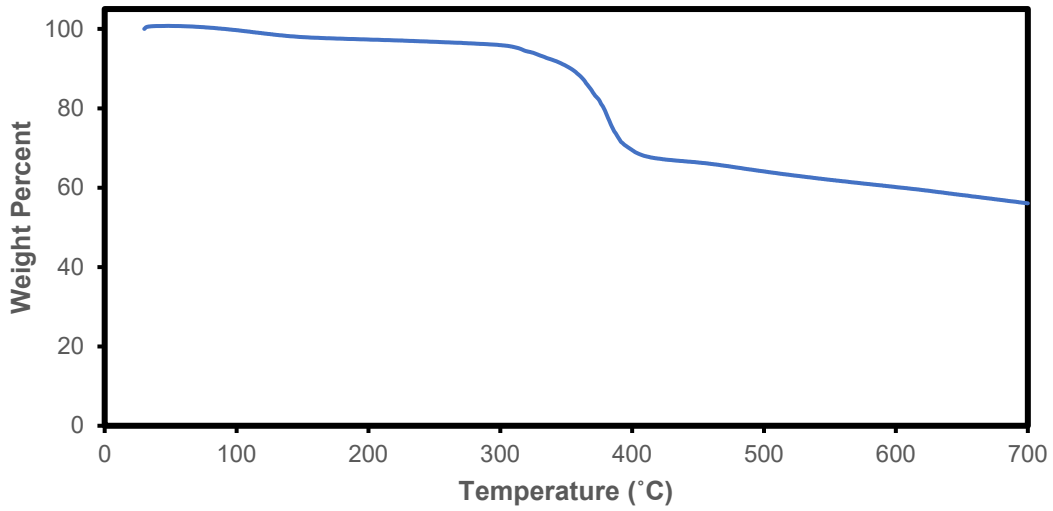

Figure 2.31. Thermogravimetric Analysis of Cu/Zn-^{ISO}CN-5. Significant mass loss occurred at the onset temperature of ~310 ˚C.

Gas Sorption and Surface Area Analysis

Gas sorption measurements were performed using a Micrometrics ASAP 2020 Adsorption Analyzer. Approximately 54 mg of material was transferred to a pre-weighed sample

tube and degassed at 80 ˚C for at least 24 hours or until the outgas rate was below 5 mmHg. The sample tube was reweighed to obtain a mass for the sample. Analyses performed on Cu/Zn-^{ISO}CN-5 degassed at 80 ˚C revealed insignificant surface areas in response to N_2 sorption, but showed marginally greater sorption and surface area in the case CO_2.

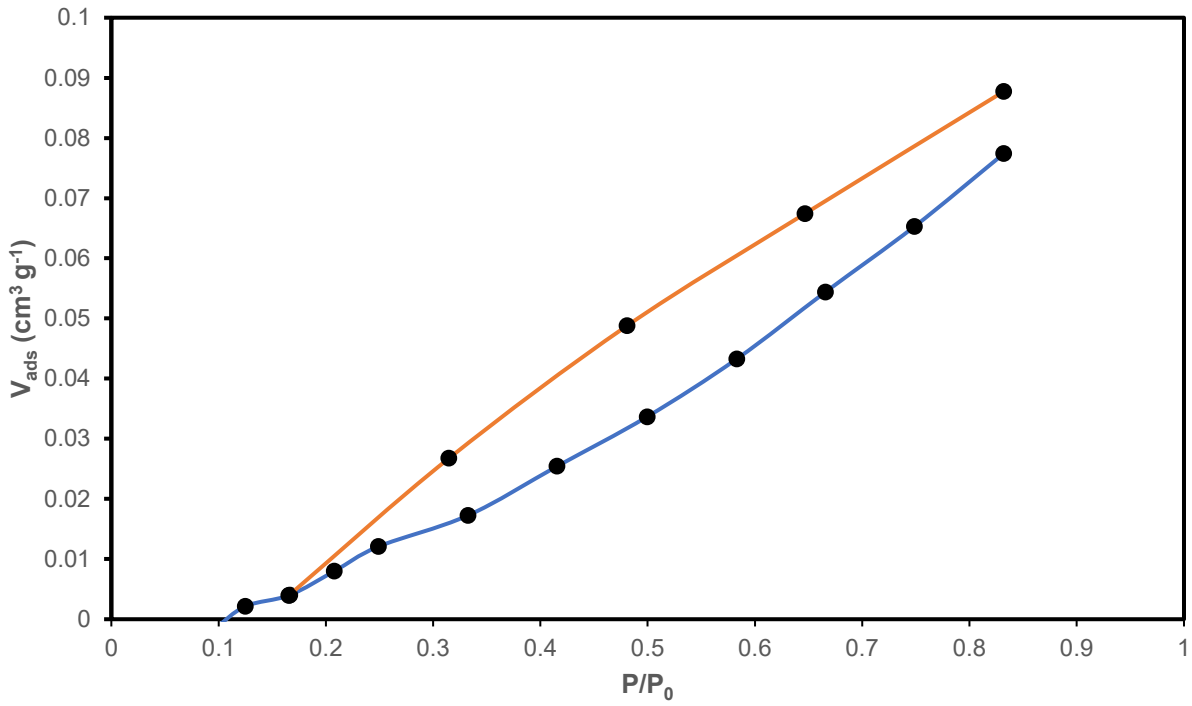

Figure 2.32. N_2 sorption isotherm of activated Cu-^{ISO}CN-5 showing negligible gas uptake; blue= adsorption, orange = desorption.

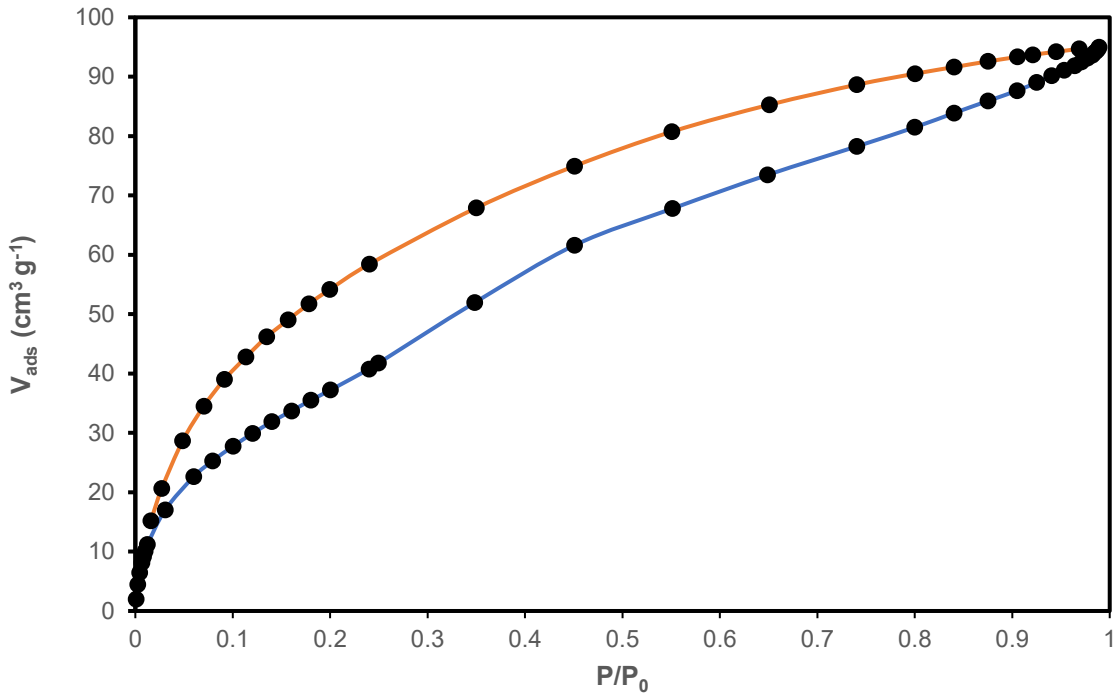

Figure 2.33. First run of CO_2 sorption isotherm of activated Cu-^{ISO}CN-5; blue = adsorption, orange = desorption.

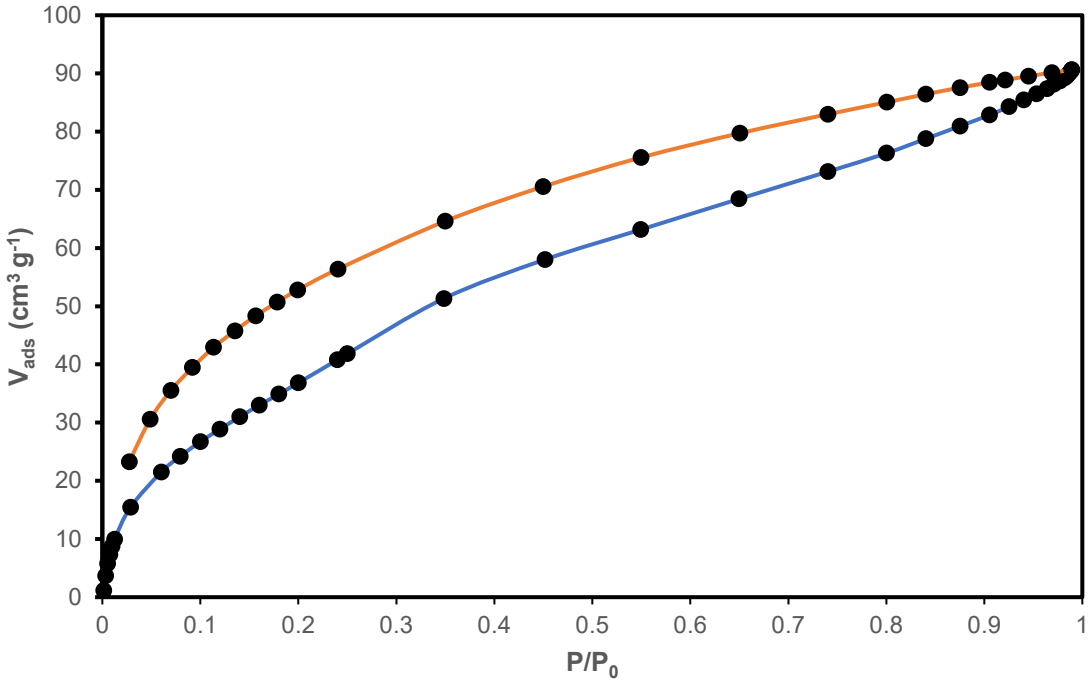

Figure 2.34. Second independent run of CO_2 sorption isotherm of activated Cu-^{ISO}CN-5; blue = adsorption, orange = desorption.

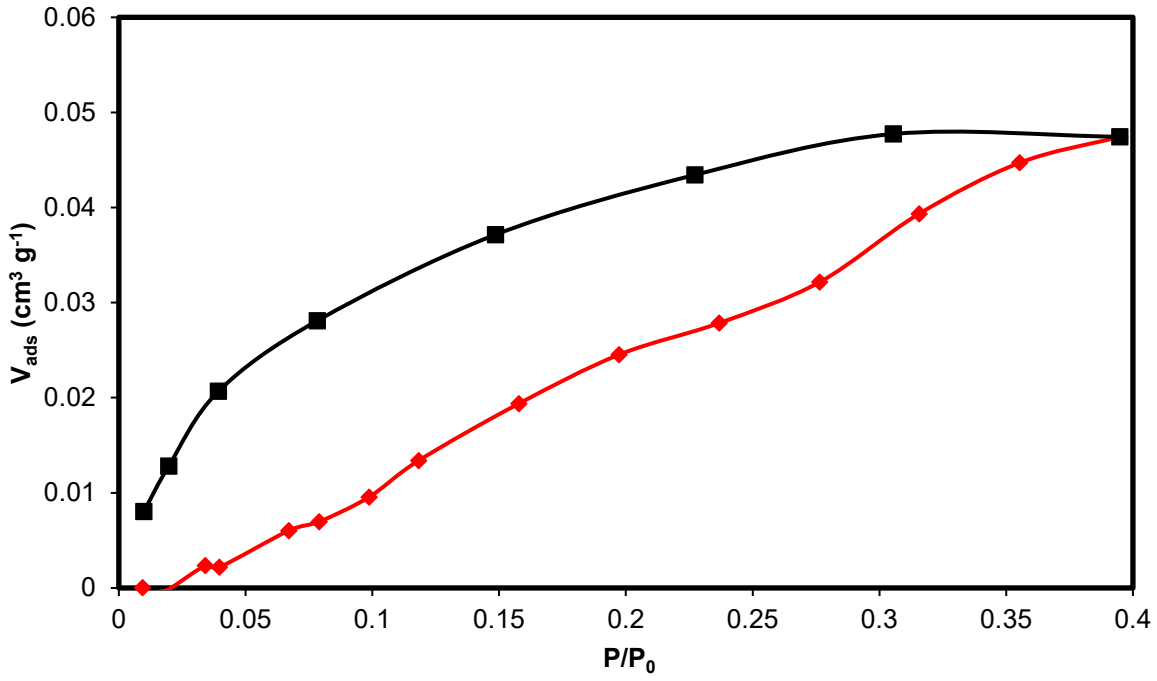

Figure 2.35. O_2 sorption isotherm of activated Cu-^{ISO}CN-5, showing negligible gas uptake; red = adsorption, black = desorption.

Results of Single Crystal X-ray Diffraction Studies.

Single crystal X-ray structure determinations were carried out at low temperature on Platform Diffractometers equipped with either Cu Kα radiation sources and Bruker APEX II detectors. All structures were solved by direct methods with SHELXS[1-2] and refined by full-matrix least-squares procedures utilizing SHELXL within Olex2 small-molecule solution, refinement, and analysis software package.[3] Crystallographic data collection and refinement information are listed in Table S5.1. Powder X-ray diffraction studies on Cu/Zn-^{ISO}CN-5 were performed at room temperature on a Bruker D8 Advanced LynxEye CCD diffractometer, equipped with Cu Kα radiation (λ = 1.54178 Å) and Kβ filter. Diffraction measurements were set to 40V and 40 mA.

Details of Single-Crystal Refinement.

$[Cu(TIB)_4]PF_6$. The $[PF_6]^-$ counterion is located on a special position in the $P4_2/n$ space group, which results in significant positional disorder. Due to the fact that 0.25 $[PF_6]^-$ units are present in the asymmetric unit, the anion was modeled with hard SADI and RIGU restraints on the P-F bonds to account for the disorder. This structure was also found to contain disordered, sub-stoichiometric molecules of CH_2Cl_2 of co-crystallization which could not be modeled as discrete entities. To account for the disorder, the residual electron density fitted and refined as floating Cl and C atoms, which gave better refinement statistics than structure factor elimination using the Platon/SQUEEZE procedure.

Cu^{ISO}CN-5. The benzoate unit one TIB^{Mes2} linker possesses positional disorder, which was modeled and refined anisotropically. Significant positional disorder was also observed for THF molecules of co-crystallization and could not be reasonably modeled. These were treated with Platon/SQUEEZE to remove structure factors/electron density prior to refinement.

Table 2.1. Crystallographic data collection and refinement information.

Name	1,4-(CNAr^{Mes2})$C_6H_4CO_2H$	$[Cu(TIB)_4]PF_6$	Cu/Zn-^{ISO}CN-5
Formula	$C_{32}H_{29}NO_2$	$C_{133.06}H_{122.29}Cl_{15.19}CuF_6N_4O_8P$	$C_{96}H_{84}Cl_2CuN_3O_6Zn_2$
Crystal System	Monoclinic	Tetragonal	Orthorhombic
Space Group	*P*2/*c*	$P4_2/n$	*Fdd*2
***a*, Å**	19.5157(7)	16.4879(4)	21.9954(7)
***b*, Å**	8.0632(3)	16.4879(4)	27.005(8)
***c*, Å**	16.3195(6)	26.0255(8)	43.0962(11)
a, deg	90	90	90
b, deg	106.966(2)	90	90
g, deg	90	90	90
V, Å^3	2456.25(16)	7075.1(4)	26257.8(13)
Z	4	2	8
Radiation (λ, Å)	Cu-Ka, 1.54178	Cu-Ka, 1.54178	Cu-Ka, 1.54178
ρ (calcd.), g/cm^3	1.243	1.245	0.830
μ (Mo Ka), mm^{-1}	0.599	3.457	1.266
Temp, K	100	100	100
θ max, deg	72.782	63.232	49.549
data/parameters	4670 / 0 / 324	5761/111/499	6487/17/514
***R*$_1$**	0.0434(4339)	0.0771	0.0506(5243)
***wR*$_2$**	0.1152(4887)	0.2258	0.1372(6487)
GOF	1.080	1.075	1.000

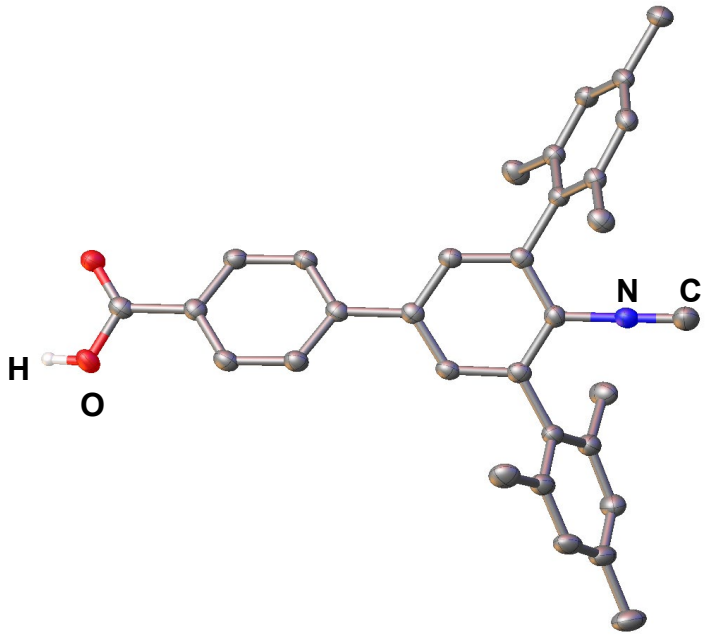

Figure 2.36 Molecular structure of 1,4-(CNAr^{Mes2})$C_6H_4CO_2H$ (TIB^{Mes2}H).

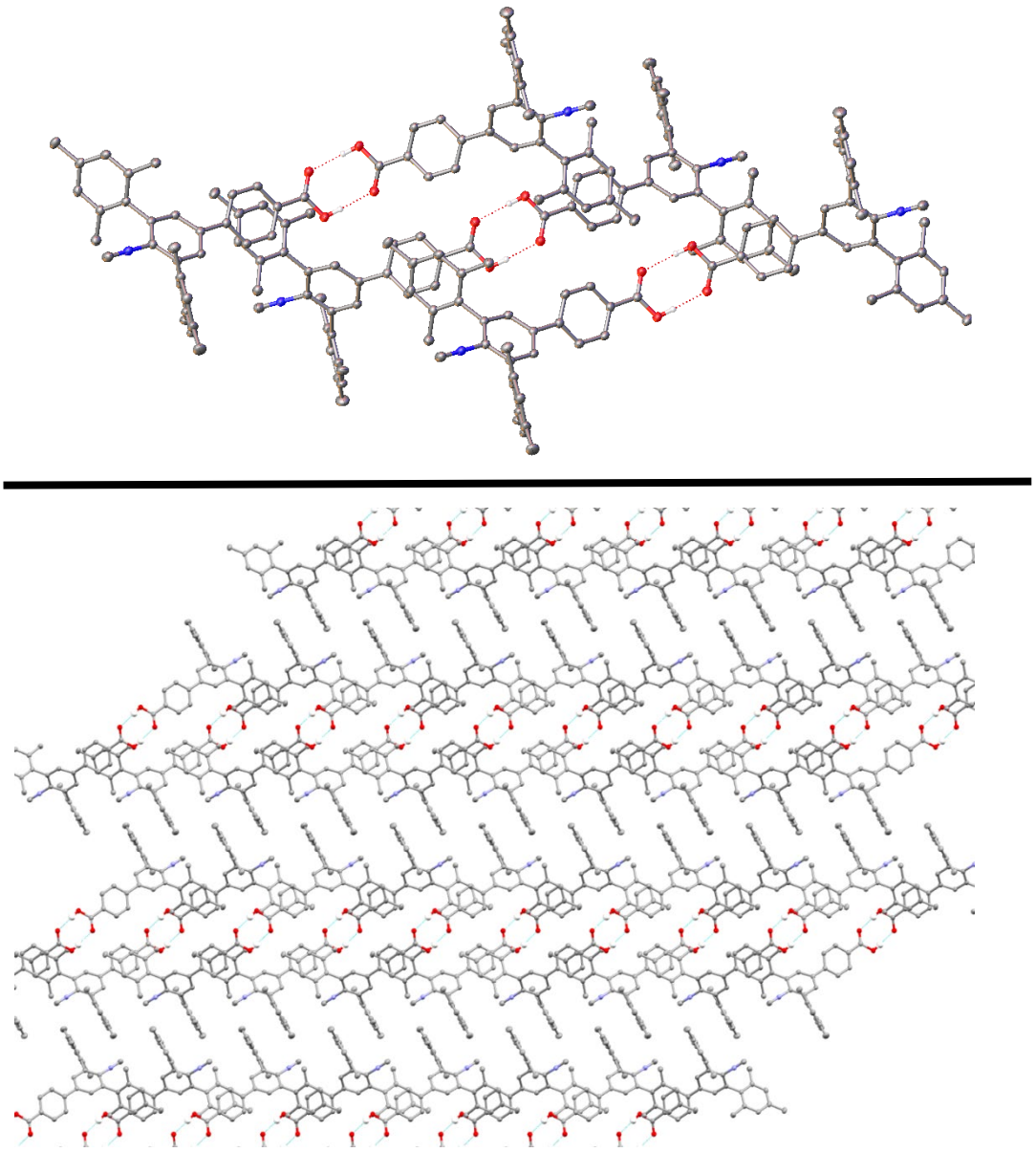

Figure 2.37. Packing Diagram for 1,4-(CNAr^{Mes2})$C_6H_4CO_2H$ (TIB^{Mes2}) showing intermolecular hydrogen bonding interactions (top). View down crystallographic b axis (bottom) showing herringbone structure.

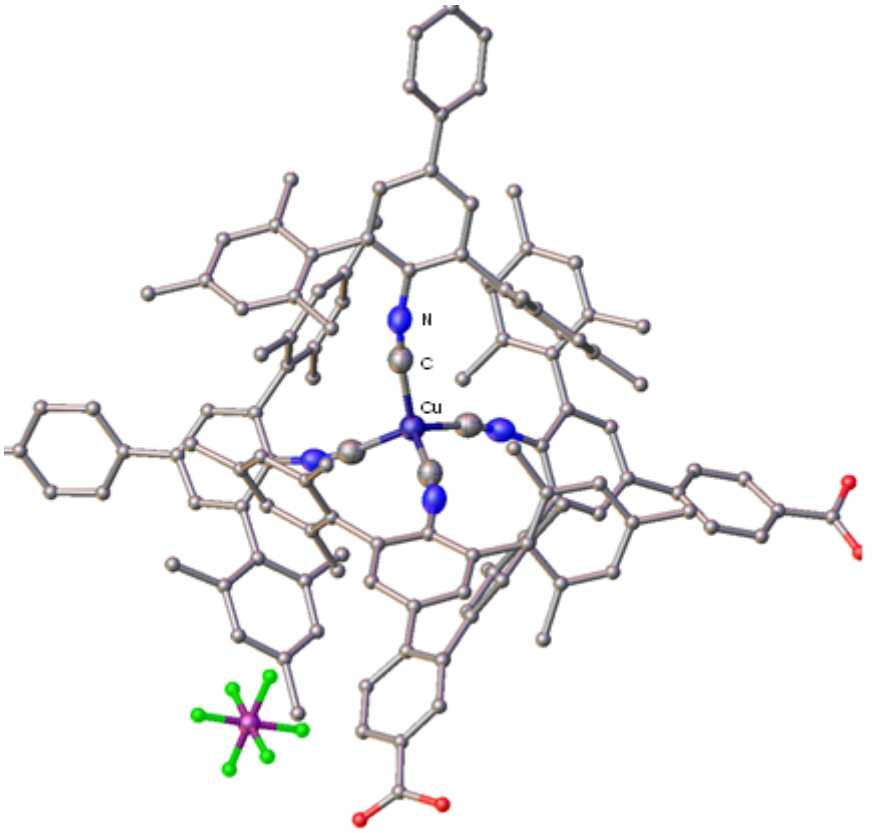

Figure 2.38 Structure of the Molecular Core for $[Cu(TIB^{Mes2}H)_4]PF_6$.

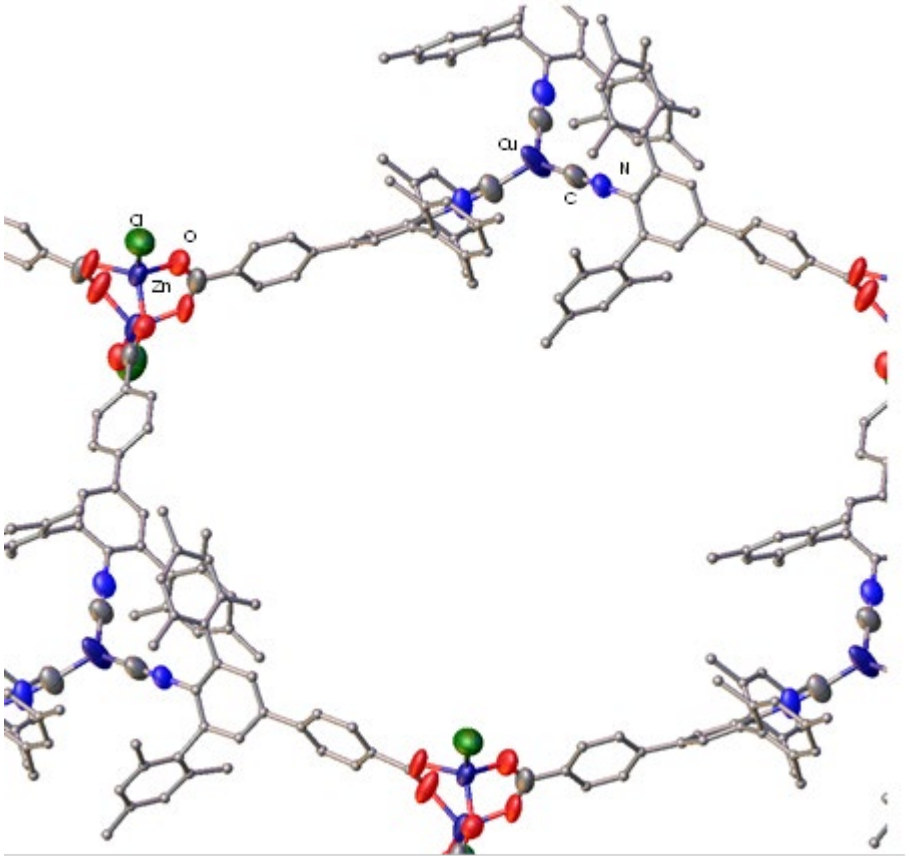

Figure 2.39. Structure Dual-SBU Repeat Unit in Cu/Zn-^{ISO}CN-5 containing a tris-isocyanide Cu(I) core and Zn paddlewheel unit with axial Cl ligands.

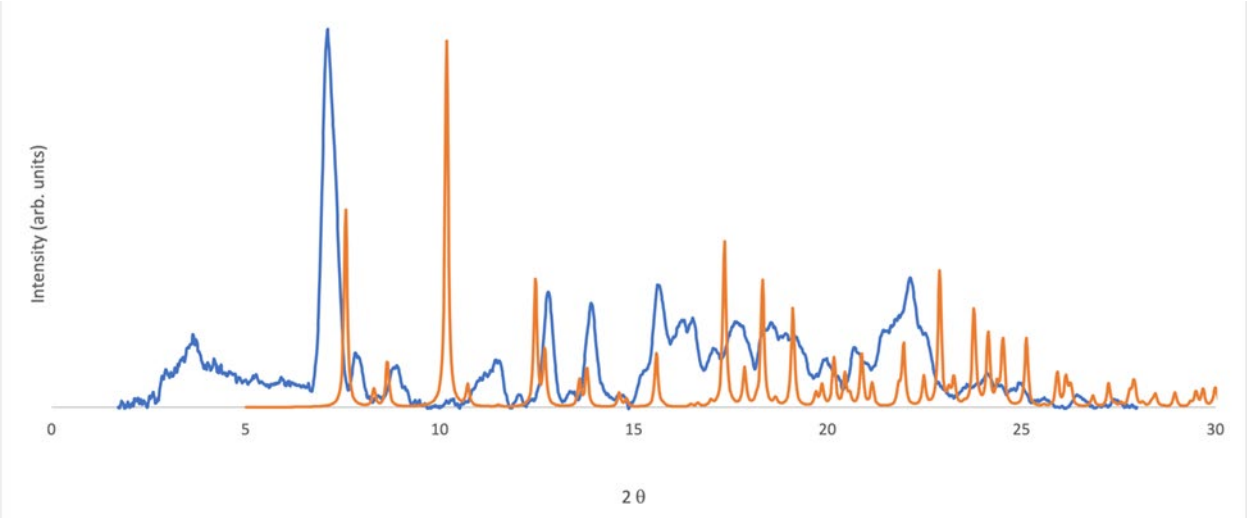

Figure 2.40. PXRD overlay of solid material obtained from the reaction between $[Cu(NCMe)_4]PF_6$ and 3.0 equiv of TIB^{Mes2} (blue trace) and simulated powder pattern from single-crystalline $[Cu(TIB^{Mes2})_4]PF_6$ (orange trace). The difference between the powder patterns indicates differing phases for these materials.

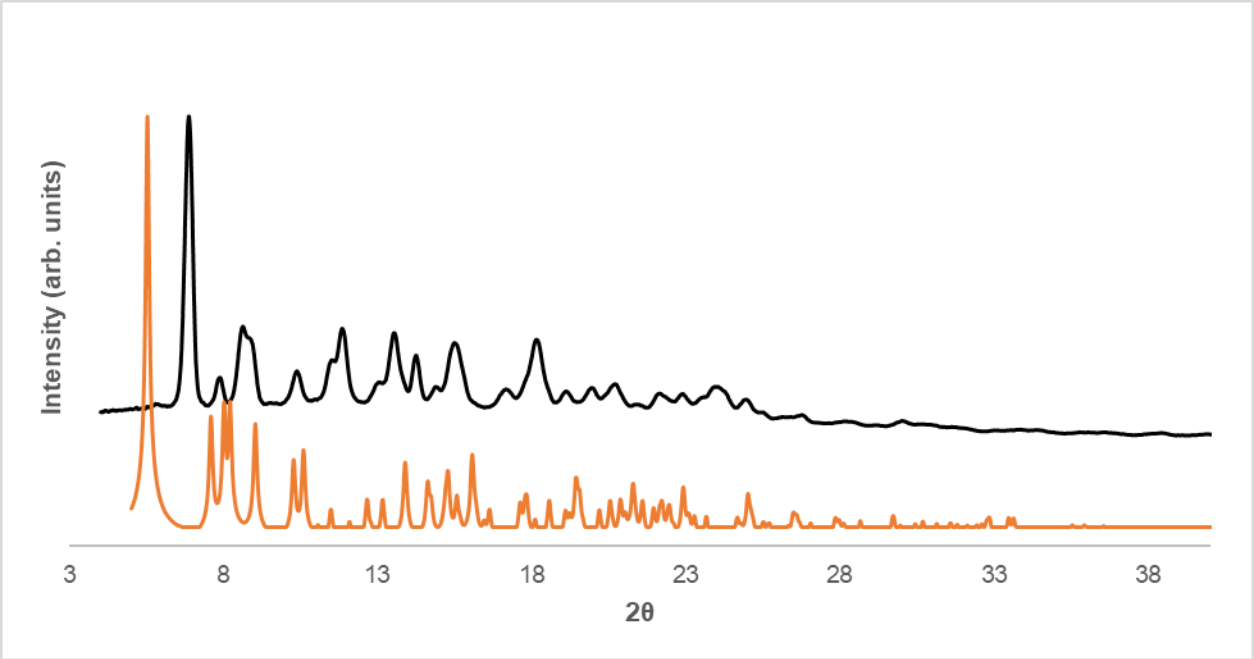

Figure 2.41. Powder X-ray Diffraction Pattern of Cu/Zn-^{ISO}CN-5, experimental (black) and simulated from single crystal diffraction (orange).

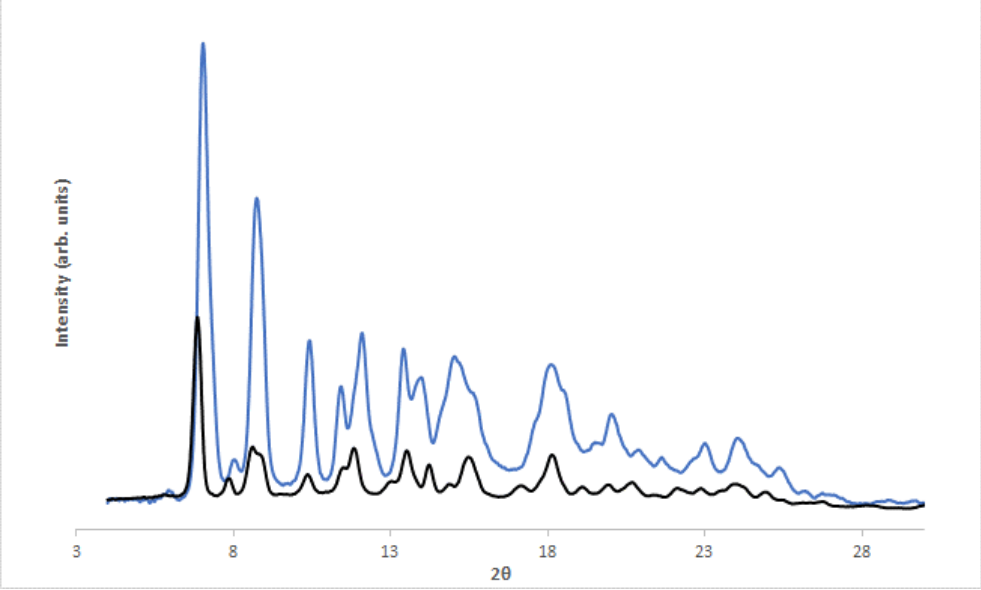

Figure 2.42. Powder X-ray diffraction pattern of Cu-^{ISO}CN-5 as synthesized (black) and after exposure to air for 20 days (blue).

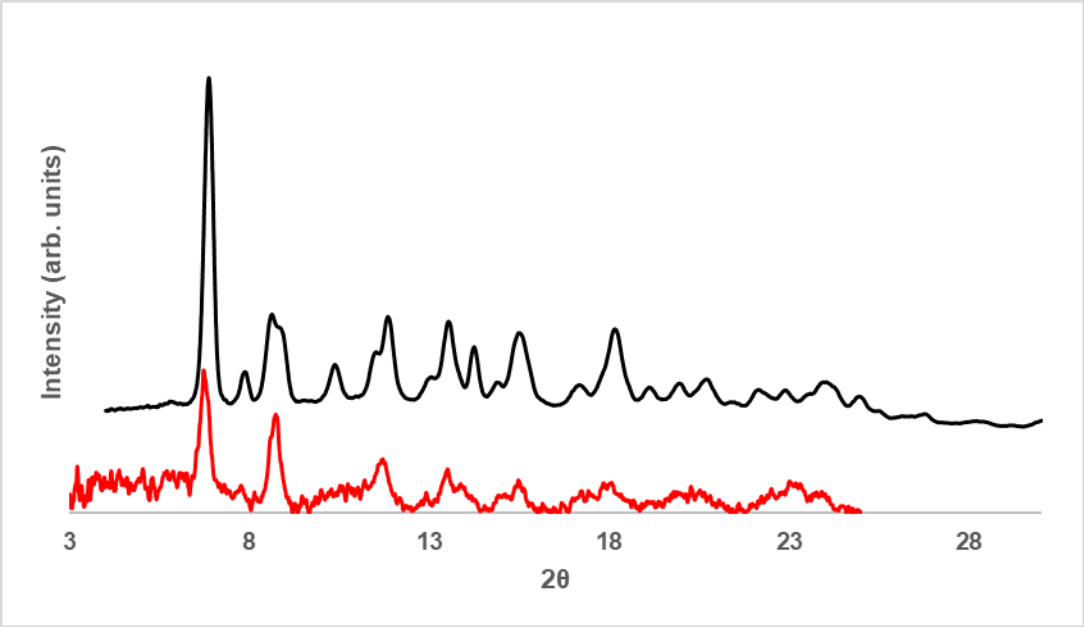

Figure 2.43. Powder X-ray diffraction pattern of Cu-^{ISO}CN-5 as synthesized (black) and after suspension in water for 24 hrs (red). A loss of crystallinity is observed over the course of 24 hours.

2.5. Acknowledgements

Chapter 2, in full, is a reprint of the material as it appears in Inorganic Chemistry: Balto, K.P.; Gembicky, M.; Rheingold, A. L.; Figueroa, J. S. "Crystalline Hydrogen-Bonding Networks and Mixed-Metal Framework Materials Enabled by an Electronically Differentiated Heteroditopic Isocyanide/Carboxylate Linker Group" *Inorganic Chemistry*. **2021**, *60 (16),* 12545-12554. The dissertation author was the primary investigator and author of this paper.

2.6. References.

(1) Lee, J.; Farha, O. K.; Roberts, J.; Scheidt, K. A.; Nguyen, S. T.; Hupp, J. T., Metal–organic Framework Materials as Catalysts. *Chem. Soc. Rev.* **2009**, *38*, 1450-1459.

(2) Li, J.-R.; Kuppler, R. J.; Zhou, H.-C., Selective Gas Adsorption and Separation in Metal–Organic Frameworks. *Chem. Soc. Rev.* **2009**, *38*, 1477-1504.

(3) Li, H.; Wang, K.; Sun, Y.; Lollar, C. T.; Li, J.; Zhou, H.- C., Recent Advances in Gas Storage and Separation Using Metal–Organic Frameworks. *Mater. Today* **2018**, *21*, 108-121.

(4) Pascanu, V.; González Miera, G.; Inge, A. K.; Martín- Matute, B., Metal–Organic Frameworks as Catalysts for Organic Synthesis: A Critical Perspective. *J. Am. Chem. Soc.* **2019**, *141*, 7223-7234.

(5) Solanki, V. A.; Borah, B., Ranking of Metal–Organic Frameworks (MOFs) for

Separation of Hexane Isomers by Selective Adsorption. *Ind. Eng. Chem. Res.* **2019**, *58*, 20047-20065.

(6) Yang, D.; Gates, B. C., Catalysis by Metal Organic Frameworks: Perspective and Suggestions for Future Research. *ACS Catal.* **2019**, *9*, 1779-1798.

(7) Yaghi, O. M.; O'Keeffe, M.; Ockwig, N. W.; Chae, H. K.; Eddaoudi, M.; Kim, J., Reticular Synthesis and the Design of New Materials. *Nature* **2003**, *423*, 705-714.

(8) Tranchemontagne, D. J.; Mendoza-Cortés, J. L.; O'Keeffe, M.; Yaghi, O. M., Secondary Building Units, Nets and Bonding in the Chemistry of Metal–Organic Frameworks. *Chem. Soc. Rev.* **2009,** *38*, 1257-1283.

(9) Long, J. R.; Yaghi, O. M., The Pervasive Chemistry of Metal–Organic Frameworks. *Chem. Soc. Rev.* **2009**, *38*, 1213-1214.

(10) O'Keeffe, M.; Yaghi, O. M., Deconstructing the Crystal Structures of Metal–Organic Frameworks and Related Materials into Their Underlying Nets. *Chem. Rev.* **2012**, *112*, 675-702.

(11) Deng, H.; Grunder, S.; Cordova, K. E.; Valente, C.; Furukawa, H.; Hmadeh, M.; Gándara, F.; Whalley, A. C.; Liu, Z.; Asahina, S.; Kazumori, H.; O'Keeffe, M.; Terasaki, O.; Stoddart, J. F.; Yaghi, O. M., Large-Pore Apertures in a Series of Metal-Organic Frameworks. *Science* **2012**, *336* 1018-1023.

(12) Chatt, J., The Stabilisation of Low Valent States of the Tansition Metals: Introductory Lecture. *J. Inorg. Nucl. Chem.* **1958**, *8*, 515-531.

(13) Ellis, J. E., Adventures with Substances Containing Metals in Negative Oxidation States. *Inorg. Chem.* **2006**, *45*, 3167-3186.

(14) Masoomi, M. Y.; Morsali, A.; Dhakshinamoorthy, A.; Garcia, H., Mixed-Metal MOFs: Unique Opportunities in Metal–Organic Framework (MOF) Functionality and Design. *Angew. Chem. Int. Ed.* **2019**, *58* (43), 15188- 15205.

(15) Abednatanzi, S.; Gohari Derakhshandeh, P.; Depauw, H.; Coudert, F.-X.; Vrielinck, H.; Van Der Voort, P.; Leus, K., Mixed-Metal Metal–Organic Frameworks. *Chem. Soc. Rev.* **2019**, *48*, 2535-2565.

(16) Wang, Z.; Cohen, S. M., Postsynthetic modification of metal–organic frameworks. *Chem. Soc. Rev.* **2009**, *38*, 1315-1329.

(17) Cohen, S. M., Postsynthetic Methods for the Functionalization of Metal–Organic Frameworks. *Chem. Rev.* **2012**, *112*, 970-1000.

(18) Li, Z.; Schweitzer, N. M.; League, A. B.; Bernales, V.; Peters, A. W.; Getsoian, A. B.; Wang, T. C.; Miller, J. T.; Vjunov, A.; Fulton, J. L.; Lercher, J. A.; Cramer, C. J.; Gagliardi, L.; Hupp, J. T.; Farha, O. K., Sintering- Resistant Single-Site Nickel Catalyst Supported by Metal–Organic Framework. *J. Am. Chem. Soc.* **2016**, *138*, 1977-1982.

(19) Abdel-Mageed, A. M.; Rungtaweevoranit, B.; Parlinska- Wojtan, M.; Pei, X.; Yaghi, O. M.; Behm, R. J., Highly Active and Stable Single-Atom Cu Catalysts Supported by a

Metal–Organic Framework. *J. Am. Chem. Soc.* **2019**, *141*, 5201-5210.

(20) Van Velthoven, N.; Waitschat, S.; Chavan, S. M.; Liu, P.; Smolders, S.; Vercammen, J.; Bueken, B.; Bals, S.; Lillerud, K. P.; Stock, N.; De Vos, D. E., Single-site metal–organic framework catalysts for the oxidative coupling of arenes via C–H/C–H activation. *Chem. Sci.* **2019**, *10*, 3616-3622.

(21) Syed, Z. H.; Sha, F.; Zhang, X.; Kaphan, D. M.; Delferro, M.; Farha, O. K., Metal–Organic Framework Nodes as a Supporting Platform for Tailoring the Activity of Metal Catalysts. *ACS Catalysis* **2020**, *10*, 11556-11566.

(22) Goldberg, I., Crystal Engineering of Porphyrin Framework Solids. *Chem. Commun.* **2005**, 1243-1254.

(23) Garibay, S. J.; Stork, J. R.; Cohen, S. M., The Use of Metalloligands in Metal-Organic Frameworks. *Prog. Inorg. Chem.* **2009**, *56*, 335-378.

(24) Kumar, G.; Gupta, R., Molecularly Designed Architectures – the Metalloligand Way. *Chem. Soc. Rev.* **2013**, *42*, 9403-9453.

(25) Burgess, S. A.; Kassie, A.; Baranowski, S. A.; Fritzsching, K. J.; Schmidt-Rohr, K.; Brown, C. M.; Wade, C. R., Improved Catalytic Activity and Stability of a Palladium Pincer Complex by Incorporation into a Metal–Organic Framework. *J. Am. Chem. Soc.* **2016**, *138*, 1780-1783.

(26) Agnew, D. W.; Gembicky, M.; Moore, C. E.; Rheingold, L. A; Figueroa, J. S., Robust, Transformable, and Crystalline Single-Node Organometallic Networks Constructed from Ditopic *m*-Terphenyl Isocyanides. *J. Am. Chem. Soc.* **2016**, *138*, 15138-15141.

(27) Agnew, D. W.; DiMucci, I. M.; Arroyave, A.; Gembicky, M.; Moore, C. E.; MacMillan, S. N.; Rheingold, A. L.; Lancaster, K. M.; Figueroa, J. S., Crystalline Coordination Networks of Zero-Valent Metal Centers: Formation of a 3-Dimensional Ni(0) Framework with m- Terphenyl Diisocyanides. *J. Am. Chem. Soc.* **2017**, *139*, 17257-17260.

(28) Arroyave, A.; Gembicky, M.; Rheingold, A. L.; Figueroa, J. S., Aqueous Stability and Ligand Substitution of a Layered Cu(I)/Isocyanide-Based Organometallic Network Material with a Well-Defined Channel Structure. *Inorg. Chem.* **2020**, *59*, 11868-11878.

(29) Cotton, F. A.; Zingales, F., The Donor-Acceptor Properties of Isonitriles as Estimated by Infrared Study. *J. Am. Chem. Soc.* **1961**, *83*, 351-355.

(30) Carpenter, A. E.; Mokhtarzadeh, C. C.; Ripatti, D. S.; Havrylyuk, I.; Kamezawa, R.; Moore, C. E.; Rheingold A. L.; Figueroa, J. S., Comparative Measure of the Electronic Influence of Highly Substituted Aryl Isocyanides. *Inorg. Chem.* **2015**, *54*, 2936-2944.

(31) Malatesta, L.; Bonati, F., Isocyanide Complexes of Transition Metals" ; Wiley: New York, 1969

(32) Malatesta, L., Palladium(0) Compounds. Part I. Diisonitrilopalladium(0) Compounds. *J. Chem. Soc.* **1955**, 3924-3926.

(33) Yamamoto, Y., Zerovalent Transition Metal Complexes of Organic Isocyanides. *Coord. Chem. Rev.* 1980, *32*, 193-233.

(34) Yamamoto, Y.; Yamazaki, H., Low-Valent Isocyanide Complexes and Clusters of Palladium and Platinum. Crystal Structure of [Pt{C(=NR)N(R)C(=NR}(RNC)2](R = 2,6-Me2C6H3). *J. Chem. Soc., Dalton Trans.* **1989,** , 2161-2166.

(35) Weber, L., Homoleptic Isocyanide Metalates. Angew. Chem. Int. Ed. 1998, 37, 1515-1517.

(36) Ivasenko, O.; Perepichka, D. F., Mastering Fundamentals Supramolecular Design with Carboxylic Acids. Common Lessons from X-ray Crystallography and Scanning Tunneling Microscopy. Chem. Soc. Rev. 2011, 40, 191-206.

(37) Adachi, T.; Ward, M. D., Versatile and Resilient Hydrogen-Bonded Host Frameworks. Acc. Chem. Res. 2016, 49, 2669-2679.

(38) Luo, J.; Wang, J.-W.; Zhang, J.-H.; Lai, S.; Zhong, D.-C., Hydrogen-Bonded Organic Frameworks: Design, Structures and Potential Applications. Cryst. Eng. Comm. 2018, 20, 5884-5898.

(39) Lin, R.-B.; He, Y.; Li, P.; Wang, H.; Zhou, W.; Chen, B., Multifunctional Porous Hydrogen-Bonded Organic Framework Materials. Chem. Soc. Rev. 2019, 48, 1362-1389.

(40) Hisaki, I.; Xin, C.; Takahashi, K.; Nakamura, T., Designing Hydrogen-Bonded Organic Frameworks (HOFs) with Permanent Porosity. Angew. Chem. Int. Ed. 2019, 58, 11160-11170.

(41) Li, P.; Ryder, M. R.; Stoddart, J. F., Hydrogen-Bonded Organic Frameworks: A Rising Class of Porous Molecular Materials. Acc. Mater. Res. 2020, 1, 77-87.

(42) Fox, B. J.; Sun, Q. Y.; Dipasquale, A. G.; Fox, A. R.; Rheingold, A. L.; Figueroa, J. S., Solution Behavior and Structural Properties of Cu(I) Complexes Featuring m-terphenyl Isocyanides. Inorg. Chem. 2008, 47, 9010-9020.

(43) Fox, B. J.; Millard, M. D.; DiPasquale, A. G.; Rheingold, A. L.; Figueroa, J. S., Thallium(I) as a Coordination Site Protection Agent: Preparation of an Isolable Zero-Valent Nickel Tris-Isocyanide. Angew. Chem. Int. Ed. 2009, 48, 3473-3477.

(44) Sheldrick, G., A short history of SHELX. Acta Crystallographica Section A 2008, 64 (1), 112-122.

(45) Sheldrick, G., Crystal structure refinement with SHELXL. Acta Crystallographica Section C 2015, 71 (1), 3-8.

(46) Dolomanov, O. V.; Bourhis, L. J.; Gildea, R. J.; Howard, J. A. K.; Puschmann, H., OLEX2: a complete structure solution, refinement and analysis program. Journal of Applied Crystallography 2009, 42 (2), 339-341.

Chapter 3 A Permanently Porous Crystalline Ni(0) Hydrogen Bonding Network.

3.1. Introduction.

Hydrogen-bonded organic frameworks (HOFs) are two- or three-dimensional frameworks constructed by intermolecular hydrogen bonding interactions between organic or metal-organic molecules.[1] Importantly, HOFs are soluble in polar solvents, allowing for their regeneration upon successive dissolution and recrystallization cycles, which is not a characteristic of other permanently porous materials, such as metal-organic frameworks (MOFs) or covalent-organic frameworks (COFs).[2,3] In addition to facile crystallization and regeneration, HOFs can be used in areas such as catalysis and in gas storage and separations.[2,4] While the first HOF structure was isolated from trimesic acid (1,3,5-benzenetricarboxylic acid) in 1969, little was known about the application of these materials until the isolation of HOF-1 from the linker 4,4',4'',4'''-tetra(4,6-diamino-s-triazin-2-yl)tetraphenylmethane.[5,6] This is because the trimesic acid HOF was not stable or permanently porous, as its structure collapsed upon removal of solvent molecules.[7] HOF-1, however, was reported as the first known permanently porous HOF material despite removal of solvent molecules.[8,9] Moreover, HOF-1 is capable of facilitating the separation of ethylene and acetylene (C_2H_2/C_2H_4) and had the highest BET_{CO2} surface area of any HOF material when reported.

The isolation of HOF-1 led to an increased interest in permanently porous HOFs, and new ligand designs featuring hydrogen-bonding groups (carboxylic acids, pyridines, amines and porphyrin derivatives) were reported.[10,11] Many of these multitopic ligand scaffolds are also precursors to MOF formation, as they feature functional groups capable of binding higher-valent metals. Interestingly, heteroditopic ligands featuring two or more functional groups capable of binding different metals enable step-wise synthesis of mixed-metal MOF materials. Since they

feature different functional groups appended to an organic backbone, heteroditopic ligands can also be used to isolate metal-containing HOFs.[12] One popular scaffold used to generate these materials is the porphyrin-type ligand, where higher-valent metals can be incorporated into the pyrrole core, and the second functional group can be used to generate either a HOF or a mixed-metal MOF upon addition of a second metal ion. Another heteroditopic ligand with the potential to form unique HOFs and mixed-metal MOFs is one featuring an isocyanide group (CN-R) and a functional group capable of hydrogen-bonding. For example, a metal-containing HOF featuring Pd(II) and Fe(II) nodes was isolated using a heteroditopic ligand featuring an isocyanide and an oxime (RHC=N−OH) group.[13,14] Importantly, the isocyanide group in this heteroditopic ligand selectively binds Pd(II) and Fe(II) metals while the oxime groups participate in hydrogen-bonding interactions to form a 2-D network. While these metal-organic HOFs were characterized by single crystal X-ray diffraction (sc-XRD), their materials properties, such as surface area measurements and thermal stability, were not assessed.

While HOF materials featuring isocyanide groups have been previously reported, to our knowledge, few feature low-valent metal centers. Importantly, isocyanides have been extensively studied in organometallic chemistry and are excellent at stabilizing reduced, electron-rich metals on account of their ability to function as good σ-donors and effective π-acids. Due to this this synergistic bonding, we have previously utilized *m*-terphenyl isocyanide ligands to kinetically stabilize low-valent, coordinatively unsaturated organometallic complexes. More recently, we have utilized the same *m*-terphenyl backbone to isolate a HOF featuring Cu(I) nodal centers using the heteroditopic ligand 1,4-CNAr^{Mes2}C$_6$H$_4$CO$_2$H (TIB^{Mes2}H; TIB = terphenyl isocyanide benzoate; Ar^{Mes2} = 2,6-(2,4,6-Me$_3$C$_6$H$_2$)$_2$C$_6$H$_2$). Indeed, addition of four equivalents of TIB^{Mes2}H to one equivalent of [Cu(NCMe)$_4$]PF$_6$ leads to the generation of a seven fold-interpenetrated Cu(I)

HOF network, $[Cu(TIB^{Mes2}H)_4]PF_6$, featuring tetrakis isocyanide Cu(I) nodal centers and free carboxylic acid groups participating in hydrogen bonding. Importantly, $[Cu(TIB^{Mes2}H)_4]PF_6$ was found to have negligible surface area due to its high level of interpenetration and the presence of PF_6^- counter-anions occupying the 6.5 × 16.1 Å rectangular channels in the material. However, it was thermally stable up to 500 °C. Due to the ability of isocyanides to bind low-valent metals, we reasoned formation of a Ni(0) HOF was possible through the use of $TIB^{Mes2}H$.[15-18] Herein, we report the synthesis and characterization of the permanently porous hydrogen-bonding network $Ni(TIB^{Mes2}H)_4$, featuring tetrakis-isocyanide Ni(0) nodes.

3.2. Results and Discussion.

While we previously determined isocyanides in $TIB^{Mes2}H$ selectively bind Cu(I) metals, we did not establish its ability to bind zero-valent metal centers. To determine if the isolation of zero-valent HOFs was possible, we assessed the ability of $TIB^{Mes2}H$ to bind Ni(0) centers. The ability of isocyanides to bind Ni(0) has been well-studied by us and others, however the use of a heteroditopic ligand featuring a carboxylic acid group has never been explored, especially since zero-valent metal centers are known to react with carboxylic acid groups to form metal-hydrides. Addition of a tetrahydrofuran (THF) solution containing 4 equivalents of $TIB^{Mes2}H$ to a stirring THF solution containing one equivalent of $Ni(PPh_3)_4$ ($PPh_3 = C_{18}H_{15}P$) (Scheme 3.1), followed by crystallization from a THF/ difluorobenzene mixture resulted in dark pink needle-like single crystals of $Ni(TIB^{Mes2}H)_4$. Importantly, single crystal quality material was isolated exclusively from the reaction of $Ni(PPh_3)_4$ with $TIB^{Mes2}H$. Attempts at isolating single crystals from the reaction of $TIB^{Mes2}H$ with another Ni(0) source, $Ni(COD)_2$ (COD= 1,5-cyclo-octadiene) were unsuccessful, however the powder pattern obtained from this reaction was consistent with the powder pattern obtained from the reaction with $Ni(PPh_3)_4$ as a starting material. We reasoned use of $Ni(COD)_2$ resulted in the isolation of $Ni(TIB^{Mes2}H)_4$ as a microcrystalline solid because COD

is an extremely labile ligand, unlike PPh_3. Due to the increased stabilization of zero-valent nickel from the use of π-acidic phosphine ligands, ligand substitution kinetics are slowed substantially during the reaction with $TIB^{Mes2}H$, allowing for the formation of single-crystal quality material.

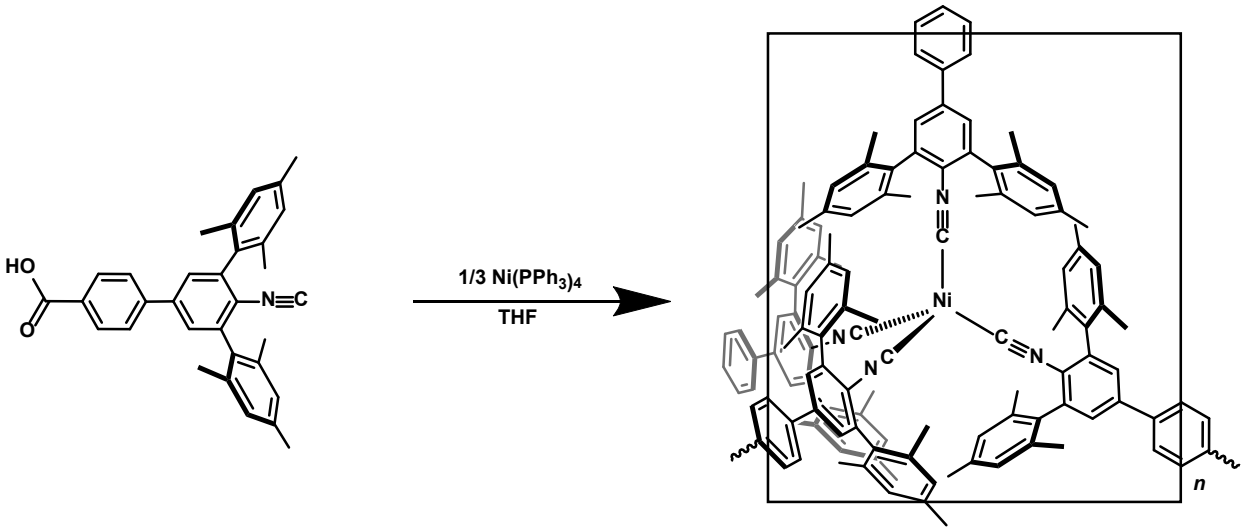

Figure 3.1. Synthetic Route to $Ni(TIB^{Mes2}H)_4$.

X-ray crystallographic analysis of single crystals of $Ni(TIB^{Mes2}H)_4$ revealed a hydrogen bonding network (HOF) featuring tetrakis-isocyanide Ni(0) nodes (Figure 4.1). Attenuated total reflectance-infrared (ATR-IR) analysis of single crystals of $Ni(TIB^{Mes2}H)_4$ revealed a significantly red shifted isocyanide stretching frequency (ν_{CN}) at 1950 cm^{-1} from free $TIB^{Mes2}H$ (ν_{CN} = 2117 cm^{-1}). As we have previously shown for both the molecular tetrakis-isocyanide Ni(0) molecular complex $Ni(CNAr^{Mes2})_4$, and the isocyanide coordination network (^{ISO}CN) featuring tetrahedral Ni(0) nodes, this lower energy band is diagnostic of a zero-valent NiL_4 coordination environment.[19,20] The isolation of a four-coordinate Ni(0) hydrogen bonding network confirms the isocyano-group of $TIB^{Mes2}H$ selectively binds to low-valent, electron-rich metal centers. Furthermore, inspection of the single crystal X-ray structure of $Ni(TIB^{Mes2}H)_4$ indicates an average Ni-C bond length of 1.78(21) Å. This is significantly shorter than both molecular $Ni(CNAr^{Mes2})_4$ ($Ni\text{-}C_{avg}$ = 1.84(14) Å) and $Ni\text{-}^{ISO}CN\text{-}2\cdot([CNAr^{Mes2}]_2)_{0.5}$ ($Ni\text{-}C_{avg}$ =1.84(64) Å).[19,20] This contracted

M-C bond length, accompanied by the red shifted isocyanide stretching frequency seen in $Ni(TIB^{Mes2}H)_4$, suggests an increase in π back-bonding from the Ni(0) metal center into π* molecular orbitals of the isocyanide.[21] In addition, simple calculation of the Houser τ_4, (τ_4 =0.95) value suggests a near idealized (τ_4 =1) tetrahedral geometry about Ni(0) centers in $Ni(TIB^{Mes2}H)_4$.[20] We attribute this lack of distortion about Ni(0) nodal centers to constraints from lattice formation, whereas molecular $Ni(CNAr^{Mes2})_4$ (τ_4=0.85) is free to adopt non-negligible structural distortions from an idealized tetrahedral geometry in the solid state.

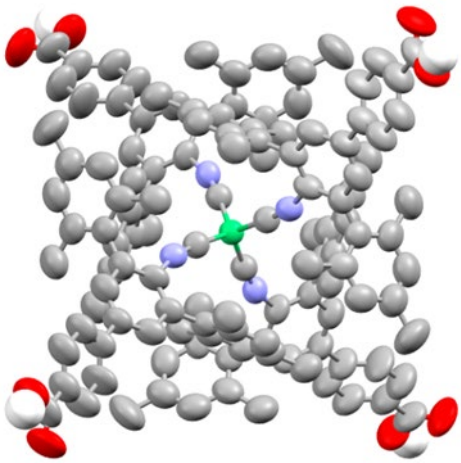

Figure 3.2. X-ray crystal structure of the molecular core of the hydrogen bonded network $Ni(TIB^{Mes2}H)_4$ along the crystallographic *c* axis. H atoms aside from those associated with the carboxylic acids and co-crystallized solvent molecules have been omitted for clarity.

Zero-valent metal centers are known to react with carboxylic acid groups to form metal-hydrides. Since the formation of $Ni(TIB^{Mes2}H)_4$ is possible as determined by sc-XRD and no reaction with the carboxylic acid groups in $TIB^{Mes2}H$ were observed by ATR-IR spectroscopy or ^{1}H-NMR spectroscopy, we reasoned use of encumbering *m*-terphenyl isocyanide ligand scaffolds inhibit the reactivity of Ni(0) with carboxylic acid groups. To test this hypothesis, a THF solution containing $Ni(COD)_2$ (1 equivalent, 50 mg) was added to THF solution containing benzoic acid (1 equivalent, 22 mg). Due to the lability of COD as a ligand, a reaction was expected to occur

upon addition of benzoic acid. After 30 minutes, the reaction mixture turned from a light yellow to a dark orange and was analyzed using ^{1}H-NMR spectroscopy. The ^{1}H-NMR spectrum confirmed the reaction of $Ni(COD)_2$ with benzoic acid, providing evidence of the reactivity of Ni(0) centers with aryl carboxylic acids (Figure 3.23).

To provide further rationale that the sterically encumbering *m*-terphenyl groups of the isocyanide ligands $CNAr^{Mes2}$ and $TIB^{Mes2}H$ inhibit the reactivity of zero-valent nickel centers with aryl carboxylic acids, a THF solution containing the molecular Ni(0) tetrakis-isocyanide system, $Ni(CNAr^{Mes2})_4$ (1 equivalent, 50 mg), was added to a THF solution containing benzoic acid (1 equivalent, 4.3 mg). After 30 minutes, ATR-IR analysis of the reaction mixture revealed isocyanide stretching frequencies of ν_{CN} = 1969cm $^{-1}$ and 2009 cm $^{-1}$ which correlate the previously reported isocyanide frequencies of the starting material, $Ni(CNAr^{Mes2})_4$. ^{1}H-NMR analysis in C_6D_6, revealed benzoic acid starting material as well as the presence of $Ni(CNAr^{Mes2})_4$. The presence of the starting material $Ni(CNAr^{Mes2})_4$ in both IR and ^{1}H-NMR spectrums indicate the encumbering *m*-terphenyl groups limit the reactivity of the Ni (0) centers in both $Ni(CNAr^{Mes2})_4$ and $Ni(TIB^{Mes2}H)_4$, thereby allowing the formation of the Ni(0) hydrogen-bonding network, $Ni(TIB^{Mes2}H)_4$.

Due to the encumbering nature of the *m*-terphenyl isocyanide zero-valent nickel does not react with the carboxylic acids in $TIB^{Mes2}H$. Instead, carboxylic acid groups of the Ni(0)-coordinated $TIB^{Mes2}H$ ligand form $R_2^2(8)$ hydrogen-bonds to the nearest neighbor $Ni(TIB^{Mes2}H)_4$ units (Figure 3.2).[22] Inspection of the extended structure of $Ni(TIB^{Mes2}H)_4$ indicates it organizes diamondoid (**dia**) structure in the $P4_2/n$ space group. Notably, five independent three-dimensional networks are generated by these hydrogen-bonding interactions to form a five-fold interpenetrated extended structure. This is significantly different than the seven-fold interpenetrated structure

generated by hydrogen-bonding interactions in the HOF $[Cu(TIB^{Mes2}H)_4]PF_6$. Additionally, while the extended lattice in $[Cu(TIB^{Mes2}H)_4]PF_6$ has rectangular channels of ca. 16.5 x 16.1 Å along the crystallographic *b* axis, examination of the void space in $Ni(TIB^{Mes2}H)_4$ reveals circular channels of 31 Å x 32 Å along the crystallographic *c* axis (Figure 3.3). Inspection of $Ni(TIB^{Mes2}H)_4$ along the crystallographic *a* and *b* axes reveal smaller channels of ca. 13 Å x 10 Å. We attribute the larger channels in this Ni(0) HOF to the decreased interpenetration observed in the structure of $Ni(TIB^{Mes2}H)_4$. Furthermore, we theorized these channels would be accessible to guest molecules, and surface area measurements were performed using N_2 and CO_2 gases. While $Ni(TIB^{Mes2}H)_4$ exhibits a negligible Brunauer-Emmett-Teller (BET) surface area to N_2, it does exhibit a BET surface area of 246 m^2/g to CO_2 (Figure 3.16). Due to the polarizability of CO_2, $Ni(TIB^{Mes2}H)_4$ displays significantly higher surface area to CO_2. Furthermore, this BET_{CO2} surface area demonstrates $Ni(TIB^{Mes2}H)_4$ is a permanently porous HOF. Indeed, a major disadvantage of many HOF materials is their structural fragility, and most are known to collapse upon activation due to loss of solvent molecules in addition to weak hydrogen bonding interactions.[4] We attribute the permanently porous nature of $Ni(TIB^{Mes2}H)_4$ to several factors. Most significantly, THF solvent molecules do not participate in the hydrogen-bonding interactions between $Ni(TIB^{Mes2}H)_4$ units as

determined by sc-XRD. Additionally, $Ni(TIB^{Mes2}H)_4$ degree of interpenetration, which leads to an increase in structural stability.[23]

In addition to exhibiting structural stability upon activation, the $Ni(TIB^{Mes2}H)_4$ exhibits high thermal stability as well. The HOF displays multistage decomposition beginning at ~ 250 °C (Figure 3.28). This is significantly higher than the previously reported $[Cu(TIB^{Mes2}H)_4]PF_6$ HOF which displays a multi-step decomposition process between 150 and 500 °C.[24] Additionally, unlike

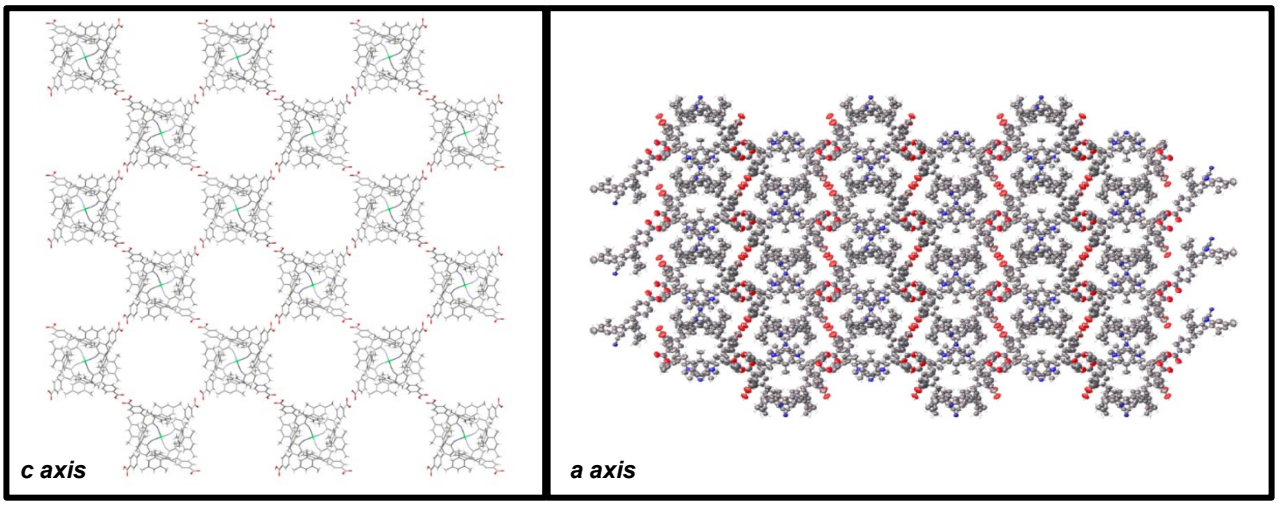

Figure 3.3. Full interpenetrated views of the extended structure of the hydrogen bonding network, $Ni(TIB^{Mes2}H)_4$, along the crystallographic c axis (left) and the crystallographic a axis (right). The diameter of the channels observed down the crystallographic c axis are ~30 Å. Co-crystallized solvent molecules have been omitted for clarity.

$[Cu(TIB^{Mes2}H)_4]PF_6$, $Ni(TIB^{Mes2}H)_4$ is not indefinitely stable on the benchtop, and a rapid color change from pink to yellow is observed. Indeed, ATR-IR analysis on a sample of $Ni(TIB^{Mes2}H)_4$ after 60 seconds of air exposure indicates the generation of free $TIB^{Mes2}H$ and the isocyanide stretching frequency indicative of a low valent NiL_4 species is no longer detected (Figure 3.9). This rapid decomposition upon air exposure is expected since $Ni(TIB^{Mes2}H)_4$ contains Ni(0) centers and contains large pores.[25]

In a similar manner to other HOF materials, $Ni(TIB^{Mes2}H)_4$ can be readily dissolved in polar organic solvents, such as THF, however it is insoluble in non-polar solvents such as benzene.[26] Subsequent dissolution of microcrystalline $Ni(TIB^{Mes2}H)_4$ and recrystallization from THF

generates the same $Ni(TIB^{Mes2}H)_4$ HOF as determined by ATR-IR spectroscopy and pXRD analysis. This solubility in polar solvents enables the facile regeneration of the framework upon re-crystallization.[1] Dissolution of the previously reported HOF, $[Cu(TIB^{Mes2}H)_4]PF_6$, exhibits an isocyanide-exchange equilibrium in solution as a result of the sterically encumbering nature of $TIB^{Mes2}H$, where ligand dissociation produces an equivalent of free $TIB^{Mes2}H$ and $[(THF)Cu(TIB^{Mes2}H)_3]PF_6$. Therefore, we reasoned the ligation properties of $TIB^{Mes2}H$ could lead to a similar equilibrium in $Ni(TIB^{Mes2}H)_4$. Indeed, Fourier transform infrared (FT-IR) analysis of a THF solution containing $Ni(TIB^{Mes2}H)_4$ reveals isocyanide stretching frequencies (ν_{CN}) of 1944 cm^{-1}, 2025 cm^{-1} and 2117 cm^{-1}. These isocyanide stretching frequencies observed in solution are characteristic of a trigonal planar NiL_3 coordination environment, where $\nu_{CN(assym)} = 1944cm^{-1}$, and $\nu_{CN(sym)} =$ 2025 cm^{-1}. The free isocyanide at ν_{CN} = 2117 cm^{-1} indicates dissociation of one equivalent of ligand from the Ni(0) centers upon dissolution. As such, the presence of free $TIB^{Mes2}H$ is indicative of an isocyanide exchange equilibrium, which was further assayed by variable temperature (VT) ^1H nuclear magnetic resonance (NMR) spectroscopy from 298K to 338K (Figure 3.3A). Importantly, as temperature increased, the singlet at δ 6.91 ppm, correlating to protons on the benzoic acid backbone of $TIB^{Mes2}H$ in $Ni(TIB^{Mes2}H)_3$, increased in intensity (Figure 3.3B). Moreover, a concomitant decrease in intensity was observed in the singlet associated the species $Ni(TIB^{Mes2}H)_4$ (δ 6.86 ppm), thereby implicating a dynamic equilibrium process where ligand dissociation produces an equivalent of $Ni(TIB^{Mes2}H)_3$ and free $TIB^{Mes2}H$ from $Ni(TIB^{Mes2}H)_4$. Unfortunately, strong overlap of the chemical shifts for $Ni(TIB^{Mes2}H)_4$, $Ni(TIB^{Mes2}H)_3$, and $TIB^{Mes2}H$ prevented meaningful integrations required for a Van't Hoff analysis.

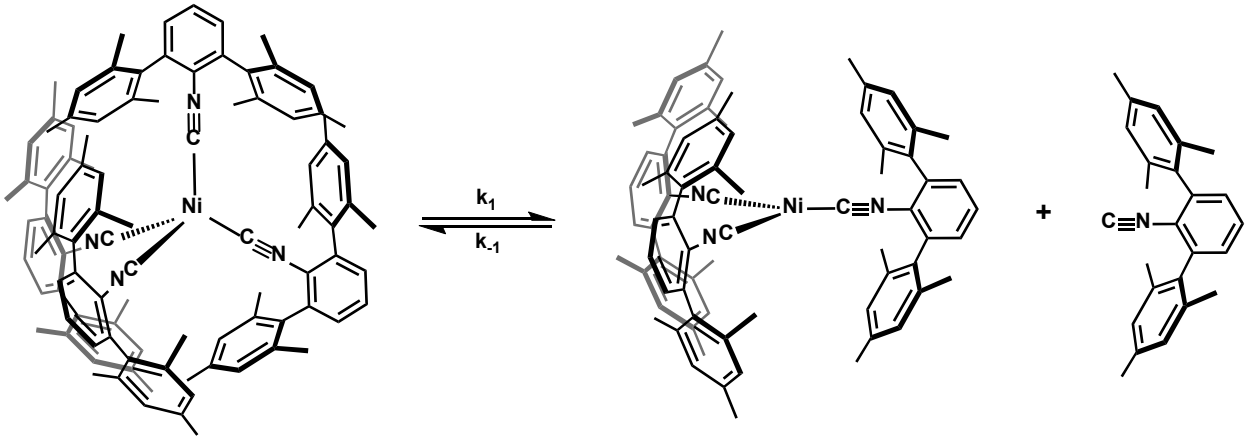

Figure 3.4. Ligand dissociation/association equilibrium observed for nickel(0) *m*-terphenyl isocyanide complexes in THF-d_8.

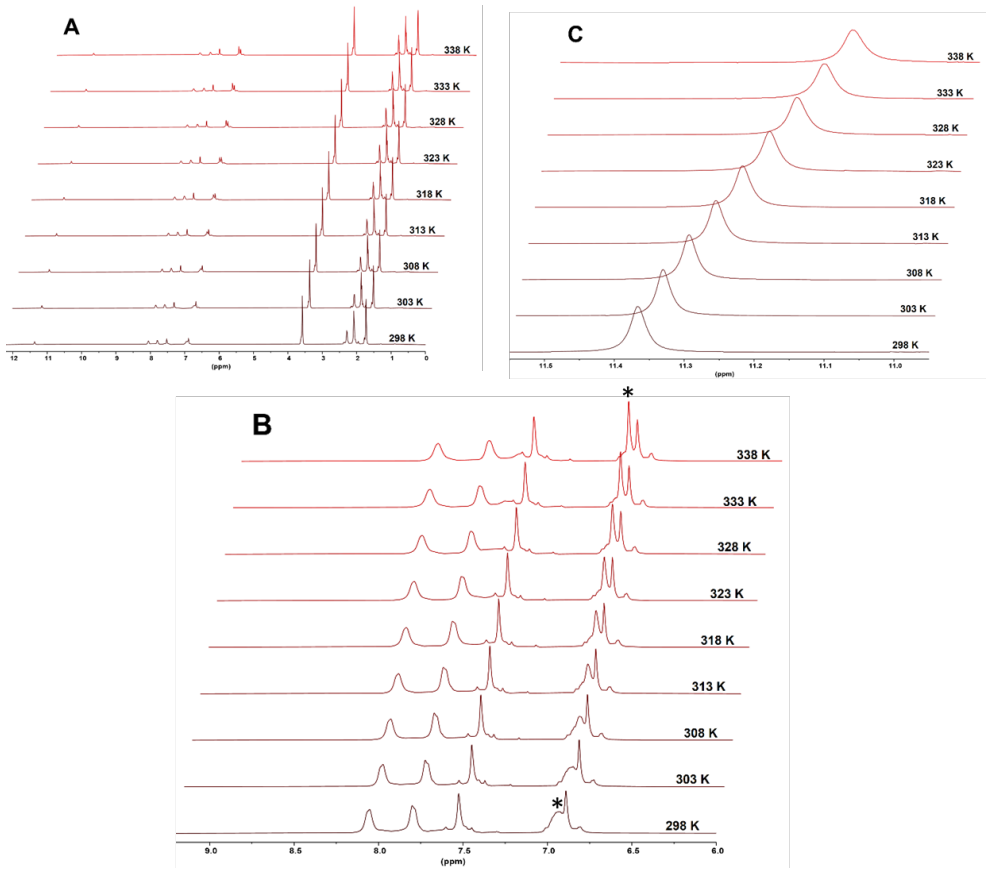

Figure 3.5. Variable temperature ^{1}H NMR of Ni(TIB^{Mes2}H)$_4$ in THF-d_8 between 298 K to 333 K for the (A) full window, (B) aryl region, and (C) H-bonding region. (*) in panel B represents signal at δ 6.91 ppm indicating the dynamic equilibrium process where ligand dissociation produces an equivalent of Ni(TIB^{Mes2}H)$_3$ and free TIB^{Mes2}H.

Despite the inability to perform a Van't Hoff analysis on $Ni(TIB^{Mes2}H)_4$, we reasoned insight into the equilibrium process in $Ni(TIB^{Mes2}H)_4$ could be obtained through analysis of $Ni(CNAr^{Mes2})_4$ since both ligands feature similar steric properties. Indeed, $Ni(CNAr^{Mes2})_4$ exhibits a similar isocyanide equilibrium exchange process in solution and can be fully characterized using both ATR-IR and ^{1}H-NMR spectroscopies. Single crystals of $Ni(CNAr^{Mes2})_4$ give rise to an isocyanide stretching frequency of 1950 cm^{-1} by ATR-IR spectroscopy. However, FT-IR analysis of a THF solution containing $Ni(CNAr^{Mes2})_4$ indicates isocyanide stretching frequencies at 1985 cm^{-1} and 2117 cm^{-1}, respectively.[19] The presence of free isocyanide at 2117 cm^{-1} suggests an isocyanide exchange equilibrium between $Ni(CNAr^{Mes2})_4$ and $Ni(CNAr^{Mes2})_3$ in solution. In addition, ^{1}H-NMR spectroscopy on a sample of $Ni(CNAr^{Mes2})_4$ at room temperature provides further evidence of a dynamic equilibrium process occurring in solution, where a chemical shift at δ 2.30 ppm, corresponding to the *o*-Me group on free $CNAr^{Mes2}$ is observed. Moreover, this equilibrium is further characterized by VT ^{1}H-NMR experiments (Figure 3.25.). In solution, $Ni(CNAr^{Mes2})_4$ rapidly establishes an equilibrium processes wherein a ligand dissociation event produces an equivalent of $Ni(CNAr^{Mes2})_3$ and free $CNAr^{Mes2}$, and a ligand association reaction reforms $Ni(CNAr^{Mes2})_4$ (Scheme 3.2). As such, Van't Hoff analysis of the VT ^{1}H-NMR spectra indicate the ligand dissociation/association equilibrium process is endothermic, with the dissociation of ligand from $Ni(CNAr^{Mes2})_4$ to form $Ni(CNAr^{Mes2})_3$ and $CNAr^{Mes2}$ being favored at higher temperatures.

When comparing data from the association/dissociation equilibrium process in $Ni(CNAr^{Mes2})_4$, it is evident $Ni(TIB^{Mes2}H)_4$ exhibits a similar isocyanide exchange equilibrium in solution where the tris-isocyanide complex, $Ni(TIB^{Mes2}H)_3$, and an equivalent of free ligand are favored even at room temperature. However, crystallization of both complexes at room

temperature leads to the isolation of products, $Ni(CNAr^{Mes2})_4$ and $Ni(TIB^{Mes2}H)_4$, as determined by single crystal X-ray diffraction. Evidently, lattice formation prefers the generation of the tetrakis-isocyanide Ni(0) HOF, despite the dynamic equilibrium process taking place in solution.

3.3. Conclusions.

Isolation of permanently porous hydrogen bonding networks (HOFs) remains a challenge due to their structural fragility. Furthermore, incorporation of low valent metal centers into these frameworks is even more challenging, as most HOFs are synthesized exclusively from organic building blocks. We have previously reported a linker, $TIB^{Mes2}H$, capable of stabilizing lower valent metal centers, like Cu(I), enabling the formation of lower valent HOF materials. Using the approach described above, here, we demonstrate $TIB^{Mes2}H$ is capable of stabilizing Ni(0) metal centers, allowing the formation of the permanently porous HOF, $Ni(TIB^{Mes2}H)_4$. In solution, this HOF undergoes a dynamic isocyanide equilibrium exchange process similar to that observed in its model system, $Ni(CNAr^{Mes2})_4$. Inspection of the extended structure reveals $Ni(TIB^{Mes2}H)_4$ is a five-fold interpenetrated, diamondoid network with a measurable BET_{CO2} surface area following activation. Accordingly, we believe the linker $TIB^{Mes2}H$ can reliably generate many permanently porous HOF materials featuring low valent metal centers. As such, synthetic investigations using two different carboxylic acids are underway to increase pore size and accessibility.

3.4 Experimental Section.

General Procedures. Unless otherwise stated, all manipulations were performed under an atmosphere of dry dinitrogen using standard Schlenk and glovebox techniques. Solvents were dried and degassed according to standard procedures.[27] Unless otherwise stated, reagent grade starting materials were purchased from commercial sources and purified where necessary according to standard procedures.[28] Solid-state IR spectra were collected at 2 cm^{-1} resolution as either a KBr pellet or using a Bruker Platinum Alpha ATR-IR equipped with a diamond crystal.

The following abbreviations are used to describe the intensity and characteristics of important IR absorption bands: vs = very strong, s = strong, m = medium, w = weak, vw = very weak, b = broad, vb = very broad, sh = shoulder.

Synthesis of Ni(TIB^{Mes2}H)$_4$. A THF solution containing TIB^{Mes2}H (0.050 g, 0.110 mmol, 4.0 equiv) was added to a stirring THF solution containing Ni(PPh$_3$)$_4$ (0.010 g, 0.025 mmol, 1.0 equiv). The reaction mixture was allowed to stir for 15 min, after which the sample was filtered through celite and all volatiles were removed under reduced pressure. The resultant red powder was redissolved in minimal THF and recrystallized from n-hexane and 1,3 difluorobenzene at room temperature through slow evaporation. Dark pink single crystalline needles of Ni(TIB^{Mes2}H)$_4$ were obtained and filtered through a fine fritted funnel. Yield: 0.010 g, 0.015 mmol, 59%. FTIR-ATR (diamond surface, 20 °C, crystalline sample): ν_{CN} 1950(s), also ν_{CO} 1718 (s), 1984 (s), 1610 (s), 1244 (m), 852(s), 776 (s), 494 (s) cm^{-1}.

Dissolution of Ni(TIB^{Mes2}H)$_4$ in THF resulted in spectroscopic signatures indicative of the product resulting from a 3:1 Ni/TIB^{Mes2}H mixture and free TIB^{Mes2}.

IR Spectroscopic Data.

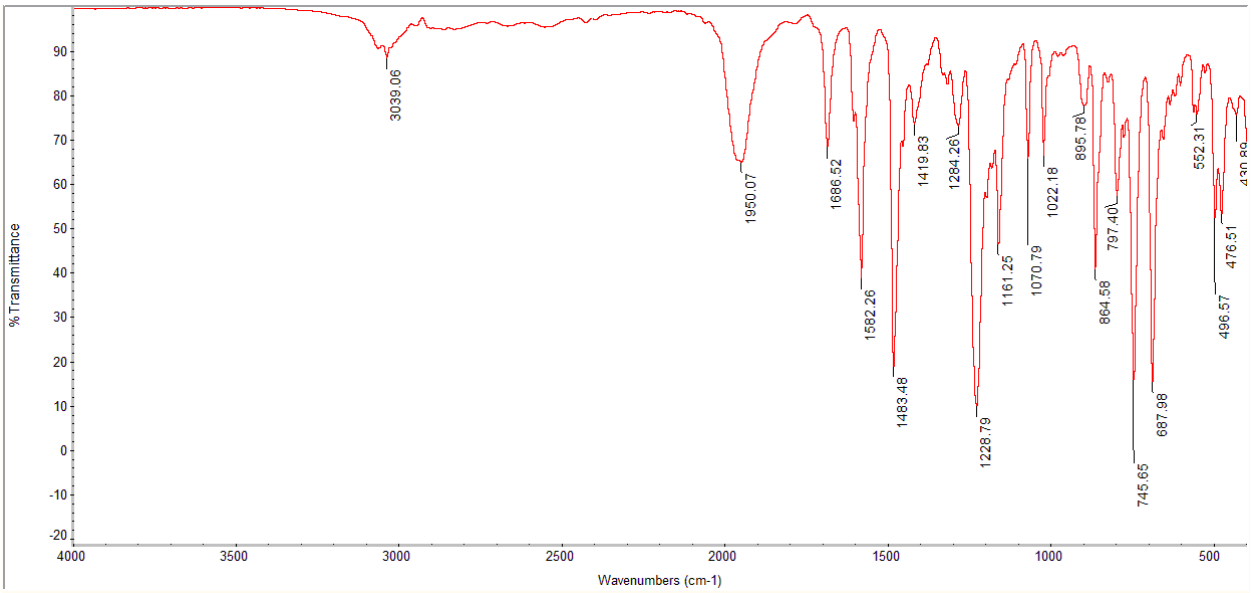

Figure 3.6. ATR-IR spectra of a single crystalline sample of Ni(TIB^{Mes2}H)$_4$. The diagnostic isocyanide stretching frequency at ν_{CN}=1950 cm^{-1} is characteristic of four- coordinate *m*-terphenyl isocyanide Ni(0) complexes.

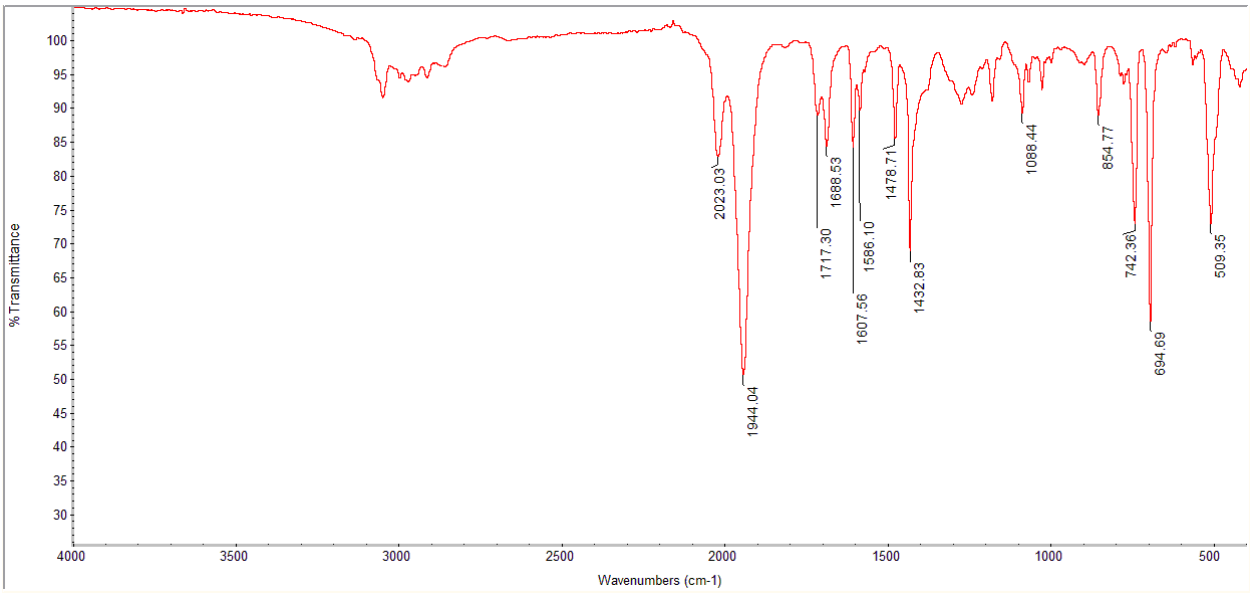

Figure 3.7. FT-IR spectrum of a THF solution containing 3 equivalents of TIB^{Mes2}H and 1 equivalent of Ni(PPh$_3$)$_4$. No free ligand is observed and the diagnostic isocyanide stretching frequencies observed appear at 1944 cm^{-1} and 2023 cm^{-1}, suggesting a NiL$_3$ coordination environment.

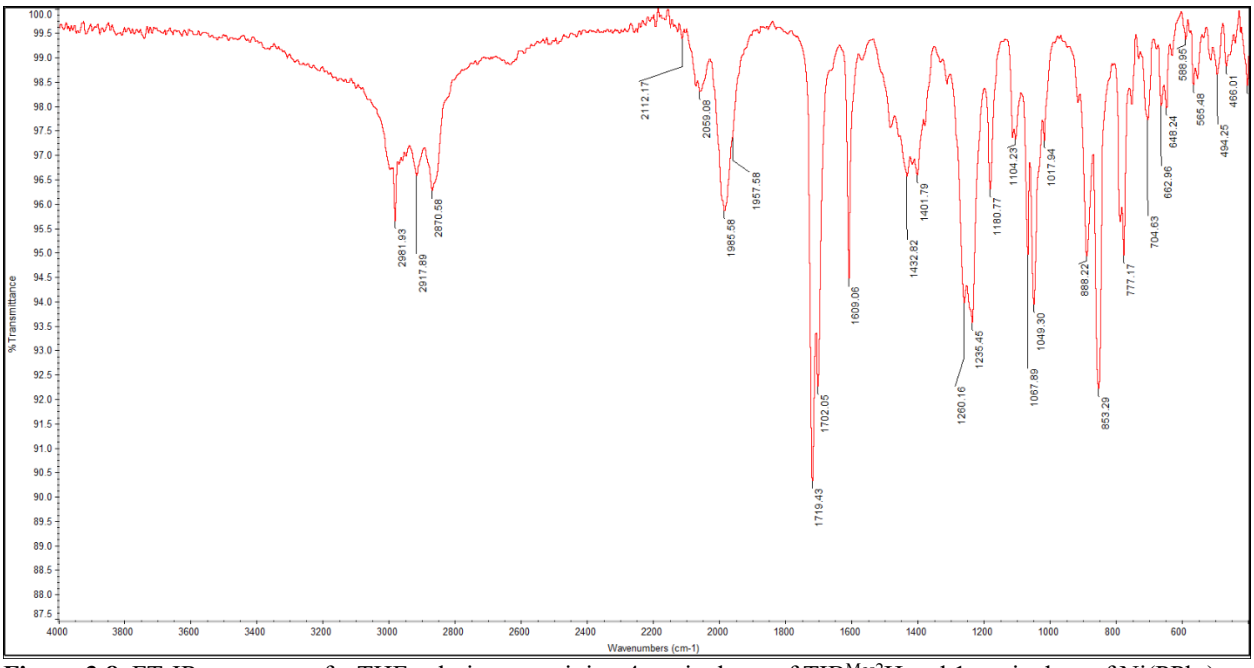

Figure 3.8. FT-IR spectrum of a THF solution containing 4 equivalents of $TIB^{Mes2}H$ and 1 equivalent of $Ni(PPh_3)_4$.

Figure 3.9. ATR-IR spectrum of a sample of single crystalline $Ni(TIB^{Mes2}H)_4$ after 2 minutes of air exposure. Free $TIB^{Mes2}H$ isocyanide is observed in the spectra at 2112 cm^{-1}.

Figure 3.10. ATR-IR spectrum of a crystalline sample of $Ni(TIB^{Mes2}H)_4$ after CO_2 gas sorption measurements were taken. The isocyanide stretching frequency at 1962 cm^{-1} indicates $Ni(TIB^{Mes2}H)_4$ did not decompose during activation and gas sorption measurements. There is some isocyanide observed at 2250 cm^{-1} due to air exposure after measurement was taken and the sample was removed from the instrument.

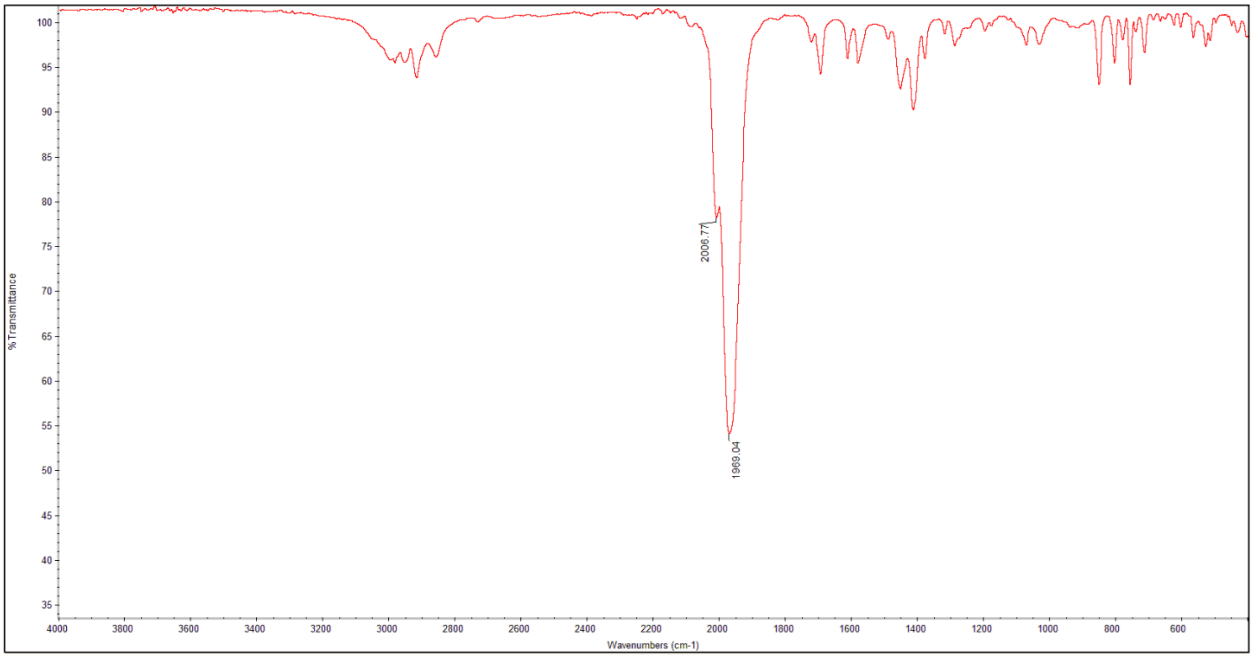

Figure 3.11. ATR-IR spectrum of the THF reaction mixture containing one equivalent of $Ni(DMP)_4$ and one equivalent of benzoic acid after 30 minutes. The isocyanide stretching frequencies correlating to the starting material, $Ni(CNAr^{Mes2})_4$, are still present. This indicates no reaction took place.

Crystallographic Structure Determination. Single X-ray structure determinations were performed at 100 K on Bruker Kappa Diffractometers equipped with either Cu-Ka or Mo-Ka radiation sources and an APEX-II CCD area detector. All structures were solved via direct methods with SHELXS13 and refined by full-matrix least-squares procedures using SHELXL1 within the Olex214 software. In cases of highly disordered solvent molecules, the Platon routine SQUEEZE15 was used to account for the corresponding electrons as a diffuse contribution to the overall scattering without specific atom positions. Crystallographic data collection and refinement information is listed in Table S3.1.

Table 3.1. X-ray crystallographic data of $Ni(TIB^{Mes2}H)_4$.

Name	$Ni(TIB^{Mes2}H)_4$
Formula	$C_{192}H_{276}N_4NiO_{24}$
Crystal System	tetragonal
Space Group	$P4_2/n$
***a*, Å**	30.925(3)
***b*, Å**	30.925(3)
***c*, Å**	12.8489(18)
α, deg	90
β, deg	90
γ, deg	90
V, Å^3	12288(3)
Z	2
Radiation (λ, Å)	MoKα (λ = 0.71073)
ρ (calcd.), g/cm^3	0.833
μ (Mo Ka), mm^{-1}	0.127
Temp, K	100.15
θ max, deg	39.836
data/parameters	5621/325
***R*$_1$**	0.0694
***wR*$_2$**	0.2172
GOF	1.033

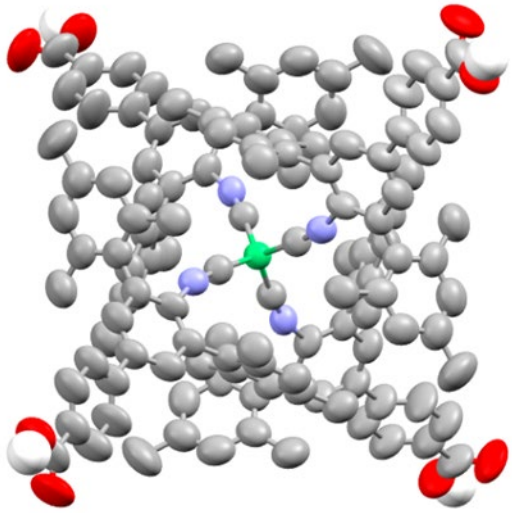

Figure 3.12. X-ray crystal structure of the molecular core of the hydrogen bonded network $Ni(TIB^{Mes2}H)_4$ along the crystallographic *c* axis. H atoms aside from those associated with the carboxylic acids and co-crystallized solvent molecules have been omitted for clarity.

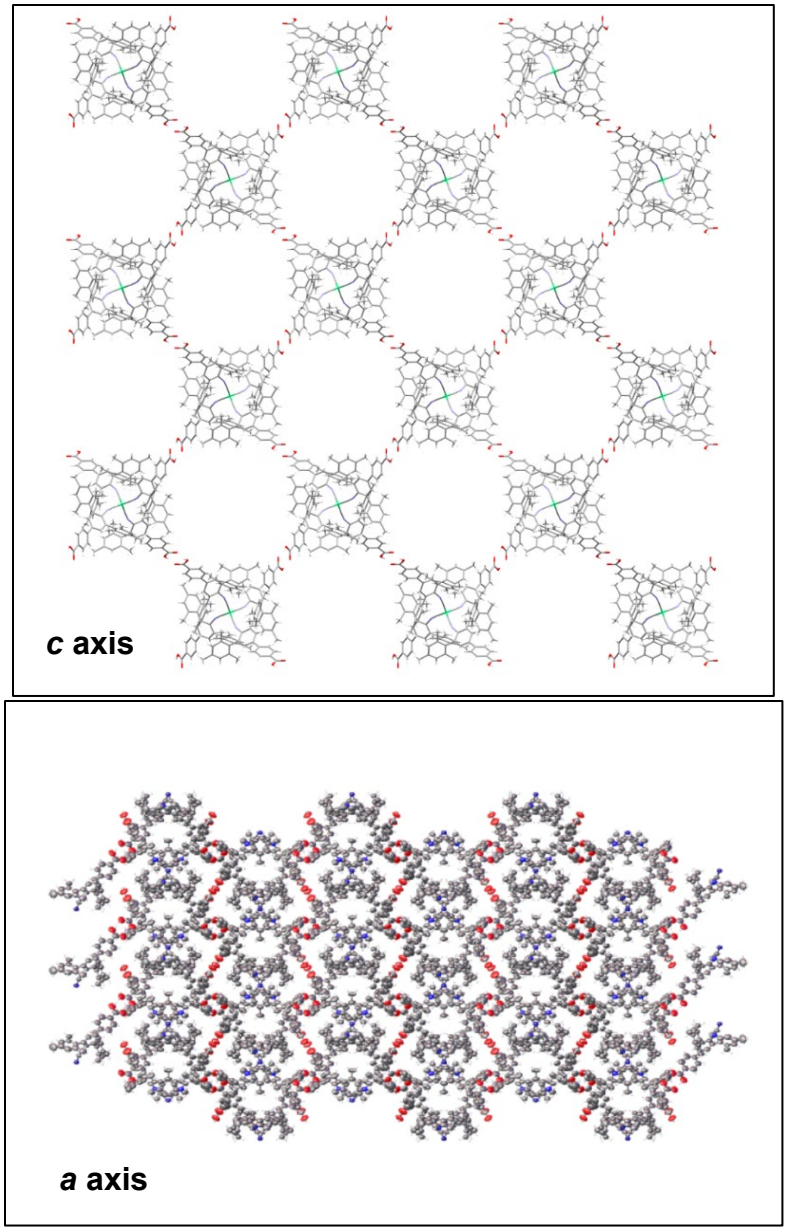

Figure 3.13. Full interpenetrated views of the extended structure of the hydrogen bonding network, $Ni(TIB^{Mes2}H)_4$, along the crystallographic c axis (top) and the crystallographic *a* axis (bottom). The diameter of the channels observed down the crystallographic *c* axis are ~30 Å in diameter. Co-crystallized solvent molecules have been omitted for clarity.

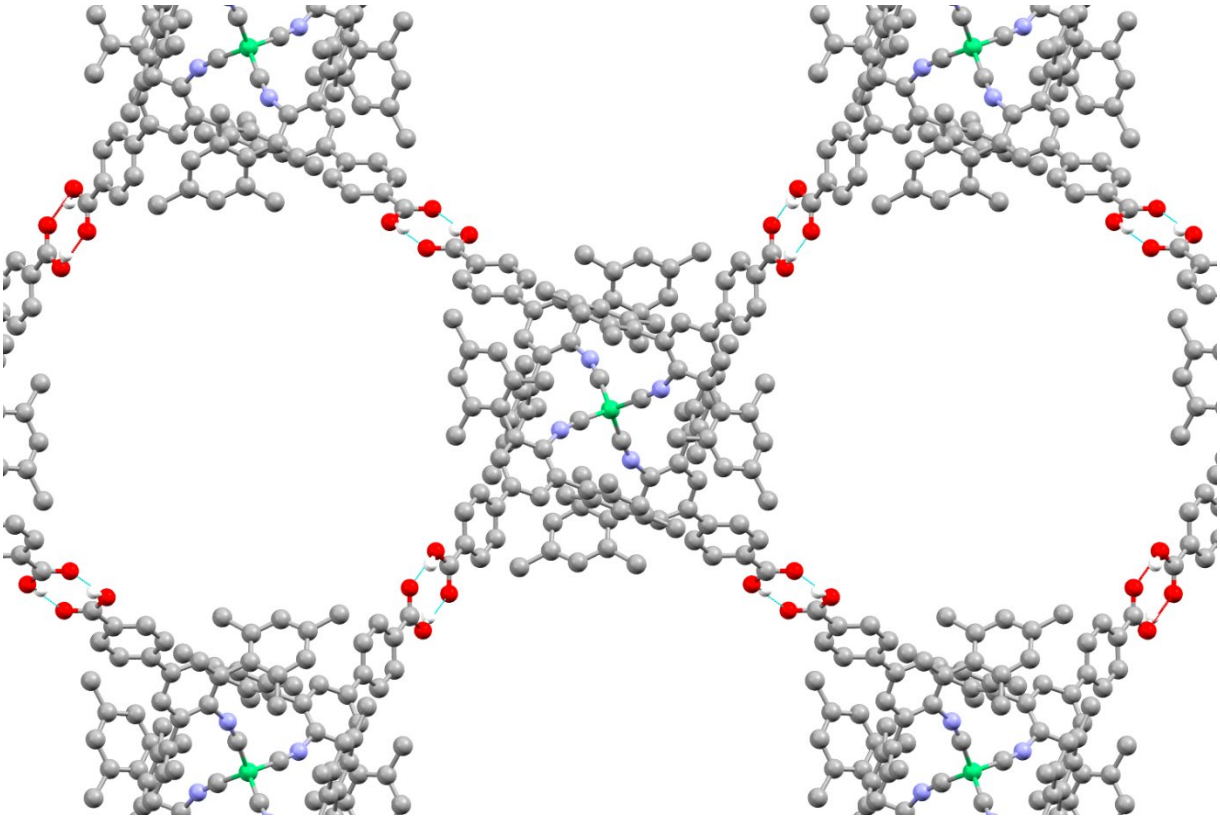

Figure 3.14. Zoomed in view of the extended structure of the hydrogen bonding network, Ni(TIB^{Mes2}H)$_4$, along the crystallographic *c* axis. Interpenetration, H atoms not associated with carboxylic acids and co-crystallized solvent molecules have been omitted for clarity.

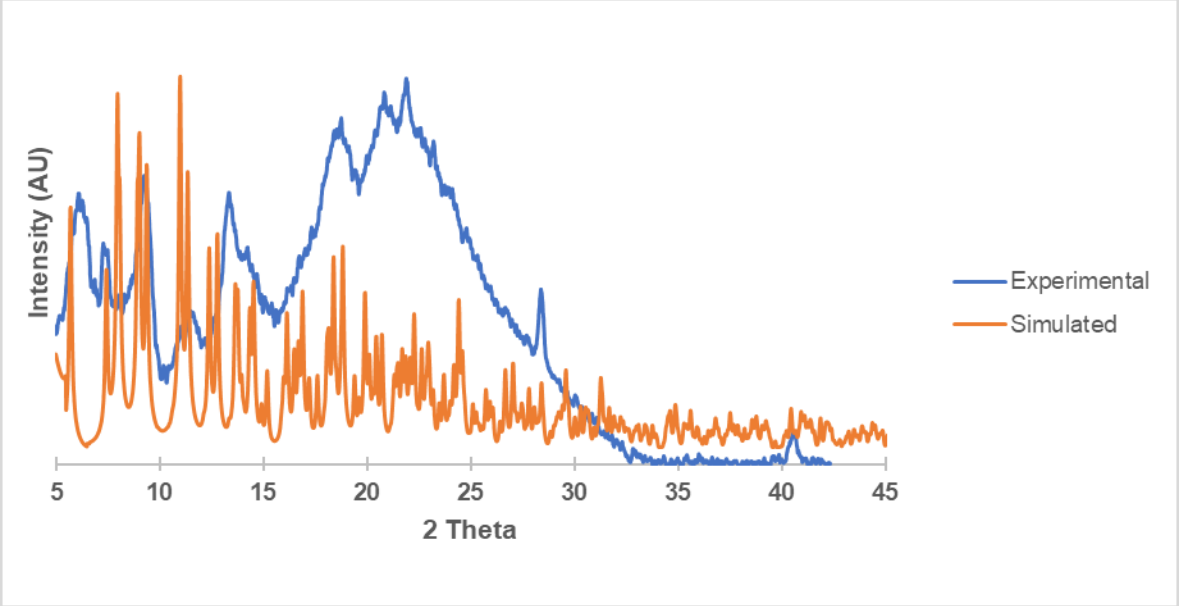

Figure 3.15. Powder X-ray diffraction pattern of simulated (orange) and experimental (blue) spectra of Ni(TIB^{Mes2}H)$_4$. Broadness of the experimental spectrum is likely due to defects in the extended structure and oil impurity.

Surface Area Measurements.

Samples were prepared on and measured using a Micrometrics ASAP 2020 Adsorption Analyzer. Approximately 40-60 mg of material was transferred to a pre-weighed sample tube under inert atmosphere and degassed at 50˚C for at least 24 hours or until the outgas rate was below 5 mmHg. The sample tube was reweighed to obtain sample mass. Measurements were collected on three independent samples at 77 K employing N_2 of 99.999% purity using the volumetric technique.

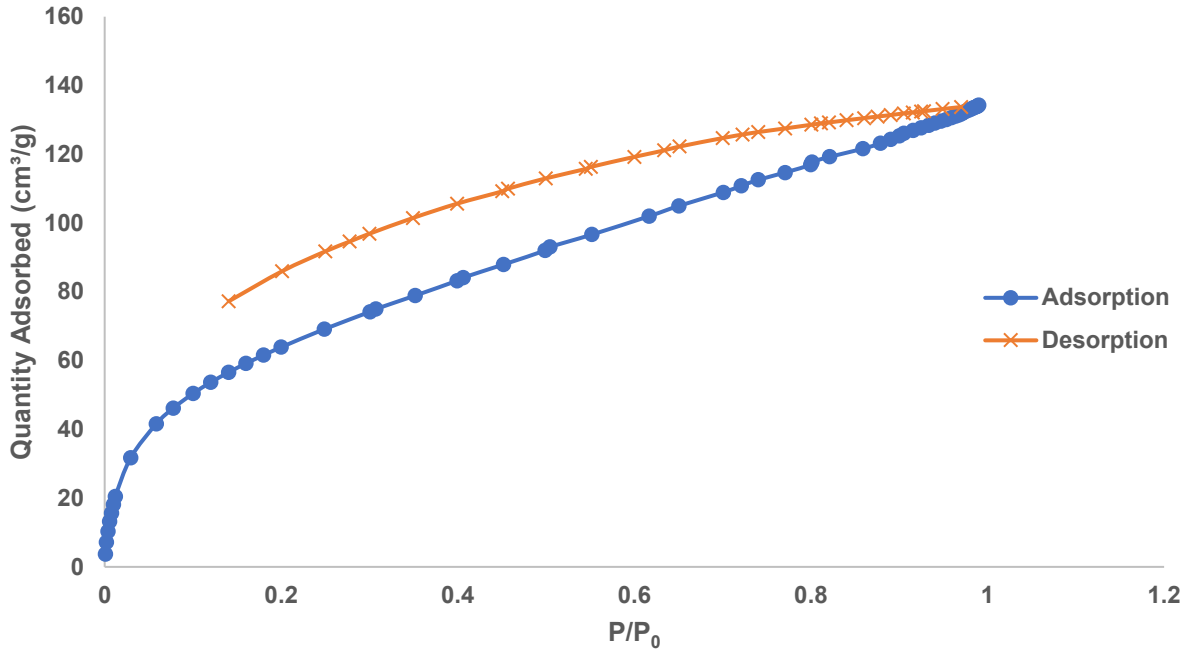

Figure 3.16. CO_2 sorption isotherm of a crystalline sample of $Ni(TIB^{Mes2}H)_4$. The measured Brunauer-Emmett-Teller (BET) surface area is 246 m^2/g.

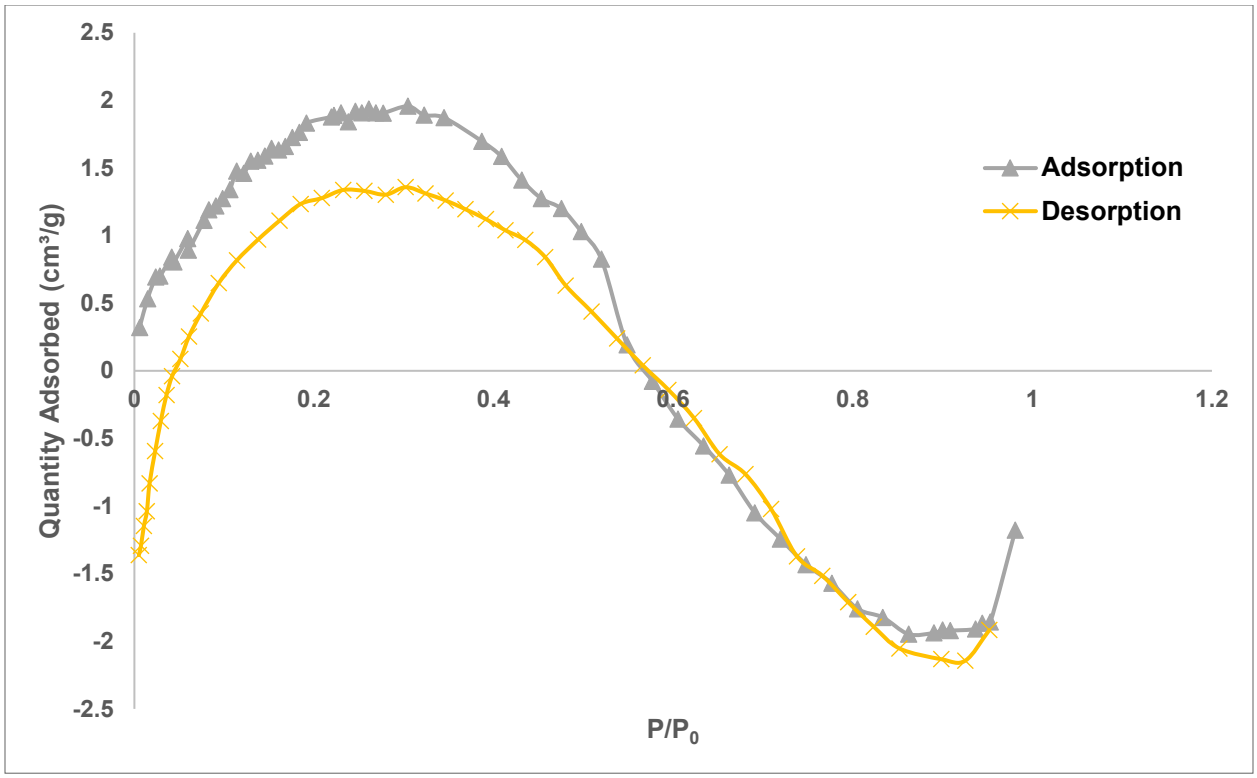

Figure 3.17. N_2 sorption isotherm of a crystalline sample of $Ni(TIB^{Mes2}H)_4$. The measured Brunauer-Emmett-Teller (BET) surface area is negligible at ~7 m^2/g.

^{1}H-NMR Spectra.

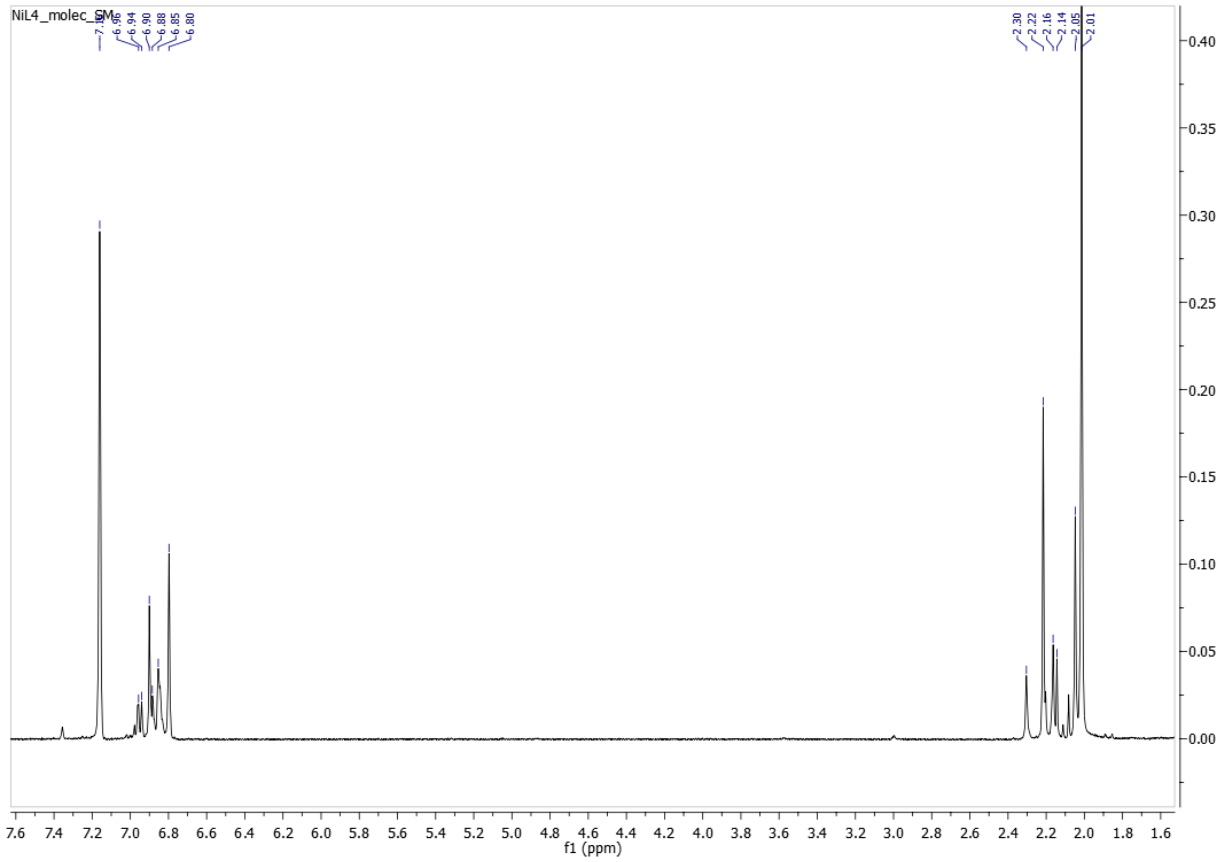

Figure 3.18. ^{1}H-NMR Spectra of Ni(CNAr^{Mes2})$_4$ in C_6D_6.

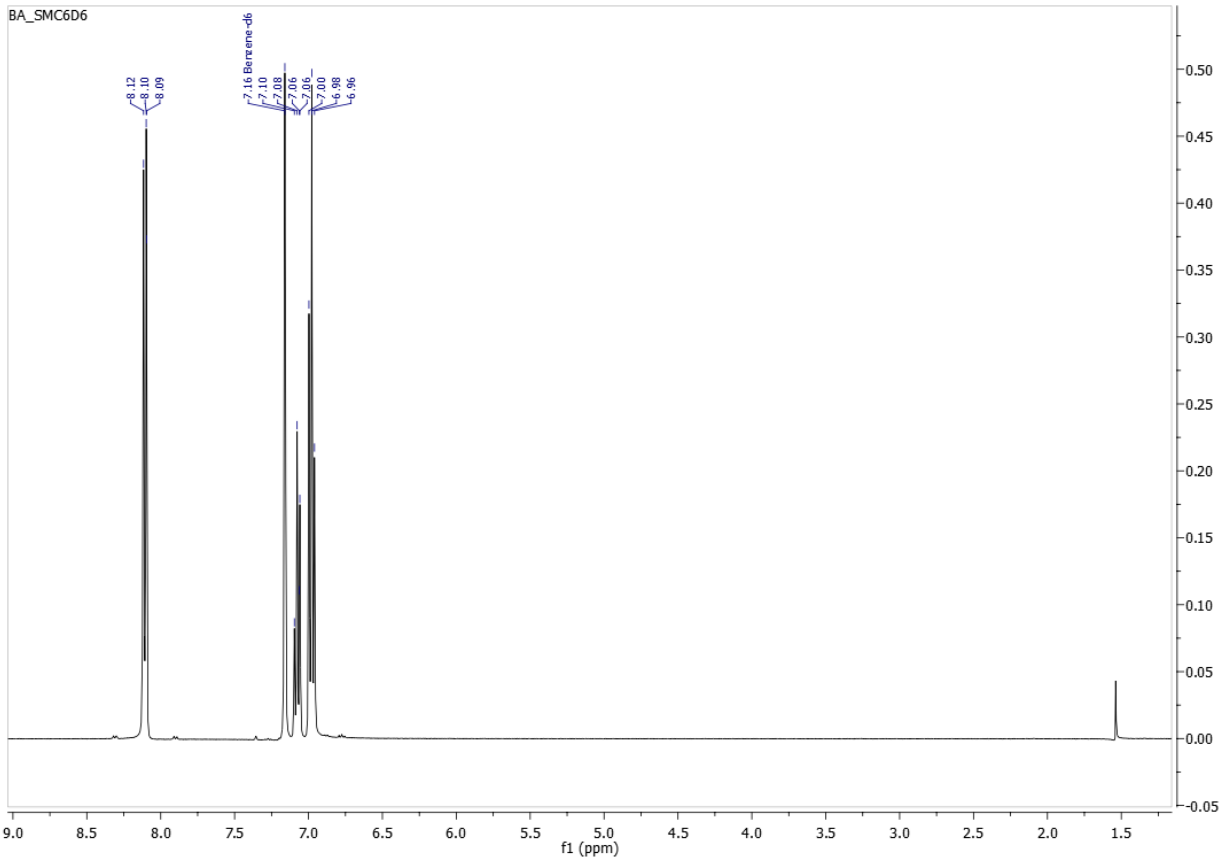

Figure 3.19. ^{1}H-NMR Spectra of benzoic acid in C_6D_6.

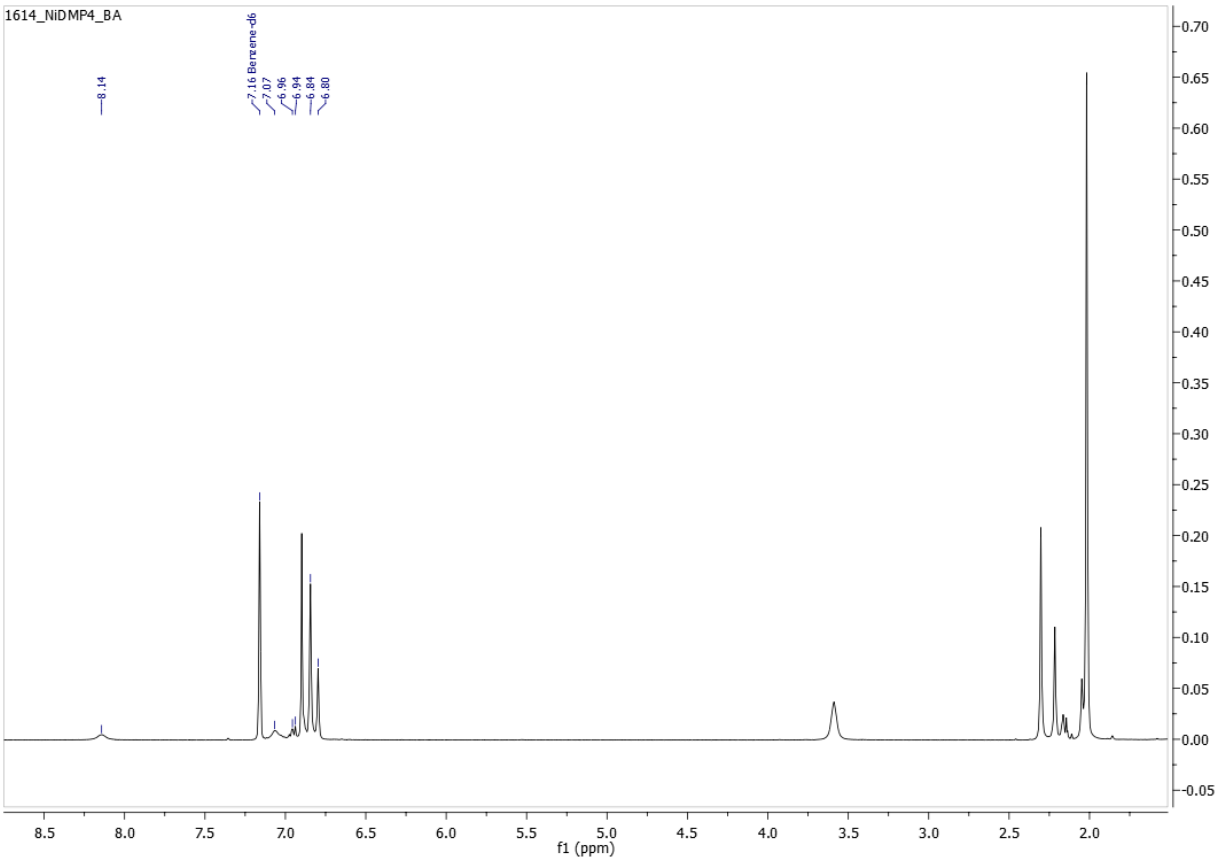

Figure 3.20. ^{1}H-NMR spectra of the reaction mixture containing 1.0 equiv. Ni(CNAr^{Mes2})$_4$ and 1.0 equiv. benzoic acid in C_6D_6. No reaction appears to have occurred, as indicated by the presence of the starting material benzoic acid peaks in the aromatic region.

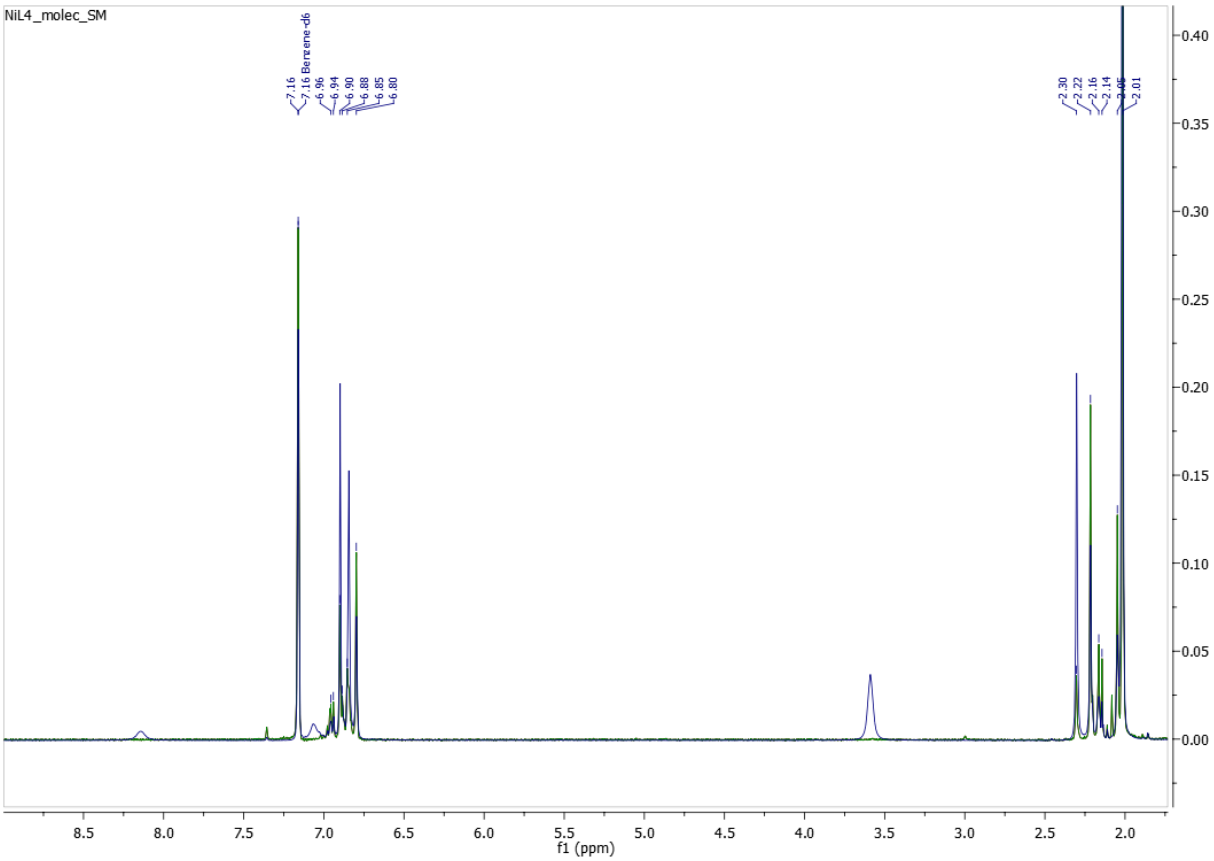

Figure 3.21. Overlay of the ^{1}H-NMR Spectra of the reaction mixture containing 1.0 equiv. Ni(CNAr^{Mes2})$_4$ and 1.0 equiv. benzoic acid in C_6D_6 (blue) and the starting material Ni(CNAr^{Mes2})$_4$ (green).

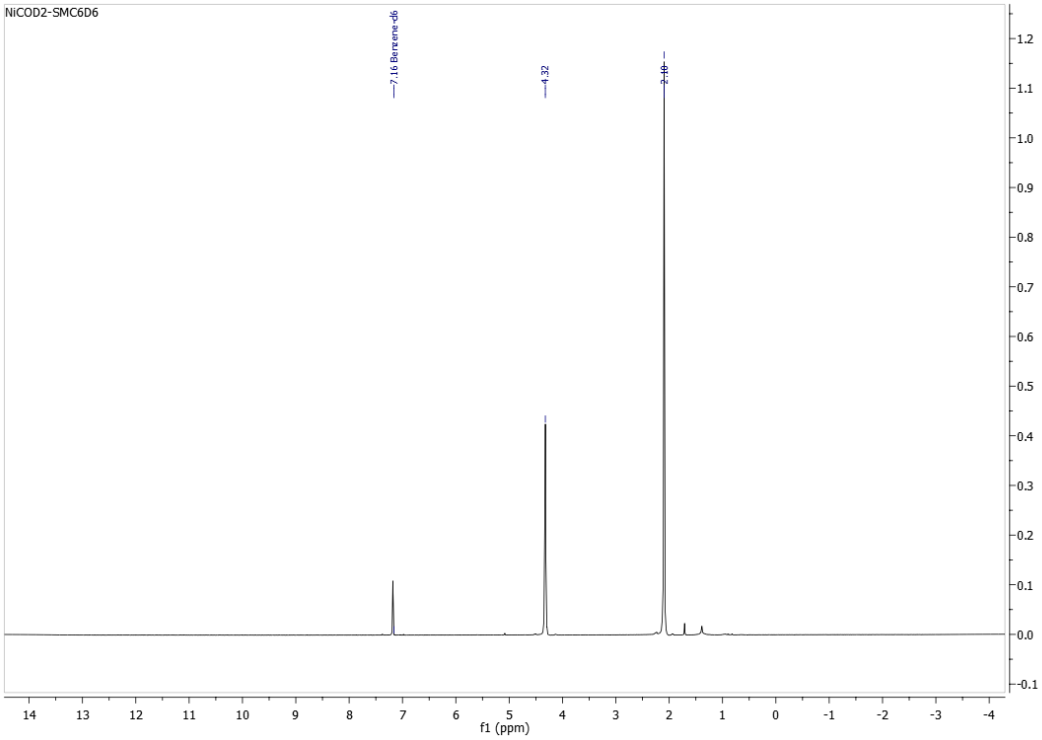

Figure 3.22. ^{1}H-NMR spectra of $Ni(COD)_2$ in C_6D_6.

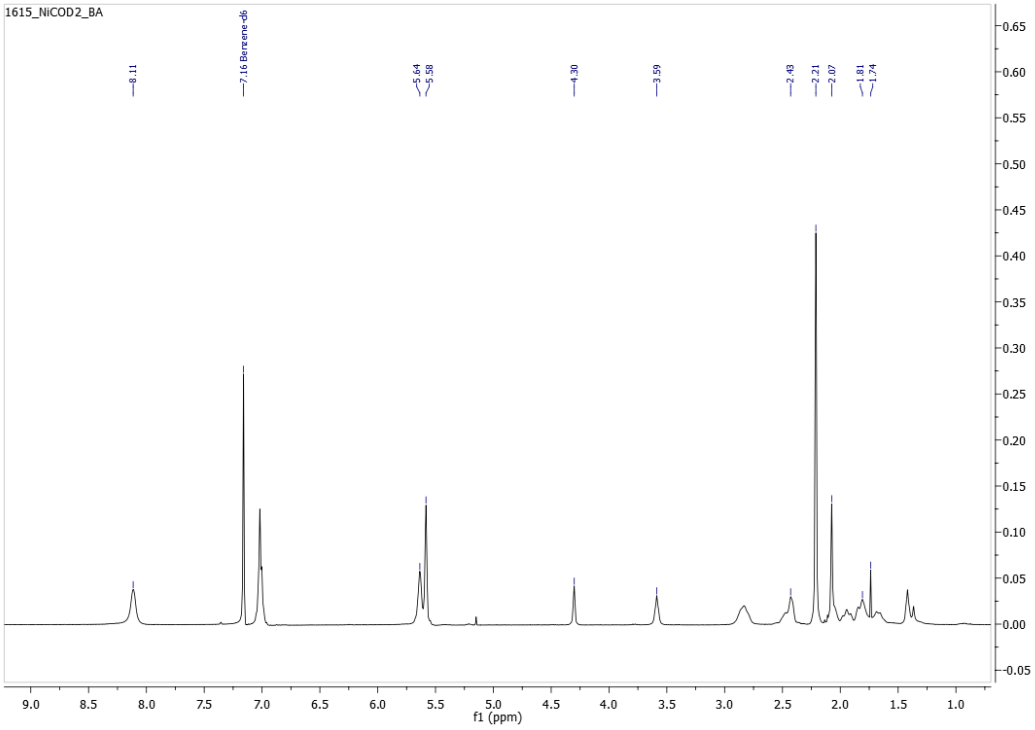

Figure 3.23. ^{1}H-NMR spectra of the reaction mixture containing 1.0 equiv. $Ni(COD)_2$ and 1.0 equiv. benzoic acid in C_6D_6 after 30 minutes. A reaction between benzoic acid and $Ni(COD)_2$ occurs rapidly.

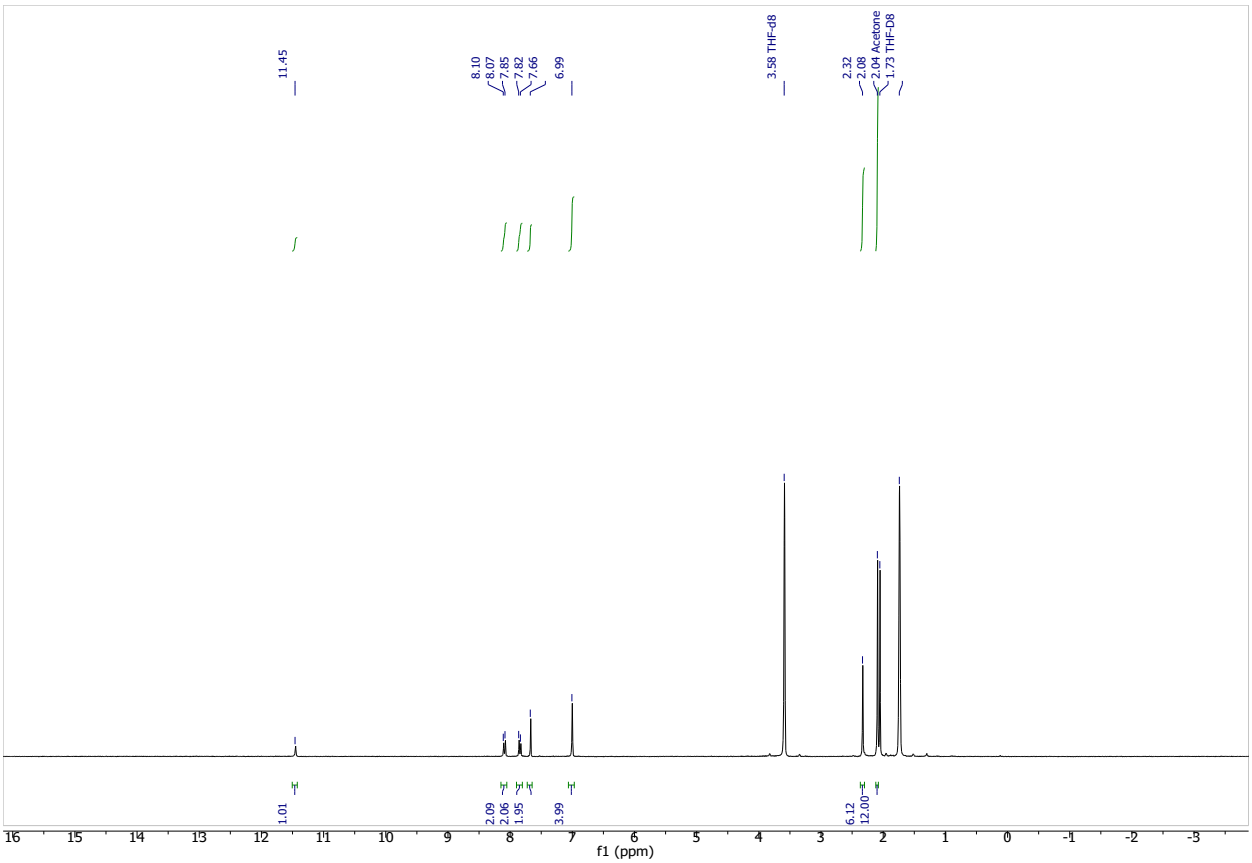

Figure 3.24. ^{1}H-NMR spectrum of free TIB^{Mes2}H in THF-*d8*.

Variable Temperature ^{1}H NMR of Ni(TIB^{Mes2}H)$_4$. Ni(TIB^{Mes2}H)$_4$ (21.1 mg, 0.0111 mmol) was solubilized in THF-d_8 (1.8 mL, 0.0062 M) and transferred into a sealed J. Young NMR tube. The tube was inserted into a temperature-controlled probe set to an initial temperature of 298 K. ^{1}H NMR spectra (402 MHz) were collected at 5 K intervals from 298 K to 338 K (Figure 4.3). Before taking each measurement, 10 minutes were given to allow for equilibration. Importantly, as temperature increased, the chemical shift at δ 6.91 ppm increased in intensity. Moreover, a concomitant decrease in intensity was observed in the chemical shift appearing at δ 6.86 ppm, thereby implicating a dynamic equilibrium process where ligand dissociation produces an equivalent of Ni(TIB^{Mes2}H)$_3$ and free TIB^{Mes2}H. Unfortunately, strong overlap of the chemical

shifts for Ni(TIB^{Mes2}H)$_4$, Ni(TIB^{Mes2}H)$_3$, and TIB^{Mes2}H prevented us from obtaining meaningful integrations and performing a Van't Hoff analysis.

Variable Temperature ^{1}H NMR of Ni(CNAr^{Mes2})$_4$. To gain a better understanding of the equilibrium observed for Ni(TIB^{Mes2}H)$_4$, Ni(CNAr^{Mes2})$_4$ was used as a model system. Ni(CNAr^{Mes2})$_4$ (7.9 mg, 0.0056 mmol) was dissolved in THF-d_8 (0.9 mL, 0.0062 M) and transferred to a sealed J. Young NMR tube. The tube was inserted into a temperature-controlled probe set to an initial temperature of 295.5 K. ^{1}H NMR spectra (402 MHz) were collected at 2.5 K intervals from 295.5 K to 320.5 K (Figure 4.23). Before taking each measurement, 10 minutes were given to allow for equilibration. Notably, an increase in Ni(CNAr^{Mes2})$_3$ could be observed by intensification of the chemical shift at δ 2.20 ppm. This increase in intensity coincides with the decrease in intensity of the signal corresponding to Ni(CNAr^{Mes2})$_4$ at δ 2.21 ppm.

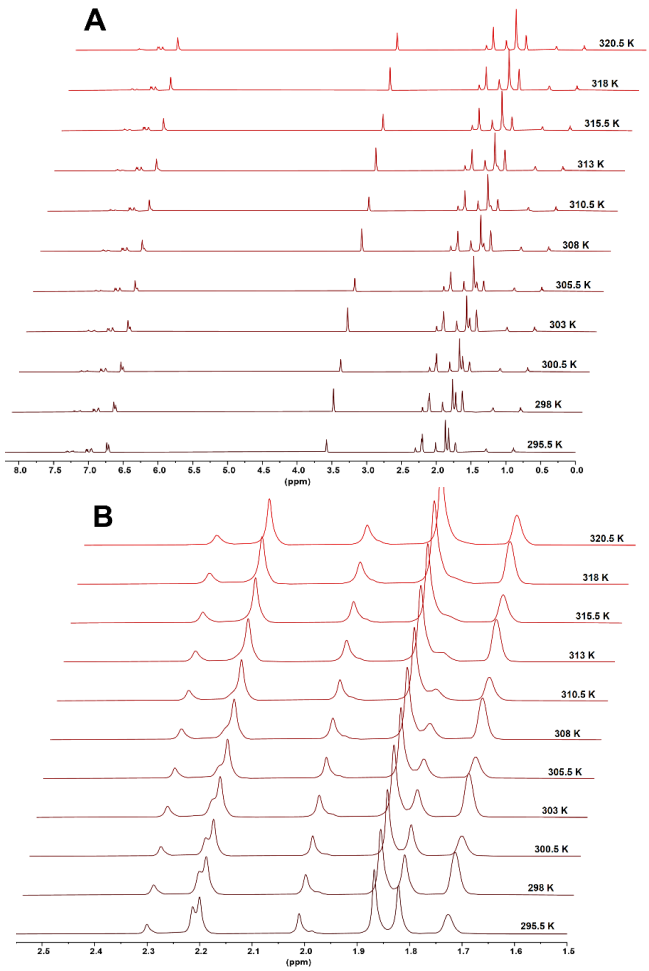

Figure 3.25. Variable temperature ^{1}H NMR of Ni(CNAr^{Mes2})$_4$ in THF-d_8 between 295.5 K to 320.5 K for the (A) full window and (B) DMP-Me region.

Van't Hoff Analysis of Variable Temperature ^{1}H NMR Studies on Ni(CNAr^{Mes2})$_4$. In solution, Ni(CNAr^{Mes2})$_4$ rapidly establishes an equilibrium processes wherein a ligand dissociation event produces an equivalent of Ni(CNAr^{Mes2})$_3$ and free CNAr^{Mes2}, and a ligand association reaction reforms Ni(CNAr^{Mes2})$_4$ (Scheme 3.3).

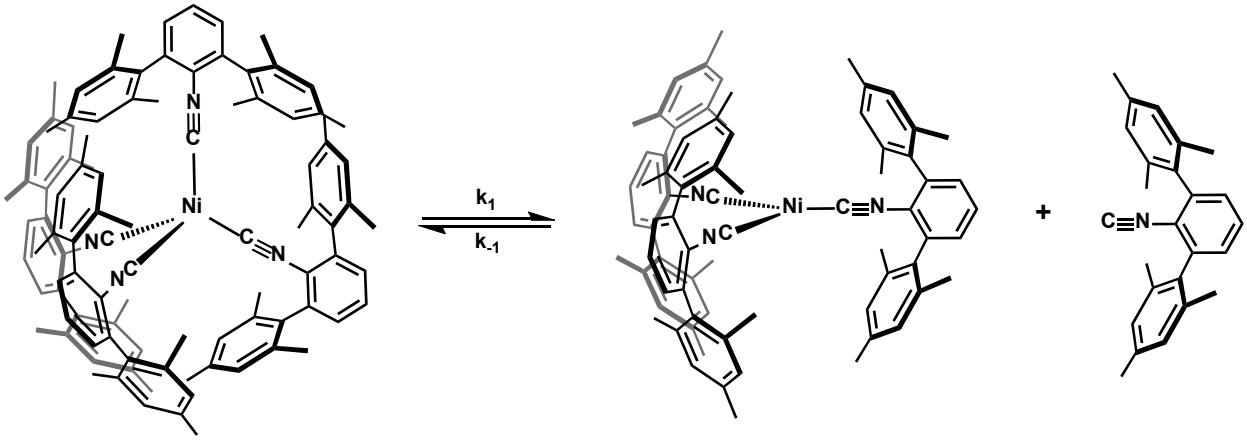

Figure 3.26. Ligand dissociation/association equilibrium observed for nickel(0) *m*-terphenyl isocyanide complexes in THF-d_8.

The equilibrium constant (k_{eq}) for a given temperature can be calculated using the equation:

$$k_{eq} = \frac{[CNAr^{Mes2}][Ni(CNAr^{Mes2})_3]}{[Ni(CNAr^{Mes2})_4]} \quad \textbf{(1)}$$

Although there is a strong overlap between the chemical shifts of the *o*-Me group on the flanking rings for $Ni(CNAr^{Mes2})_4$ (δ 2.21 ppm, 24H) and $Ni(CNAr^{Mes2})_3$ (δ 2.20 ppm 18H), the chemical shift for $CNAr^{Mes2}$ has a distinct chemical shift for the *o*-Me group (δ 2.30 ppm, 6H). Since the reaction system is closed, the moles and concentration can be calculated by relative integration of the signal at 2.32-2.27 ppm vs. the signal at 2.24-2.16 ppm using the following equations:

$$\delta_{2.32-2.27} = \delta_L = \frac{\delta_{NiL3}}{3} = 1 \quad \textbf{(2)}$$

$$\delta_{NiL4} = \delta_{2.24-2.16} - (\delta_{NiL3} - \delta_L) = \delta_{2.24-2.16} - 3 \quad \textbf{(3)}$$

$$Equiv_{NiL4} = \frac{\delta_{NiL4}}{4} \quad \textbf{(4)}$$

$$x_{NiL4} = \frac{Equiv_{NiL4}}{(Equiv_{NiL4} + Equiv_{NiL3+L})} \quad \textbf{(5)}$$

$$n_{NiL4} = x_{NiL4} * n_{NiL4,i} = x_{NiL4} * 0.0056 \quad \textbf{(6)}$$

$$[Ni(CNAr^{Mes2})_4] = \frac{n_{NiL4}}{V} = \frac{n_{NiL4}}{0.9} \quad \textbf{(7)}$$

$$n_{NiL3} = n_L = n_{NiL4,i} - n_{NiL4} = 0.0056 - n_{NiL4} \quad \textbf{(8)}$$

$$[Ni(CNAr^{Mes2})_3] = [CNAr^{Mes2}] = \frac{n_L}{V} = \frac{n_L}{0.9} \quad \textbf{(9)}$$

$$k_{eq} = \frac{[CNAr^{Mes2}][Ni(CNAr^{Mes2})_3]}{[Ni(CNAr^{Mes2})_4]} \quad \textbf{(10)}$$

Plotting ln(k_{eq}) against 1/T produced a linear trend of the form (Figure 3.27):

$$\ln(k_{eq}) = \frac{-\Delta H}{RT} + \frac{\Delta S}{R}$$

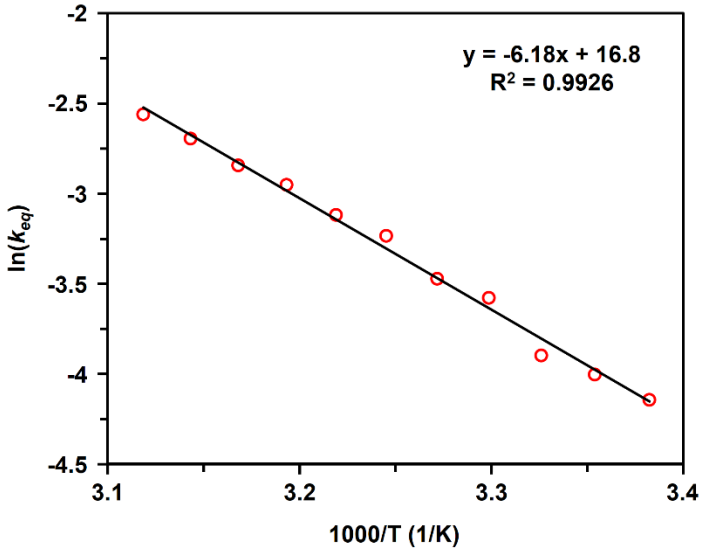

Figure 3.27. Van't Hoff plot derived from variable temperature ^{1}H NMR spectra of the equilibrium ligand dissociation/association for Ni(CNAr^{Mes2})$_4$.

The enthalpy (ΔH = 0.178 kcal•mol^{-1}) and entropy (ΔS = 0.482 cal•K^{-1}•mol^{-1}) of the reaction were then calculated from the slope and the intercept, respectively. Variable temperature and Van't Hoff analysis of the ligand dissociation/association equilibrium indicates the process is endothermic, with the dissociation of ligand from Ni(CNAr^{Mes2})$_4$ to form Ni(CNAr^{Mes2})$_3$ and CNAr^{Mes2} being favored at higher temperatures.

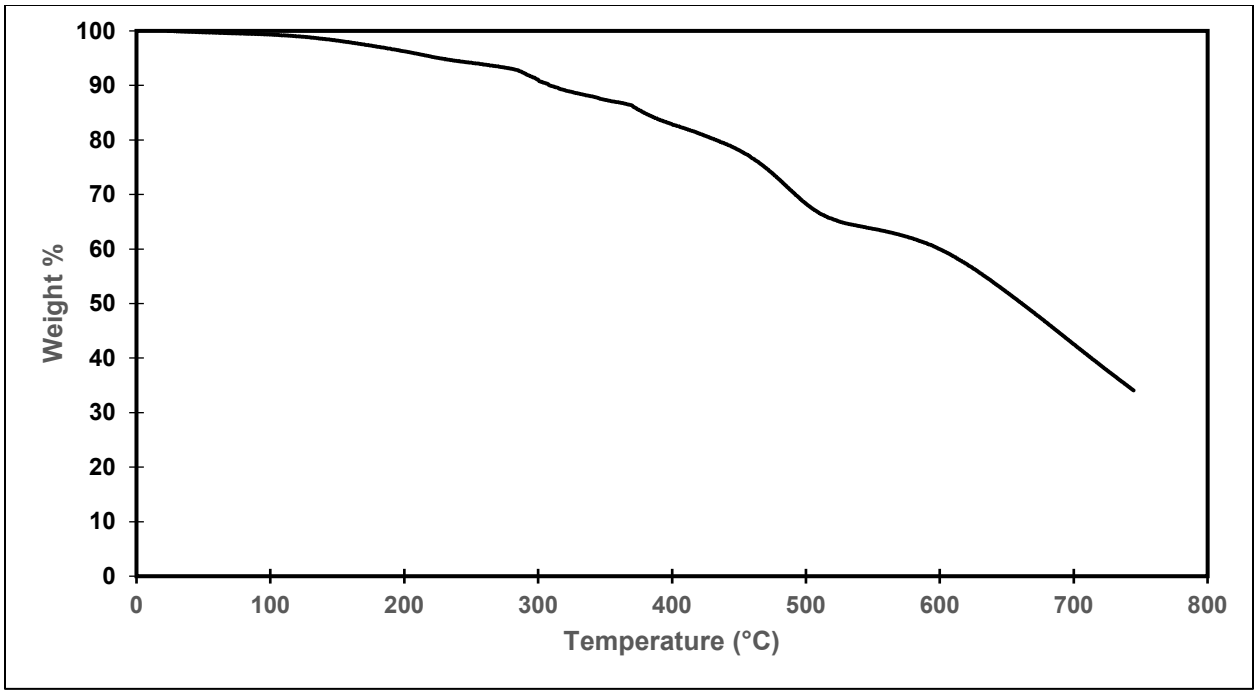

Figure 3.28. Thermogravimetric analysis curve on a crystalline sample of $Ni(TIB^{Mes2}H)_4$ under N_2 gas. Multi-step decomposition is observed in the sample, however decomposition begins at roughly 250 °C.

3.5. References.

(1) Li, P. H.; Ryder, M. R.; Stoddart, J. F. "Hydrogen-Bonded Organic Frameworks: A Rising Class of Porous Molecular Materials" *Accounts Mater Res* **2020**, *1*, 77.

(2) Luo, J.; Wang, J. W.; Zhang, J. H.; Lai, S.; Zhong, D. C. "Hydrogen-bonded organic frameworks: design, structures and potential applications" *Crystengcomm* **2018**, *20*, 5884.

(3) Baumann, A. E.; Burns, D. A.; Liu, B. Q.; Thoi, V. S. "Metal-organic framework functionalization and design strategies for advanced electrochemical energy storage devices" *Commun Chem* **2019**, *2*.

(4) Hisaki, I.; Chen, X.; Takahashi, K.; Nakamura, T. "Designing Hydrogen-Bonded Organic Frameworks (HOFs) with Permanent Porosity (vol 58, pg 11160, 2019)" *Angew Chem Int Edit* **2019**, *58*, 14794.

(5) Duchamp, D. J.; Marsh, R. E. "Crystal Structure of Trimesic Acid (Benzene-1,3,5-Tricarboxylic Acid)" *Acta Crystall B-Stru* **1969**, *B 25*, 5.

(6) Sanchez-Sala, M.; Vallcorba, O.; Domingo, C.; Ayllón, J. A. "A Flexible Hydrogen Bonded Organic Framework That Reversibly Adsorbs Acetic Acid: γ Trimesic Acid" *Cryst Growth Des* **2018**, *18*, 6621.

(7) Yang, J. Y.; Wang, J. K.; Hou, B. H.; Huang, X.; Wang, T.; Bao, Y.; Hao, H. X. "Porous hydrogen-bonded organic frameworks (HOFs): From design to potential applications" *Chem Eng J* **2020**, *399*.

(8) Zhang, Z. J.; Xiang, S. C.; Chen, B. L. "Microporous metal-organic frameworks for acetylene storage and separation" *Crystengcomm* **2011**, *13*, 5983.

(9) Wang, H. L.; Li, B.; Wu, H.; Hu, T. L.; Yao, Z. Z.; Zhou, W.; Xiang, S. C.; Chen, B. L. "A Flexible Microporous Hydrogen-Bonded Organic Framework for Gas Sorption and Separation" *J Am Chem Soc* **2015**, *137*, 9963.

(10) Morshedi, M.; Thomas, M.; Tarzia, A.; Doonan, C. J.; White, N. G. "Supramolecular anion recognition in water: synthesis of hydrogen-bonded supramolecular frameworks" *Chem Sci* **2017**, *8*, 3019.

(11) Ivasenko, O.; Perepichka, D. F. "Mastering fundamentals of supramolecular design with carboxylic acids. Common lessons from X-ray crystallography and scanning tunneling microscopy" *Chem Soc Rev* **2011**, *40*, 191.

(12) Zhang, Y.; Tian, M. F.; Majeed, Z.; Xie, Y. X.; Zheng, K. L.; Luo, Z. D.; Li, C. Y.; Zhao, C. J. "Application of Hydrogen-Bonded Organic Frameworks in Environmental Remediation: Recent Advances and Future Trends" *Separations* **2023**, *10*.

(13) Lau, K. Y.; Mayr, A.; Cheung, K. K. "Synthesis of transition metal isocyanide complexes containing hydrogen bonding sites in peripheral locations" *Inorg Chim Acta* **1999**, *285*, 223.

(14) Sarapu, A. C.; Fenske, R. F. "Transition Metal-Isocyanide Bond - Approximate Molecular-Orbital Study" *Inorganic Chemistry* **1975**, *14*, 247.

(15) Drance, M. J.; Sears, J. D.; Mrse, A. M.; Moore, C. E.; Rheingold, A. L.; Neidig, M. L.; Figueroa, J. S. "Terminal coordination of diatomic boron monofluoride to iron" *Science* **2019**, *363*, 1203.

(16) Wang, S.; Sears, J. D.; Moore, C. E.; Rheingold, A. L.; Neidig, M. L.; Figueroa, J. S. "Side-on coordination of diphosphorus to a mononuclear iron center" *Science* **2022**, *375*, 1393.

(17) Carpenter, A. E.; Margulieux, G. W.; Millard, M. D.; Moore, C. E.; Weidemann, N.; Rheingold, A. L.; Figueroa, J. S. "Zwitterionic Stabilization of a Reactive Cobalt Tris-Isocyanide Monoanion by Cation Coordination" *Angew Chem Int Edit* **2012**, *51*, 9412.

(18) Carpenter, A. E.; Wen, I.; Moore, C. E.; Rheingold, A. L.; Figueroa, J. S. "[1,1-Co(CO)(CNAr^{Mes2})]: A Structural Mimic of the Elusive Isomer of [Co(CO)]" *Chem-Eur J* **2013**, *19*, 10452.

(19) Fox, B. J.; Millard, M. D.; DiPasquale, A. G.; Rheingold, A. L.; Figueroa, J. S. "Thallium(I) as a Coordination Site Protection Agent: Preparation of an Isolable Zero-Valent Nickel Tris-Isocyanide" *Angew Chem Int Edit* **2009**, *48*, 3473.

(20) Agnew, D. W.; DiMucci, I. M.; Arroyave, A.; Gembicky, M.; Moore, C. E.; MacMillan, S. N.; Rheingold, A. L.; Lancaster, K. M.; Figueroa, J. S. "Crystalline Coordination Networks of Zero-Valent Metal Centers: Formation of a 3-Dimensional Ni(0) Framework with

-Terphenyl Diisocyanides" *J Am Chem Soc* **2017**, *139*, 17257.

(21) Singleton, E.; Oosthuizen, H. E. "Metal Isocyanide Complexes" *Adv Organomet Chem* **1983**, *22*, 209.

(22) Aitipamula, S.; Thallapally, P. K.; Thaimattam, R.; Jaskólski, M.; Desiraju, G. R. "Topological equivalences between organic and coordination polymer crystal structures:: An organic ladder formed with three-connected molecular and supramolecular synthons" *Org Lett* **2002**, *4*, 921.

(23) Jiang, H. L.; Makal, T. A.; Zhou, H. C. "Interpenetration control in metal-organic frameworks for functional applications" *Coordin Chem Rev* **2013**, *257*, 2232.

(24) Balto, K. P.; Gembicky, M.; Rheingold, A. L.; Figueroa, J. S. "Crystalline Hydrogen-Bonding Networks and Mixed-Metal Framework Materials Enabled by an Electronically Differentiated Heteroditopic Isocyanide/Carboxylate Linker Group" *Inorg Chem* **2021**, *60*, 12545.

(25) Schilter, D. "Nickel don't care about no air" *Nat Rev Chem* **2020**, *4*, 171.

(26) Chen, L. F.; Zhang, B. Y.; Chen, L. L.; Liu, H. N.; Hu, Y. Q.; Qiao, S. L. "Hydrogen-bonded organic frameworks: design, applications, and prospects" *Mater Adv* **2022**, *3*, 3680.

(27) Pangborn, A. B.; Giardello, M. A.; Grubbs, R. H.; Rosen, R. K.; Timmers, F. J. "Safe and convenient procedure for solvent purification" *Organometallics* **1996**, *15*, 1518.

(28) Armarego, W. L. F.; Chai, C. L. L. "Purification of Laboratory Chemicals, 6th Edition" *Purification of Laboratory Chemicals, 6th Edition* **2009**, 1.

Chapter 4 A Porous Crystalline Ni(0) Organometallic Framework with Redox Properties

4.1. Introduction

Metal-organic frameworks (MOFs) are a class of coordination networks recognized for their high surface areas, porosities, and well-defined crystalline lattices.[1-5] Traditionally, MOFs are synthesized using multitopic anionic linker groups (i.e. carboxylates or imidazolates) and high-valent metal centers to form secondary building units (SBUs). As a result of their strong, ionic metal-ligand bonding interactions, MOFs formed using these precursors are often structurally robust, making them ideal targets for applications in gas separations, chemical storage, and heterogenous catalysis.[6-10] While MOFs containing high-oxidation state metal centers have found use in a variety of applications due to their structural stability, their metal-based chemical reactivity is often limited to Lewis-acid/base reactions at the oxidized metal centers.[11-14] In contrast, multi-electron chemical transformations, which are the hallmark of organometallic complexes, are often precluded in MOF-based materials due to the high oxidation states of their metal centers.

To access multi-electron reactivity within MOFs, incorporation of low valent, electron-rich metal centers has been targeted. This is commonly accomplished by pre-assembly of a molecular organometallic complex on a linker group prior to MOF formation, or by post-synthetic addition of low-valent metal centers to SBUs or pendant ligands anchored to the linker groups.[15-19] However, these approaches have limitations that often lead the reactivity of the low-valent metals to be degraded.[20-23] For example, in the pendant-group approach, the low-valent metal complex does not benefit from the added stability gained from lattice formation, and is therefore subject to the same fundamental ligand substitution processes as coordination complexes in solution. Accordingly, high levels of metal expulsion (i.e. leaching) are often observed from pendant-linker groups within MOF pores. Similarly, low-valent metals adsorbed onto high-valent SBUs often lack stability due to the inherent electronic mismatch of placing highly-reduced metal

centers in a coordination environment consisting of hard anionic ligands. A third, less-explored, approach entails the incorporation of low-valent metal centers directly into MOF structural nodes.[24-26] This approach can potentially allow for direct multi-electron reactions and redox behaviors to occur at the metal-nodes, in a manner similar to molecular organometallic complexes in solution. However, this latter approach requires the use of linking ligands that are electronically matched with low-valent metal centers (i.e. electronically "soft" ligands).

In recent years, we have pursued the latter approach, seeking to develop a class of coordination networks featuring low-valent metal structural nodes using sterically encumbering multi-topic isocyanide ligands.[27-29] Importantly, the dual s-donor/p-acid bonding character exhibited by isocyanide linkers, in conjunction with their structural rigidity, allows for the incorporation of low-valent metal centers into the nodes of organometallic coordination networks.[30,31] The zero-valent nickel isocyanide coordination network (^{ISO}CN), Ni^{ISO}CN-2·([CNAr^{Mes2}]$_2$)$_{0.5}$ (Ar^{Mes2} = 2,6-(2,4,6,Me$_3$C$_6$H$_2$)C$_6$H$_3$), was prepared using this approach by utilizing the ditopic isocyanide ligand [CNAr^{Mes2}]$_2$. This linker is a directly coupled ditopic variant of the monotopic *m*-terphenyl isocyanide ligand CNAr^{Mes2}, which has been well-established to stabilize highly reduced low-valent transition metal centers. However, as [CNAr^{Mes2}]$_2$ has a relatively short linker length (12.19 Å) between the isocyanide donor groups, NiISOCN-2·([CNAr^{Mes2}]$_2$)$_{0.5}$ exhibited negligible porosity due to a free equivalent of [CNAr^{Mes2}]$_2$ being trapped within its pores. Accordingly, the pore-blocked nature of Ni^{ISO}CN-2·([CNAr^{Mes2}]$_2$)$_{0.5}$ limited our ability to investigate the redox behavior of its Ni(0) nodes.[32] Therefore, we postulated that increasing the length of the diisocyanide linker would allow for the generation of larger pores and/or channels, potentially leading to increased accessibility to low-valent metal centers within an isocyanide-based network material. Indeed, substrate accessible porosity properties was

observed previously for the Cu(I) isocyanide coordination network $Cu^{ISO}CN$-4, which was formed using the expanded, phenylene-spaced diisocyanide linker 1,4-$(CNAr^{Mes2})_2C_6H_4$ (16.5 Å).[27] Accordingly, here we report the use of 1,4-$(CNAr^{Mes2})_2C_6H_4$ to prepare $Ni^{ISO}CN$-3, which is a porous, crystalline isocyanide coordination network featuring tetrahedral Ni(0) nodes. Importantly, Ni-^{ISO}CN-3 exhibits significantly enhanced in porosity relative to Ni-^{ISO}CN-2·$([CNAr^{Mes2}]_2)_{0.5}$, thereby allowing a systematic exploration of the redox properties of the Ni(0) structural nodes. We show through a combination of spectroscopic and material characterization studies that these Ni(0) nodes can undergo $1e^-$ oxidation via a close-proximity, outer-sphere process rather than oxidative events at the surface of the MOF crystallite. Moreover, these oxidation events are fully reversible, which has allowed for a detailed understanding of the consequences of multiple redox cycles on framework structure and porosity.

4.2. Results and Discussion

Similar to Ni-^{ISO}CN-2·$([CNAr^{Mes2}]_2)_{0.5}$, Ni-^{ISO}CN-3 was obtained by solvothermal synthesis under anaerobic conditions. Addition of an acetonitrile (MeCN) solution of $Ni(COD)_2$ (COD = 1,5-cyclooctadiene) to a MeCN solution containing the ditopic 1,4-$(CNAr^{Mes2})_2C_6H_4$, leads to the precipitation of an amorphous red solid. Subsequent heating of the

resultant slurry at 100 °C in a pressure tube under N_2 for 24 hours leads to the formation of dark red single crystals of Ni-^{ISO}CN-3 (Figure 5.1).

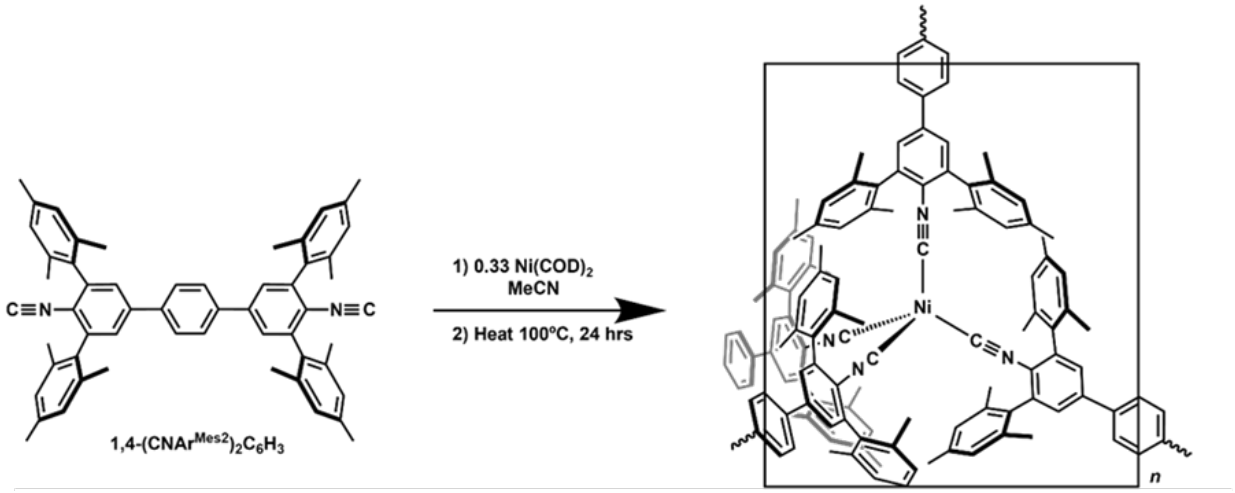

Figure 4.1. Synthesis of Ni^{ISO}CN-3.

X-ray crystallographic analysis on these single crystals indicated Ni^{ISO}CN-3 adopts a three-dimensional diamondoid structure in the solid state, featuring Ni(0) nodes coordinated to four isocyanide ligands (Figure 4.2). ATR-IR analysis on single crystals of Ni-^{ISO}CN-3 revealed a broad isocyanide stretching band (ν_{CN}) at 1950 cm^{-1}, which is significantly red shifted when compared to free isocyanide (ν_{CN} = 2114 cm^{-1}) and indicative of the presence of zero-valent Ni centers (Figure 4.15).[27,32,33] Inspection of the extended solid-state structure revealed a four-fold-interpenetrated framework in the tetragonal *P*4*b*2 space group, with the extended linker providing a Ni-Ni separation of 30 Å between direct neighbors (Figure 4.42, Figure 4.43).

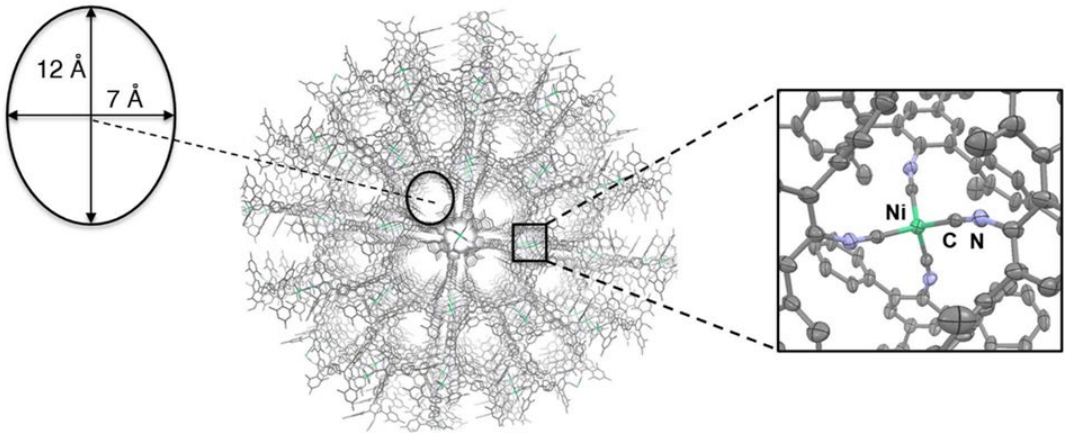

Figure 4.2. Crystal structure of Ni-^{ISO}CN-3. Inset (right) of Ni(0) node demonstrating coordinated isocyanide linkers. Inset (left) the void space available within the pore of the framework of Ni-^{ISO}CN-3.

Additionally, examination of void space in Ni^{ISO}CN-3 reveals accessible micropores of approximately 12 Å x 7 Å in diameter along the crystallographic *c* axis (Figure 4.43). These pores are significantly larger in size compared to those found in Ni-^{ISO}CN-2·([CNAr^{Mes2}]$_2$)$_{0.5}$ (4.2 Å × 3.6 Å and 6.3 × 4.5 Å) which are fully obstructed by free [CNAr^{Mes2}]$_2$. This indicates an increased linker length is effective at increasing pore size. Despite its four-fold interpenetration, Ni^{ISO}CN-3 exhibits modest porosity to both N_2 and CO_2, with Brunauer–Emmett–Teller (BET) surface areas of 160 m^2/g and 324 m^2/g, respectively (Figure 4.6, Figure 4.7).

Table 4.1. Structural and spectroscopic comparison across four-coordinate Ni(0) centers containing isocyanide ligands.

	Ni^{ISO}CN-3	**Ni-^{ISO}CN-2·([CNAr^{Mes2}]$_2$)$_{0.5}$**	**Ni(CNAr^{Mes2})$_4$**
Interpenetration	Four-fold	Two-fold	N/A
Houser τ_4	0.96	0.98	0.85
Avg. Ni-C Bond	1.830(18) Å	1.84(64) Å	1.84(14) Å
ν_{CN}	1950 cm^{-1}	1950 cm^{-1}	1984 cm^{-1}

Notably, the isolation and characterization of Ni^{ISO}CN-3 allows for comparison of the structural and electronic properties across a series of tetrahedral Ni(0) isocyanide centers in both

molecular and network-material contexts (Table 5.1). Indeed, the nodal structure of both Ni-^{ISO}CN-2·([CNAr^{Mes2}]$_2$)$_{0.5}$ and Ni^{ISO}CN-3 are direct analogues to the previously reported molecular complex, Ni(CNAr^{Mes2})$_4$, which contains monodentate *m*-terphenyl isocyanide ligands. As seen in Table 1, the average Ni-C bond length in Ni^{ISO}CN-3 is in good agreement with both Ni-^{ISO}CN-2·([CNAr^{Mes2}]$_2$)$_{0.5}$ and Ni(CNAr^{Mes2})$_4$, thereby indicating that network formation does not significantly affect the core metrical parameters of the mononuclear Ni(0) centers. Additionally, simple calculation of the Houser τ_4 values of Ni^{ISO}CN-3, Ni-^{ISO}CN-2·([CNAr^{Mes2}]$_2$)$_{0.5}$ and Ni(CNAr^{Mes2})$_4$ demonstrate the Ni centers within the framework materials are closer to an idealized tetrahedral coordination geometry (τ_4 =1). We attribute this lack of distortion about Ni(0) nodal centers to constraints from lattice formation, whereas Ni(CNAr^{Mes2})$_4$ is free to adopt non-negligible structural distortions from an idealized tetrahedral geometry in the solid state. In addition, this lack of structural distortion affects the spectroscopic properties of the isocyanide network materials when compared to their molecular counterpart. Comparison of the isocyanide stretching frequencies of Ni^{ISO}CN-3, Ni-^{ISO}CN-2·([CNAr^{Mes2}]$_2$)$_{0.5}$ and Ni(CNAr^{Mes2})$_4$ shows Ni(0) isocyanide coordination networks are significantly more red-shifted when compared to Ni(CNAr^{Mes2})$_4$. We associate this red-shift with more effective orbital overlap between π-symmetric Ni(0) d-orbitals and the isocyanide (C-N) π* orbitals in the more idealized tetrahedral geometry. Due to the increased pore accessibility displayed by Ni^{ISO}CN-3, we reasoned the framework could be accessed by mild chemical oxidants and reductants to screen redox events at Ni- nodal centers in a manner analogous to those observed in low-valent metal isocyanide coordination complexes.[49-54] While frequently observed in organometallic complexes, redox reactions in MOFs are not as common or well-studied.[55-60] Furthermore, even fewer examples are reported in which oxidation/reduction processes occur at the metal nodes of the framework instead

of at organic linkers.[61-65] To further understand multi-electron transformations in MOFs, the redox behavior of Ni(0) nodes in Ni^{ISO}CN-3 was investigated.

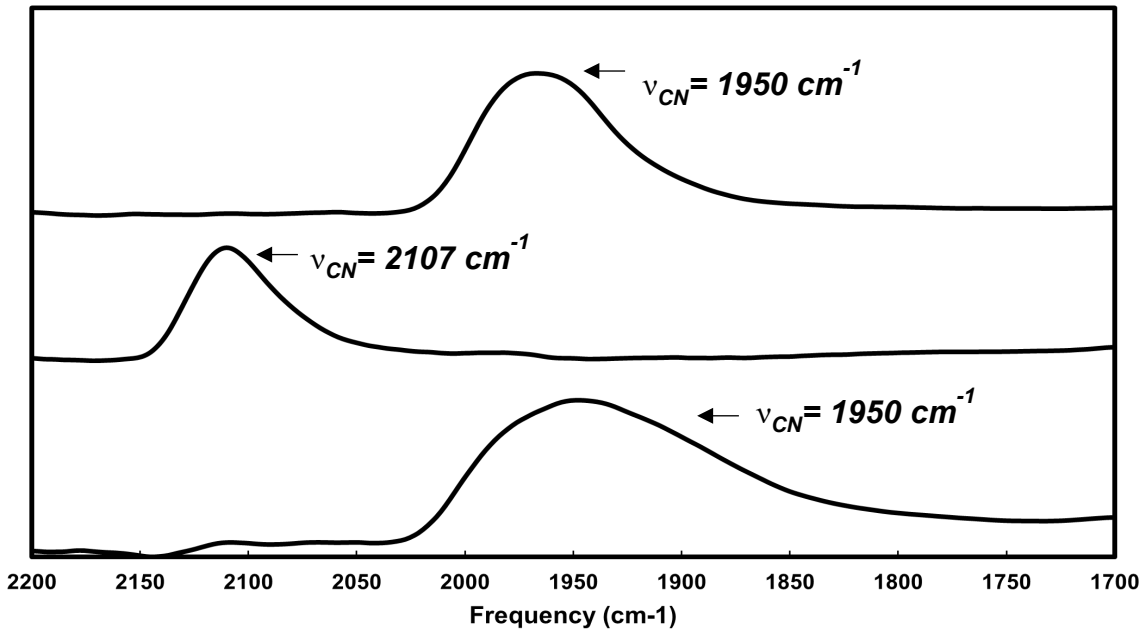

Figure 4.3. Stacked ATR-IRs of the one electron chemical redox cycle for Ni-ISOCN-3. (bottom) As-prepared sample with one νCN stretch observable. (middle) One-electron oxidation of sample with 100 mM of ferrocenium triflate blue shifted ~ 160 cm-1. (top) Subsequent one-electron reduction with 100 mM of cobaltocene shifted back to the original νCN frequency.

Accordingly, a 100 mM solution of ferrocenium triflate (FcOTf, FcOTf = $[Fe(C_5H_5)_2][SO_3CF_3]$, 1 equiv.) in MeCN was added to a stirring suspension of Ni^{ISO}CN-3 and left for 30 minutes at room temperature under N_2, whereafter the framework changed color from bright red to yellow. Spectroscopic analysis via ATR-IR demonstrates a blue-shift of ~160 cm^{-1} (Figure 4.3) from the as-prepared sample to ν_{CN} = 2107 cm^{-1}, a one-electron oxidation from Ni(0) to Ni(I) as similar energy shifts have been seen from previously reported mononucelar nickel (I) systems.[32,33,52] To confirm the observed blue shift is a result of a one-electron oxidation event at nickel nodes, excess FcOTf (5 equiv.) was added to a separate crystalline Ni^{ISO}CN-3 sample. Rapid and full dissolution of Ni^{ISO}CN-3 occurred after only 60 seconds, and a green MeCN solution was observed. Analysis of the ATR-IR spectrum obtained from the reaction revealed an isocyanide

stretching frequency at ν_{CN} = 2183 cm^{-1}, indicating formation of a molecular Ni(II) isocyanide species in solution (Figure 4.19).[51]

Additionally, Ni K-edge X-ray absorption spectroscopy was performed on an oxidized sample of Ni^{ISO}CN-3 (**2**) and provides evidence of Ni(I) metal centers throughout the material. Two pre-edge features were observed in the experimentally acquired spectrum of **2** at 8332.4 eV and 8334.4 eV (Figure 4.4). These features can be compared to the previously reported spectra

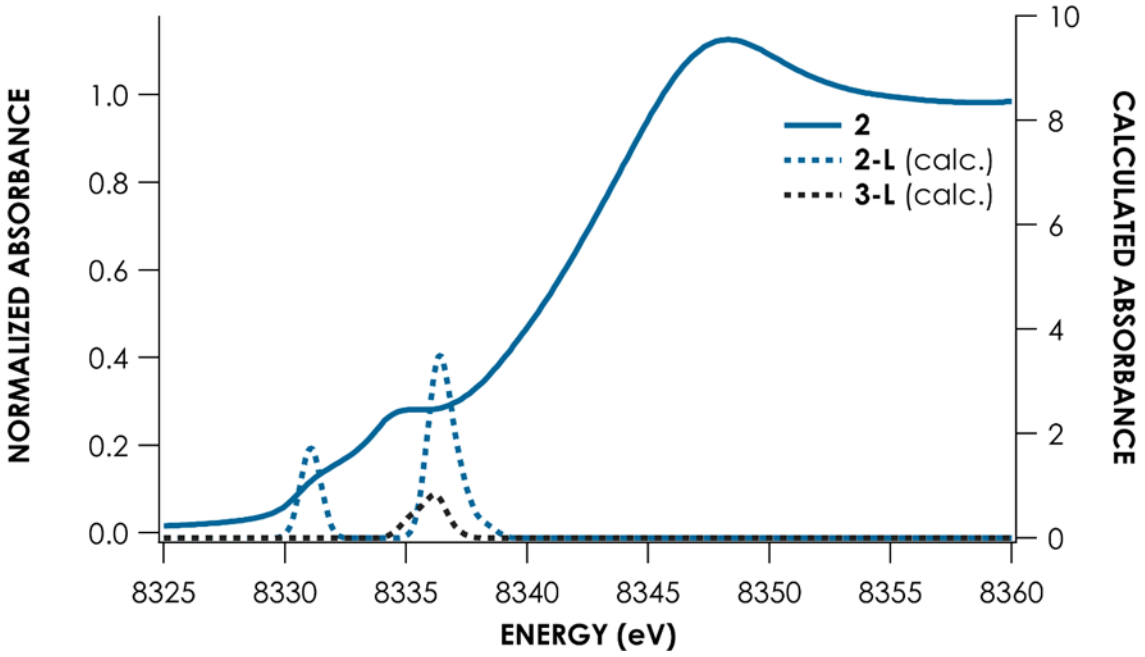

Figure 4.4. Overlay of the calculated pre-edge features of [Ni($CNAr^{Mes2}$)$_4$]OTf (**2-L**), Ni^{ISO}CN-3 (**3-L**), and the measured Ni K-edge XAS of oxidized Ni^{ISO}CN-3 (**2**).

obtained for [Ni($CNAr^{Mes2}$)$_4$]OTf (**2-L**) and provide further evidence of Ni(I) nodes in the framework.[32] The first pre-edge feature of **2-L** was calculated to correspond to an excitation from the Ni *1s* → SOMO (orbital 377b, Figure 4.52, Figure 4.53). Significant mixing of Ni *4p* orbitals (14.4% character) with the Ni *3d* orbitals (33.2% character) accounts for the strong intensity of this transition and is consistent with a tetrahedral geometry. The second pre-edge transition is calculated to be shifted blue by ca. 3 eV relative to the experimentally observed feature. Inspection

of the principal components of the transitions associated with this feature revealed that these largely correspond to Ni *1s* → L π^* orbital transitions. The discrepancy between the observed and calculated positions for this pre-edge feature likely originates in the truncation of the isocyanide linker, where **2-L** has monotopic ligands and **2** features multitopic ligands. These conclusions are supported by comparison to the measured and calculated Ni K-edge XAS spectrum of the neutral framework, $Ni^{ISO}CN$-3 (**3-L**) and its molecular mimic, $Ni(CNAr^{Mes2})_4$ (**3**) (Figure 4.54, Figure 4.55). In the spectrum of the neutral species, only a single pre-edge feature corresponding to Ni *1s* → L π^* orbitals are calculated. The intensity of this pre-edge feature is both observed and calculated to be diminished when compared to the cationic system, providing further confidence in the assignment of the Ni nodes of $Ni^{ISO}CN$-3 as cationic after treatment with FcOTf.

Attempts to obtain a single crystal X-ray structure of $Ni^{ISO}CN$-3 post-oxidation failed due to cracking and broadening of diffraction spots. This cracking is attributed to the change in coordination environment around Ni(0) nodes upon oxidation. Through X-ray crystallographic analysis, we have previously demonstrated the molecular mimic of Ni nodes in $Ni^{ISO}CN$-3, $Ni(CNAr^{Mes2})_4$, undergoes a change from Jahn-Teller unstable tetrahedral symmetry to D_{2d} -symmetry upon one electron oxidation using FcOTf to form $[Ni(CNAr^{Mes2})_4]OTf$. This distortion is also observed in the isoelectronic molecule, $Na[Co(CNAr^{Mes2})_4]$, which modulates between D_{2d} and C_{2v}-symmetric forms upon oxidation to the neutral $Co(CNAr^{Mes2})_4$ species.[66] In a similar manner to these molecular species, we theorize Ni-nodal centers in the framework distort from tetrahedral to D_{2d}-symmetry upon oxidation. This transition to lower symmetry causes significant changes about Ni-nodal centers and in lattice structure, leading to crystal cracking. While scXRD did not provide interpretable results on the structure of the oxidized material, powder X-ray diffraction (pXRD) patterns suggest the material undergoes a structural change yet maintains

crystallinity upon oxidation (Figure 4.47). This structural change is further confirmed by gas sorption analysis, where oxidized Ni^{ISO}CN-3 becomes non-porous to N_2 (Figure 4.8), and its BET CO_2 surface area decreases from ~324 m^2/g to ~111 m^2/g (Figure 4.9).[67] This reduction in porosity is attributed to the triflate counterions (OTf^-) now occupying pores of oxidized Ni^{ISO}CN-3. To confirm the observed surface area reduction is not a result of ferrocene blocking the pores, a sample of the oxidized material was analyzed by inductively coupled plasma-mass spectrometry (ICP-MS). No ^{57}Fe was detected in the sample, confirming the reduction in surface area is due to triflate ions occupying pores and not due to the presence of ferrocene (Table 4.2). Importantly, a full one-electron reduction of the oxidized material back to Ni^{ISO}CN-3 is possible with the addition of a 100 mM solution of cobaltocene (1 equiv.). The reduced material has a spectroscopic signal of ν_{CN} = 1950 cm^{-1} and maintains crystallinity as seen by pXRD (Figure 4.3, Figure 4.45). Remarkably, the reduced material remains porous to CO_2 after undergoing a one electron redox cycle, displaying a BET surface area of 183 m^2/g (Figure 4.11.). To determine if the decrease in surface area (BET_{CO2}) of reduced Ni^{ISO}CN-3 when compared to its original counterpart is a result of decreased pore accessibility, a digested sample of reduced Ni^{ISO}CN-3 after the first redox cycle was analyzed by ICP-MS. The concentrations of ^{60}Ni and ^{59}Co were measured to determine if cobaltocenium triflate was present in the sample. Evidently, no cobalt was detected in the ICP-MS data, indicating the change in surface area was not due to cobaltocenium triflate remaining in the pores, but due to degradation of the framework (Table 4.3). This decomposition was also confirmed through pXRD experiments, where an increase in peak broadness, accompanied with a decrease in peak intensity, was observed (Figure 4.45).

We believe multiple redox cycles, consisting of one complete oxidation and one complete reduction at nickel nodal centers, lead to a loss of structural integrity in the framework of Ni^{ISO}CN-

3. To determine the onset of structural degradation, a sample of $Ni^{ISO}CN$-3 was characterized by ATR-IR, gas sorption and pXRD measurements throughout multiple redox cycles. More specifically, pXRD measurements confirm $Ni^{ISO}CN$-3 continues to lose crystallinity after the fifth redox cycle (Figure 4.49, Figure 4.50). The ability of the material to undergo an oxidation and reduction cycle stops at the sixth cycle, where the framework collapses and free ligand is observed in solution by ATR-IR (Figure 4.33). Remarkably, up to this point, the reduced product after the fifth cycle remains porous to CO_2, with a BET surface area of 147 m^2/g (Figure 4.13). This is less than both the reported CO_2 surface area of both the original material and the material after the first redox cycle, indicating multiple reduction cycles impact porosity as well as crystallinity. Despite this observed decomposition, $Ni^{ISO}CN$-3 is the first low-valent MOF to exhibit redox activity. $Ni^{ISO}CN$-3 withstanding a one-electron redox cycle while maintaining structural integrity is attributed to the chemical and physical stability of an isocyanide-based framework.

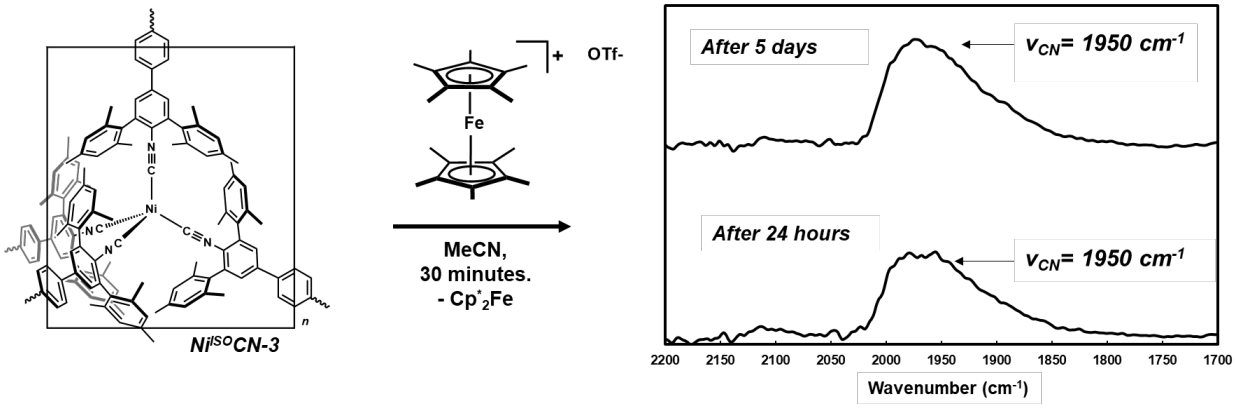

Figure 4.5. ATR-IR spectra (bottom) after 24 hours since the addition of Fc*OTf to NiISOCN-3 and (top) after 5 days since the addition of Fc*OTf. No change is observed in the IR spectra, suggesting Fc*OTf cannot access Ni(0) nodes in the framework. NiISOCN-3 starting material has a isocyanide stretching frequency at 1950 cm^{-1}.

To determine if the mechanism of oxidation of Ni(0) nodes was through an outer sphere close-proximity electron transfer process or due to the intrinsic conductivity of $Ni^{ISO}CN$-3, a

derivative of FcOTf, decamethylferrocenium triflate (Fc^*OTf) was synthesized according to a previously published procedure.[68,69] Due to its bulky nature when compared to FcOTf (centroid diameter = 6.60Å), we theorized Fc^*OTf (centroid-Me diameter = 8.48Å) would be unable to access the pores of $Ni^{ISO}CN$-3 (12 Å x 7 Å), and if oxidation was observed, it would be a result of intrinsic conductivity in the material. Upon addition of 1.05 equivalents of Fc*OTf to a MeCN suspension of $Ni^{ISO}CN$-3, no change was observed in the ATR-IR spectrum of $Ni^{ISO}CN$-3 after 5 days (Figure 4.17). To ensure reduction potential was not the reason for $Ni^{ISO}CN$-3's lack of oxidation ($[Fc^*]^+$ = -0.59V vs. $[Fc]^+$), a benzene solution containing the molecular mimic, $Ni(CNAr^{Mes2})_4$, was added to a benzene suspension containing 1 eq. of Fc*OTf. Over the course of an hour, a yellow color was observed, and FT-IR spectroscopic analysis revealed a blue shift in the isocyanide stretching frequency from ν_{CN} = 2017 and 1984 cm^{-1} to ν_{CN} = 2111 cm^{-1} (Figure 4.18), representing a one electron oxidation event consistent with the reported oxidized species, [Ni(CNAr^Mes2)4]OTf. In addition to the blue-shifted IR spectroscopic signal obtained, a broadened ^{1}H-NMR spectra of the sample indicated the presence of a paramagnetic Ni(I) species in solution, confirming the presence of previously reported $[Ni(CNAr^{Mes2})_4]OTf$. This confirmed the lack of oxidation observed at Ni(0) nodal centers in $Ni^{ISO}CN$-3 is not due to the reduction potential of Fc*OTf but is a result of its inability to access pores. Evidently, oxidation occurs through an outer sphere, close-proximity electron transfer process in this material.

To further probe the reactivity of this Ni(0) system, we assessed $Ni^{ISO}CN$-3's ability to perform $1e^-$ and $2e^-$ reductions of organic substrates. Molecular Ni(0) compounds are known to catalyze sp^3/sp^2 C-C bond formations using alkyl halides as the electrophile.[36,70,71] Specifically, $Ni^{ISO}CN$-3's one electron chemistry was probed by soaking the material in an MeCN solution containing benzyl bromide (BnBr, 3 equiv. per Ni center) at room temperature. Analysis of the

reaction after 24 hours indicates complete decomposition of the material, as determined by the presence of free ligand in both IR and ^{1}H-NMR spectra and dissolution of the material (Figure 4.27, Figure 4.28, Figure 4.36). Additionally, Ni^{ISO}CN-3's ability to oxidatively add small molecule substrates was probed through addition of methyl iodide (MeI, 3 equiv. per Ni, 20mM in MeCN) to a MeCN suspension containing Ni^{ISO}CN-3 at room temperature (30 $^{\circ}$C). Interestingly, no reaction is observed upon inspection of the ATR-IR spectrum obtained after 24 hours (Figure 5.29). However, when heat is applied (80 $^{\circ}$C), the material dissolves within two hours. ATR-IR analysis of the yellow solution displays a sharp isocyanide stretching frequency at 2115 cm^{-1}, characteristic of free 1,4-(CNAr^{Mes2})$_2$C$_6$H$_4$) (Figure 4.30). The presence of free ligand suggests decomposition of the framework material upon addition of the substrate. As expected, while Ni^{ISO}CN-3 can facilitate electrochemical redox cycling, it is coordinatively saturated and is unable to display reactivity towards small molecule substrates while maintaining structural integrity.

4.3. Conclusion.

In conclusion, a novel 3-D diamondoid isocyanide-based coordination network featuring Ni(0) nodal centers was reported. Notably, Ni^{iso}CN-3 chemically endures a one-electron redox cycle, speaking to the chemical tolerance found between a zero-valent metal center and a neutral isocyanide ligand. While the material performs redox cycling, it is unable to mediate 1e$^-$ and 2e$^-$ reductions of organic substrates without losing structural integrity. Nonetheless, we believe these studies support isocyanide-based frameworks as being chemically and structurally stable alternatives to anionic ligands for exploration into low-valent metal centers.

4.4. Experimental Section.

General Considerations. Unless otherwise stated, all manipulations were performed under an atmosphere of dry dinitrogen using standard Schlenk and glovebox techniques. Solvents were dried and degassed according to standard procedures.[1] Unless otherwise stated, reagent grade

starting materials were purchased from commercial sources and purified where necessary according to standard procedures.[2] Solid-state IR spectra were collected at 2 cm^{-1} resolution as either a KBr pellet or using a Bruker Platinum Alpha ATR-IR equipped with a diamond crystal. The following abbreviations are used to describe the intensity and characteristics of important IR absorption bands: vs = very strong, s = strong, m = medium, w = weak, vw = very weak, b = broad, vb = very broad, sh = shoulder.

Synthesis of Ni-^{ISO}CN-3. To a warm pressure tube, a previously stirred $Ni(COD)_2$ (0.012 g, 0.045 mmol, 1 eq) solution in MeCN for 15 minutes was added. Followed by the quick addition of a MeCN solution of (1,4-$(CNAr^{Mes2})_2C_6H_4$) (0.061 g, 0.090 mmol, 2 eq). The dark red mixture was quickly sealed with a Teflon screw cap equipped with a Viton O-ring and placed in the oven for a temperature program that was set to heat at 120 °C for 24 hrs. Red single crystals of diffraction quality are produced. Gentle washing with MeCN 5 times produces material for further analysis. FTIR-ATR (diamond surface, 20 °C) ν_{CN} =1950 cm^{-1}.

Synthesis of Oxidized Ni-^{ISO}CN-3. An MeCN FcOTf solution (100mM, 1 equiv.) was added dropwise to an MeCN suspension containing Ni-^{ISO}CN-3 (1 equiv.). The suspension was left overnight and washed once with MeCN, and twice with benzene to extract ferrocene, yielding a yellow powder. FTIR-ATR (diamond surface, 20 °C) ν_{CN} = 2107cm^{-1}.

Synthesis of decamethyl ferrocenium triflate (Fc*OTf). To a THF solution containing decamethylferrocene (1 equiv.) (purchased from Aldrich), a suspension of silver(I) trifluoromethanesulfonate (1 equiv.) was added. The reaction was covered with aluminum foil and left to stir overnight at room temperature. The resultant green solution was filtered through a medium fritted funnel to remove silver metal and washed with THF. Volatiles were removed under

dynamic vacuum to yield a green powder. Analytically pure crystals were obtained from a concentrated solution of MeCN at room temperature over the course of 5 days.

Synthesis of [Ni(CNAr^{Mes2})$_4$]OTf using Fc*OTf. A solution containing Ni(CNAr^{Mes2})$_4$ was added to a benzene suspension of decamethyl ferrocenium triflate. Over the course of an hour, the solution turned from dark red to yellow. The resultant solution was filtered through a fiberglass plug, and volatiles were removed under reduced pressure. The dark yellow solid obtained was washed with pentane (5 x 5 mL) to remove ferrocene, providing a light yellow solid. The product was then placed under dynamic vacuum for 3 h to remove trace solvent. FTIR-ATR (diamond surface, 20 °C) ν_{CN} = 2111, 2122 cm^{-1} .

Reduction of Oxidized Ni-^{ISO}CN-3. An MeCN solution containing cobaltocene (100mM, 1 equiv.) was added to a MeCN suspension of oxidized Ni-^{ISO}CN-3. The yellow solid immediately turned to red and was washed three times with MeCN before drying, yielding a dark red powder. FTIR-ATR (diamond surface, 20 °C) ν_{CN} = 1950 cm^{-1}.

Reactivity Studies on Ni-^{ISO}CN-3 with benzyl bromide (BnBr). To a 20mL scintillation vial containing an MeCN suspension of Ni-^{ISO}CN-3 (10mg, 1 equiv.), neat benzyl bromide (x uL, 3 equiv.) was added. The suspension was stirred at room temperature overnight and turned yellow. No solid remained in the vial. FTIR-ATR (diamond surface, 20 °C) ν_{CN} = 2116 cm^{-1}.

Reactivity Studies on Ni-^{ISO}CN-3 with methyliodide (MeI). To a 20mL scintillation vial containing an MeCN suspension of Ni-^{ISO}CN-3 (10mg, 1 equiv.), an MeCN solution of MeI (20mM 1, 3 equiv.) was added. The suspension was stirred at room temperature and no reaction occured. The same procedure was followed and the sample was heated at 80C, yielding dissolution of the material. FTIR-ATR (diamond surface, 20 °C) ν_{CN} = 2115 cm^{-1}.

Surface Area Analysis. Samples were prepared on and measured using a Micrometrics ASAP 2020 Adsorption Analyzer. Approximately 40-60 mg of material was transferred to a pre-weighed sample tube under inert atmosphere and degassed at 50˚C for at least 24 hours or until the outgas rate was below 5 mmHg. The sample tube was reweighed to obtain sample mass. Measurements were collected on three independent samples at 77 K employing N_2 of 99.999% purity using the volumetric technique.

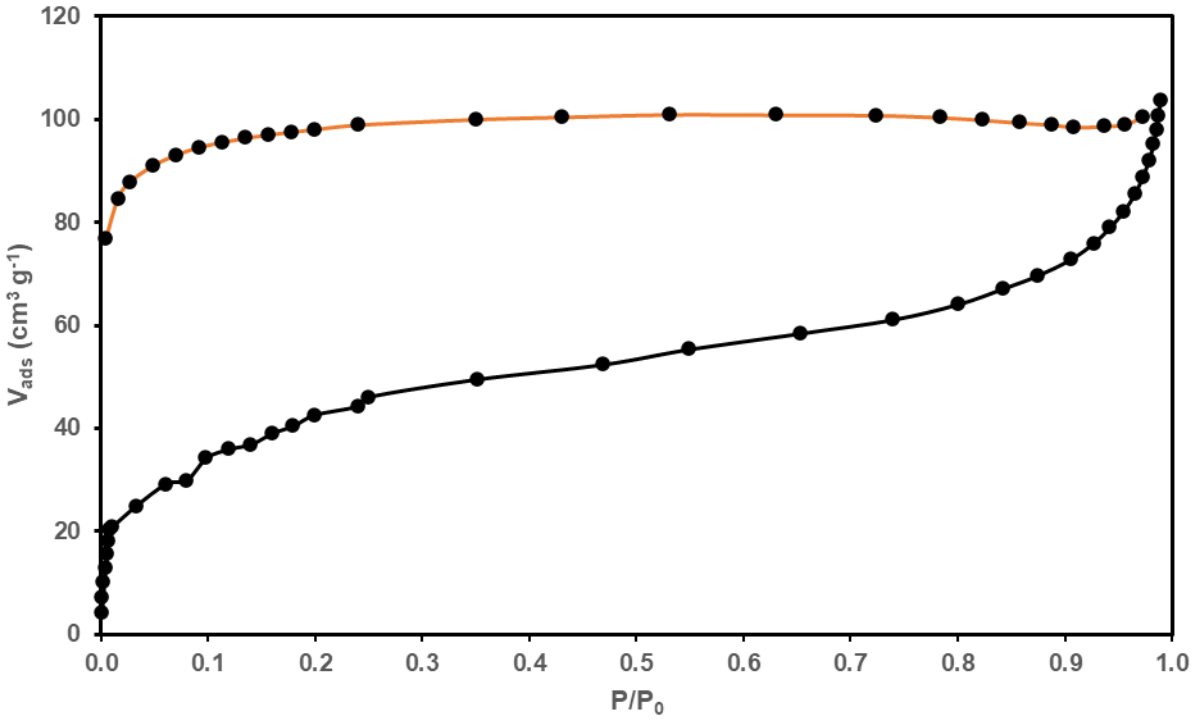

Figure 4.6. N_2 isotherm collected at 77 K of Ni-^{ISO}CN-3. Black curve is adsorption and orange curve is desorption. BET surface area reported is 160 m^2/g.

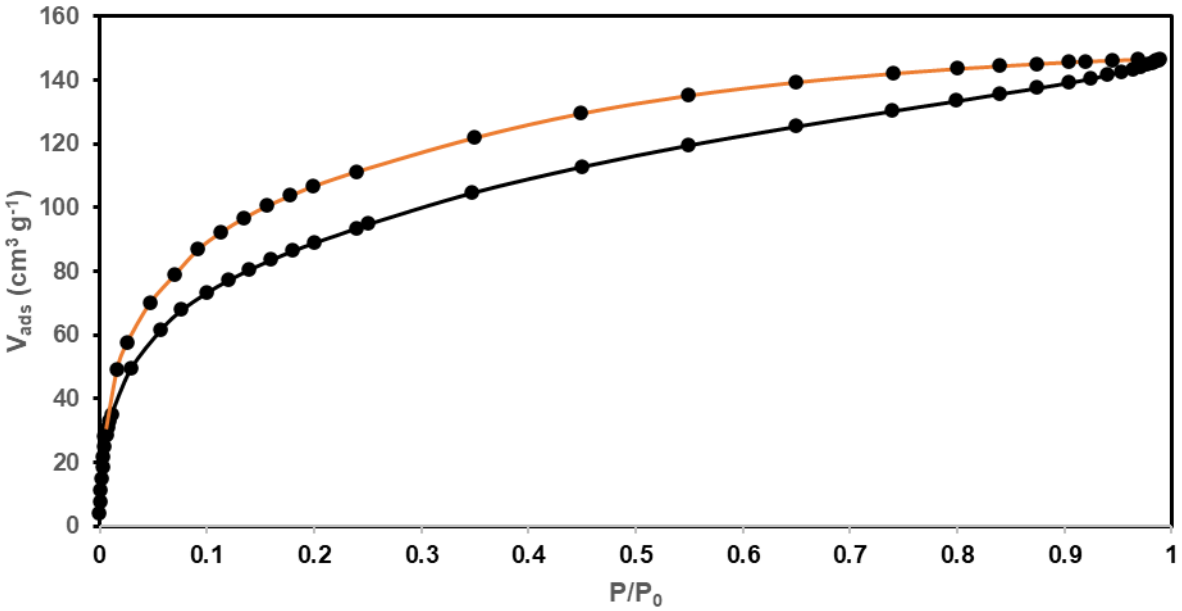

Figure 4.7. CO_2 isotherm collected at 195 K of Ni-^{ISO}CN-3. Black curve is adsorption and the orange curve is desorption. The BET surface area reported is 324 m^2/g.

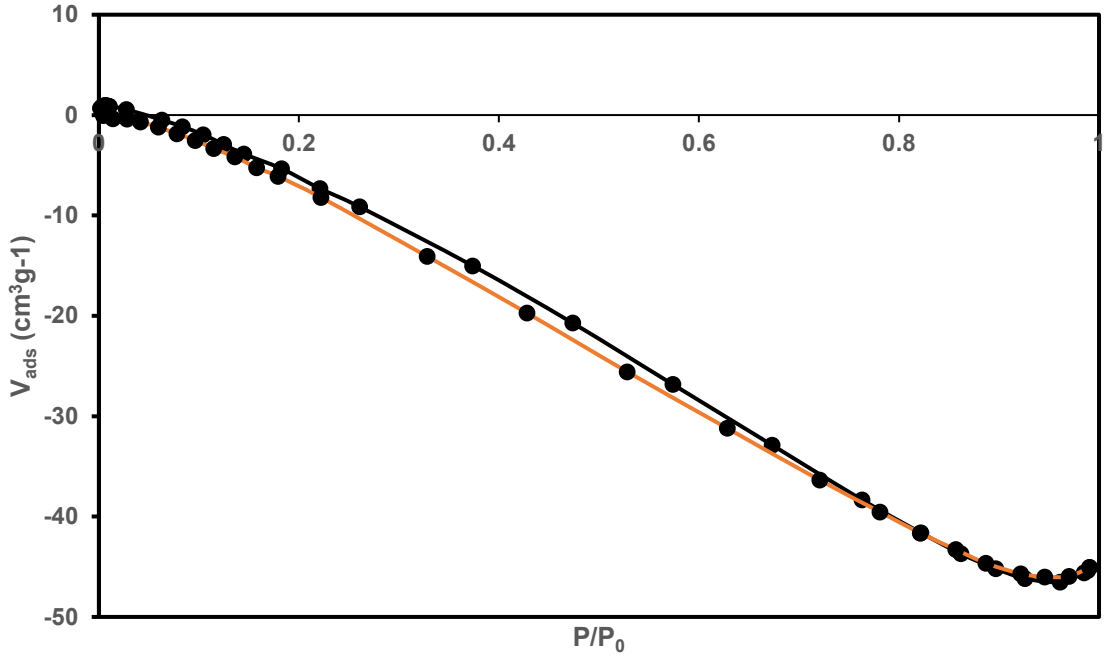

Figure 4.8. N_2 isotherm collected at 77 K of oxidized Ni-^{ISO}CN-3. Black curve is adsorption and orange curve is desorption. There is negligible surface area.

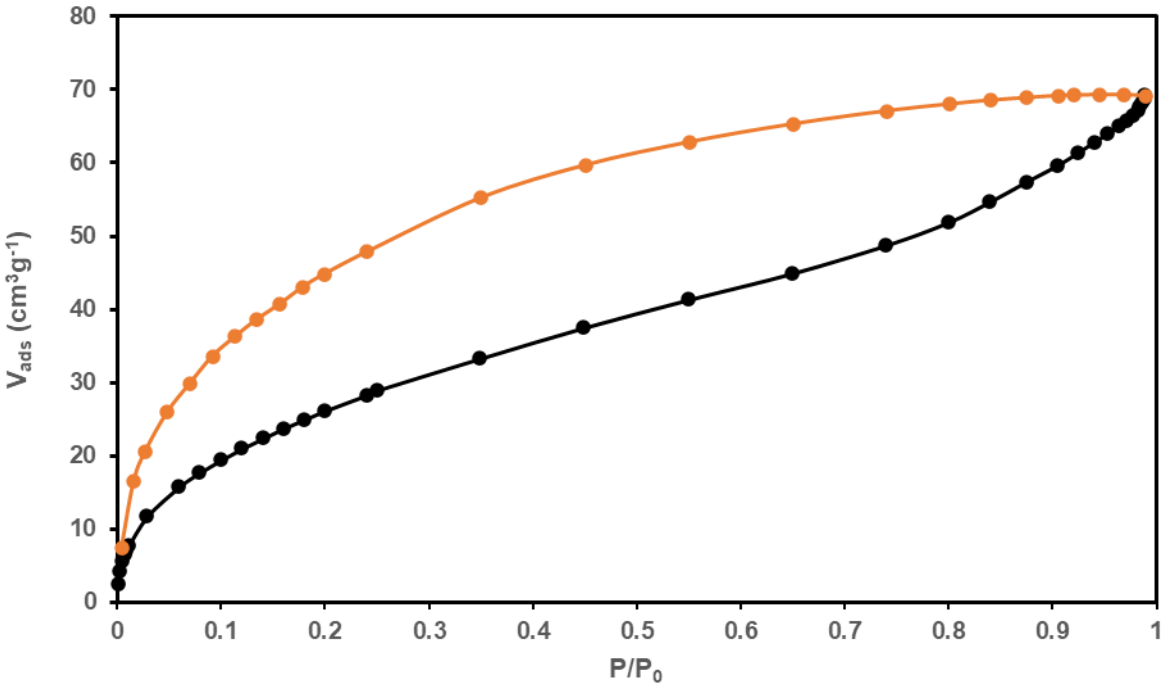

Figure 4.9. CO_2 isotherm collected at 195 K of oxidized Ni-^{ISO}CN-3. Black curve is adsorption and orange curve is desorption. BET surface area is ~111 m^2/g.

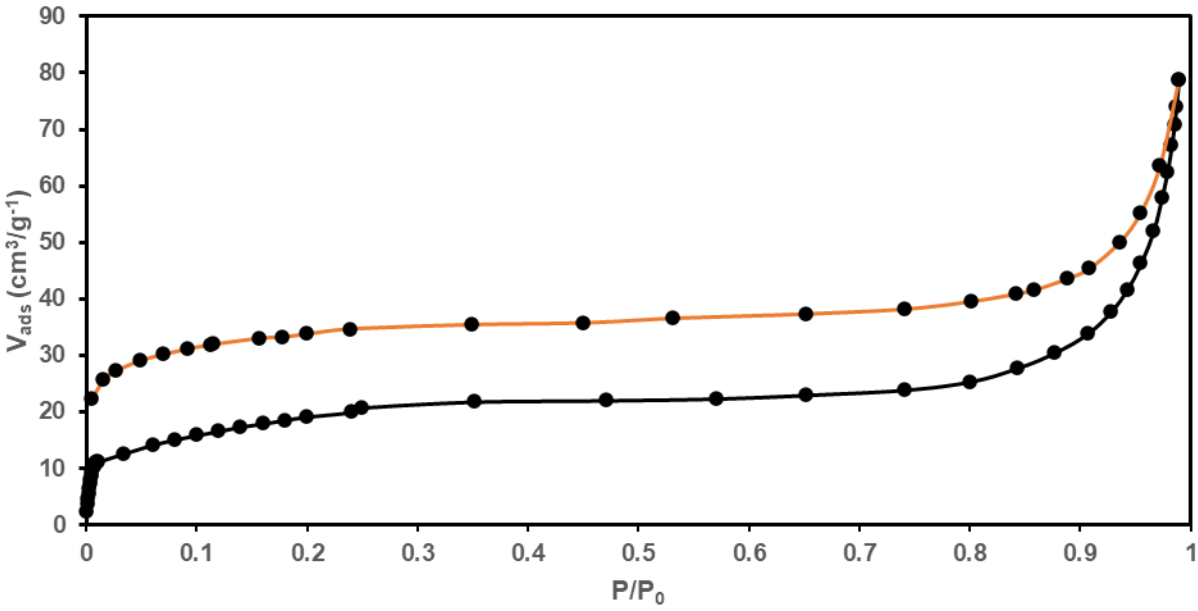

Figure 4.10. N_2 isotherm collected at 77 K of reduced Ni-^{ISO}CN-3 after one oxidation cycle. Black curve is adsorption and orange curve is desorption. BET surface area is ~69 m^2/g.

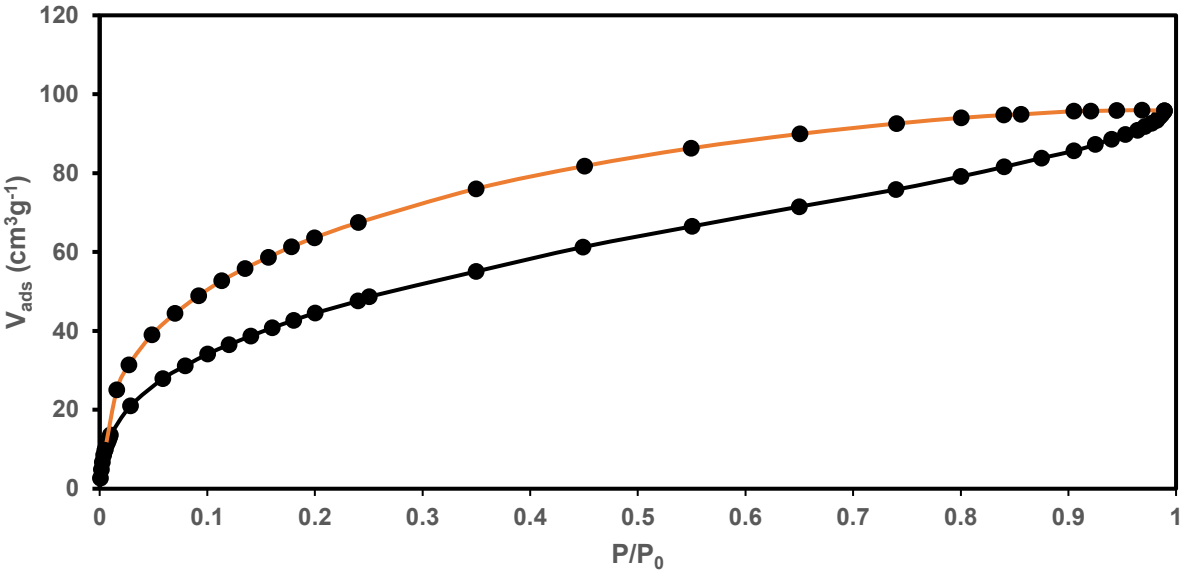

Figure 4.11. CO_2 isotherm collected at 195 K of reduced Ni-^{ISO}CN-3. Black curve is adsorption and orange curve is desorption. BET surface area reported is ~183 m^2/g.

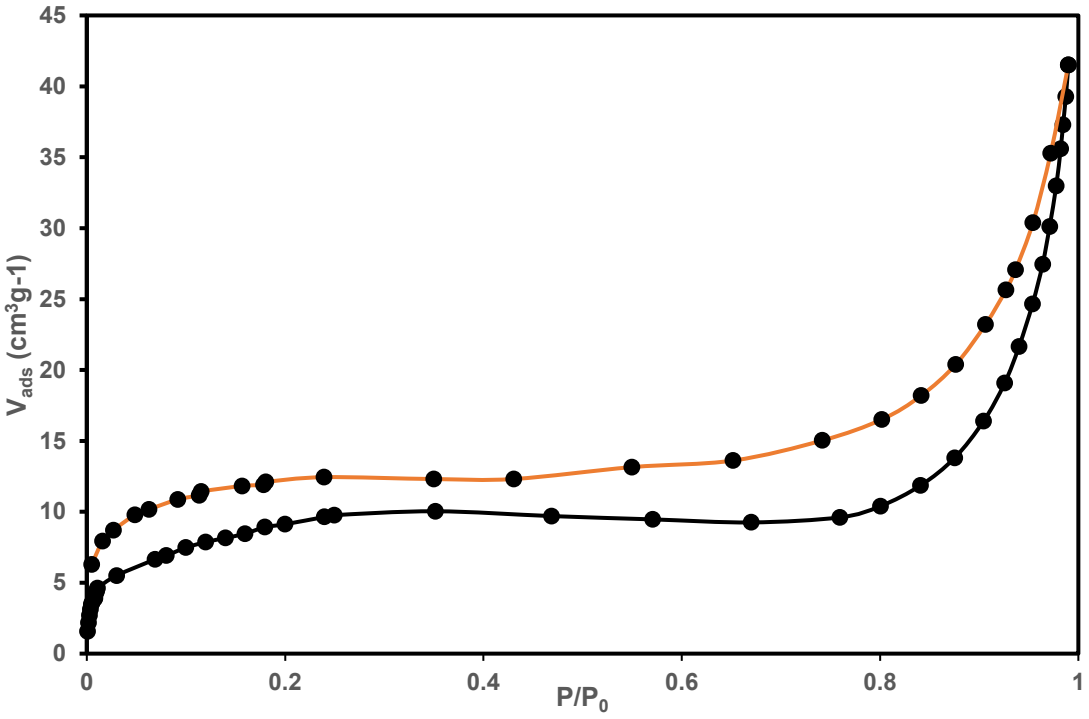

Figure 4.12. N_2 isotherm collected at 77K of reduced Ni-^{ISO}CN-3 after the 5th redox cycle. Black curve represents adsorption and orange curve is desorption. BET surface area reported is ~34 m^2/g.

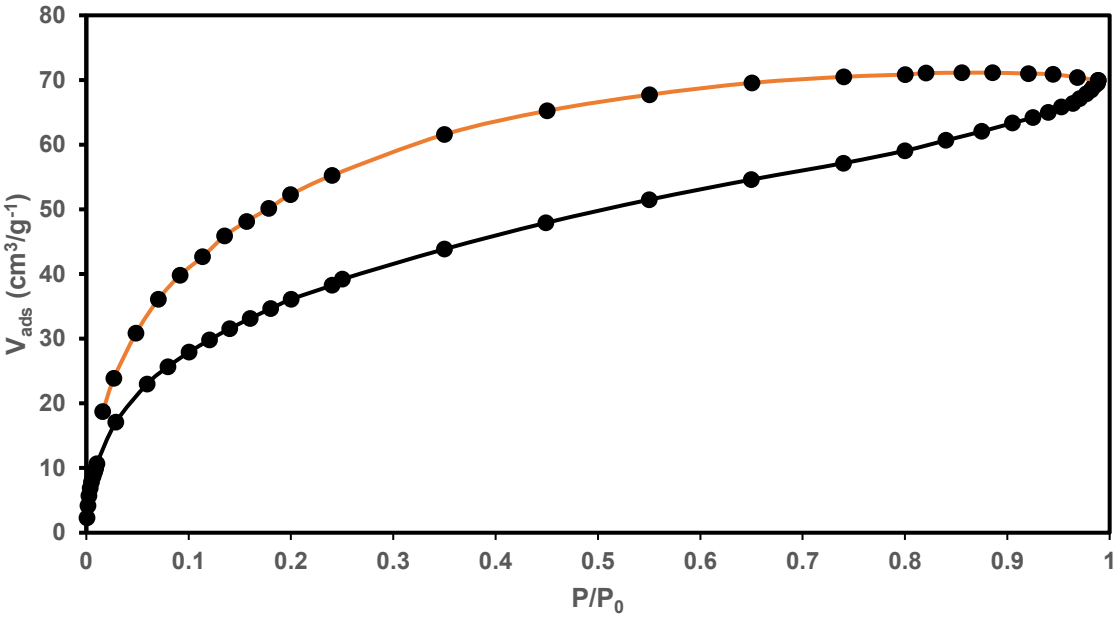

Figure 4.13. CO_2 sorption isotherm at 195K of reduced $Ni^{ISO}CN$-3 after the 5th redox cycle. Black curve represents adsorption and orange curve is desorption. BET surface area reported is ~147 m^2/g.

IR Spectroscopic Data

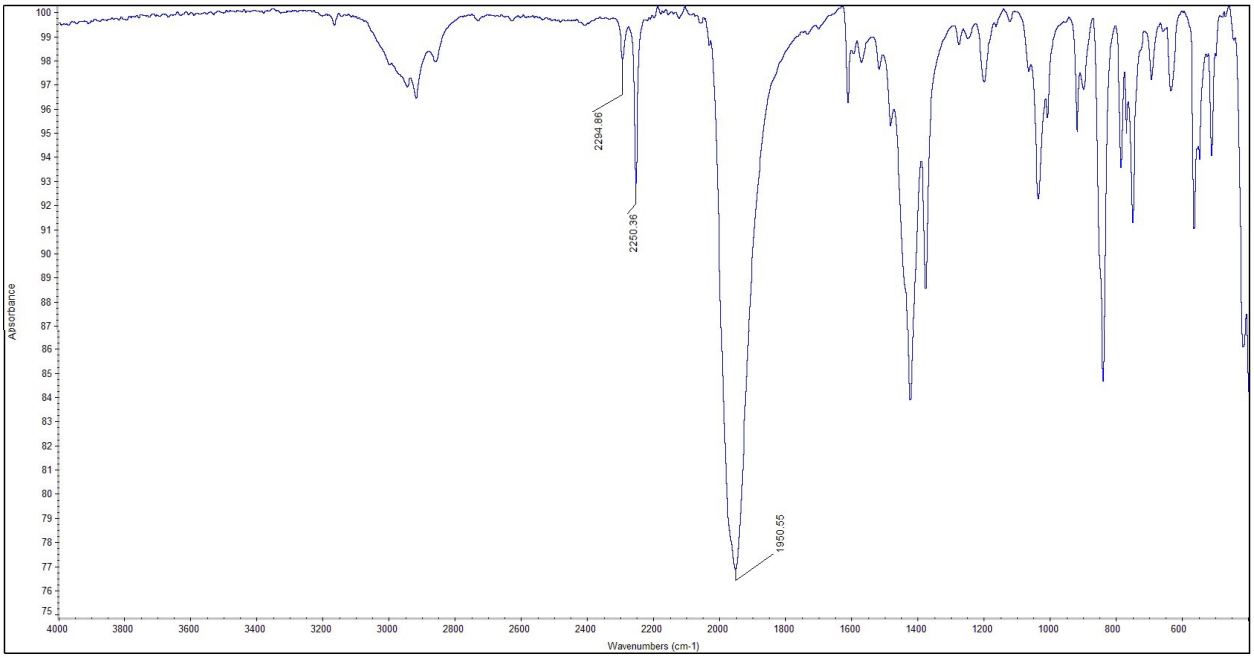

Figure 4.14. ATR-IR of as prepared sample of Ni-^{ISO}CN-3. Sharp bands at 2250 and 2294 cm^{-1} correlate to acetonitrile and benzonitrile, respectively.

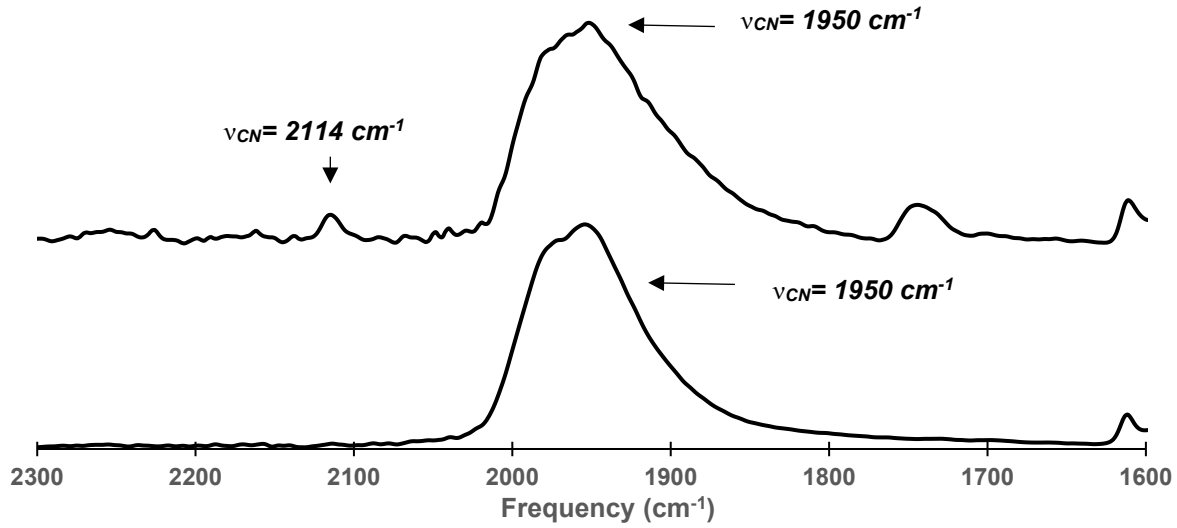

Figure 4.15. ATR-IR spectra of Ni^{ISO}CN-3 after 24 hours of pure water exposure (bottom) and 72 hours of pure water exposure (top). Free isocyanide is observed in the spectra after 72 hours, indicating decomposition of the material.

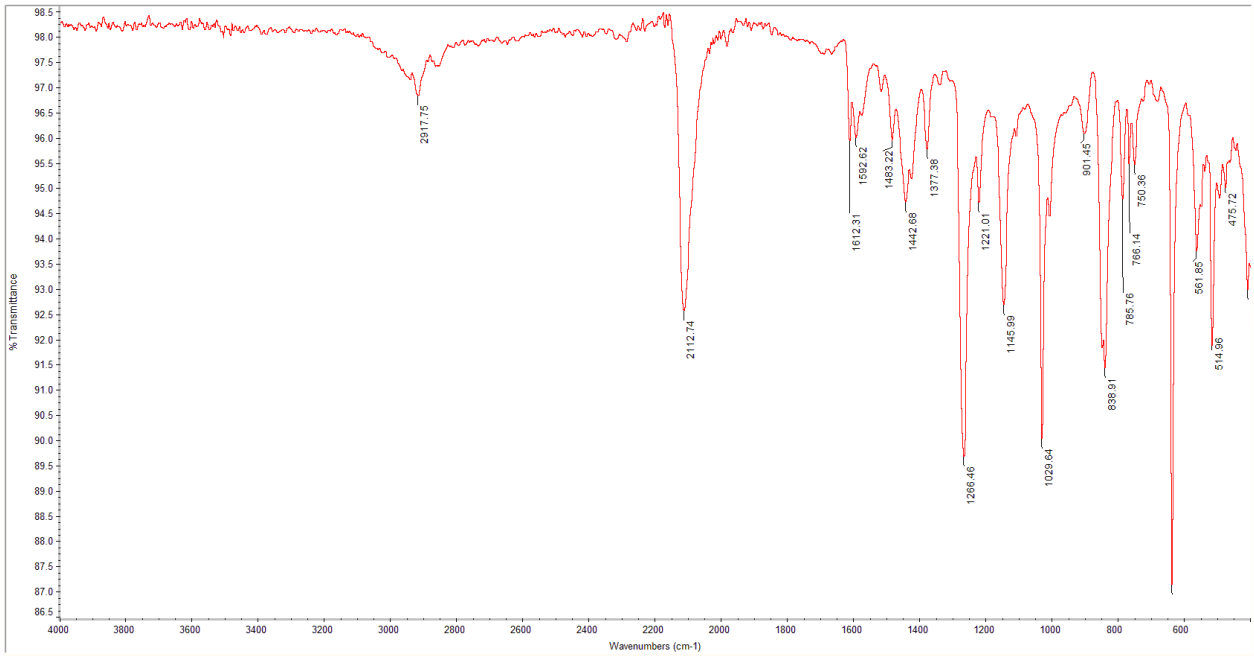

Figure 4.16. ATR-IR of oxidized Ni-^{ISO}CN-3 (first cycle) prior to gas sorption analysis. Material was treated with FcOTf.

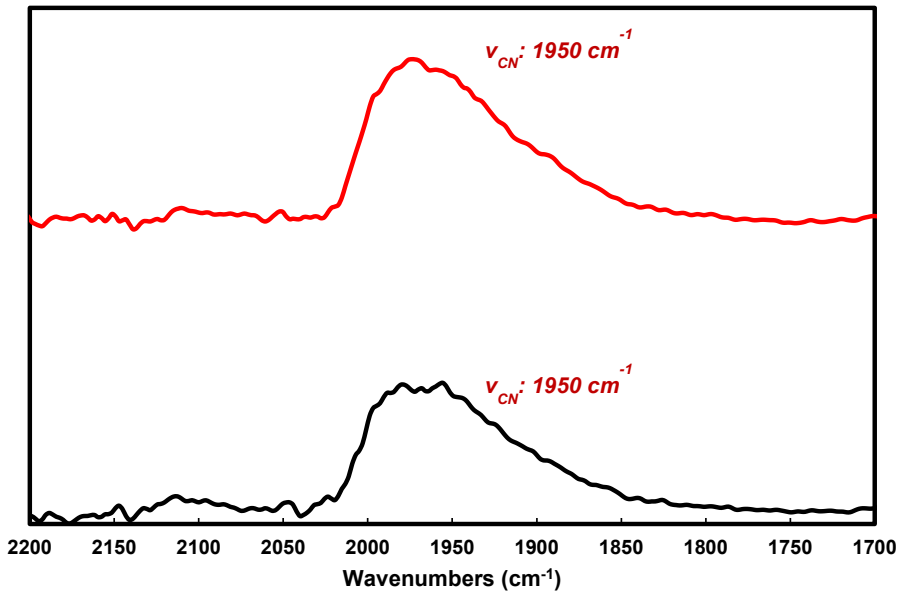

Figure 4.17. ATR-IR of crystalline Ni^{ISO}CN-3 5 days after addition of Fc*OTf (top) and 24 hours after addition of Fc*OTf (bottom). No change in the IR is observed.

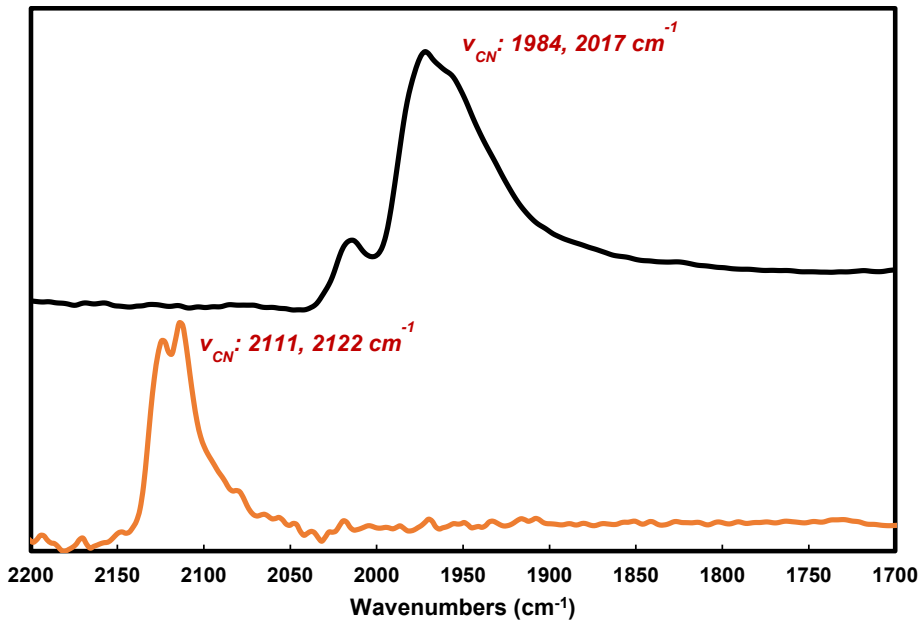

Figure 4.18. ATR-IR of crystalline Ni(CNAr^{Mes2})$_4$ (top) and [Ni(CNAr^{Mes2})$_4$]OTf (bottom). Oxidation was done using Fc*OTf.

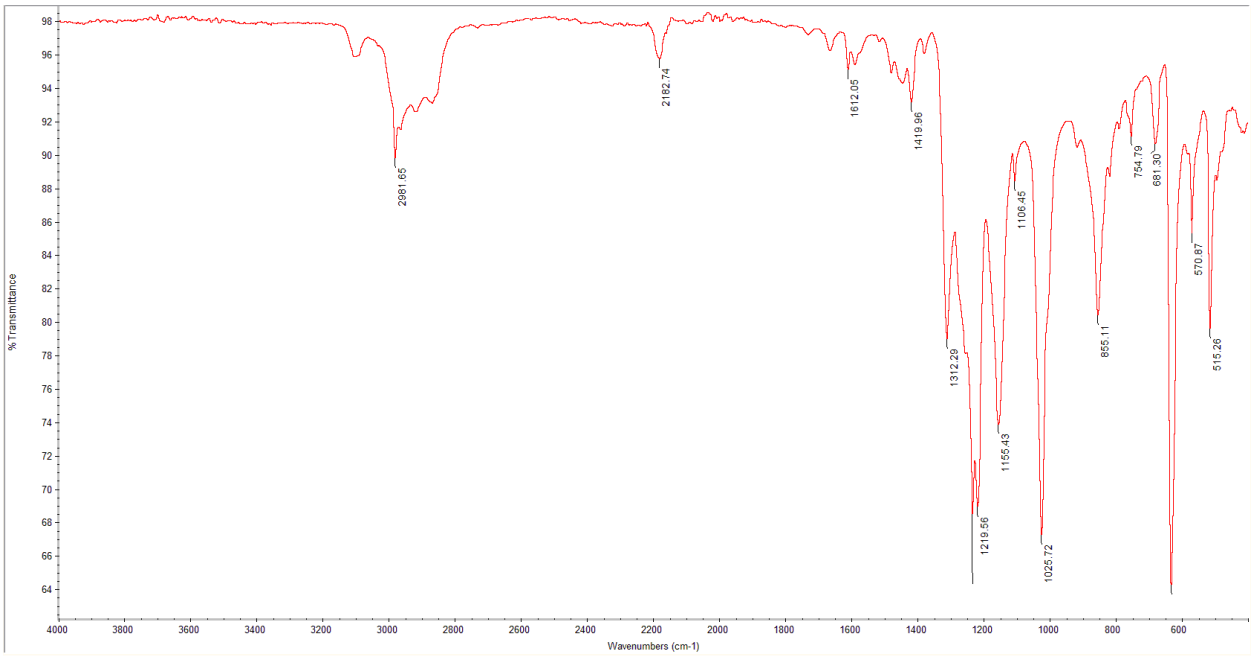

Figure 4.19. ATR-IR of the reaction of Ni^{ISO}CN-3 with excess FcOTf. Dissolution of material suggests formation of molecular species and decomposition of the framework.

Figure 4.20. ATR-IR of oxidized Ni-^{ISO}CN-3 used for gas sorption analysis. IR was taken post analysis, indicating material is unchanged at the Ni(0) centers.

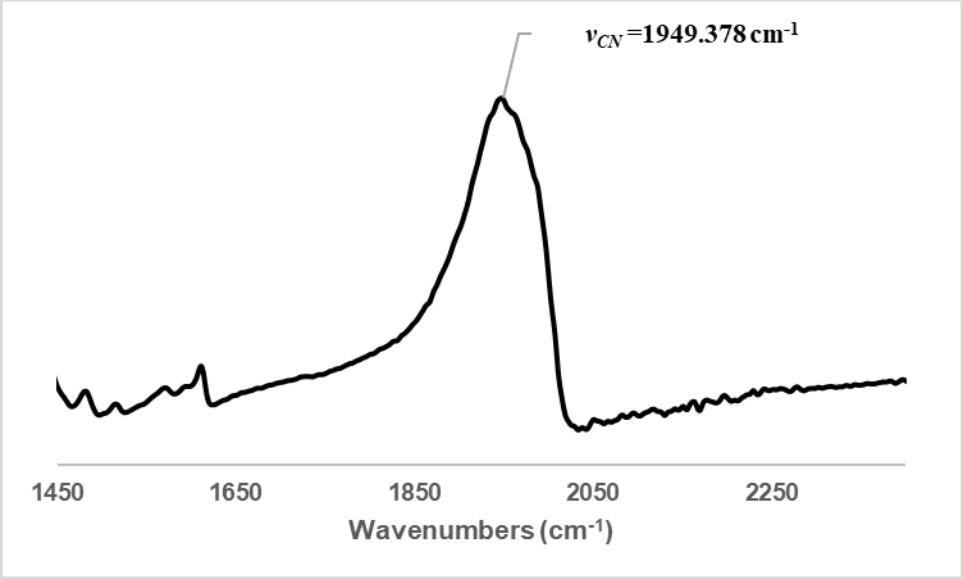

Figure 4.21. ATR-IR of Ni-^{ISO}CN-3 treated with 1 atm of O_2 (g) after 24hr. No decomposition of material observed.

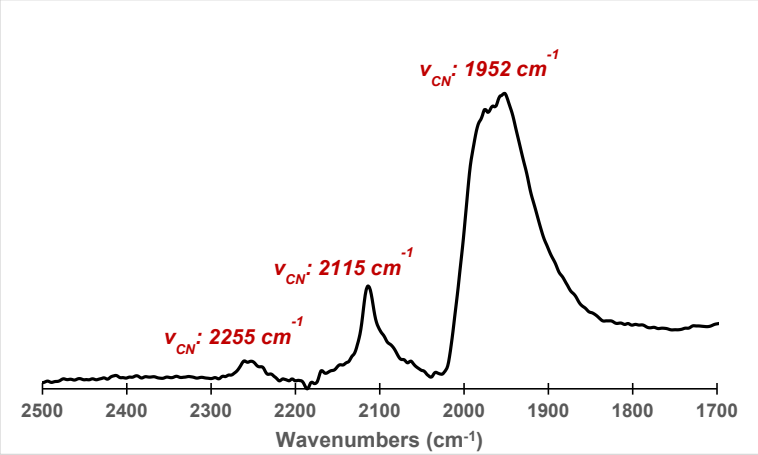

Figure 4.22. ATR-IR of Ni-^{ISO}CN-3 treated with 1 atm of O_2 (g) after 72 hr.

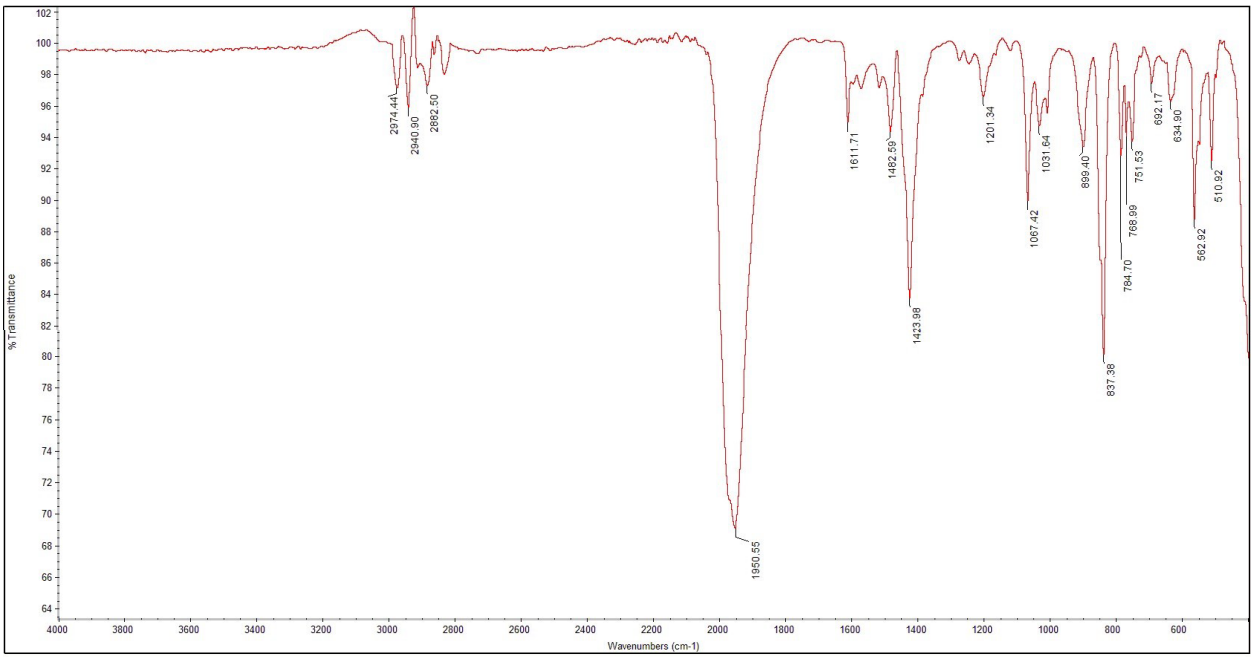

Figure 4.23. ATR-IR of Ni-^{ISO}CN-3 after being treated with 3 mL of Millipore water for 24 hours. No change is observed from as-prepared sample.

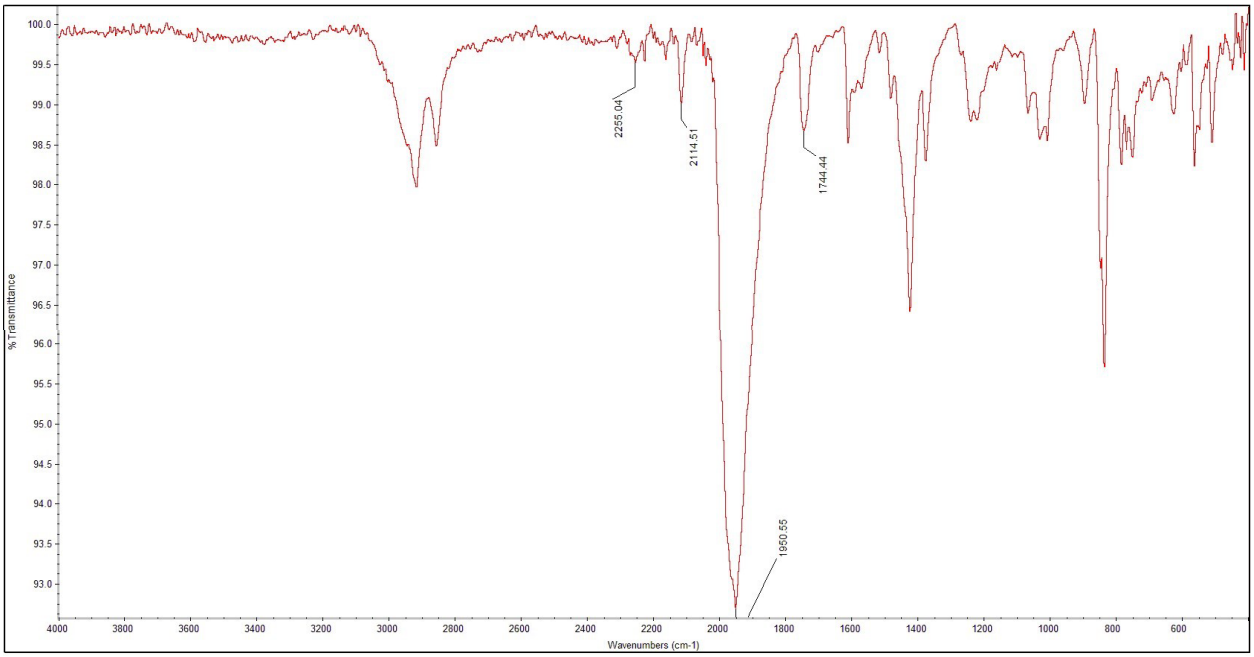

Figure 4.24. ATR-IR of Ni-^{ISO}CN-3 after being treated with 3 mL of Millipore water for 72 hours. The presence of both free isocyanide and isocyanate are now detected.

Figure 4.25. Ni-^{ISO}CN-3 in an ampoule with 3 mL of Millipore water. The red sample floats on top and sticks to the walls of ampoule and does not mix with the water.

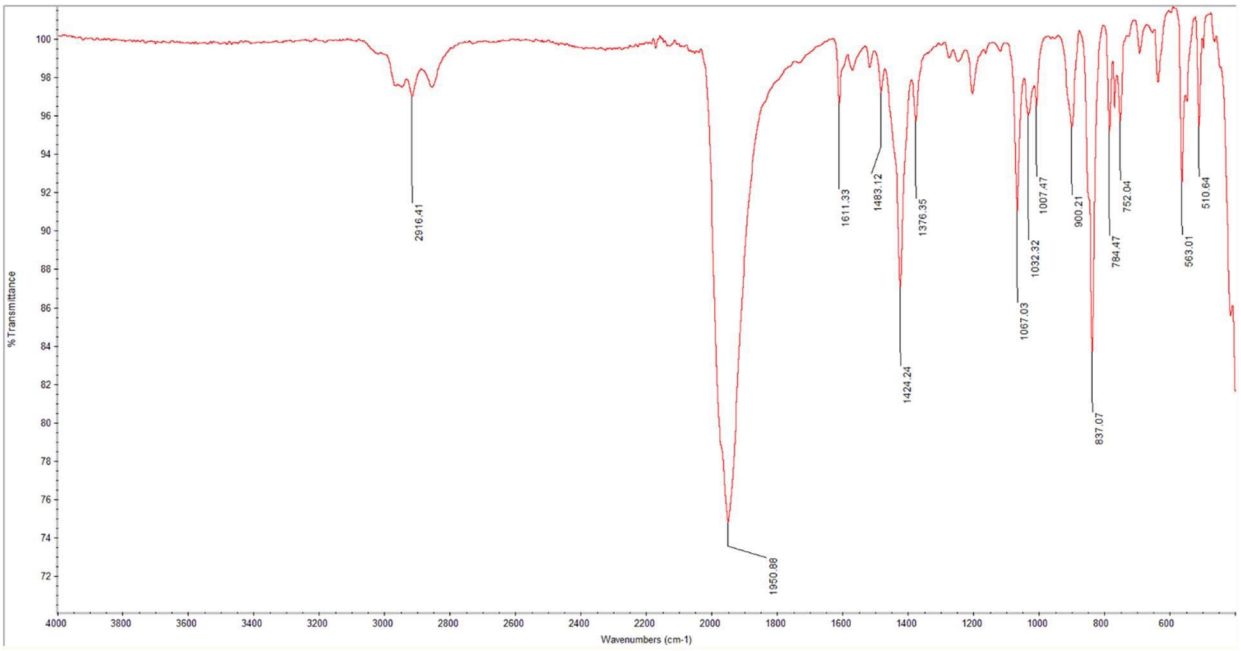

Figure 4.26. ATR-IR of a sample of Ni-^{ISO}CN-3 after a N_2 isotherm analysis run. No change in the IR.

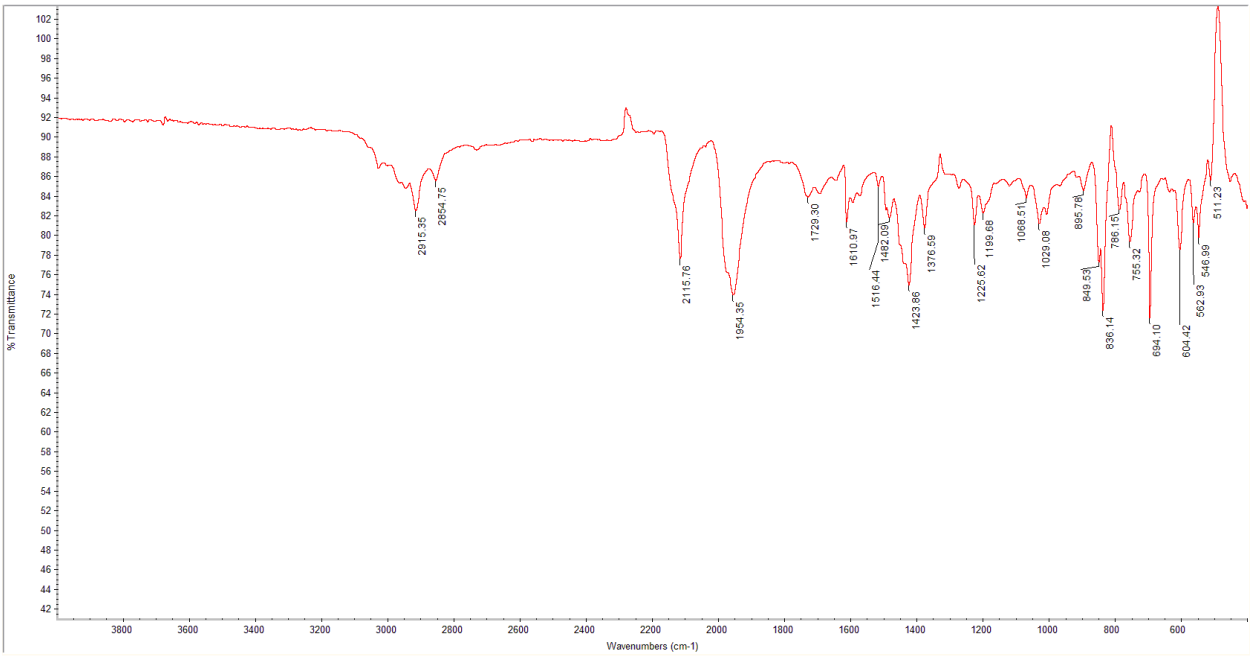

Figure 4.27. ATR-IR of a sample of $Ni^{ISO}CN$-3 after treatment with 3 eqvt. BnBr at room temperature for three hours. Oxidation of the Ni(0) nodes is observed by the presence of the broad peak at ν_{CN} =2116 cm^{-1}.

Figure 4.28. ATR-IR of a sample of $Ni^{ISO}CN$-3 after treatment with 3 eqvt. BnBr at room temperature over the course of 24 hours. Decomposition of the material is observed as free ligand is the only present isocyanide stretch.

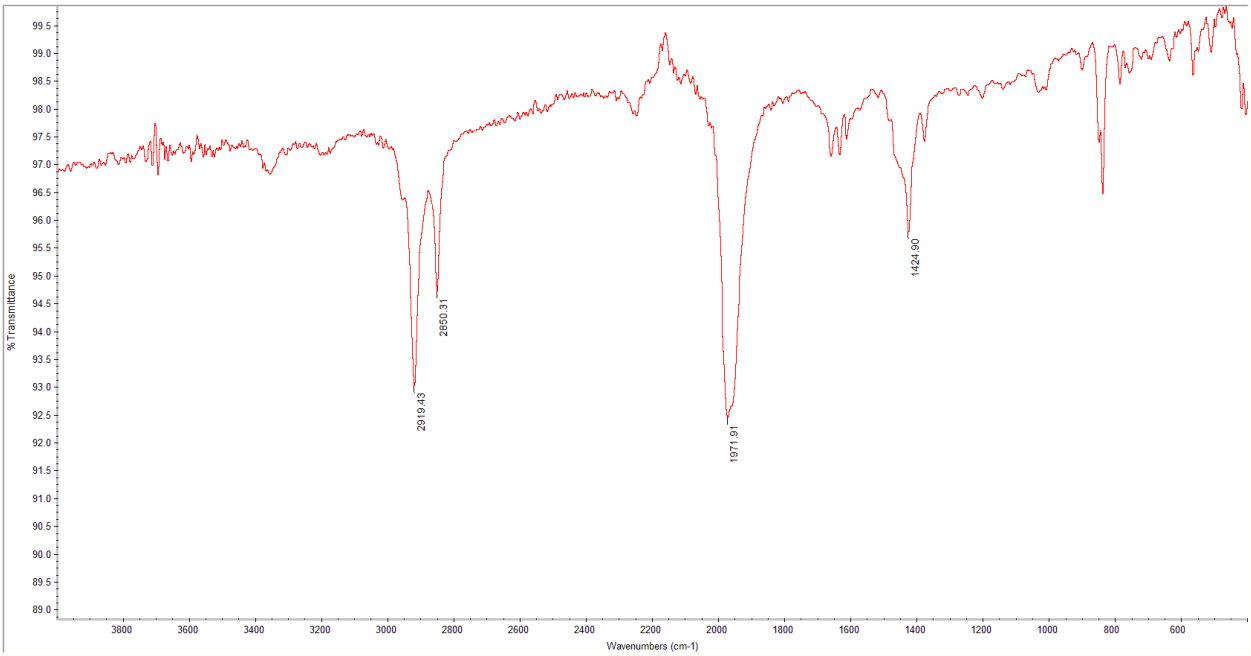

Figure 4.29. ATR-IR of a sample of solid NiISOCN-3 after treatment with 3 eqvt. MeI at room temperature for 24 hours. No change in the starting material is detected.

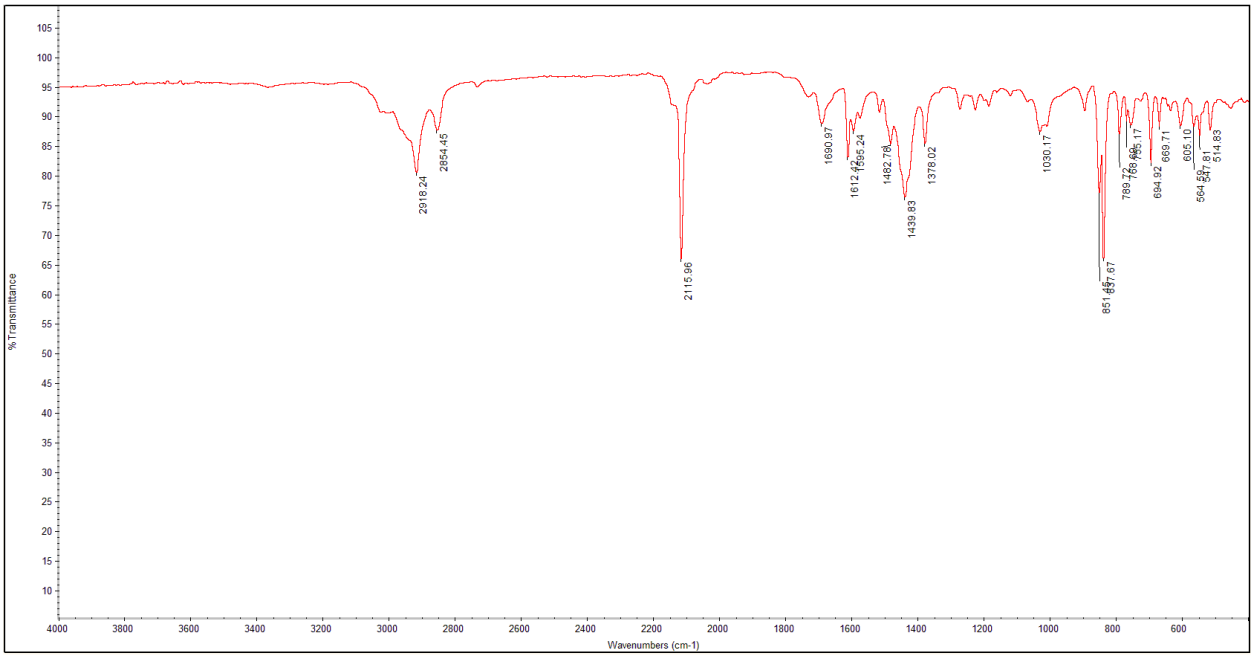

Figure 4.30. ATR-IR of a sample of $Ni^{ISO}CN$-3 after treatment with 3 eqvt. MeI at 80˚C for 24 hours. Decomposition of the material is observed as free ligand is the only present isocyanide stretch.

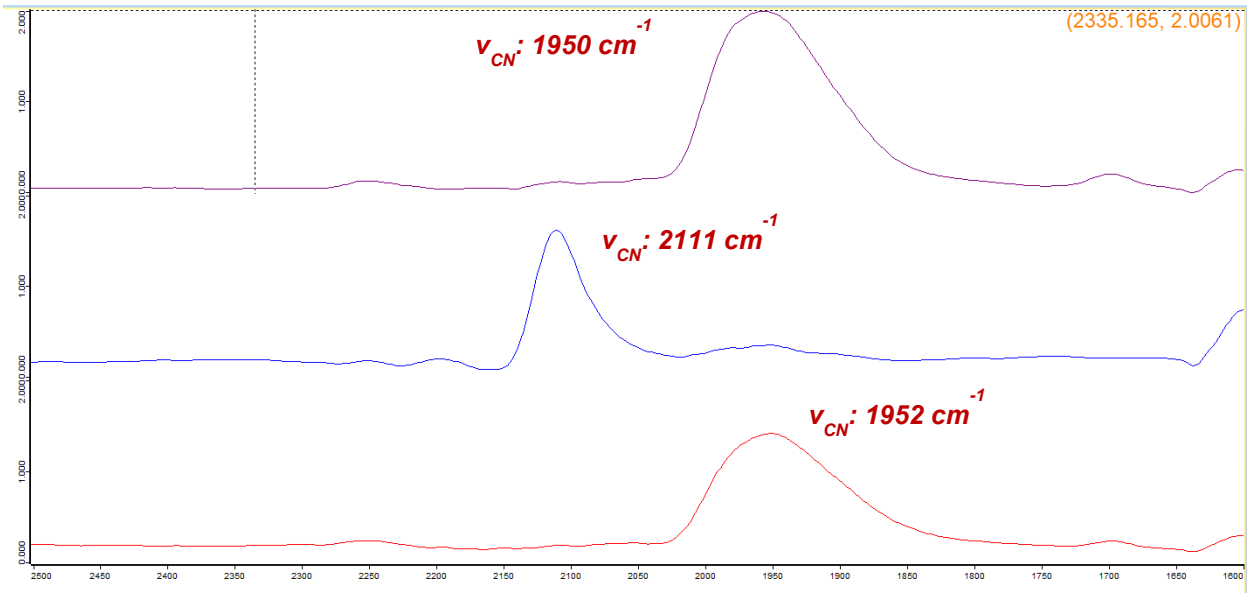

Figure 4.31. Zoomed in ATR-IR measurements of a sample of Ni^{ISO}CN-3 as prepared (red, bottom), after the second oxidation of Ni^{ISO}CN-3 (blue, middle), and second reduction of oxidized Ni^{ISO}CN-3 (purple, top). IR shifts are consistent with one electron oxidation and reductions, respectively.

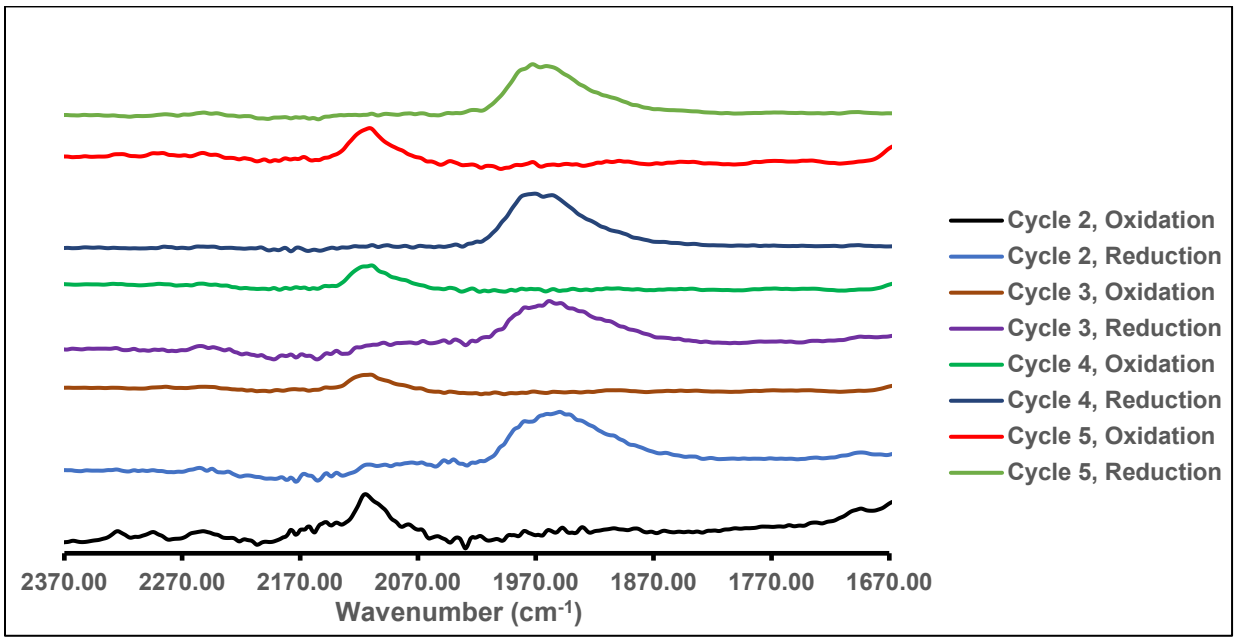

Figure 4.32. Zoomed in ATR-IR spectra of a sample of Ni^{ISO}CN-3 undergoing multiple redox cycles. The bottom spectra is the IR of Ni^{ISO}CN-3 after its second oxidation, followed by the IR of reduced Ni^{ISO}CN-3 after its second reduction (second spectra from bottom). The following spectra consist of the third oxidation and third reduction products through the fifth reduction of Ni^{ISO}CN-3 (top spectra). ATR-IR data indicates the material undergoes a minimum of five cycles of full oxidation and reduction before decomposing.

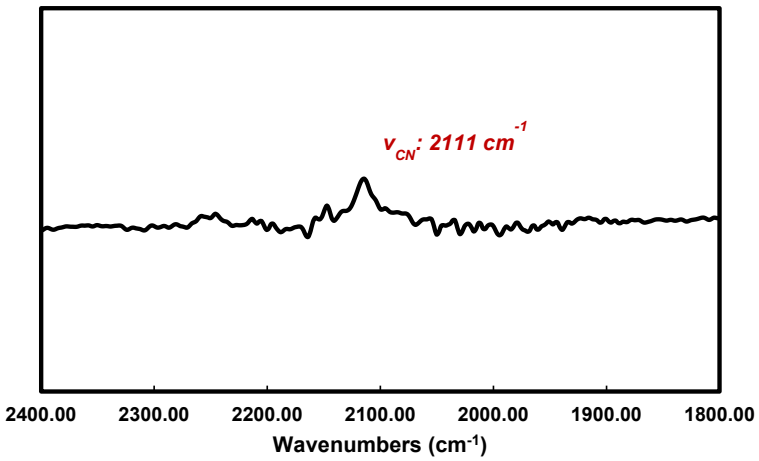

Figure 4.33. Zoomed in ATR-IR spectra of a sample of re-reduced Ni^{ISO}CN-3 (fifth cycle) once treated with Fc*OTf. Oxidation of the metal nodes occurs, indicating the material is no longer structurally ordered.

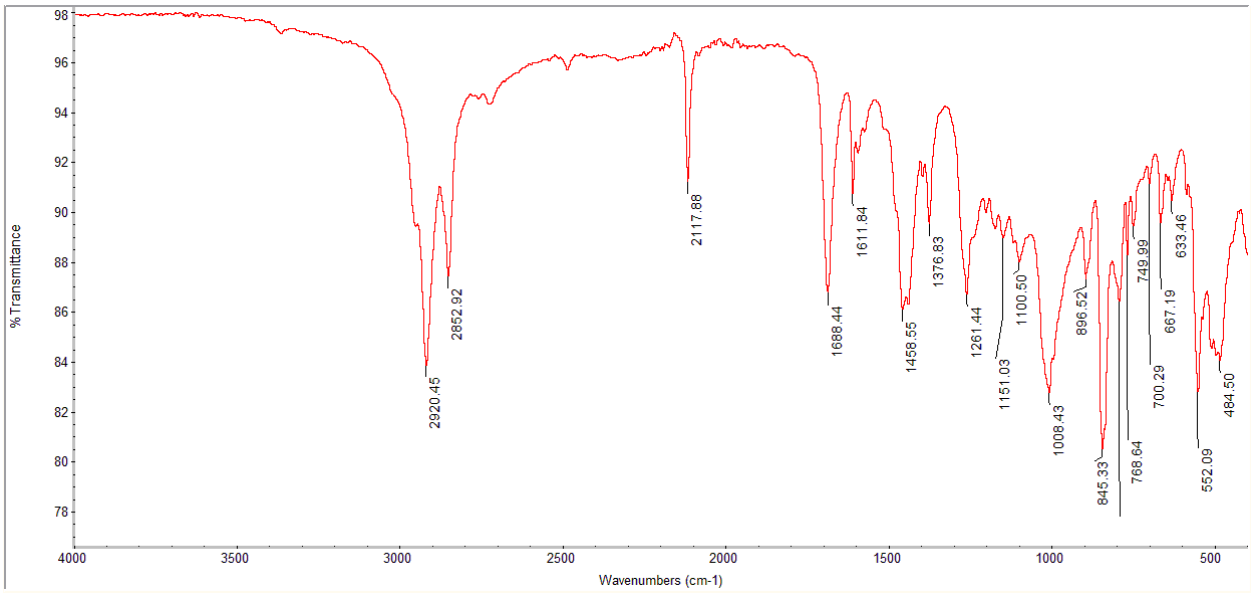

Figure 4.34. ATR-IR spectra of solution after oxidation of Ni^{ISO}CN-3 (sixth cycle). Free ligand is observed in the spectra, indicating degradation of the material.

1H-NMR Spectra

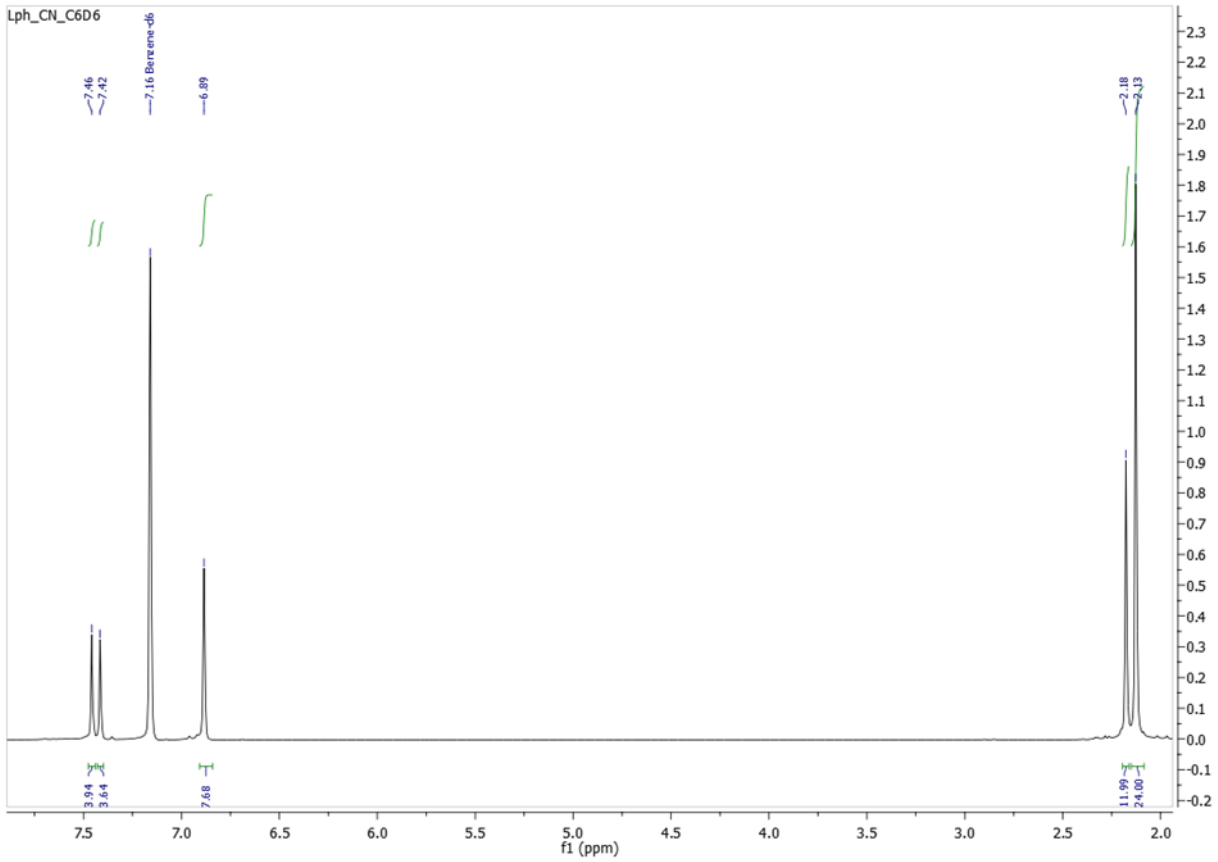

Figure 4.35. ^{1}H-NMR of free 1,4-(CNAr^{Mes2})$_2$C$_6$H$_4$ in C$_6$D$_6$.

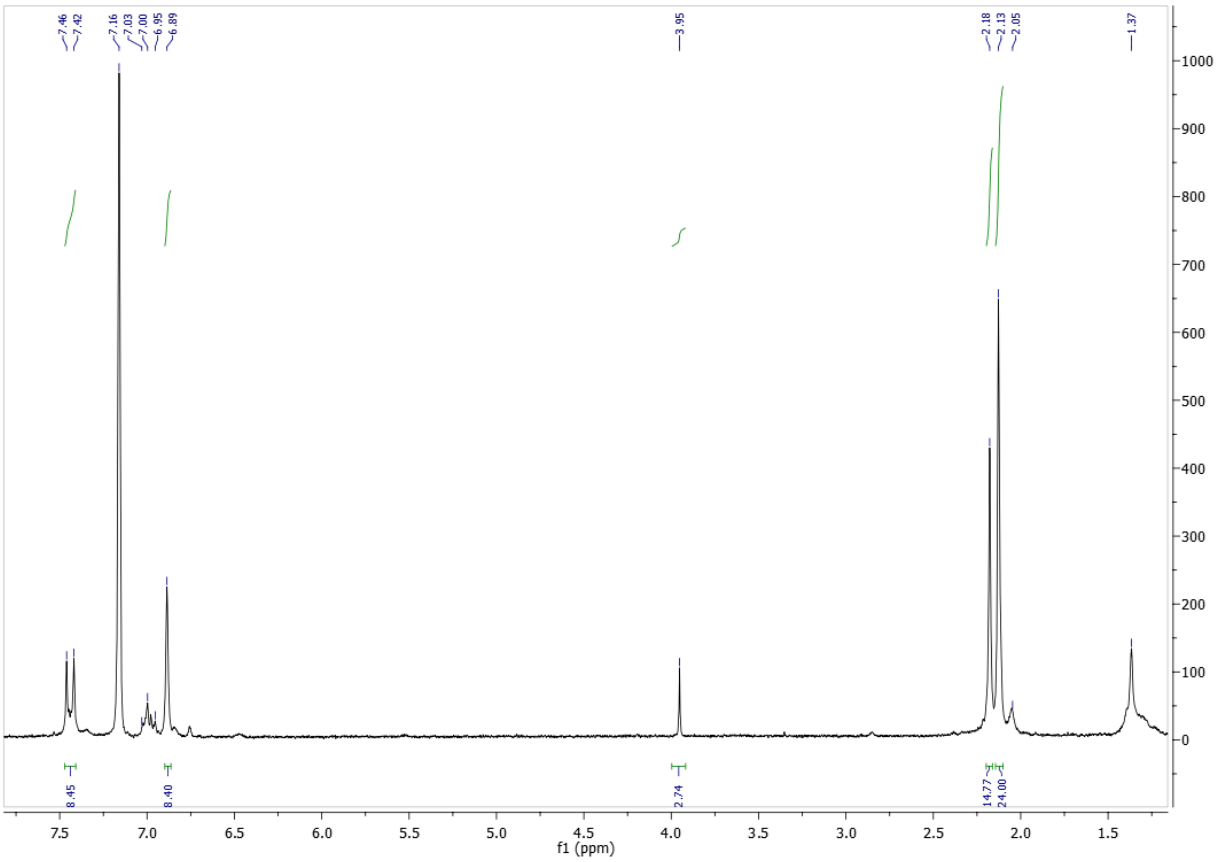

Figure 4.36. ^{1}H-NMR spectrum of product from reaction between Ni^{ISO}CN-3 and 3 EQVT BnBr after 24 hours at room temperature in C_6D_6. Free ligand is present. The solution is red.

EPR Experimental Data and Simulations.

The X-Band continuous wave (CW) EPR spectrum of oxidized Ni^{ISO}CN-3 was measured on a Bruker E500 spectrometer equipped with a Bruker ER 041 X Microwave Bridge and a liquid nitrogen cooling system. The spectrum was recorded in a 4 mm quartz tube at 10 K, and the magnetic field was calibrated with DPPH. The sample was prepared in an argon-filled glovebox. Data were fitted using EasySpin package.[3]

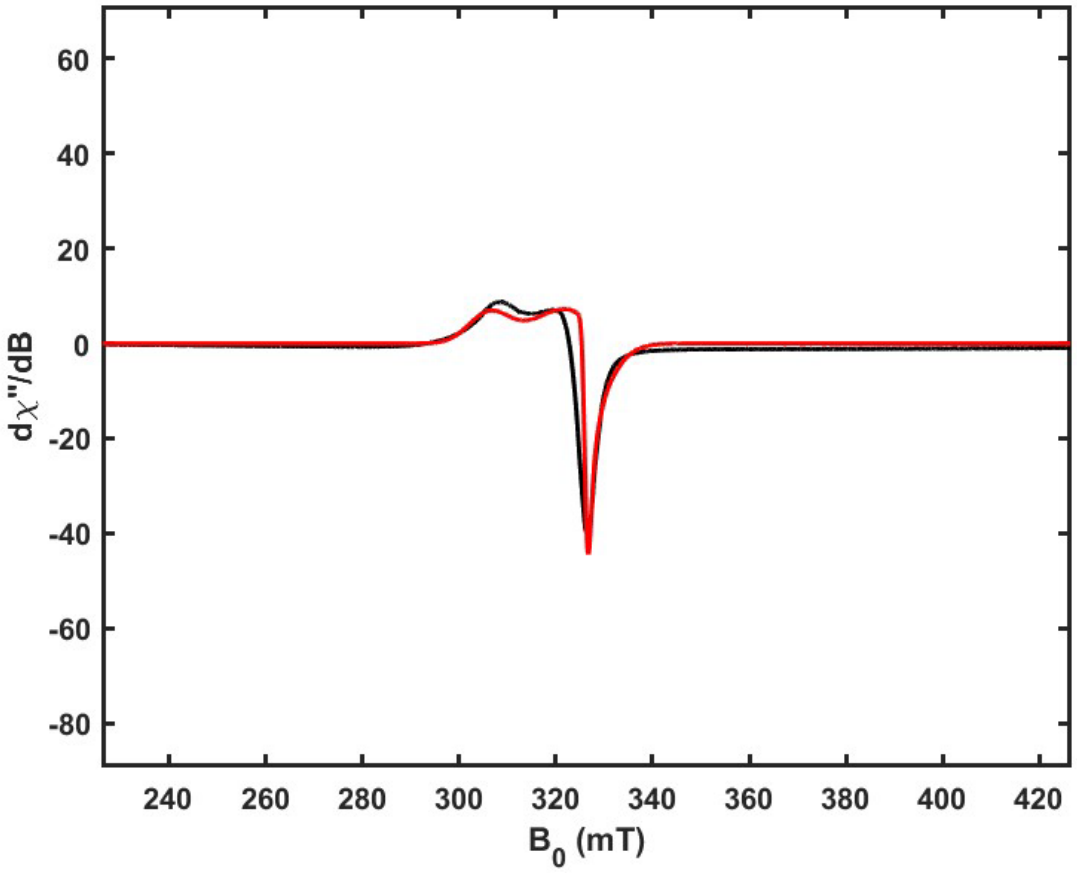

Figure 4.37. 10K X-band CW EPR spectrum (black trace) of the metalloradical generated from oxidation of Ni^{ISO}CN-3 compared to simulated spectrum (red).

Input File for Easyspin EPR Simulation of Oxidized Ni^{ISO}CN-3.

```
Exp.mwFreq = 9.360;
Sys1.Nucs = 'Ni';
Sys1.S = 1/2;
Sys1.g = [2.29 2.13 2.129];
Sys1.gStrain = [0.075 0.09 0.008];
A_Ni = [80.4811 74.9897 123.3078];
Sys1.AStrain = [5 5 2.009];
pepper(Sys1,Exp);
```

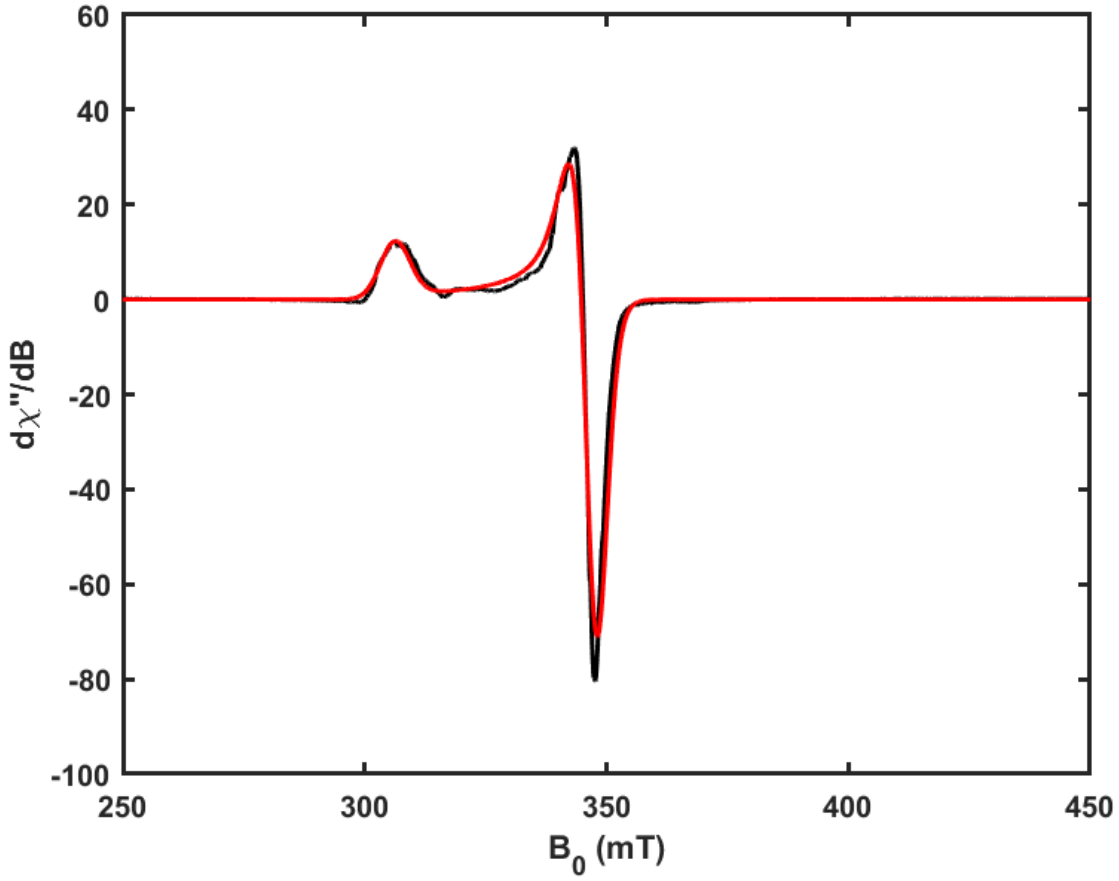

Figure 4.38. 10K X-band CW EPR spectrum (black trace) of the metalloradical generated from [Ni(CNAr^{Mes2})$_4$]OTf compared to simulated spectrum (red).

Input File for Easyspin EPR Simulation of [Ni(CNAr^{Mes2})$_4$]OTf.

```
Exp.mwFreq = 9.363;
Sys1.Nucs = 'Ni';
Sys1.S = 1/2;
Sys1.g = [2.3619 2.0695 2.065]
Sys1.gStrain = [0.06 0.05 0.03]
A_Ni = [150.5852 172.9414 101.8574];
Sys1.AStrain = [5.02 5 22];
pepper(Sys1,Exp)
```

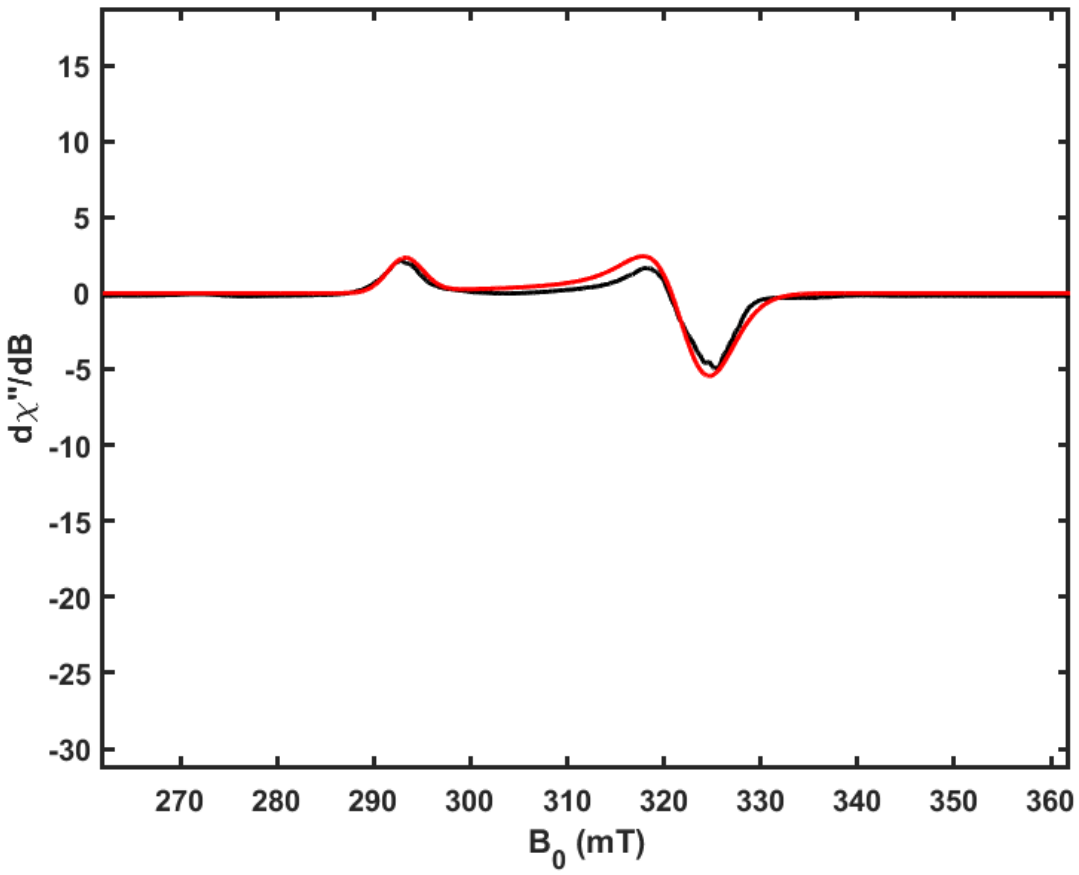

Figure 4.39. 10K X-band CW EPR spectrum (black trace) of the metalloradical generated from [Ni(CNAr^{Mes2})$_3$]OTf compared to simulated spectrum (red).

Input File for Easyspin EPR Simulation of [Ni(CNAr^{Mes2})$_3$]OTf.

```
Exp.mwFreq = 9.366;
Sys1.Nucs = 'Ni';
Sys1.S = 1/2;
Sys1.g = [2.3619 2.1354 2.1381]
Sys1.gStrain = [0.0358 0.06 0.04]
A_Ni = [202.5852 34.9414 211.8574];
Sys1.AStrain = [5.02 12 22];
pepper(Sys1,Exp)
```

Thermal Analysis. Thermogravimetric analysis was performed on ~5–15 mg of material been dried under dynamic vacuum. Analysis was conducted under a stream of dry dinitrogen gas (80

mL/min) using a Mettler Toledo TGA/DSC 1 STARe System running from 30 ˚C to 800 ˚C with a ramping rate of 5 ˚C/min.

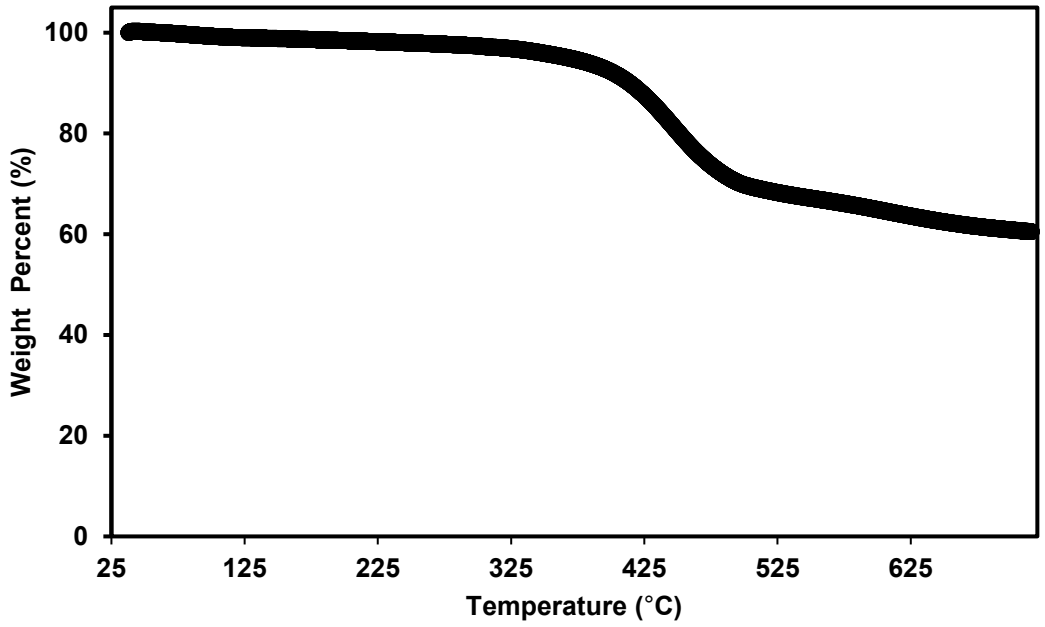

Figure 4.40. Thermogravimetric analysis (TGA) (black trace) of Ni-^{ISO}CN-3.

General Crystallographic Information. Single X-ray structure determinations were performed at 100 K on Bruker Platform Diffractometers equipped with Mo-K_α or Cu-K_α radiation source and an APEX-II CCD area detector. All structures were solved via direct methods with SHELXS[4,5] and refined by full-matrix least-squares procedures using SHELXL within the Olex2 software package.[6] Crystallographic data collection and refinement information are listed in Table 4.2. MeCN solvent molecules of co-crystallization are present within the solvent-accessible channels. The Platon routine SQUEEZE[7] was used to account for the electron density of this disordered solvent as a diffuse contribution to the overall scattering without specific atom positions. Powder X-ray diffraction studies on Ni-^{ISO}CN-3 were performed at 100 K on a Bruker D8 Advanced LynxEye CCD diffractometer, equipped with Cu-K_α radiation (λ = 1.54178 Å) and K_β filter. Diffraction measurements were set to 40V and 40 mA.

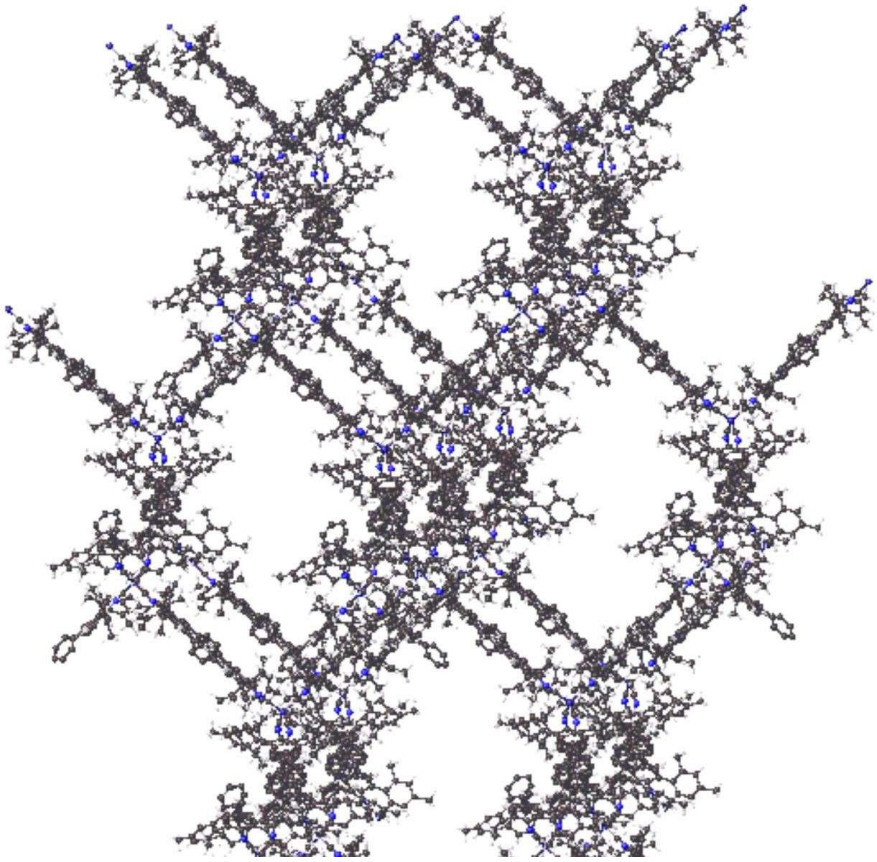

Figure 4.41. View of an individual network of the diamondoid Ni-^{ISO}CN-3.

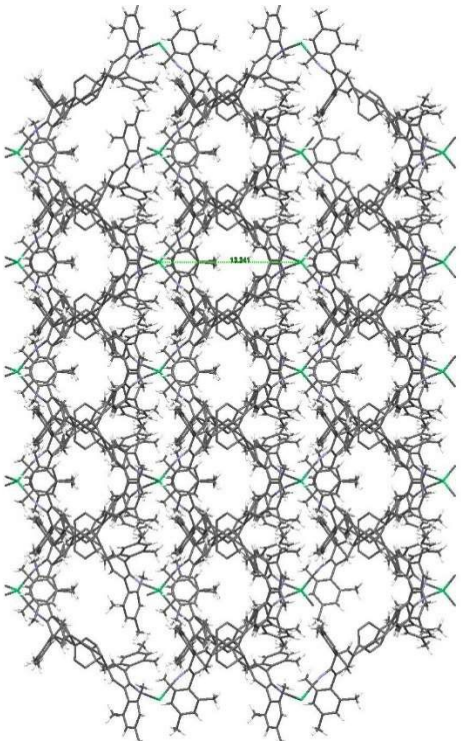

Figure 4.42. View along the b-axis of four-fold interpenetrated Ni-^{ISO}CN-3.

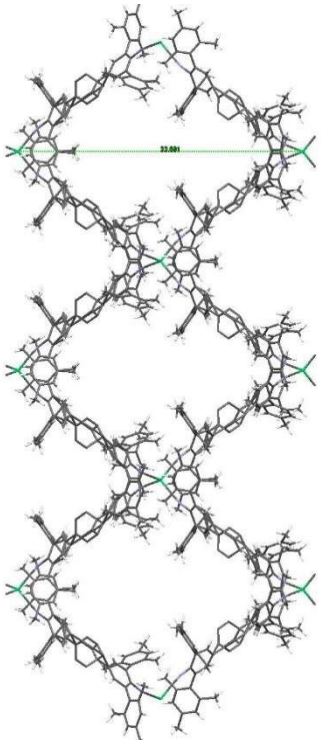

Figure 4.43. View along the b-axis of Ni-^{ISO}CN-3 of an individual framework of Ni-^{ISO}CN-3.

Table 4.2. Crystallographic refinement information for $Ni^{ISO}CN$-3.

Name	**$Ni^{ISO}CN$-3**
Formula	$C_{112}H_{104}N_4Ni$
Crystal System	Tetragonal
Space Group	*P*-4*b*2
a, Å	20.5707(8)
b, Å	20.5707(8)
c, Å	13.3409(8)
α, deg	90
β, deg	90
γ, deg	90
V, $Å^3$	5645.36
Z	2
Radiation (λ, Å)	Cu-Kα, 1.54178
ρ (calcd.), g/cm^3	0.984
μ(Mo Ka), mm^{-1}	0.552
Temp. K	100
Θ max, deg	134.52
Data/parameters	2419/288
R_1	0.0906
wR_2	0.2245
GOF	1.0722

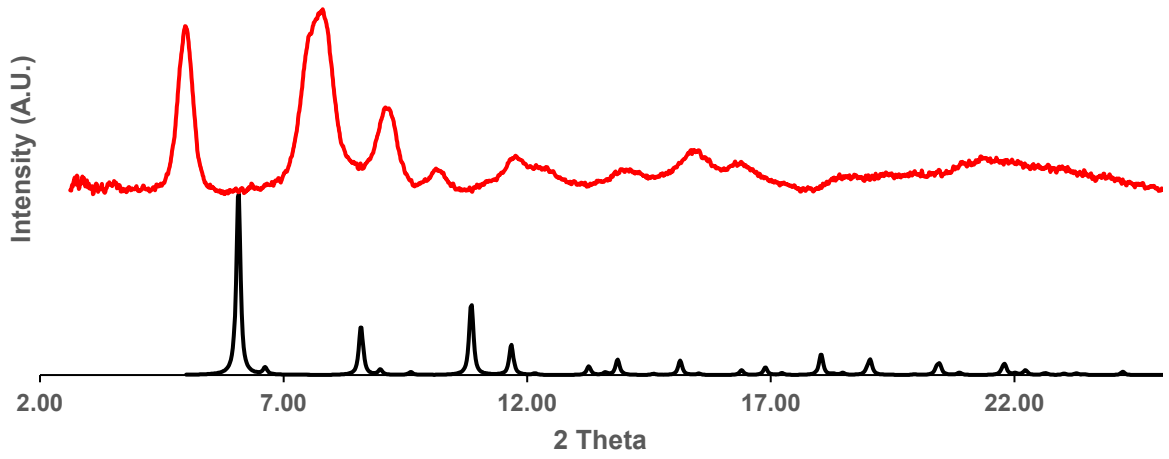

Figure 4.44. Powder X-Ray Diffraction pattern of as synthesized Ni-^{ISO}CN-3 (red) and simulated (black).

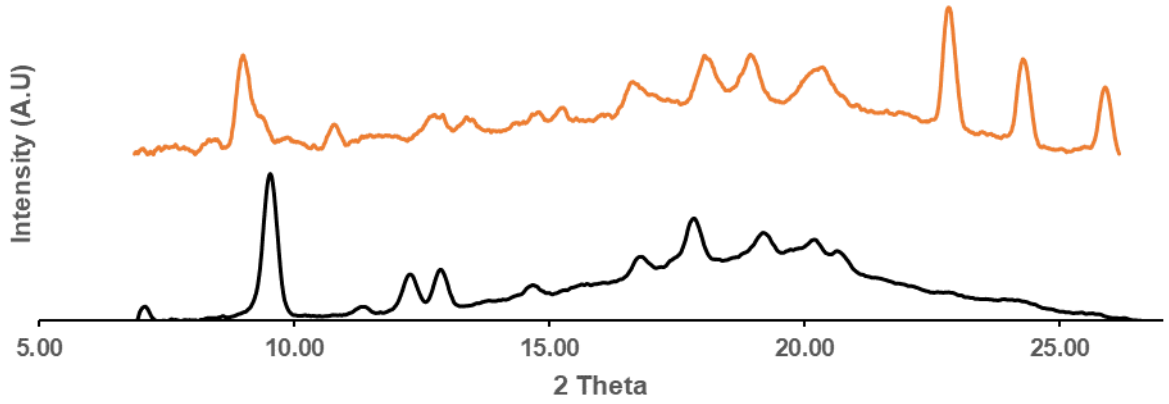

Figure 4.45. Powder X-Ray Diffraction patterns of oxidized Ni-^{ISO}CN-3 (black) and reduced Ni-^{ISO}CN-3 (orange). As displayed by the figure, it is evident the material stays crystalline.

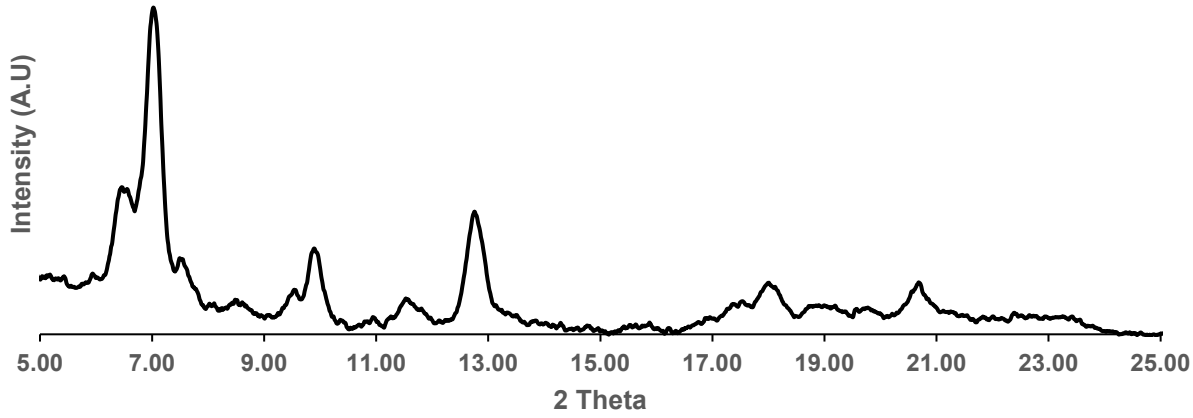

Figure 4.46. Powder X-Ray Diffraction patterns of Ni-^{ISO}CN-3 (black) post gas-sorption measurements. The material remains crystalline, there is no indication of collapse.

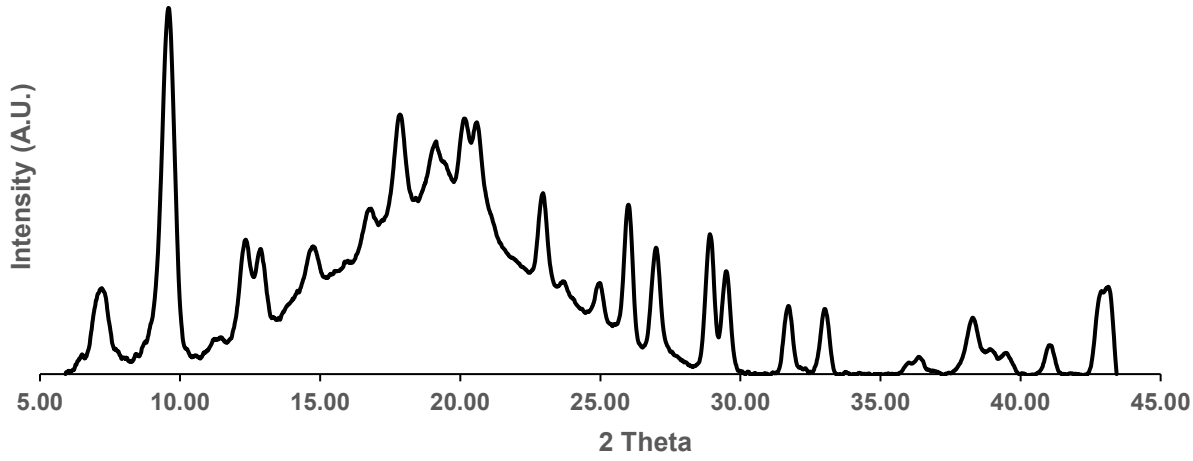

Figure 4.47. Powder X-Ray diffraction patterns of oxidized Ni-^{ISO}CN-3 (black) post gas-sorption measurements. The material maintains crystallinity.

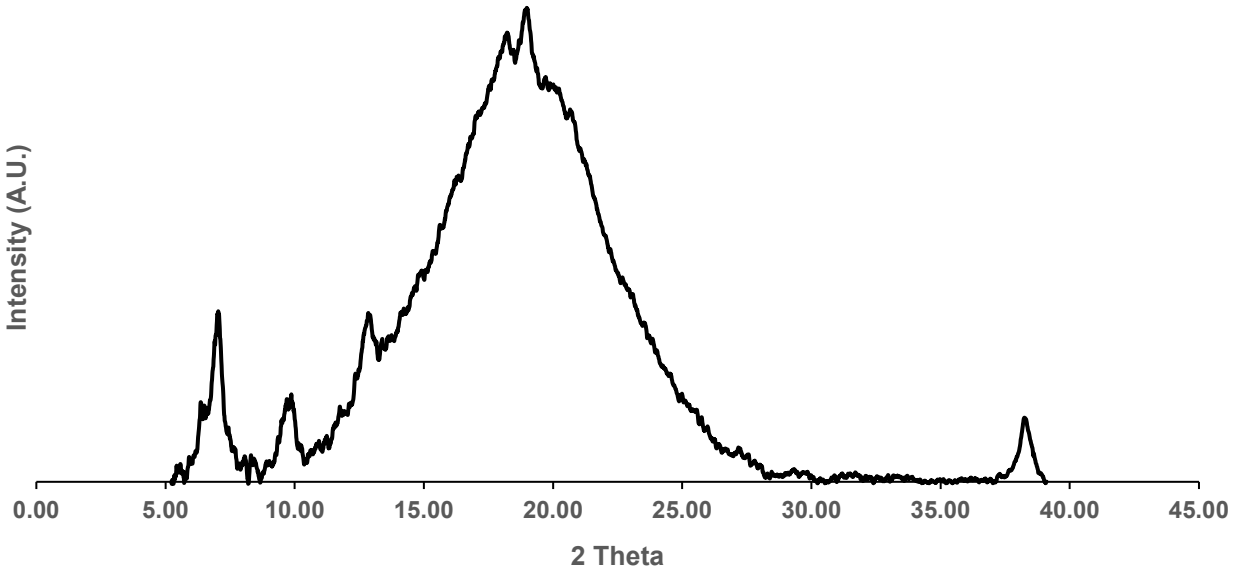

Figure 4.48. Powder X-Ray Diffraction patterns of re-reduced Ni-^{ISO}CN-3 (black) post gas-sorption measurements. The material maintains some crystallinity, however defects are more prominent.

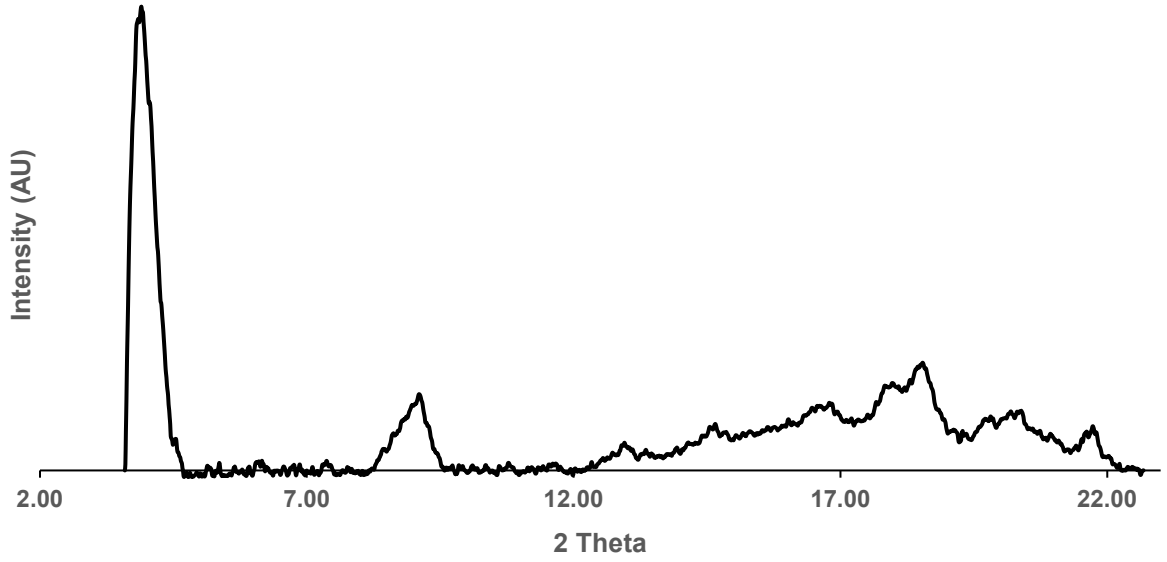

Figure 4.49. Powder X-ray Diffraction pattern of re-reduced Ni-^{ISO}CN-3 after two redox cycles. Loss of crystallinity observed.

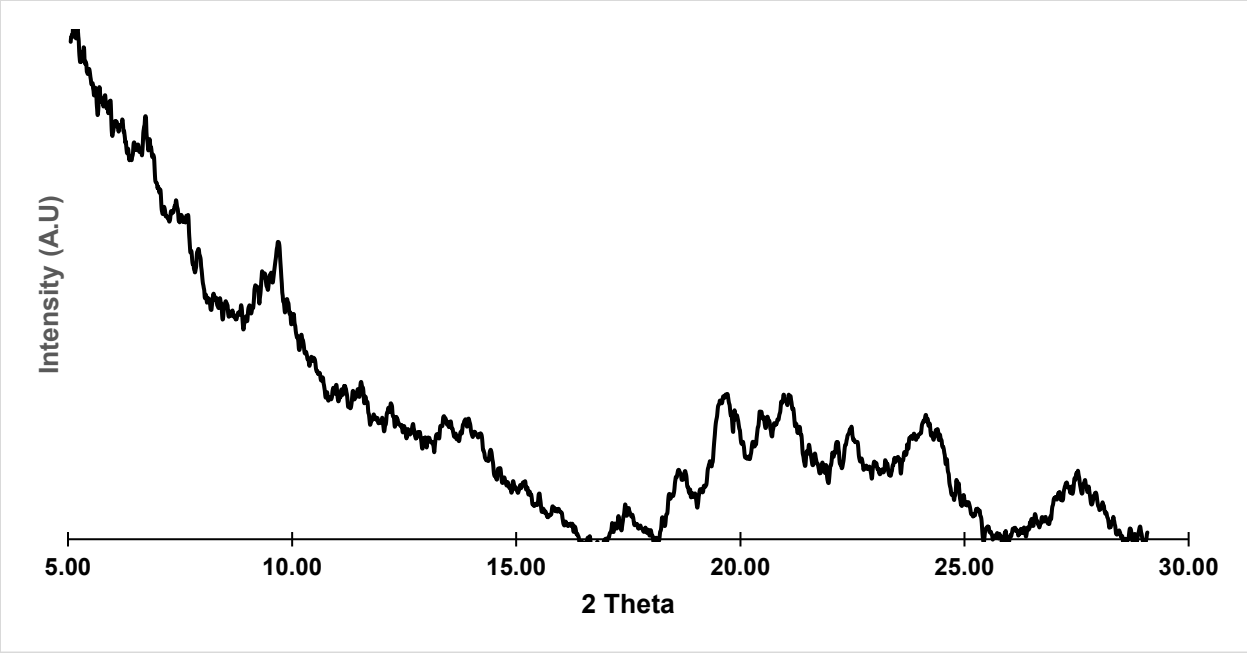

Figure 4.50. Powder X-ray Diffraction pattern of re-reduced Ni-^{ISO}CN-3 after the fifth redox cycle.

Ni K-Edge X-ray Absorption Spectroscopy (XAS) Measurements and Analysis.

Experimental details.

Solid samples for X-ray spectroscopic analysis were prepared in an inert-atmosphere glovebox. Solid samples were finely ground using an agate mortar and pestle with boron nitride (BN) into a homogeneous mixture comprising 5% (w/w) Ni. These mixtures were pressed into 1 mm Al spacers and sealed with 38 μm Kapton tape. XAS data were obtained at the Stanford Synchrotron Radiation Lightsource (SSRL) at beamline 9-3 under ring conditions of 3 GeV and 500 mA. Incident X-ray radiation was monochromated using a double Si(220) crystal monochromator and a Rh-coated mirror (set to an energy cutoff of 13 keV) was used for harmonic rejection. Spectra were collected in fluorescence mode, with X-rays detected by a PIPs detector placed at a 90° angle to the sample. A Ni foil and a third ionization chamber upstream of the sample were used for internal energy calibration, setting the first inflection point of the Ni foil scan to 8331.6 eV.

Data were collected from 8010 eV to 8730 eV. Four scans were measured and averaged with the Athena software package.[8] No spectral changes due to photodamage were observed after multiple scans for these complexes. E_0 was set at 8350 eV, and the region below 8300 eV was used to fit a linear background, while the region above 8350 eV was flattened with a piecewise spline and set to an average intensity of 1.0.

DFT Calculations.

All calculations were performed in Orca 4.2.0.[9] TDDFT calculations were performed at the def2-tzvpp(C,H,N,I)/CP(PPP)(Ni)//B3LYP level of theory. UB3LYP was used for the open shell species **2**. The RIJCOSX approximation and associated auxiliary basis sets were used. Relativistic corrections were performed with the Zeroth Order Relativistic Approximation (ZORA). The Lebedev 302 point integration grid (Orca Grid4) was selected for C, H, and N atoms, while the Lebedev 770 point integration grid (Orca Grid7) was used for Ni and I atoms. Solvent corrections were applied with the continuous polarizable continuum model (CPCM).[10] Calculated spectra were shifted by a scalar correction, derived from the average of the difference between the calculated and measured first pre-edge feature.

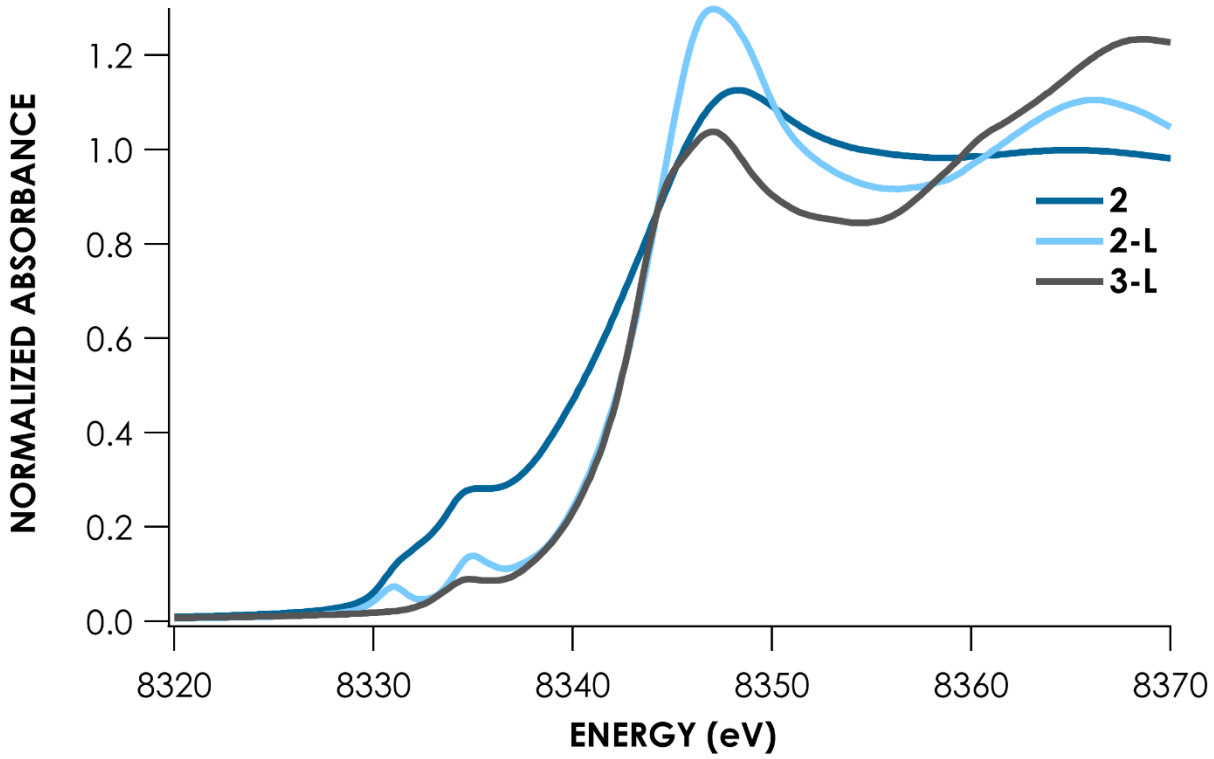

Figure 4.51. XAS experimental spectra of oxidized Ni^{ISO}CN-3 (2), [Ni(CNAr^{Mes2})$_4$]OTf (2-L) and neutral Ni(CNAr^{Mes2})$_4$ (3-L).

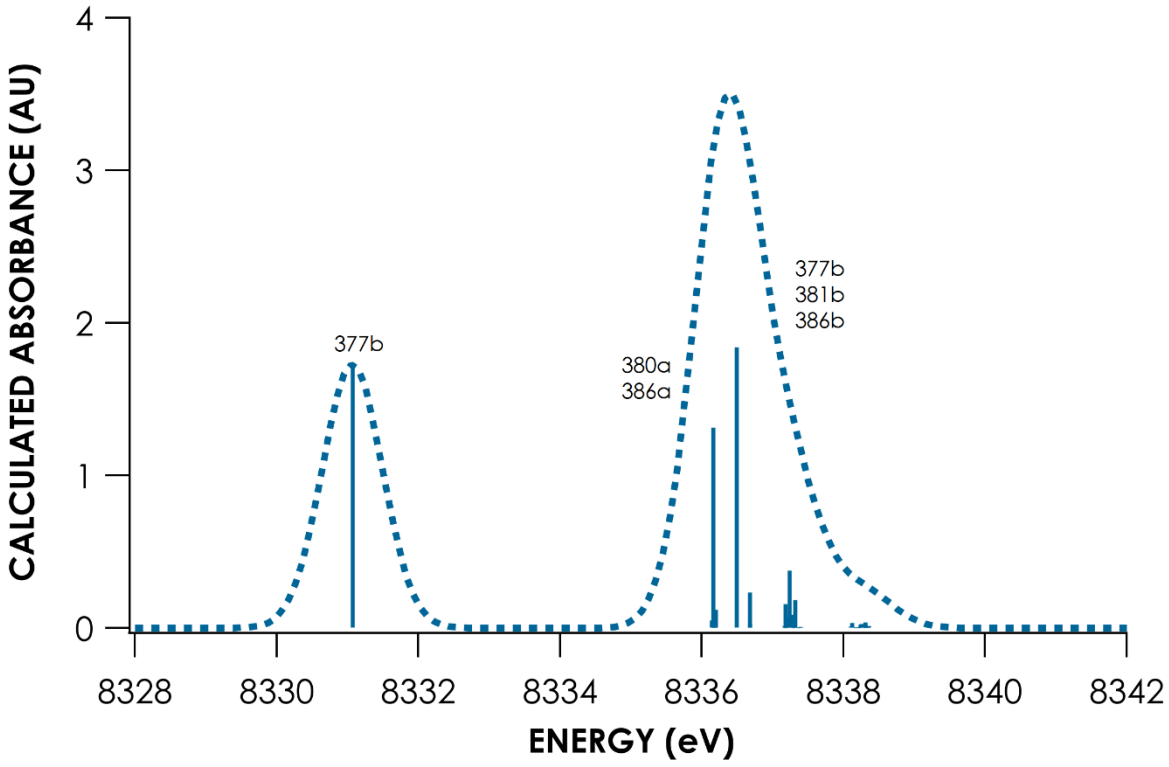

Figure 4.52. Calculated pre-edge features on structure 2-L, with associated orbitals annotated for major transitions.

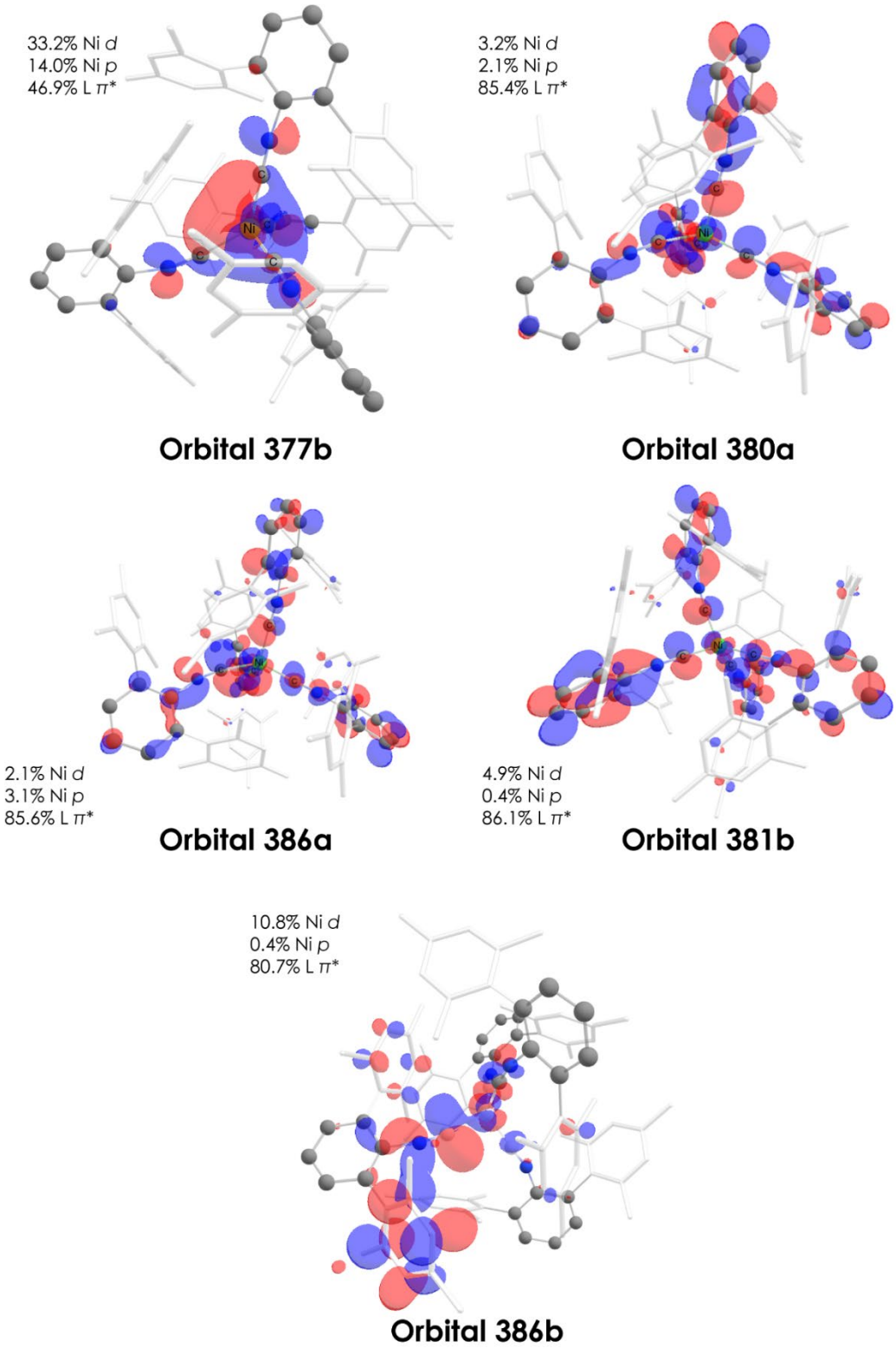

Figure 4.53. Orbitals associated with calculated transition described in Figure 5.52.

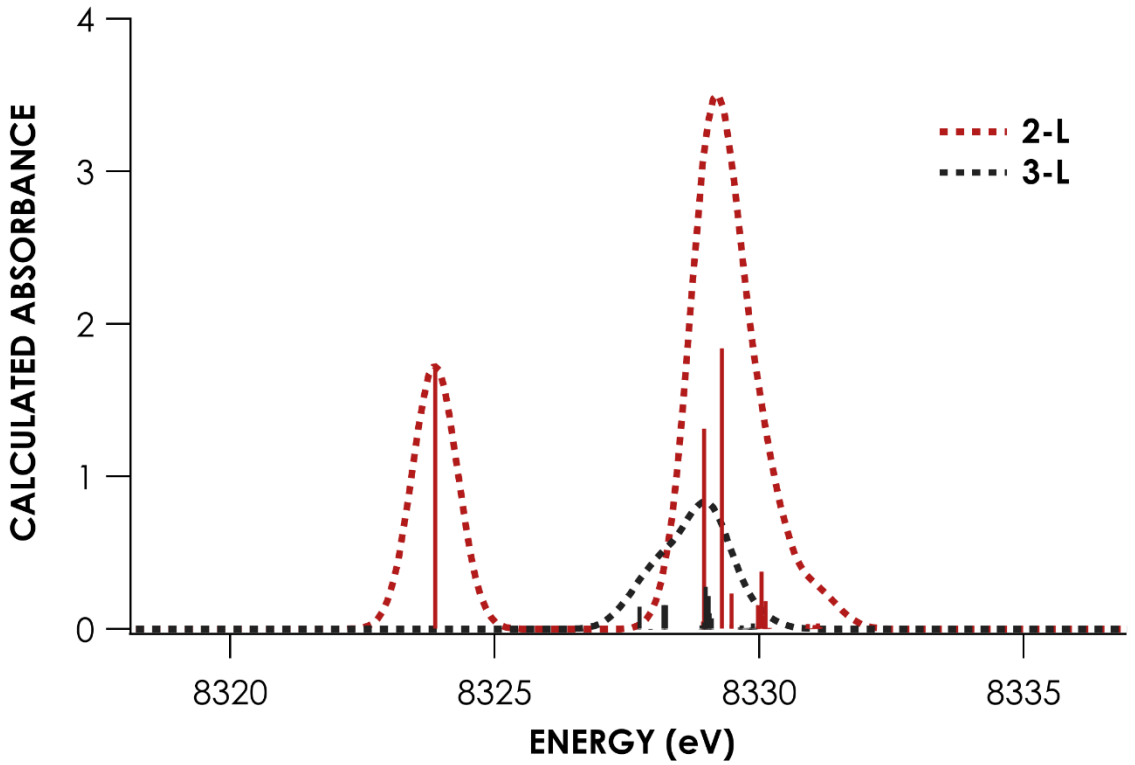

Figure 4.54. Overlay of the calculated Ni K-edge pre-edge of the neutral molecular NiL_4 species (3-L) with the cationic species (2-L).

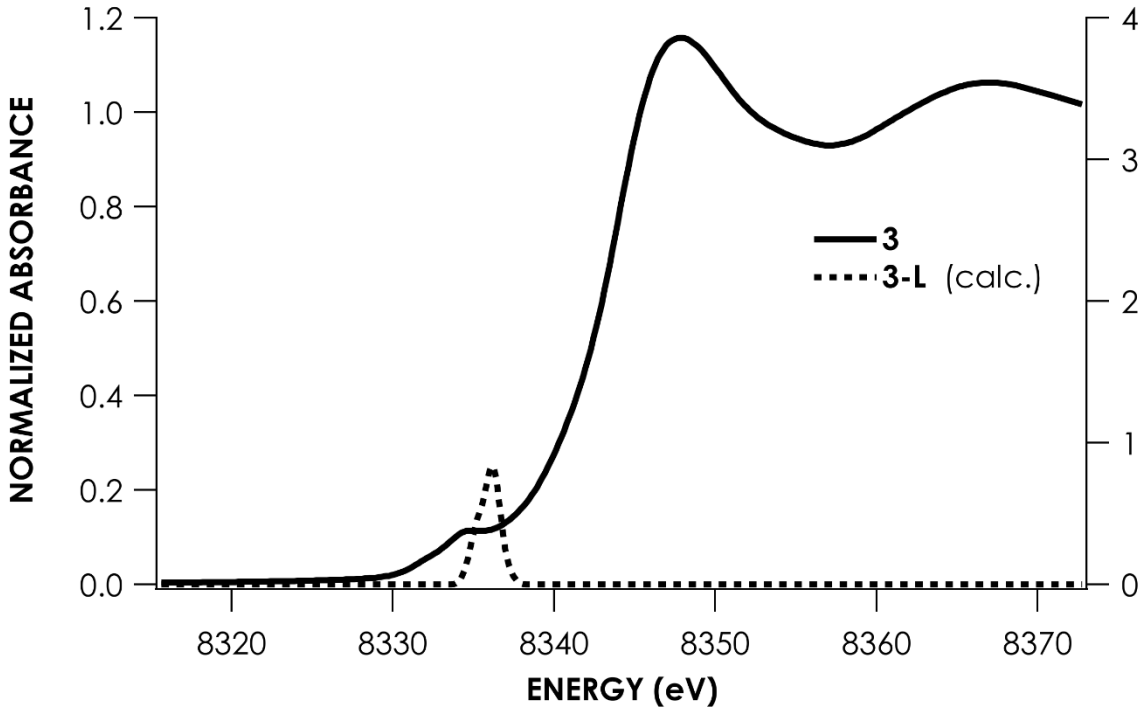

Figure 4.55. Overlay of the calculated pre-edge features of neutral $Ni(CNAr^{Mes2})_4$ (3-L) with the measured Ni K-edge XAS of neutral $Ni^{ISO}CN$-3 (3).

ICP-MS Analysis.

General Considerations.

Inductively Coupled Plasma-Mass Spectrometry measurements were carried out at UCSD's Environmental and Complex Analysis Laboratory (ECAL) on a single Quadrupole Thermo iCAP RQ ICP-MS. Samples of Ni^{ISO}CN-3 was washed three times with dry THF and n-hexanes, dried in vacuo and dissolved in commercially available trace metal HNO_3 (67-69%) from Fisher. The sample was then filtered and diluted to 10-100 ppb of Ni metal in 10mL of a solution containing 1% HNO_3 in S-15 MilliQ water. 4 x 10 mL calibration solutions containing 1ppb, 10 ppb, 100 ppb, 1000 ppb of respectively were prepared using a solution containing 1% HNO_3 in ultrapure MilliQ water. These calibration solutions were prepared with the ICP-MS Complete Standard reagent (3% v/v HNO_3) purchased from Inorganic Ventures containing various metals, including 10 µg/mL Ni, Fe and Co. 50 µL of the commercially available Internal Standard from Inorganic Ventures were added to all calibration solutions in addition to the sample solution prepared. A 10 mL blank solution was also prepared containing 1% HNO_3 in MilliQ water and the internal standard. All sample centrifuge tubes were cleaned beforehand by soaking in 2% HNO_3 (aq) overnight, then rinsed with ultrapure MilliQ water.

Table 4.3. ICP- MS Results for oxidized Ni^{ISO}CN-3.

	^{60}Ni [ppb]	^{57}Fe [ppb]
Mean	1392.782936	-18.09850052
RSD [%]	0.584457605	7.286140306
SD	8.14022579	1.318682141

No ^{57}Fe detected in ICP-MS sample, indicating ferrocene is not occupying the pores and leading to decreased surface area.

Table 4.4. ICP-MS Results for reduced Ni^{ISO}CN-3.

	^{60}Ni [ppb]	^{59}Co [ppb]
Mean	32.22794953	-0.258621642
RSD [%]	1.318131988	1.859611425
SD	0.424806912	0.004809358

No ^{59}Co detected in ICP-MS sample, indicating cobaltocenium triflate is not the cause of decreased surface area upon reduction.

4.5. Acknowledgements.

Chapter 4, in full, is a manuscript in preparation. The dissertation author was the primary investigator and author of this paper. Permission to use data presented in this dissertation was obtained from all co-authors.

4.6. References.

(1) Furukawa, H.; Ko, N.; Go, Y. B.; Aratani, N.; Choi, S. B.; Choi, E.; Yazaydin, A. Ö.; Snurr, R.Q. ; O'Keeffe, M.; Kim, *J. Science* **2010**, *329*, 424–428.

(2) Farha, O. K.; Eryazici, I.; Jeong, N. C.; Hauser, B. G.; Wilmer, C. E.; Sarjeant, A. A.; Snurr, R. Q.; Nguyen, S. T.; Yazaydin, A. Ö.; Hupp, J. T. *J. Am. Chem. Soc.* **2012**, *134*, 15016–15021.

(3) Farha, O. K.; Özgür Yazaydın, A.; Eryazici, I.; Malliakas, C. D.; Hauser, B. G.; Kanatzidis, M. G.; Nguyen, S. T.; Snurr, R. Q.; Hupp, J. T. *Nat. Chem.* **2010**, *2*, 944–948.

(4) Hönicke, I. M.; Senkovska, I.; Bon, V.; Baburin, I. A.; Bönisch, N.; Raschke, S.; Evans, J. D.; Kaskel, S. *Angew. Chemie - Int. Ed.* **2018**, *57*, 13780–13783.

(5) Grünker, R.; Bon, V.; Müller, P.; Stoeck, U.; Krause, S.; Mueller, U.; Senkovska, I.; Kaskel, R. *Chem. Commun*. **2014**, *50*, 3450–3452.

(6) Eddaoudi, M.; Kim, J.; Rosi, N.; Vodak, D.; Wachter, J.; O'Keeffe, M.; Yaghi, O. M. *Science* **2002**, *295*, 469–472.

(7) Bux, H.; Chmelik, C.; Krishna, R.; Caro, J. *J. Memb. Sci.* **2011**, *369*, 284–289.

(8) Zhao, Z.; Ma, X.; Kasik, A.; Li, Z.; Lin, Y. S. *Ind. Eng. Chem. Res.* **2013**, *52*, 1102-1108.

(9) Li, H.; Wang, K.; Sun, Y.; Lollar, C. T.; Li, J.; Zhou, H. C. *Mater. Today* **2018**, *21*, 108–121.

(10) Desai, S. P.; Ye, J.; Islamoglu, T.; Farha, O. K.; Lu, C. C. *Organometallics* **2019**, *38*, 3466–3473.

(11) Ji, P.; Feng, X.; Oliveres, P.; Li, Z.; Murakami, A.; Wang, C.; Lin, W.; *J. Am. Chem. Soc.* **2019** *141*, 14878-14888.

(12) Wang, Z.; Tanabe, K. K.; Cohen, S. *M. Chem. Soc. Rev.* **2009**, *38*, 1315-1329.

(13) Ren, J.; Lan, P. C.; Chen, M.; Zhang, W.; Ma, S. *Organometallics* **2019**, *38*, 3460–3465.

(14) Huxley, M. T.; Young, R. J.; Bloch, W. M.; Champness, N. R.; Sumby, C. J.; Doonan, C. *J. Organometallics* **2019**, *38*, 3412–3418.

(15) Meilikhov, M.; Yusenko, K.; Esken, D.; Turner, S.; Van Tendeloo, G.; Fischer, R. A. *Eur. J. Inorg. Chem.* **2010**, *2010*, 3701–3714.

(16) Thornton, A. W.; Nairn, K. M.; Hill, J. M.; Hill, A. J.; Hill, M. R. *J. Am. Chem. Soc.* **2009**, *131*, 10662–10669.

(17) Hermannsdörfer, J.; Friedrich, M.; Kempe, R. *Chem. - A Eur. J.* **2013**, *19* , 13652–13657.

(18) Oisaki, K.; Li, Q.; Furukawa, H.; Czaja, A. U.; Yaghi, O. M. *J. Am. Chem. Soc.* **2010,** *132*, 9262–9264.

(19) Dincă, M.; Gabbaï, F. P.; Long, J. R. *Organometallics.* **2019**, *38,* 3389–3391.

(20) Dunning, S. G.; Reynolds, J. E.; Walsh, K. M.; Kristek, D. J.; Lynch, V. M.; Kunal, P.; Humphrey, S. M. *Organometallics* **2019**, *38*, 3406–3411.

(21) Dong, Y.; Jv, J. J.; Wu, X. W.; Kan, J. L.; Lin, T.; Dong, Y. Bin. *Chem. Commun.* **2019**, *55*, 14414–14417.

(22) Agnew, D. W.; DiMucci, I. M.; Arroyave, A.; Gembicky, M.; Moore, C. E.; MacMillan, S. N.; Rheingold, A. L.; Lancaster, K. M.; Figueroa, J. S. *J. Am. Chem. Soc*. **2017**, *139*, 17257–17260.

(23) Balto, K.P.; Gembicky, M.; Rheingold, A. L.; Figueroa, J. S. *Inorg. Chem.* **2021** *60,* 12545-12554.

(24) Arroyave, A.; Gembicky, M.; Rheingold, A. L.; Figueroa, J. S. *Inorg. Chem.* **2020**, *59*, 11868–11878.

(25) *Fox, B. J.; Sun, Q. Y.; DiPasquale, A.G.; Fox, A. R.; Rheingold, A. L.; Figueroa, J. S. Inorg. Chem.* **2008***, 47, 9010-9020.*

(26) Otsuka, S.; Nakamura A.; Tatsuno, Y. *J. Am. Chem. Soc*. **1969** 91, 6994-6999.

(27) Mokhtarzadeh, C.; Chan, C.; Moore, C. E.; Rheingold, A. L.; Figueroa, J. S.; *J. Am. Chem. Soc.* **2019,** *141*, 15003-15007.

(28) *Fox, B. J.; Millard, M. D.; DiPasquale, A. G.; Arnold L. Rheingold, A. L.; Figueroa, J. S. Angew. Chem. Int. Ed.* **2009***, 48, 3473-3477.*

(29) Yang, L.; Powell, D. R.; Houser, R. P. *Dalt. Trans*. **2007**, *9,* 955–964.

(30) Johnson, H. W.; Daughhetee, P. H. *J. Org. Chem.* **1964**, 29, 246–247.

(31) Baldwin, J. E.; Bottaro, J. C.; Riordan, P. D.; Derome, A. E. *Chem. Commun*.**1982**, *16*, 942-943.

(32) Bihani, M.; Bora, P. P.; Nachtegaal, M.; Jasinski, J. B.; Plummer, S.; Gallou, F.; Handa, S. *ACS Catal.* **2019**, *9*, 7520–7526.

(33) Clement, N. D.; Cavell, K. J.; Jones, C.; Elsevier, C. J. *Angew. Chemie Int. Ed.* **2004**, *43*, 1277–1279.

(34) Handa, S.; Slack, E. D.; Lipshutz, B. H. *Angew. Chemie Int. Ed.* **2015**, *54*, 11994–11998.

(35) Metin, Ö.; Özkar, S. *Int. J. Hydrogen Energy* **2011**, *36*, 1424–1432.

(36) Oh, K.; Mériadec, C.; Lassalle-Kaiser, B.; Dorcet, V.; Fabre, B.; Ababou-Girard, S.; Joanny, L.; Gouttefangeas, F.; Loget, G. *Energy Environ. Sci.* **2018**, *11*, 2590–2599.

(37) Ittel, S. D.; Berke, H.; Dietrich, H.; Lambrecht, J.; Härter, P.; Opitz, J.; Springer, W. Complexes of Nickel(0) John Wiley & Sons, Ltd, 2007.

(38) Zhang, Z.; Awaga, K. *MRS Bull.* **2016**, *41*, 883–889.

(39) Chen, Q.; Sun, J.; Li, P.; Hod, I.; Moghadam, P. Z.; Kean, Z. S.; Snurr, R. Q.; Hupp, J. T.; Farha, O. K.; Stoddart, J. F. *J. Am. Chem. Soc.* **2016**, *138*, 14242–14245.

(40) Mohammad-Pour, G. S.; Hatfield, K. O.; Fairchild, D. C.; Hernandez-Burgos, K.; Rodríguez-López, J.; Uribe-Romo, F. J. *J. Am. Chem. Soc.* **2019**, *141,* 19978–19982.

(41) Cheon, Y. E.; Suh, M. P. *Angew. Chemie - Int. Ed.* **2009**, *48*, 2899–2903.

(42) Xu, Y.; Yin, X. B.; He, X. W.; Zhang, Y. K. *Biosens. Bioelectron.* **2015**, *68*, 197–203.

(43) Moon, H. R.; Kim, J. H.; Suh, M. P. *Angew. Chemie - Int. Ed*. **2005**, *44*, 1261–1265.

(44) Barybin, M. V.; Meyers, J. J.; Neal, B. M. Renaissance of Isocyanoarenes as Ligands in Low-Valent Organometallics. In Isocyanide Chemistry; Wiley-VCH Verlag GmbH & Co. KGaA, 2012.

(45) Sarapu, A. C.; Fenske, R. F. *Inorg. Chem.* **1975**, *14*, 247–253.

(46) Drance, M. J.; Mokhtarzadeh, C. C.; Melaimi, M.; Agnew, D. W.; Moore, C. E.; Rheingold, A. L.; Figueroa, J. S. *Angew. Chemie Int. Ed.* **2018**, *57*, 13057–13061.

(47) Tamaru, Y. Modern Organonickel Chemistry; Wiley, 2005.

(48) Xi, L.S.; Skorupskii, G.; Dinca, M. *Chem. Rev.* **2020**, 120, 16, 8536–8580.

(49) Saouma, C. T.; Tsou, C. C.; Richard, S.; Ameloot, R.; Vermoortele, F.; Smolders, S.; Bueken, B.; DiPasquale, A. G.; Kaminsky, W.; Valdez, C. N.; De Vos, D. E.; Mayer, J. M. *Chem. Sci.,* **2019**, 10, 1322.

(50) Mancuso, J. L.; Fabrizio, K.; Brozek, C.K.; Hendon, C.H. *Chem. Sci.,* **2021**, 12, 11779.

(51) Tulchinsky, Y.; Hendon, C. H.; Lomachenko, K. A.; Borfecchia, E.; Melot, B. C.; Hudson, M. R.; Tarver, J. D.; Korzynski,´ M. D.; Stubbs, A. W.; Kagan, J. J.; Lamberti, C.; Brown, C. M.; Dinca,˘M. *J. Am. Chem. Soc.* **2017**, 139, 5992−5997.

(52) Fox, B. J.; Millard, M. D.; DiPasquale, A. G.; Rheingold, A. L.; Figueroa, J. S. *Angew. Chem. Int. Ed. Engl.* 2009, *48*, 3473–3477.

(53) Yamamoto, Y.; Takahata, H.; Takei, F. *J. Organomet. Chem.* **1997**, *545–546*, 369-379.

(54) Tanabiki, M.; Tsuchiya, K.; Kumanomido, Y.; Matsubara, K.; Motoyama, Y.; Nagashima H.*; Organometallics* **2004**, *23*, 3976–3981.

(55) *McNeece, A. J.; Mokhtarzadeh, C. C.; Moore, C. E.; Rheingold, A. L.; Figueroa, J. S. J. Coord. Chem.* **2016***, 69, 2059-2068.*

(56) Stoll S., Schweiger. A.; *J. Magn. Reson.* **2006**, *178*, 42-55.

(57) Saraeva, V. V.; Kraikivskiia, P. B.; Zelinskiia, S. N.; Vil'msa , A. I.; Matveeva, D. A.; Yundaa, A. Yu.; Fedoninaa, A. A.; Lammertsmab K. *Russ. J. Coord. Chem.* **2006**, *32*, 397–401.

(58) Soshnikov, I. E.; Semikolenova, N.V.; Bryliakov, K.P.; Antonov, A.A.; Sun, W.; Talsi, E.P. *J. Organomet. Chem.* **2019**, *880*, 267-271.

(59) Margulieux, G. W.; Weidemann, N.; Lacy, D. C.; Moore, C. E.; Rheingold, A. L.; Figueroa, J. S. *J. Am. Chem. Soc.* **2010***, 132*, 5033-5035.

(60) Mulgundmath, V. P.; Tezel, F. H.; Saatcioglu, T.; Golden, T. C. *Can. J. Chem. Eng.* **2012**, *90*, 730–738.

(61) Kochi, J.K.; *Science.* **1967**, *155,* 3761.

(62) Hamada, S.; Funasako, Y.; Mochida, T.; Kuwahara, D.; Yoza, K. *J. Organomet. Chem*. **2012**, 713, 35-41.

(63) Iwasaki, T.; Kambe, N., *Topics in Current Chemistry* **2016**, *374*, 66.

(64) Lucas, E. L.; Jarvo, E. R., *Nat. Rev. Chem.* **2017**, *1*, 0065.

(65) Pangborn, A. B.; Giardello, M. A.; Grubbs, R. H.; Rosen, R. K.; Timmers, F. J. *Organometallics* **1996**, *15*, 1518–1520.

(66) Armarego, W. L. F.; Li, C.; Chai, L.; York, N.; Purification of Laboratory Chemicals Seventh Edition; Elsevier 2013.

(67) Stoll,S.; Schweiger, A. *J. Magn. Reson.* ***2006****, 178*, 42-55.

(68) Sheldrick, G. M. *Acta Crystallogr., Sect. A: Found. Crystallogr.* **2008**, *64*, 112–122.

(69) Sheldrick, G., Crystal structure refinement with SHELXL. A Acta Crystallogr. Sec. C 2015, 71 (1), 3-8.

(70) Dolomanov, O. V.; Bourhis, L. J.; Gildea, R. J.; Howard, J. A. K.; Puschmann, H. *J. Appl. Crystallogr.* **2009**, *42,* 339–341.

(71) A.L. Spek*, J. Appl. Cryst.* **2003**, 36, 7-11.

(72) Ravel, B.; Newville, M. ATHENA, ARTEMIS, HEPHAESTUS: Data Analysis for X-Ray Absorption Spectroscopy Using IFEFFIT. *J Synchrotron Rad* **2005**, *12* (4), 537–541. https://doi.org/10.1107/S0909049505012719.

(73) Neese, F. Software Update: The ORCA Program System, Version 4.0. *WIREs Comput Mol Sci* **2018**, *8* (1), e1327. https://doi.org/10.1002/wcms.1327.

(74) Barone, V.; Cossi, M. Quantum Calculation of Molecular Energies and Energy Gradients in Solution by a Conductor Solvent Model. *J. Phys. Chem. A* **1998**, *102* (11), 1995–2001. https://doi.org/10.1021/jp9716997.

Chapter 5 Curvature Selective Nanocrystal Surface Ligation Using Sterically Encumbered Metal-Coordinating Ligands.

5.1. Introduction.

Inorganic nanocrystals are bound by crystalline facets that present highly undercoordinated surface sites at the corners and edges of the nanocrystal. Chemical modification of these surface sites can have a profound effect on the distinctive properties of a nanocrystal, including its optoelectronic function,[1] catalytic reactivity,[2] and ability to self-assemble.[3-5] Ligands that feature anchoring groups with favorable nanocrystal binding energies typically result in indiscriminate binding to all available surface sites, as exemplified by thiolated molecules where strong metal-sulfur bonds facilitate the formation of a molecular monolayer.[6] Nanocrystal surface ligation is further complicated by the consideration of solvent interactions, which can significantly alter both the thermodynamics and dynamics of surface-ligand interactions and, thus, interfere with binding site selectivity. As a result, very few strategies are successful in anchoring ligands with precision to specific nanocrystal features.

In contrast, ligand-design strategies – often implemented through synthetic organic chemistry – are routinely employed to control the coordination number, geometry and overall electronic structure of molecular transition-metal complexes.[7-9] As a general principle, ligands featuring encumbering steric profiles can enforce and stabilize low coordination numbers for transition metal centers. A particularly effective scaffold used in the synthesis and stabilization of reactive, low-coordinate metal centers is the m-terphenyl ligand class,[10-14] in which two sterically-encumbering arene groups flank a metal-binding group on a central aryl ring. This specific molecular topology places considerable steric demands in the direction pointing toward the metal primary coordination sphere and, as a result, can promote low coordination numbers in molecular complexes through *ligand-ligand* steric interference. (Fig. 5.1A) We reasoned that the *m*-terphenyl

backbone, when attached to the surface of a nanocrystal, could serve to differentiate undercoordinated binding sites via *surface-ligand* steric interference. For surfaces with high nanocurvature such as nanocrystal corners and edges, binding should result in low steric interference from neighboring surface atoms in the vicinity of ligand anchoring. Surfaces with low nanocurvature, such as nanocrystal facets, more closely approximate a planar surface where the steric pressure from neighboring surface atoms becomes more significant and potentially great enough to inhibit ligand binding. (Figure 5.1B,C)

5.2. Results and Discussion.

Here, we demonstrate that *m*-terphenyl-based anchoring groups can discriminately bind to colloidal Au nanocrystals of varying diameter (Fig. 5.1D) based on this concept of curvature-dependent steric pressure. We specifically employ encumbering *m*-terphenyl isocyanide ligands,[12-14] which provide a three-atom linker between a surface Au binding atom and the central aryl ring of the *m*-terphenyl backbone. This allows the organic substituents of the *m*-terphenyl isocyanide ligands to be synthetically tuned to either maximize or relieve steric pressures across a wide degree of nanocurvature. Nanocurvature-selective ligand binding is confirmed through nanocrystal extraction experiments and atomistic modelling, employing quantum mechanical (QM) electronic-structure calculations, and molecular dynamics (MD) simulations. We conclusively demonstrate how the steric differentiation of ligand anchoring groups can be engineered, paving the way for a new class of nanocrystal ligand chemistries for improved nanocrystal synthesis and nanomanufacturing.

Ligand exchange reactions using pseudospherical Au nanocrystals (AuNSs) and the *m*-terphenyl isocyanide ligand $CNAr^{Mes2}$ (Ar^{Mes2} = 2,6-(2,4,6-$Me_3C_6H_2$)$_2C_6H_3$)[12, 14] indicate that ligand binding is selective for nanocurvature and is consistent with ligand-surface steric interference as the dominant mechanism for selectivity. We first carried out ligand exchange of 10

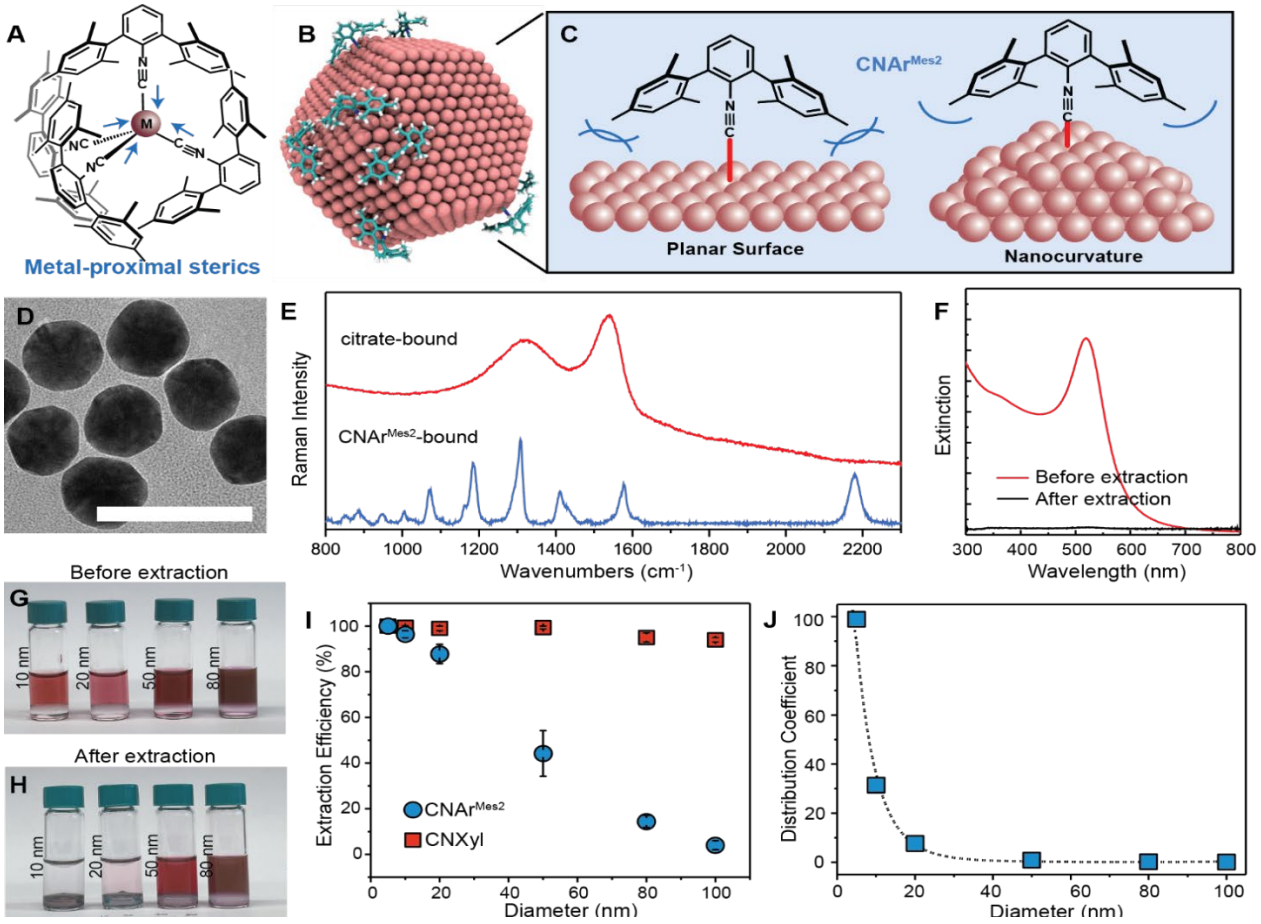

Figure 5.1. Nanocurvature selectivity enabled by surface-ligand sterics. Schematic of A) a tetrahedral coordination complex formed by m-terphenyl isocyanide ligation to a metal center. B) Computational model of m-terphenyl isocyanide ligands binding to an Au nanocrystal, where Au(100) and Au(111) surface facets generate planar, edge, and corner sites. C) Schematic of m-terphenyl isocyanide selectivity for high-curvature surface binding sites due to the molecular topology of the ligand anchoring group. D) TEM image of Au nanocrystals showing regions of high and low curvature. Scale bar = 100 nm. E) Surface-enhanced Raman spectra for the AuNSs before and after ligand exchange with $CNAr^{Mes2}$ indicating complete displacement of citrate. F) UV-Vis extinction spectra of the aqueous raffinate before and after ligand exchange showing near complete transfer of the AuNSs into the solvent phase. G,H) Photo showing the ligand exchange and solvent transfer of AuNSs of varying diameters, where the top phase is the aqueous raffinate and the bottom phase is chloroform. I) Plot comparing the extraction efficiencies for $CNAr^{Mes2}$ and for the unencumbered CNXyl ligand. J) Plot of the equilibrium distribution coefficient for extraction of the AuNSs into chloroform by $CNAr^{Mes2}$ binding.

nm citrate-stabilized AuNSs using the $CNAr^{Mes2}$ ligand to facilitate nanocrystal transfer from an

aqueous phase to chloroform. Importantly, unencumbered alkyl and aryl isocyanides have been well established to bind to Au surfaces and nanoparticles,[15-21] and can exhibit surface binding energies competitive with thiols.[18, 21] Successful $CNAr^{Mes2}$ complexation to the AuNSs was accompanied by a corresponding color change of the aqueous phase (raffinate) from red to colorless. Upon transfer into chloroform, the $CNAr^{Mes2}$-bound AuNSs aggregated to form a grey precipitate that was readily extracted via solvent evaporation or centrifugation. Transmission electron microscopy (TEM) images of the extracted precipitate showed well-separated AuNSs with no changes in the core nanocrystal sizes (Figure). Binding of $CNAr^{Mes2}$ was characterized by zeta potential measurements (Figure 5.9**)** and surface-enhanced Raman spectroscopy (Figure 5.1E), which shows complete displacement of citrate by $CNAr^{Mes2}$ and a sharp peak at 2166 cm^{-1} corresponding to the n(CN) stretching vibrations of Au-bound isocyanide.[12, 13, 15, 16, 19, 22, 23] Complete transfer of the AuNSs into chloroform was confirmed by extinction measurements (Figure 5.1F) of the raffinate, where the optical density (*OD*) goes to near-zero after ligand exchange.

The metal-proximal steric properties of $CNAr^{Mes2}$ are expected to result in less favorable binding energies for larger AuNSs, for which surface curvature is lower and steric interactions begin to dominate surface-ligand interactions. Because AuNSs possess pseudospherical morphologies with irregular faceting, the surface selectivity of $CNAr^{Mes2}$ is expected to depend not only on AuNS size, but the relative number of edge and corner sites to facet sites available for ligand adsorption, with larger AuNSs possessing a lower ratio for edge and corner sites than smaller AuNSs. To confirm this, we measured the phase transfer efficiencies for AuNSs with varying diameters, which is dictated by the ligand exchange equilibrium between citrate and $CNAr^{Mes2}$ at the water/chloroform interface. (Fig. 5.1G – I) The equilibrium distribution

coefficient (*D*) exhibits an asymptotic decay with AuNS diameter consistent with inhibition of isocyanide binding to low-curvature Au surface sites. (Figure 5.1J) In contrast, phase transfer using 2,6-dimethylphenyl isocyanide (CNXyl; Xyl = 2,6-$Me_2C_6H_3$), which possesses an

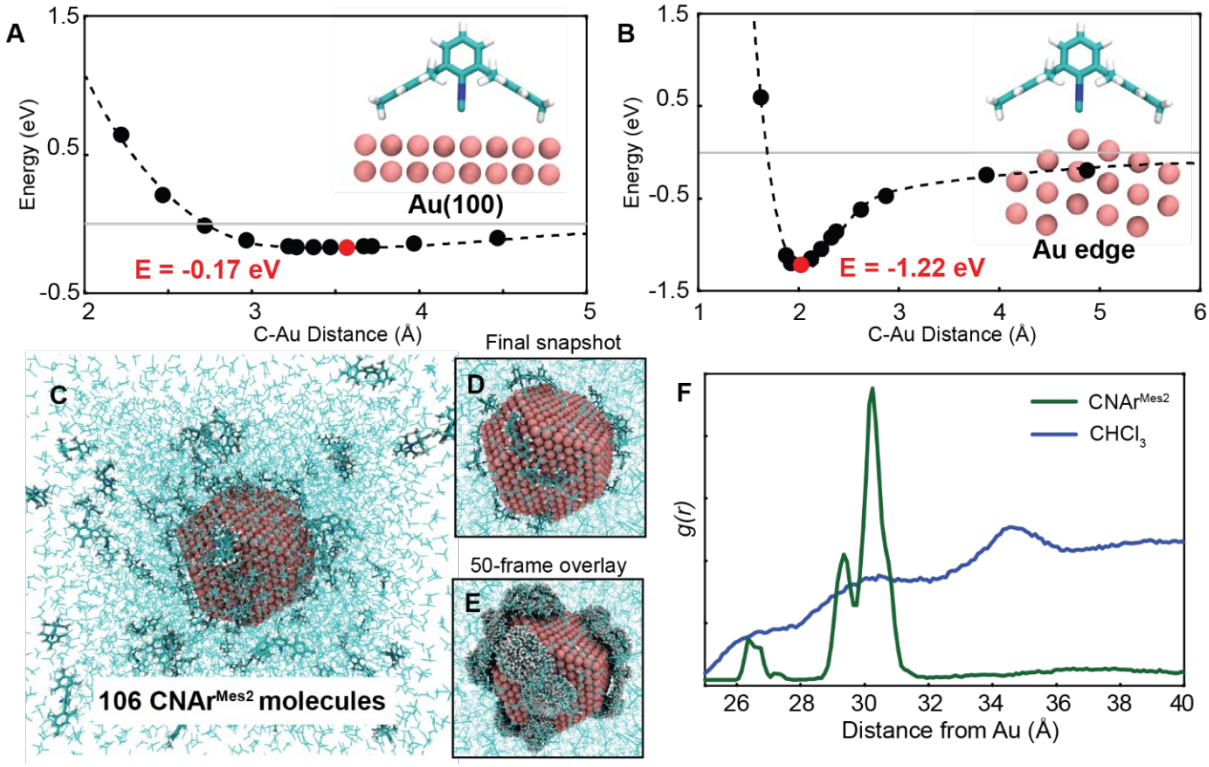

Figure 5.2. $CNAr^{Mes2}$ binding to Au nanocrystals. QM/DFT interaction energy plots of binding to (A) a flat Au(001) surface and (B) an Au edge site. The data (solid circles) are connected with a dashed line to guide the eye. The most favorable distance and energy are indicated in red. (Inset) atomistic model of the lowest energy configuration. (**C**) Final snapshot from the equilibrium MD simulation at 298K in $CHCl_3$. (**D**) Zoom-in of the Au nanocrystal with bound $CNAr^{Mes2}$ and (**E**) an overlay of the last 50 frames of the MD trajectory, illustrating edge-specific binding and diffusion. (F) Radial distribution function of $CNAr^{Mes2}$ (green) and $CHCl_3$ (blue) taken with the AuNS center of mass as the origin. AuNS facets are located at 21-24 Å away and AuNS edges are located at 26-27 Å away. The peaks for $CNAr^{Mes2}$ at 29-30 Å correspond to adsorbed $CNAr^{Mes2}$ at edge sites, consistent with our DFT results. The peaks for $CNAr^{Mes2}$ at <28 Å correspond to diffusive motion of $CNAr^{Mes2}$ on the AuNS surface, which results in some $CNAr^{Mes2}$ mass crossing over to the flat surface, as seen in (E).

unencumbered isocyanide head group, exhibits a high exchange efficiency for all AuNS sizes, consistent with indiscriminate Au surface binding.

To pinpoint how the molecular topology of $CNAr^{Mes2}$ leads to this curvature selectivity, we performed QM calculations employing density functional theory at the PBE/GGA level with

dispersion corrections. A planar Au surface was modeled as either perfect Au(100) or Au(111) slabs, while a curved surface was modeled as an edge site at the intersection of the slabs. The binding energy was taken as the lowest energy for the $CNAr^{Mes2}$ approach to each surface. We found that in vacuum, $CNAr^{Mes2}$ exhibited a larger binding energy for edge sites (E = -1.22 eV) than for the Au(100) surface (E = -0.17 eV). (Figure 5.2A, B) Closer examination shows that the steric profile of the flanking arenes on $CNAr^{Mes2}$ allows for a closer approach of the isocyanide group at the Au edge sites, with a C-Au distance of 2.0 Å. In contrast, steric interactions between these arenes and neighboring Au atoms on the Au(100) slab enforce a longer C-Au bond distance of 3.6 Å and thus weaker metal-ligand binding.

The presence of solvent modulates isocyanide ligand binding to the Au surface, as expected, an effect we quantify by means of extensive MD simulations. Here, we modeled a 5-nm diameter AuNS as a chamfered cube bound by Au(100) and Au(111) facets with edge lengths of 1.7 nm (Figure 5.12). Snapshots of the system solvated in $CHCl_3$ and structural analysis by means of radial distribution functions showed that $CNAr^{Mes2}$ selectively binds to the edges of the Au nanocrystal (Figure 5.2C- F). Our simulations also reveal that while the binding of $CNAr^{Mes2}$ to the solvated nanocrystal is strong (with no observed $CNAr^{Mes2}$ desorption), the molecules selectively diffuse along the edge sites. (Figure 5.2E) Along with accelerated MD simulations (Figure 5.15), these computational results confirm a predicted 150-fold increased $CNAr^{Mes2}$ binding to the edge sites.

Microscopic insights into the ligand exchange process were also quantified, using accelerated MD simulations of $CNAr^{Mes2}$ bound to AuNSs in water. These simulations revealed that $CNAr^{Mes2}$ binding free energies in water are reduced on the edge sites, in sharp contrast to the energetics in chloroform. We also calculated an unfavorable free energy of $CNAr^{Mes2}$ transfer from

chloroform to water based on the solvation free energies of the solvated ligand (Table 5.2). Thus, the solvent-philic forces between $CNAr^{Mes2}$ and chloroform are the major thermodynamic driving force for the complete transfer of $CNAr^{Mes2}$-bound AuNSs into the chloroform phase and our calculations support our hypothesis that it is unlikely that that any $CNAr^{Mes2}$-bound AuNSs remain in the aqueous phase.

Based on these results, we used $CNAr^{Mes2}$ to carry out liquid-liquid extraction (LLE) of AuNSs based on the observed selectivity for nanocurvature (Figure 5.3). Classical LLE is often used to separate molecular transition-metal complexes based on their relative solubilities, and involves transfer/partitioning of the desired isolate from liquid phases of differing polarity.[24] In our LLE method, AuNSs serve as the isolate and are partitioned between immiscible aqueous and chloroform phases using $CNAr^{Mes2}$ to facilitate selective solvent transfer based on nanocrystal size. We approximated an equilibrium binding threshold for $CNAr^{Mes2}$ at D=1, corresponding to 55 nm AuNSs based on the decay fit in Figure 5.1J. Nanocrystal size-focusing and size-separation experiments were designed with this size threshold in mind. For size-focusing, we used a starting feedstock of citrate-capped AuNSs with an average particle diameter of 56 ± 6 nm, as obtained by

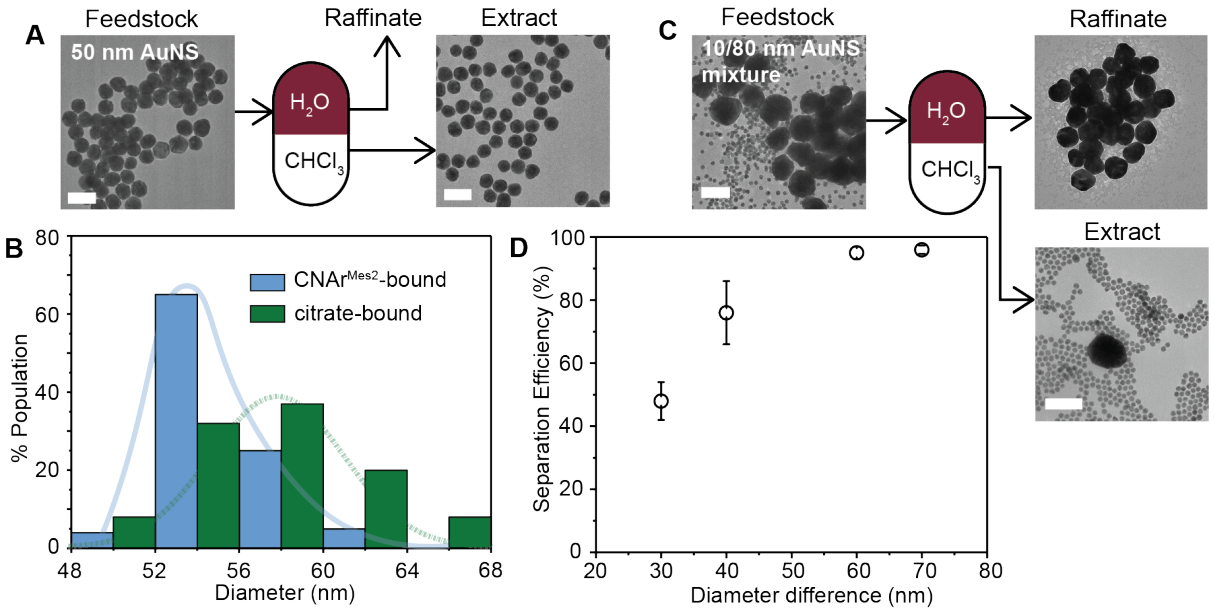

Figure 5.3. Size-selective LLE of AuNS dispersions. (A) TEM images of a AuNS dispersion before and after size-focusing. The final AuNS population is extracted from the chloroform phase. (B) Size distributions for an AuNS dispersion before (citrate-bound) and after ($CNAr^{Mes2}$-bound) size-focusing. Tick labels denote a bin size of 4 nm. (C) TEM images of AuNSs in the raffinate and extract after LLE was carried out on a binary feedstock of 10 nm and 80 nm citrate-coated AuNSs. (D) Plot of separation efficiencies for LLE experiments carried out with the following binary feedstocks: 10/80, 20/80, 10/50, and 20/50 nm AuNS mixtures. Scale bars = 100 nm.

TEM image analysis (Figure 5.3A). After LLE, the extracted AuNSs show a significant reduction in the average diameter and distribution at 54 ± 2 nm. In addition, no AuNSs larger than 64 nm are observed in the chloroform extract, demonstrating the ability to selectively retain larger AuNSs in the aqueous raffinate (Figure 5.3B). For size-separation, we used an aqueous feedstock containing a mixture of two AuNS populations with different average sizes. For a 10/80 nm feedstock, TEM analysis showed that 10 nm particles were the predominant population in the chloroform extract, while 80 nm AuNSs were the exclusive population of the corresponding raffinate (Figure 5.3C). OD measurements indicate that 96% of the 80 nm AuNSs remain in the raffinate, which we take as the overall separation efficiency for the 10/80 nm feedstock. We measured the separation efficiency of three additional binary feedstocks (20/80, 10/50, and 20/50

nm), with our results indicating a separation resolution of ~40 nm for our LLE method (Figure 5.3D).

We computationally screened two additional m-terphenyl isocyanide ligands that were expected to exhibit increased ligand-surface steric pressures: $CNAr^{Dipp2}$ (Ar^{Dipp2}= 2,6-(2,6-(*i*-Pr)$_2C_6H_3$)$_2C_6H_3$); *i*-Pr = *iso*-propyl)[13] and $CNAr^{Tripp2}$ (Ar^{Tripp2}= 2,6-(2,4,6-(*i*-Pr)$_3C_6H_2$)$_2C_6H_3$)).[14] The results for CNXyl, for which we experimentally observed uninhibited AuNS binding across all AuNS sizes, are also shown for comparison. The calculated QM interaction energies indicate that both $CNAr^{Dipp2}$ and $CNAr^{Tripp2}$ ligands exhibit weaker Au edge-site binding than $CNAr^{Mes2}$, with binding energies of -0.89 eV and -0.58 eV, respectively (Figure 5.4A-C). $CNAr^{Dipp2}$, which lacks a substituent in the *para*-position of the flanking arene ring, exhibited stronger binding to facet sites than $CNAr^{Mes2}$, with E = -0.29 eV. The more encumbering and functionalized arene groups in $CNAr^{Dipp2}$ and $CNAr^{Tripp2}$ also increased the oleophilicity of the ligands.

To better correlate these calculated free energies with experimental ligand exchange and LLE outcomes, we considered four computational descriptors for optimizing nanocurvature selectivity binding and solvent extraction of AuNSs using various ligand anchoring chemistries (Table 5.3). First is the site-binding ratio (*SBR*) calculated as the difference between the DFT interaction energies at the edge sites and a flat surface. This term describes a ligand's ability to selectively bind to high-curvature surface sites. Second is the nanocrystal edge-binding factor (*EBF*), calculated as the difference between the DFT interaction energy, corrected for zero-point

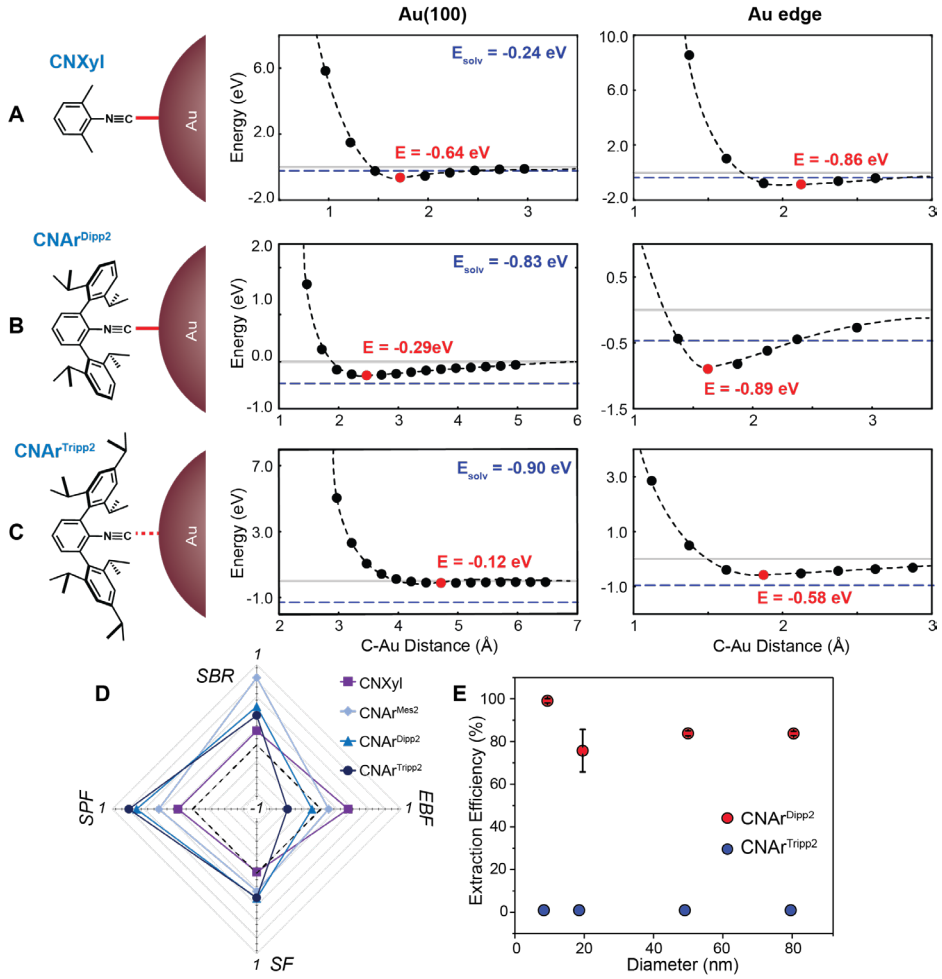

Figure 5.4. Surface-ligand steric pressure by design. Schematics of AuNS binding and QM/DFT interaction energy plots of binding for (**A**) CNXyl, (**B**) $CNAr^{Dipp2}$ and (**C**) $CNAr^{Tripp2}$, which possess organic substituents with varying degrees of bulkiness. For interaction energy plots, the data (solid circles) are connected with a dashed line to guide the eye. The most favorable distance and energy indicated in red, and solvation energies are indicated by the dashed blue line. (**D**) Spider plot showing site-binding ratio (SBR), edge-binding factor (EBF), solubility factor (SF), and solvent partition factor (SPF) values for $CNAr^{Mes2}$ and the ligands in (**A**-**C**). Normalized values range from -1 to 1, with the black dashed line indicating a value of 0. (**E**) Experimental extraction efficiencies for $CNAr^{Dipp2}$ and $CNAr^{Tripp2}$ for AuNS with varying diameters. Error bars for $CNAr^{Tripp2}$ are not shown because they are smaller than the size of the data point.

energy and differential entropy of binding effects, at an edge site and the ligand solvatiergy of the corresponding amorphous solid. This term is a thermodynamic factor related artition factor (*SPF*) calculated as the difference in solvation energy of the free ligand in chloroform and water. This last term is related to the efficiency of the LLE process. Figure 5.4D plots these parameters for the

m-terphenyl isocyanide ligands studied here, where we adopted the convention of normalized functions ranging from -1 (unfavorable) to 1 (favorable), with 0 representing the threshold.

For $CNAr^{Dipp2}$, we calculated a reduced site-binding ratio of $SBR \approx 0.6$ (compared to 1.0 for $CNAr^{Mes2}$) and an unfavorable EBF of -0.1 (compared to 0.1 for $CNAr^{Mes2}$), that would preclude binding to smaller AuNSs dominated by edge and corner sites. On the other hand, the higher *SPF* is predicted to increase the affinity of $CNAr^{Dipp2}$ for chloroform. LLE experiments using $CNAr^{Dipp2}$ were consistent with our predictions, exhibiting relatively high extraction efficiencies (Figure 5.4E) that were particularly pronounced for larger AuNSs. In fact, we found that in this larger size regime, $CNAr^{Dipp2}$ outperformed $CNAr^{Mes2}$ in facilitating AuNS LLE. The effects of steric encumbrance were even more pronounced with $CNAr^{Tripp2}$, where the large, negative edge-binding factor (EBF=-0.5) predicted unfavorable binding to nanocrystal surface sites (even regions of high curvature). Indeed, we measured extraction efficiencies of <10%, even for the smallest 10 nm AuNSs and Raman measurements indicated limited-to-no binding. Across the four isocyanide ligands studied in our experiments, tuning the steric profiles of the flanking arenes of the *m*-terphenyl group provides only moderate differentiation of ligation via *SPF* and *SF*, with all ligands providing sufficient solubility for nanocrystal post-processing.

5.3. Conclusion.

Combined, our experimental and computational results demonstrate that the steric profile of *m*-terphenyl isocyanides can enable nanocurvature-dependent binding on Au nanocrystal surfaces. We demonstrate that it is the molecular topology of the ligand anchoring group — rather than the ligand coronas — that is responsible for selective isocyanide ligation to edge and corner sites. Articulation of the ligand design principles developed in this work can now be expanded to a vast library of ligands that have already been studied for molecular metal coordination complexes. Importantly, we also find that for colloidal nanocrystals, solvent plays a critical role in

not only dictating whether this steric differentiation occurs during the ligand exchange process, but also in determining the dynamics of ligand diffusion, molecular desorption, and solvent extraction after ligand exchange has occurred. Molecular topology of nanocrystal ligands must be co-designed for surface site selectivity *and* solubility. That solvent is capable of fine-tuning ligand-surface interactions perhaps explains why precise nanocrystal surface modification is so difficult to achieve in practice, given that it is only recently that computational approaches have been accurate and efficient enough to obtain microscopic insights into binding, thereby predicting the outcomes of these many-body, complex systems.

5.4. Experimental Section.

Chemicals and Materials

Sodium citrate (≥99%), sodium borohydride ($NaBH_4$, ≥98.0%), gold(III) chloride trihydrate ($HAuCl_4 \cdot 3H_2O$, ≥99.9%), hydroxylamine hydrochloride ($NH_2OH \cdot HCl$, 98%) and Xylyl isocyanide (CNXyl; Xyl = 2,6-$Me_2C_6H_3$; 98%) were purchased from Sigma-Aldrich and used as received. Water used in experiments was obtained from a Millipore water purification system with a resistivity of 18.2 MΩ cm. The *m*-terphenyl isocyanide ligands $CNAr^{Mes2}$ (Ar^{Mes2} = 2,6-(2,4,6-$Me_3C_6H_2)_2C_6H_3$) (*25*), $CNAr^{Dipp2}$ (Ar^{Dipp2}= 2,6-(2,6-(*i*-Pr)$_2C_6H_3)_2C_6H_3$); *i*-Pr = *iso*-propyl) (*26*), and $CNAr^{Tripp2}$ (Ar^{Tripp2}= 2,6-(2,4,6-(*i*-Pr)$_3C_6H_2)_2C_6H_3$) (*27*), were prepared as previously described.

Synthesis of Citrate-Capped Gold Nanospheres (AuNSs)

Citrate-AuNSs with a diameter of 5 ± 0.7 nm were purchased from *nanoComposix Inc.* of San Diego, California.

Citrate-AuNSs 10 nm in diameter were synthesized according to the method of Bastús *et al*.(*28*) An aqueous solution of sodium citrate (150 mL, 2.2 mM) was refluxed under vigorous stirring in a 250 mL three-necked round-bottomed flask. The flask was equipped with a condenser

to prevent solvent evaporation. An aqueous solution containing $HAuCl_4 \cdot 3H_2O$ (1 mL, 25 mM) was injected into the sodium citrate solution and heating was continued for an additional 20 min. The resulting colloidal solution of AuNSs were used directly for further experiments and TEM imaging. The synthesized 10 nm citrate-AuNSs had a measured diameter of 11.5 ± 1 nm based on TEM images (**Figure 5.5**).

Citrate-AuNSs of 20 nm in diameter were synthesized in a modified Turkevich method.(*29*) An aqueous solution containing $HAuCl_4 \cdot 3H_2O$ (5 mg, 0.015 mmol, 0.3 mM) was refluxed under vigorous stirring. A aqueous solution containing sodium citrate (5 mL, 0.23 mmol, 46.5 mM) was injected into the boiling solution. The solution was heated for an additional 30 min and cooled to room temperature before further use. The resulting colloidal solution of AuNSs were used directly for further experiments and TEM imaging. The synthesized 20 nm citrate-AuNSs had a measured diameter of 22 ± 2 nm based on TEM images (**Figure 5.5**).

The 20 nm AuNSs were used as-synthesized as seed particles to synthesize AuNSs of 50 nm in diameter. An aqueous solution of the seed particles (20 nm AuNPs, 3.0 mL) and $NH_2OH \cdot HCl$ (200 μL, 0.2 M) were added to 50 mL water in a 100 mL round-bottom flask. $HAuCl_4 \cdot 3H_2O$ (3.0 mL of 0.1 wt% solution in H_2O) was added dropwise to the solution under vigorous stirring and allowed to react for 30 min at room temperature. A gradual color change from light to dark red was observed. The 50 nm citrate-AuNS had a measured diameter of 56 ± 6 nm measured based on TEM images (**Figure 5.5**).

The AuNSs of 80 nm and 100 nm diameter were synthesized by the same seeded-growth method as the 50 nm particles. For AuNSs of 80 nm diameter, 2.0 mL seed solution was used, whereas 1.0 mL of seed solution was used to prepare AuNSs of 100 nm diameter. The resulting colloidal solution of AuNSs were used directly for further experiments and TEM imaging. The 80

nm citrate-AuNS had diameter of 80 ± 7 nm and 100 nm nanospheres had diameter of 105 ± 10 nm as measured from TEM images (**Fig. 6.5**).

All gold dispersion concentrations were adjusted to maintain the same overall molar concentration of surface atoms, which is estimated to be approximately 10^{16} atoms/mL. Using UV-Vis spectroscopy, optical density measurements were performed to calculate the amount of surface gold atoms per mL (**Figure 5.8, Figure 5.15**). Assuming a AuNS has perfect spherical shape in the fcc habit, the surface atom number per AuNS (N) was calculated by:

$$N = \frac{\frac{4}{3}\pi[(\frac{D}{2})^3-(\frac{D}{2}-D_{Au})^3]}{V_{Au}} \cdot n_{fcc} \ , \qquad \text{Eq. (1)}$$

where D is the average diameter of the AuNSs, D_{Au} is the average diameter of gold atom, V_{Au} is the volume of one Au unit cell and n_{fcc} is the number of Au atoms per one unit cell. The concentration of the AuNSs in water (c) was calculated by:

$$c = \frac{OD}{\varepsilon} \ , \qquad \text{Eq. (2)}$$

$$\varepsilon = \frac{N_A}{\ln(10)} \cdot C_{ext} \ , \qquad \text{Eq. (3)}$$

where OD is the optical density measured by UV-Vis spectroscopy, ε is the molar extinction coefficient, N_A is Avogadro's constant, C_{ext} is the extinction cross-section.

Liquid-Liquid Extraction (LLE) of AuNS with Isocyanide Ligands

An aqueous dispersion of AuNSs (3.0 mL, 10^{16} atoms/mL) was layered onto a chloroform solution containing isocyanide (1.0 mL, 15 mM) in a glass vial. After layering the aqueous AuNSs dispersion onto the organic solution, the two-phase system was mixed vigorously by hand for 30 min. The aqueous layer was decanted, and the red-colored organic phase was washed with chloroform to remove excess free ligand in solution via centrifugation. The concentration of isocyanide was optimized by evaluating the extraction efficiency (**Figure 5.6.**) of 20 nm AuNSs

functionalized with $CNAr^{Mes2}$ and found to be 10 mM (**Figure 5.15**). To guarantee successful ligand exchange, the concentration of isocyanide used in the LLE process was increased to 15 mM.

Nanocrystal Characterization

Transmission electron microscopy (TEM) images were collected using a JEOL 1200 EX II TEM with an operation voltage of 80 kV. Samples were prepared by drop-casting AuNP solutions on carbon-only copper grids and allowed to settle overnight in closed vials (Fig. S2). UV–visible absorption measurements were performed on Cary 50/60 UV-Vis spectrophotometer. Raman measurements were performed on Renishaw micro-Raman spectrometer (Renishaw Invia) coupled with a Leica microscope with 50× objective (Leica N-plan) in the range of 800−2400 cm^{-1}. A wavelength of 532 nm was used as an excitation source generated by 50 mW Ar-Ion LASER. Zeta potential values were measured using a Malvern NANO-ZS90 Zetasizer.

Calculating the Change of Citrate-AuNSs Optical Density

The extraction efficiency for AuNSs with the isocyanide ligands is calculated based on the following equation:

$$Extraction\ efficiency = (1 - \frac{OD_{Raffinate}}{OD_{feedstock}}) \cdot 100\%, \qquad \text{Eq. (4)}$$

where $OD_{raffinate}$ *and* $OD_{feedstock}$ are the optical density of citrate-AuNSs in water before and after the LLE measured by UV-Vis spectroscopy

Calculation of Size Separation Efficiency of $CNAr^{Mes2}$

The separation efficiency for a mixture of two different sized AuNSs is calculated based on the number of larger sized AuNSs in water before and after LLE using the following equation:

$$Separation\ power = (1 - \frac{C_{Raffinate}}{C_{feedstock}}) \cdot 100\%\ , \qquad \text{Eq. (5)}$$

where $C_{feedstock}$ is the concentration of the larger sized AuNS in the mixture before LLE and $C_{raffinate}$ is the concentration of larger sized AuNSs remaining in the aqueous phase after LLE. These concentrations are calculated from the optical density measured by UV-Vis spectroscopy (**Figure 5.11**).

Computational Details.

Both Quantum Mechanics (QM) calculations and Molecular Dynamics (MD) simulations were used to study the binding thermodynamics and kinetics of the various ligands to the Au nanosphere surfaces. QM calculations were performed using the Q-Chem 5.2,(*30*) and Quantum Espresso (QE) (*31, 32*) electronic structure packages to determine the optimized ligand structure and the ligand-gold interaction energies, respectively. The MD simulations were performed with LAMMPS (*33*) simulation engine. In MD, the Au nanoparticles were described using EAM/Fs potential of Ackland et. al. (*34*). Ligands were described using either the GAFF (*35*) or OPLS/AA (*36*) forcefields, except for the critical C≡N bond stretching and the aromatic rings torsions, which were determined from QM to reproduce the CNXyl and $CNAr^{Mes2}$ intra-molecular motion. The $CHCl_3$ solvent was modelled using the Kamath et al. forcefield (*37*), while the SPC/E potential was used for water (*38*).

Parameterization of the ligand C≡N/AuNS Interactions

Au-ligand(s) interaction was optimized by developing a forcefield based on fitting the binding energy curves obtained from QM calculations. The ligand(s) structure was first at the 6-31G/MP2 level using DFT using Q-Chem. Various Au slabs were constructed from the fcc crystal structures and the binding energy of the rigid ligand in QE was calculated with ultrasoft pseudopotentials (*39*), a kinetic energy cutoff of 30 Ry, and a (5,5,1) K-point grid. In each case, a ligand was initially placed far from the Au slab and gradually moved onto the Au slab. The energy vs distance curve for the various ligand(s)|Au configurations were obtained. The associated

binding energy curve was further fitted to Lennard-Jones 12-6 / Morse potentials in determining the ligand(s) atoms | Au atoms interaction parameters, using a nonlinear regression approach.

Description of System used in MD Simulations

A Chamfered cube AuNS with 4033 atoms was constructed containing equal edge lengths of 12 hexagons and 6 squares faces. (**Fig. 5.16**) The system was solvated by inserting the AuNS into a 100 x100 x 100 $Å^3$ box of $CHCl_3$ molecules and removing the solvent molecules within 2 Å of the AuNS. Afterwards, ligands were then distributed randomly in the simulation box and overlapping solvent molecules were removed as necessary. The vacuum systems (**Fig. 5.1B** and **Fig. 5.19**), did not contain $CHCl_3$ solvent and the simulation box was set as 100x100x100 $Å^3$. The composition of the various systems are detailed in **Table 5.4**.

Equilibrium MD Simulations and Vibrational Spectral Analysis

The van der Waals and real space coulomb cutoffs in the MD simulations were 10Å. A cubic spline was applied to the van der Waals to ensure smooth convergence and vanishing energies and forces at the cutoff (inner cutoff distance of 9Å). The reciprocal space coulomb interactions were computed with a particle-particle-particle-mesh solver, with an error tolerance of 10^{-6} (*40*). Each MD simulation was initiated with 500 conjugated gradient steps, followed by gradual heating to 298K using 0.5 ns (500,000 steps with an integration timestep of 1 fs) dynamics in the canonical ensemble (NVT – constant number of particles N, volume V and temperature T) at 298K. A Nose-Hoover thermostat was used with a temperature relaxation window of 100 fs. Afterwards, the system was equilibrated at the correct density by performing dynamics in the iso-baric isothermal (NPT: constant N, pressure P and temperature T) ensemble. The Shinoda et al. (*41*) equations of motion, which incorporates the Martyna et al(*42*) hydrostatic equations and the strain energy formulism of Parrinello and Rahman (*43*) were adopted. The time-reversible

measure-preserving Verlet integrators derived by Tuckerman et al. (*44*) was applied for the time integration. After density equilibration, the system was simulated in the NVT ensemble for at least 5ns of NVT dynamics. Starting with snapshots of each system every 1 ns, additional 40 ps NVT simulation were run, and the velocities and coordinates were saved every 4 fs (10,000 frames in the corresponding trajectory). The vibrational density of states function was calculated, based on Fourier transform of the velocity autocorrelation functions, to analyze the ligand C≡N spectra (**Fig. 5.17)** (*45, 46*).

Radial Distribution Function Analysis

The radial distribution function, g(r), was used to calculate the ligand densities at various distance from the AuNS center of mass. The g(r) can be expressed as:

$$g(r) = \frac{d\left\langle N_{ij}(r)\right\rangle}{\rho_{ij} dV(r)} \qquad \text{Eq. (6)}$$

where *dV(r)* is the volume of the shell being considered $d\langle N_{ij}(r)\rangle$ is the average number of either atom in *dV(r)* within a distance dr of the other atom and r_{ij} is the atomic bulk density factor. In this analysis, the AuNS and each ligand molecule were taken as individual super atoms defined by the respective centers of mass and the closest contact point for each ligand is defined by the radius of the AuNS, ~ 25 Å.

Ligand Solvation Free Energy Calculations

Free Energy Perturbation (FEP), based on the advancements of Zwanzig (*47*), is a statistical approach to compute the free energy difference between two states:

$$\Delta A \text{ (from state1 to state2)} = A \text{ (state2)} - A \text{ (state1)} = -k_B T \ln\left\langle \exp\left(-\frac{U(state2) - U(state1)}{k_B T} \right) \right\rangle \qquad \text{Eq. (7)}$$

where A denotes free energy, $k_B$is the Boltzmann constant, and U is energy.

The solvation energies of the various isocyanide ligands were calculated as the sum of multi-stages free energy changes. Here, a coupling parameter λ ($0 \leq \lambda \leq 1$) is introduced to gradually change the ligand – solvent interaction energy, such that the free energy (*48*) is obtained as:

$$\Delta_0^1 A = \sum_{i=0}^{n-1} \Delta_{\lambda_i}^{\lambda_{i+1}} A = -kT \sum_{i=0}^{n-1} \ln \left\langle \exp\left(-\frac{U(\lambda_{i+1}) - U(\lambda_i)}{kT} \right) \right\rangle_{\lambda_i} \qquad \text{Eq. (8)}$$

In this study, λ = 0.01 was used and the interaction energies were modified in 100 stages (windows) over 100 ps NPT per window. These results are presented in **Table 5.2**.

Free Energy of Isocyanide Binding to Solvated AuNSs

Using accelerated MD simulations, the free energy kinetics of isocyanide ligand binding to AuNS was computed. Metadynamics (*49*) was employed to enhance the sampling and explore regions of the potential energy surfaces characterized by deep local minima. Two types of systems were considered: 1) a Au (100) slab, representative of the larger NPs with large radius of curvatures and 2) an edge site comprising a Au(110) motif on the Au (100) slab, representative of smaller NPs with small radius of curvatures (**Fig. 5.18**). Each system was first solvated and equilibrated according to the procedure above. Afterwards, Metadynamics simulations, where the carbon of the isocyanide group (C≡NR) to the Au surface was chosen as the collective variable (colvar), were performed. Each simulation was biased by depositing Gaussian functions every 0.2 ps with a height of 0.02 kcal/mol and a width of 1.25 Å. The system was evolved for a minimum of 200 ns. Convergence was checked by monitoring colvar distance until it showed ballistic behavior.

Computation of Normalized Descriptors

To straightforwardly compare the binding and solvation energies, DFT interaction energies were corrected for zero-point energy (ZPE) and entropy of binding (TΔS) effects:

$$\Delta G_{DFT-bind} = \Delta E_{DFT-bind} + \Delta ZPE + T\Delta S \qquad \text{Eq. (9)}$$

where the ΔZPE is obtained from vibrational frequency calculations of the isolated and bound isocyanides, and TΔS is taken as difference between the free (ideal gas) and bound isocyanides. Generally, it was found that these corrections account for ~ +0.2 eV for the various structures.

For the various descriptors (X), relative energies (ΔY) were calculated and divided by the norm of the largest value if it exceeds 1:

$$X = \frac{\Delta Y}{\max\left|\Delta Y\right|} \qquad \text{Eq. (10)}$$

The various descriptors thus range from -1 (unfavorable) – +1 (favorable), with a favorable/unfavorable threshold taken as 0:

$$\begin{aligned} SBR &= \Delta G^{flat}_{DFT-bind} - \Delta G^{edge}_{DFT-bind} \\ EBF &= \Delta G^{edge}_{DFT-bind} - \Delta G^{CHCl3}_{solvation} \\ SF &= \Delta G_{cohesive} - \Delta G^{CHCl3}_{solvation} \\ SPF &= \Delta G^{H2O}_{solvation} - \Delta G^{CHCl3}_{solvation} \end{aligned} \qquad \text{Eq. (11)}$$

where SBR is site binding ratio, EBF is edge-binding factor, SF is solubility factor and SPF is solvent partition factor.

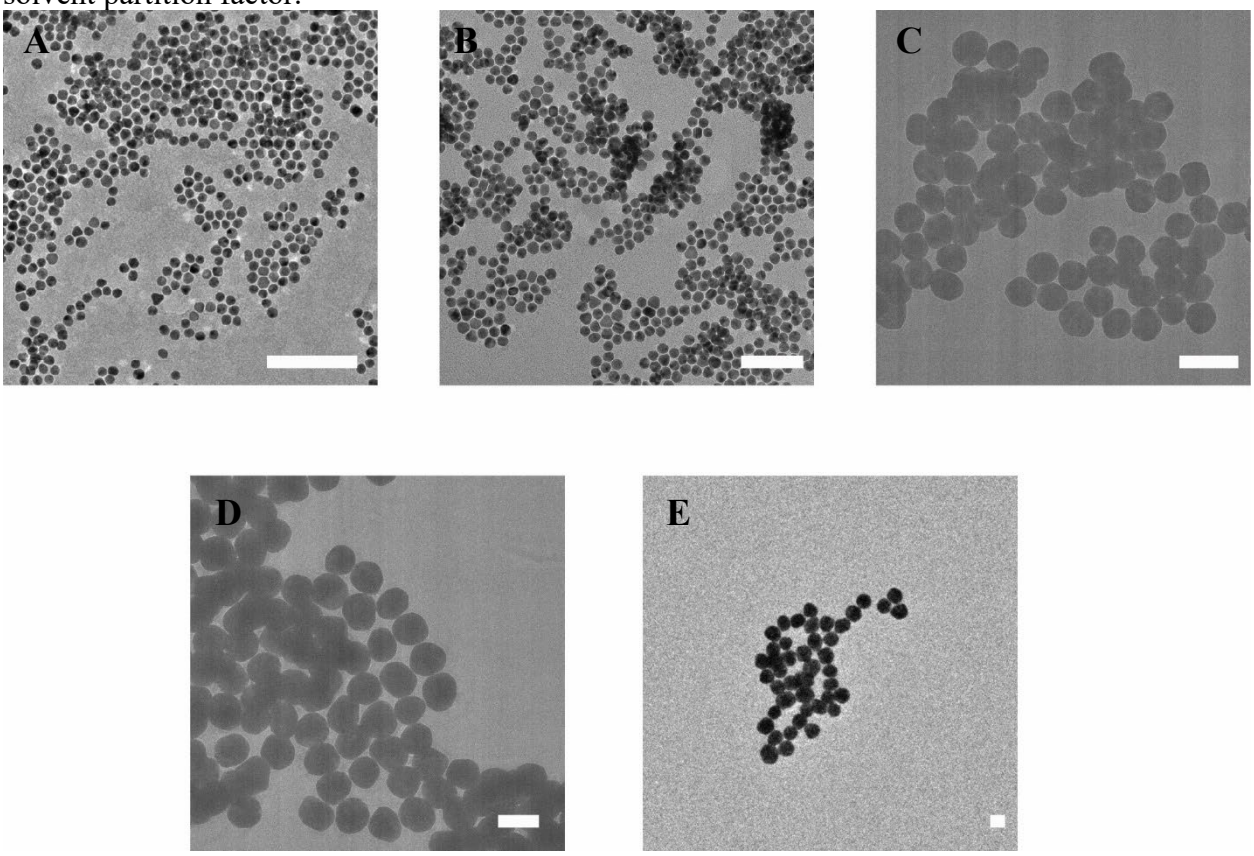

Figure 5.5. TEM images of as synthesized (A) 10 nm, (B) 20 nm (C) 50 nm (D) 80 nm and (E) 100 nm diameter AuNSs before LLE.

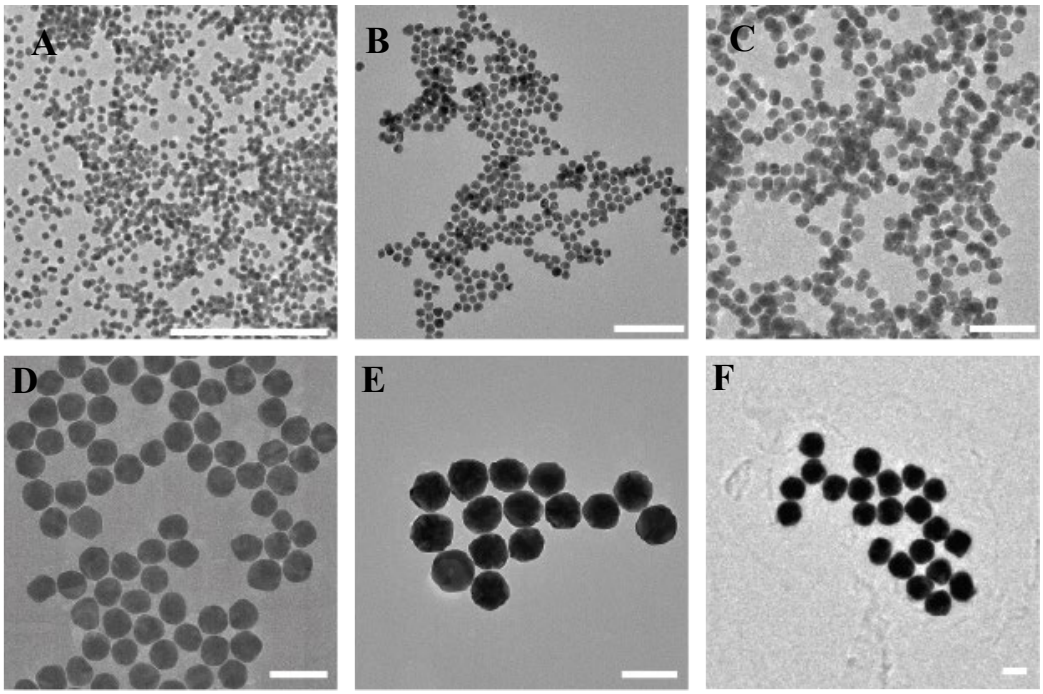

Figure 5.6. TEM images of (A) 5 nm, (B) 10 nm, (C) 20 nm (D) 50 nm (E) 80 nm and (F) 100 nm diameter AuNSs transferred into $CHCl_3$ after LLE with $CNAr^{Mes2}$ (scale bar 100 nm).

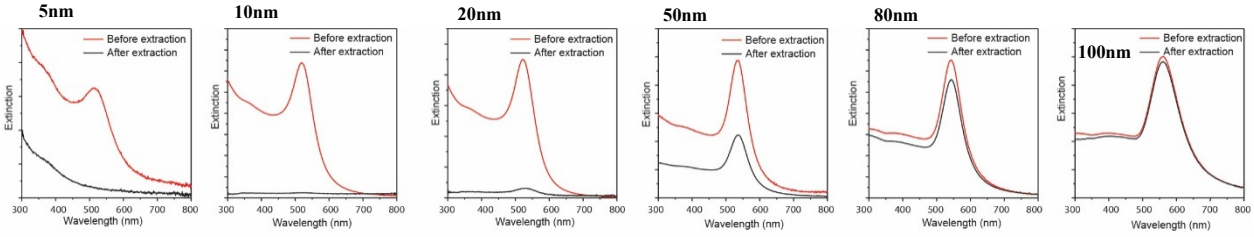

Figure 5.7. UV-Vis spectra used to calculate $CNAr^{Mes2}$–LLE extraction efficiency of (left to right) 5 nm, 10 nm, 20 nm, 50 nm, 80 nm and 100 nm AuNSs. Red spectra represent the aqueous AuNS feedstock prior to introduction of $CNAr^{Mes2}$ in $CHCl_3$. Blue spectra represent the aqueous raffinate after introduction of $CNAr^{Mes2}$ in $CHCl_3$.

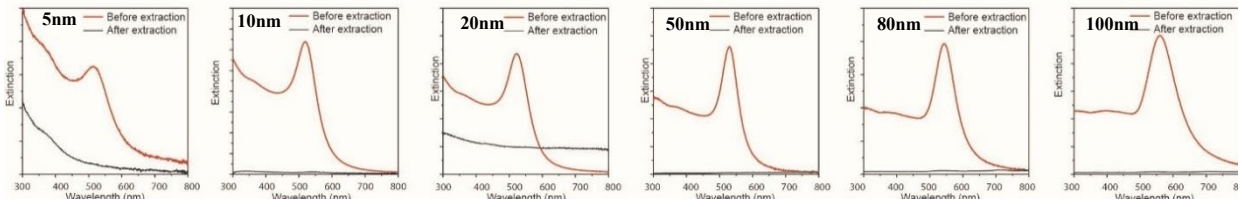

Figure 5.8. UV-Vis spectra used to calculate CNXyl–LLE extraction efficiency of (left to right) 5 nm, 10 nm, 20 nm, 50 nm, 80 nm and 100 nm AuNSs. Red spectra represent the aqueous AuNS feedstock prior to introduction of CNXyl in $CHCl_3$. Blue spectra represent the aqueous raffinate after introduction of CNXyl in $CHCl_3$.

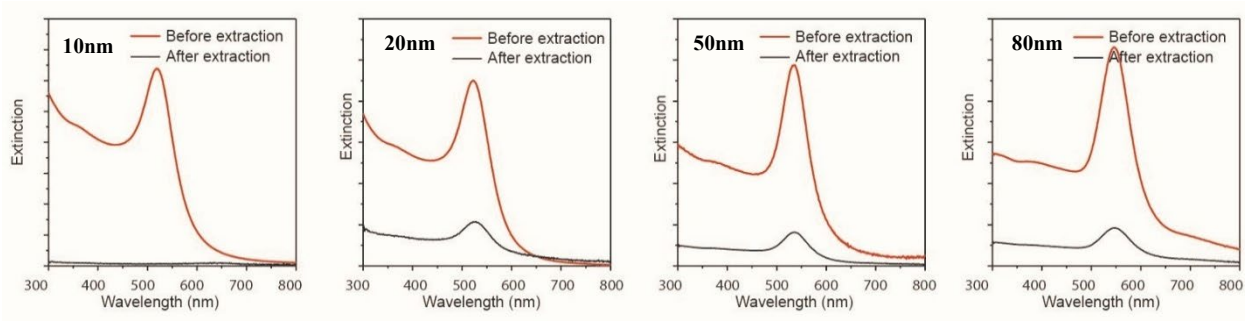

Figure 5.9. UV-Vis spectra used to calculate $CNAr^{Dipp2}$–LLE extraction efficiency of (left to right) 10 nm, 20 nm, 50 nm and 80 nm AuNSs. Red spectra represent the aqueous AuNS feedstock prior to introduction of $CNAr^{Dipp2}$ in $CHCl_3$. Blue spectra represent the aqueous raffinate after introduction of $CNAr^{Dipp2}$ in $CHCl_3$.

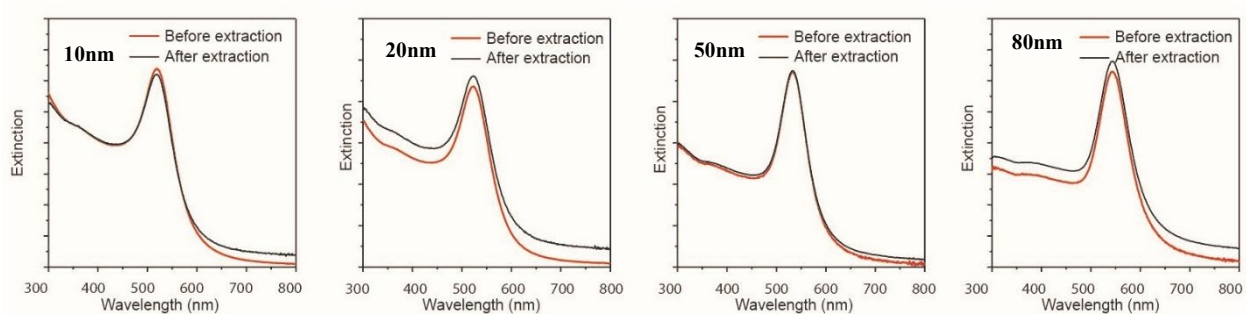

Figure 5.10. UV-Vis spectra used to calculate $CNAr^{Tripp2}$–LLE extraction efficiency of (left to right) 10 nm, 20 nm, 50 nm and 80 nm AuNSs. Red spectra represent the aqueous AuNS feedstock prior to introduction of $CNAr^{Tripp2}$ in $CHCl_3$. Blue spectra represent the aqueous raffinate after introduction of $CNAr^{Tripp2}$ in $CHCl_3$.

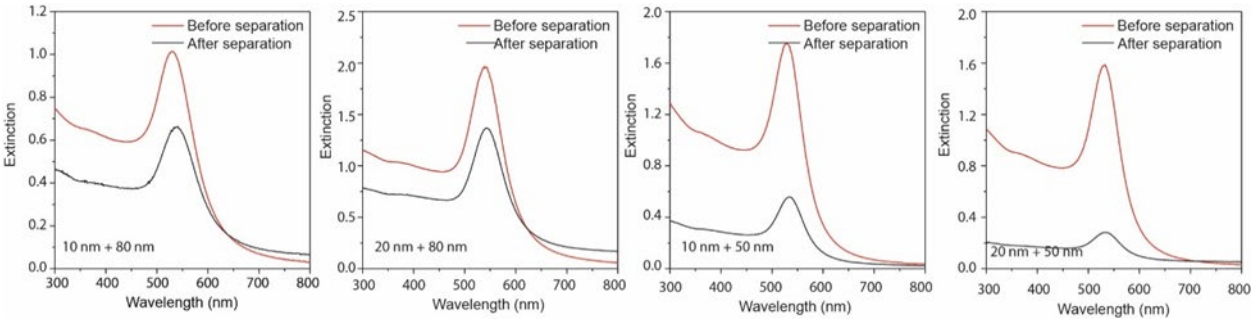

Figure 5.11. UV-Vis spectra of AuNS mixtures prior to (red) and after (blue) introduction of $CNAr^{Mes2}$ in $CHCl_3$. (left to right): 10 nm and 80 nm AuNS mixture; 20 nm and 80 nm AuNS mixture; 10 nm and 50 nm AuNS mixture; 20 nm and 50 nm AuNS mixture.

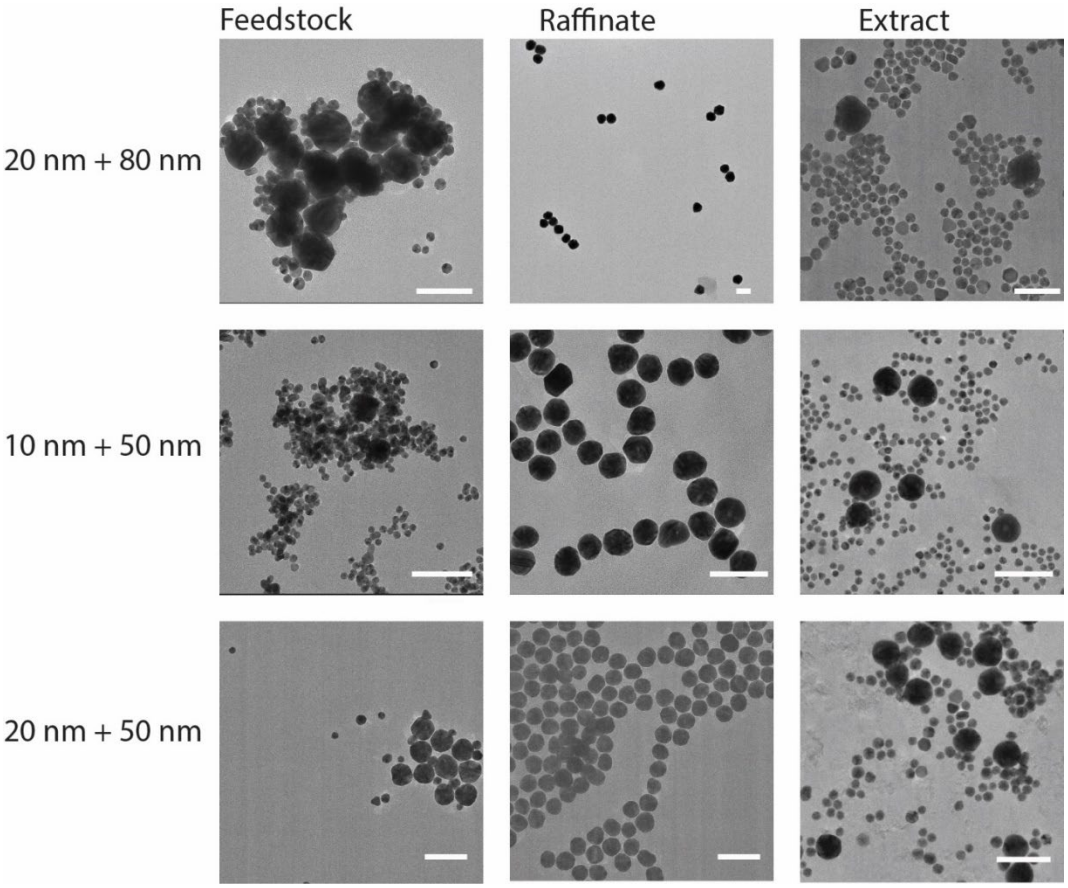

Figure 5.12. TEM images of AuNSs mixtures before (feedstock) and after (raffinate, extract) LLE with $CNAr^{Mes2}$.

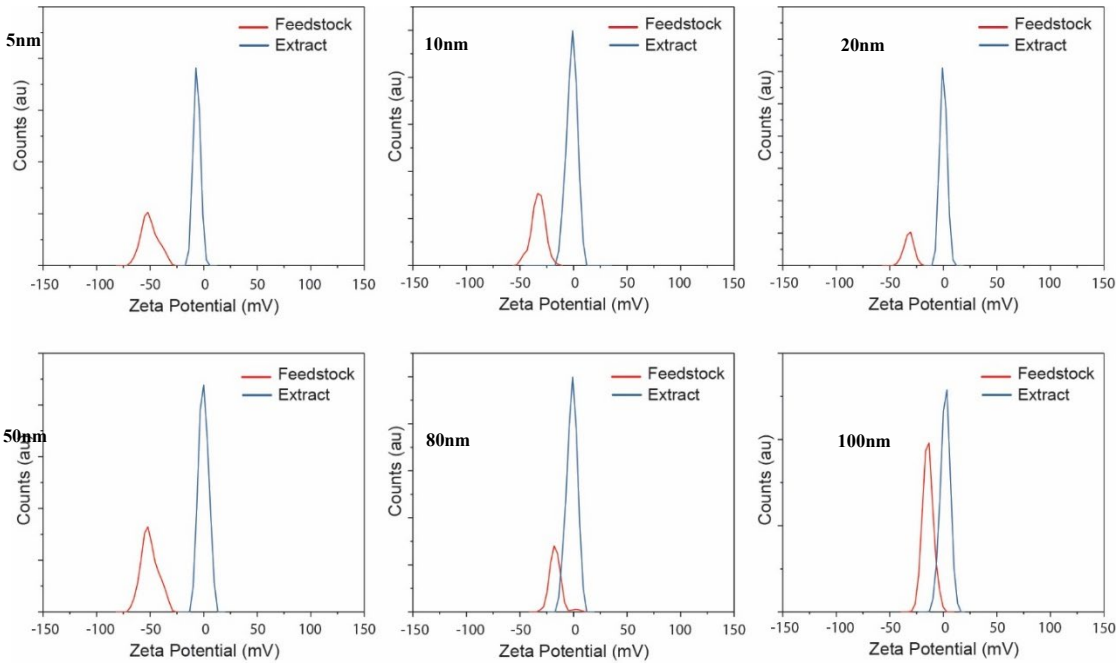

Figure 5.13. Zeta potential plots of various sized AuNSs before (red) and after LLE (blue) with $CNAr^{Mes2}$.

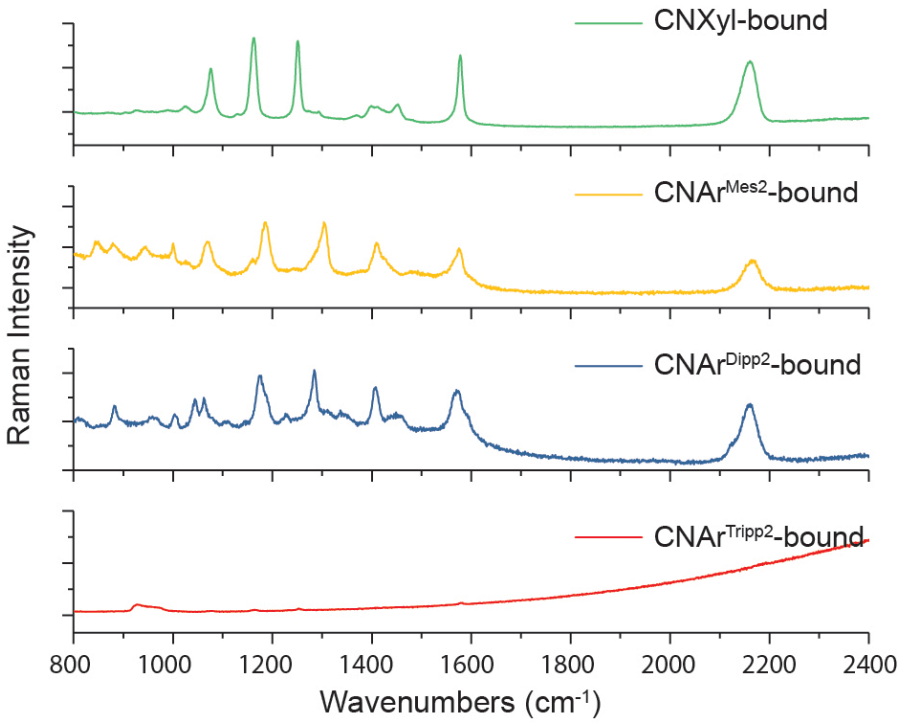

Figure 5.14. SERS spectra of 10 nm AuNSs upon binding of isocyanide ligands. Binding of isocyanide ligands CNXyl, $CNAr^{Mes2}$, and $CNAr^{Dipp2}$ to AuNSs is indicated by the v (CN) band at ~2165 cm^{-1}. A v(CN) band is not observed for $CNAr^{Tripp2}$, thereby suggesting it does not readily bind to AuNSs, including ones with high curvature.

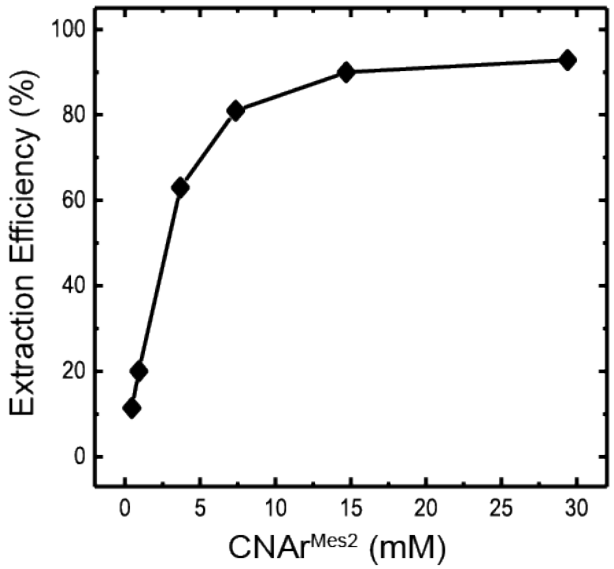

Figure 5.15. Optimization of $CNAr^{Mes2}$ concentration used in LLE of 20 nm diameter AuNSs, where the x-axis is the concentration of $CNAr^{Mes2}$ in $CHCl_3$ and the y-axis is extraction efficiency calculated based on the change of optical density (**Fig. 5.9**). Optimal $CNAr^{Mes2}$ concentration was found to be 10 mM.

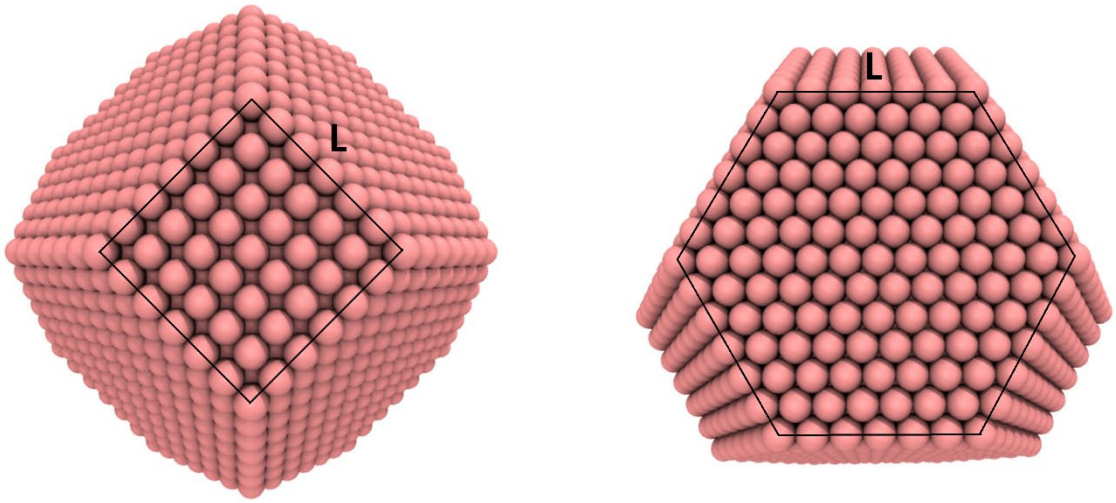

Figure 5.16. Initial AuNS structure used in MD simulations. The diameter is ~5 nm and edge length, L, is ~1.7 nm. The distances from the AuNS center of mass to the Au(001) surfaces, the Au(111) surfaces, the Au(001/111) edges, the Au(111/111) edges, and the corners of Au(001/111/111) facets, are 24.5 Å, 21.5 Å, 26 Å, 26 Å, 27 Å, respectively.

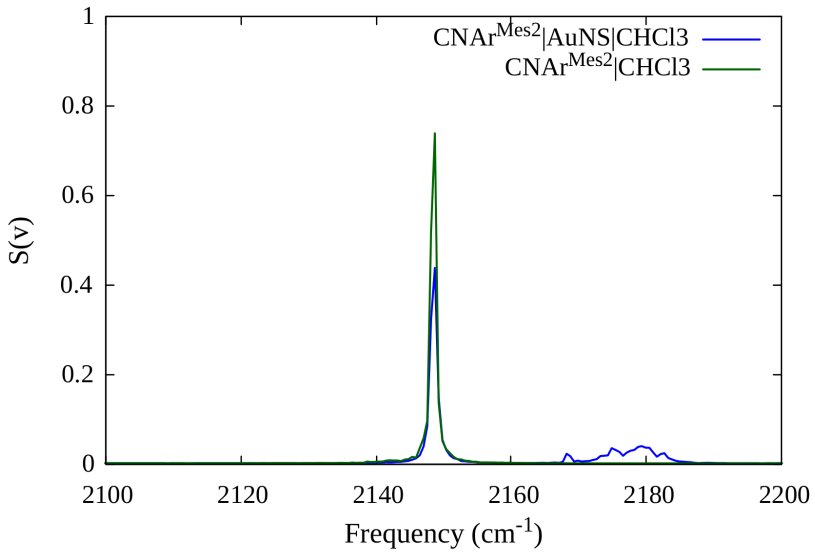

Figure 5.17. Simulated C≡N vibrational spectrum of $CNAr^{Mes2}$ as a free molecule in $CHCl_3$ (green) and as a bound-molecule to the AuNSs surface (blue). A blueshift of ~ 30 cm^{-1} is observed upon binding, in good agreement with both experimental FTIR and surface-enhanced Raman spectroscopic (SERS) data.

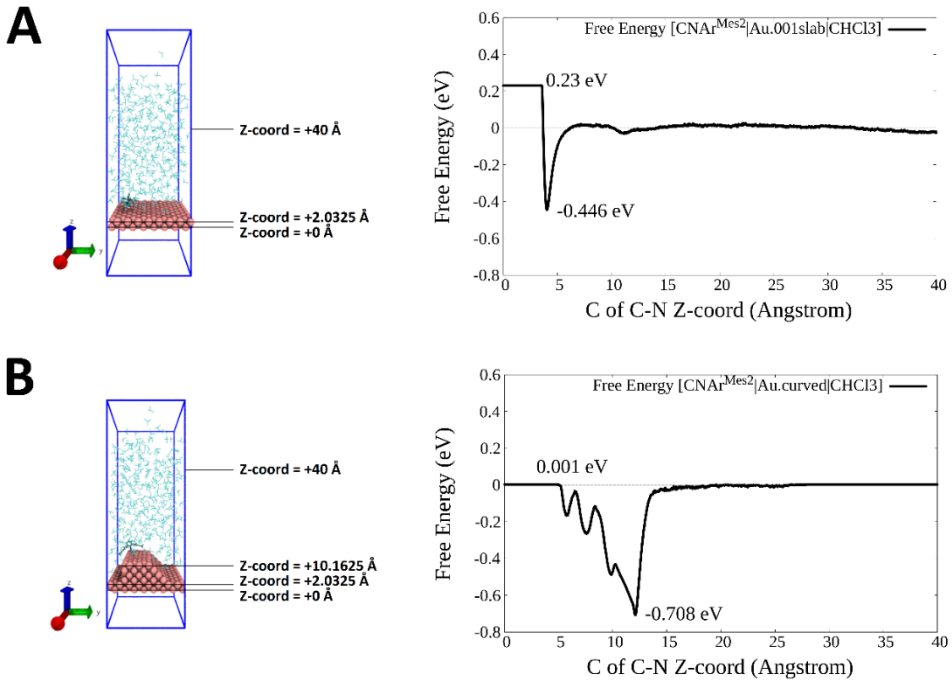

Figure 5.18. Free energy of binding of $CNAr^{Mes2}$ to (A) Au(001) slab and (B) Au(curved) slab. All calculations employed Metadynamics accelerated sampling in $CHCl_3$ at 298K. The distance, Z, was computed between the carbon of $CNAr^{Mes2}$ C≡N group and the bottom of the Au-slab (Z coordinate = 0 Å).

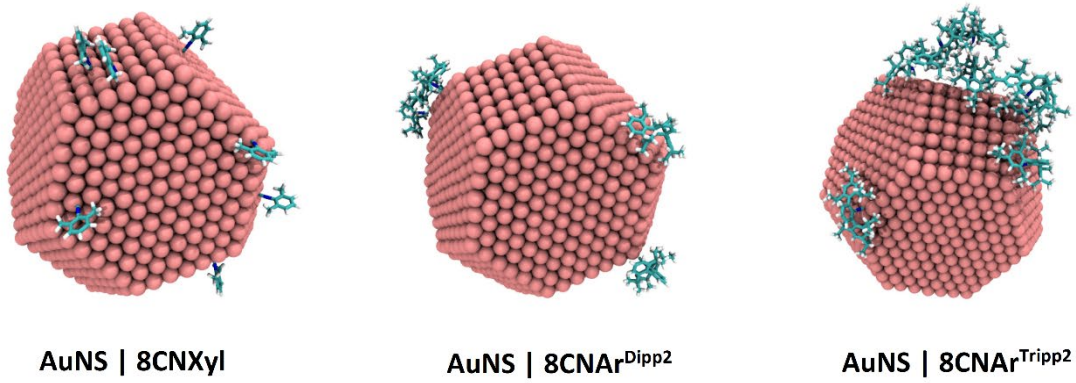

Figure 5.19. Final snapshot from equilibrium MD simulations in vacuum at 298K of (left to right) CNXyl, $CNAr^{Dipp2}$, $CNAr^{Tripp2}$ on a 5nm AuNS.

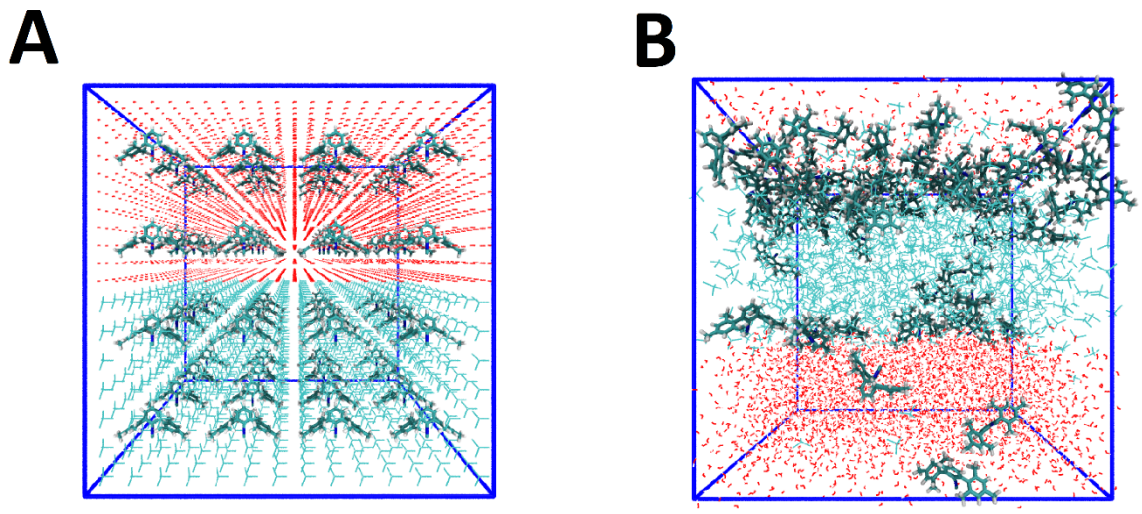

Figure 5.20. (**A**) Initial snapshot of 64 $CNAr^{Mes2}$ molecules randomly distributed in a box containing 4484 water molecules (red) and 1096 $CHCl_3$ molecules (blue). (**B**) Final snapshot after equilibrium MD simulation at 298K and 1atm, showing $CNAr^{Mes2}$ ligands transferring to the organic $CHCl_3$ phase.

Table 5.1. Simulated and experimental isocyanide stretching frequencies, ν(CN), of Au-bound and free $CNAr^{Mes2}$.

Simulated ν(CN) in $CHCl_3$		**Experimental ν(CN)**	
Free $CNAr^{Mes2}$	Adsorbed $CNAr^{Mes2}$	Free $CNAr^{Mes2}$	Adsorbed $CNAr^{Mes2}$
2149 cm^{-1}	2170-2185 cm^{-1}	2119 cm^{-1} (FTIR)	2166.5 cm^{-1} (SERS)

Table 5.2. Solvation free energies difference of various Isocyanide ligands in $CHCl_3$ and water, and cohesive free energy (self-solvation energy) from Free Energy Perturbation calculations.

Ligand	**$A_{ligand\|CHCl3}$ (eV)**	**$A_{ligand\|water}$ (eV)**	**$A_{cohesive}$ (eV)**
CNXyl	-0.24	-0.01	0.06
$CNAr^{Dipp2}$	-0.83	0.04	-0.44
$CNAr^{Mes2}$	-1.01	-0.37	-0.62
$CNAr^{Tripp2}$	-0.90	0.09	-0.52

Table 5.3. Values of computational descriptors for various isocyanide ligands.

Ligand	SBR	EBF	SF	SPF
CNXyl	**0.22**	**0.43**	**-0.02**	**0.23**
$CNAr^{Dipp2}$	**0.60**	**-0.14**	**0.40**	**0.87**
$CNAr^{Mes2}$	**1.00**	**0.12**	**0.28**	**0.52**
$CNAr^{Tripp2}$	**0.46**	**-0.52**	**0.38**	**1.00**

Table 5.4. Composition of simulation cells used in various MD simulations. The associated figures are indicated.

System	Ligand(s)	# of Ligands	# of AuNSs	# $CHCl_3$
$CNAr^{Mes2}$ on AuNS (Fig 6.1B)	$CNAr^{Mes2}$	8	1	0 (Vacuum)
$CNAr^{Mes2}$-AuNS in $CHCl_3$ (Fig 6. 2)	$CNAr^{Mes2}$	106	1	7337
Isocyanides on AuNS (Fig. 6.19)	CNXyl, $CNAr^{Dipp2}$, $CNAr^{Tripp2}$	8	1	0 (Vacuum)

5.5. Acknowledgements.

The authors acknowledge the use of facilities and instrumentation supported by National Science Foundation through the UC San Diego Materials Research Science and Engineering Center (UCSD MRSEC) with Grant DMR-2011924 and the San Diego Nanotechnology Infrastructure (SDNI) of UCSD, a member of the National Nanotechnology Coordinated Infrastructure, which is supported by the Grant ECCS-2025752. We thank the National Science Foundation, UCSD MRSEC DMR-2011924 for financial support.

Chapter 5, in full, is a reprint of the material as it appears in *ACS Nano* "Curvature Selective Nanocrystal Ligation Using Sterically Encumbered Metal-Coordinating Ligands". Permission to publish this material in this dissertation was obtained from all co-authors.

Conceptualization: J.S.F., T.A.P., and A.R.T. Methodology: Y.W., A.C., K.P.B, J.S.F., T.A.P, and A.R.T. Investigation: Y.W., A.C., K.P.B., and Y.X. Visualization: Y.W., A.C., T.A.P., and A.R.T. Funding acquisition: A.R.T. Project administration: J.S.F., T.A.P., and A.R.T. Supervision: J.S.F., T.A.P., and A.R.T. Writing – original draft: J.S.F., T.A.P., and A.R.T. Writing – review & editing: Y.W., A.C., K.P.B., J.S.F., T.A.P., and A.R.T.

5.6. References.

(1) Kovalenko Maksym, V.; Scheele, M.; Talapin Dmitri, V., Colloidal Nanocrystals with Molecular Metal Chalcogenide Surface Ligands. *Science* **2009,** *324* (5933), 1417-1420.

(2) Kim Byung, H.; Heo, J.; Kim, S.; Reboul Cyril, F.; Chun, H.; Kang, D.; Bae, H.; Hyun, H.; Lim, J.; Lee, H.; Han, B.; Hyeon, T.; Alivisatos, A. P.; Ercius, P.; Elmlund, H.; Park, J., Critical differences in 3D atomic structure of individual ligand-protected nanocrystals in solution. *Science* **2020,** *368* (6486), 60-67.

(3) Yi, C.; Liu, H.; Zhang, S.; Yang, Y.; Zhang, Y.; Lu, Z.; Kumacheva, E.; Nie, Z., Self-limiting directional nanoparticle bonding governed by reaction stoichiometry. *Science* **2020,** *369* (6509), 1369-1374.

(4) Nagaoka, Y.; Tan, R.; Li, R.; Zhu, H.; Eggert, D.; Wu, Y. A.; Liu, Y.; Wang, Z.; Chen, O., Superstructures generated from truncated tetrahedral quantum dots. *Nature* **2018,** *561* (7723), 378-382.

(5) Santos, P. J.; Gabrys, P. A.; Zornberg, L. Z.; Lee, M. S.; Macfarlane, R. J., Macroscopic materials assembled from nanoparticle superlattices. *Nature* **2021,** *591* (7851), 586-591.

(6) Villarreal, E.; Li, G. G.; Zhang, Q.; Fu, X.; Wang, H., Nanoscale Surface Curvature Effects on Ligand–Nanoparticle Interactions: A Plasmon-Enhanced Spectroscopic Study of Thiolated Ligand Adsorption, Desorption, and Exchange on Gold Nanoparticles. *Nano Letters* **2017,** *17* (7), 4443-4452.

(7) Power, P. P., Some highlights from the development and use of bulky monodentate ligands. *Journal of Organometallic Chemistry* **2004,** *689* (24), 3904-3919.

(8) Power, P. P., Stable Two-Coordinate, Open-Shell (d1–d9) Transition Metal Complexes. *Chemical Reviews* **2012,** *112* (6), 3482-3507.

(9) Rivard, E.; Power, P. P., Multiple Bonding in Heavier Element Compounds Stabilized by Bulky Terphenyl Ligands. *Inorganic Chemistry* **2007,** *46* (24), 10047-10064.

(10) Clyburne, J. A. C.; McMullen, N., Unusual structures of main group organometallic compounds containing m-terphenyl ligands. *Coordination Chemistry Reviews* **2000,** *210* (1), 73-99.

(11) Kays, D. L., The stabilisation of organometallic complexes using m-terphenyl ligands. In *In Organomet. Chem.,*, Royal Society of Chemistry: Cambridge, 2010; Vol. 36, pp 56-76.

(12) Fox, B. J.; Sun, Q. Y.; Dipasquale, A. G.; Fox, A. R.; Rheingold, A. L.; Figueroa, J. S., Solution behavior and structural properties of Cu(I) complexes featuring m-terphenyl isocyanides. *Inorganic Chemistry* **2008,** *47* (19), 9010-9020.

(13) Ditri, T.; Fox, B.; Moore, C.; Rheingold, A.; Figueroa, J., Effective Control of Ligation and Geometric Isomerism: Direct Comparison of Steric Properties Associated with Bis-mesityl and Bis-diisopropylphenyl m-Terphenyl Isocyanides. *Inorganic Chemistry* **2009,** *48* (17), 8362-8375.

(14) Carpenter, A. E.; Mokhtarzadeh, C. C.; Ripatti, D. S.; Havrylyuk, I.; Kamezawa, R.; Moore, C. E.; Rheingold, A. L.; Figueroa, J. S., Comparative Measure of the Electronic Influence of Highly Substituted Aryl Isocyanides. *Inorganic Chemistry* **2015,** *54* (6), 2936-2944.

(15) Robertson, M. J.; Angelici, R. J., Adsorption of Aryl and Alkyl Isocyanides on Powdered Gold. *Langmuir* **1994,** *10* (5), 1488-1492.

(16) Shih, K.-C.; Angelici, R. J., Equilibrium and Saturation Coverage Studies of Alkyl and Aryl Isocyanides on Powdered Gold. *Langmuir* **1995,** *11* (7), 2539-2546.

(17) Ontko, A. C.; Angelici, R. J., Effects of Alkyl Chain Length on the Adsorption of n-Alkyl Isocyanides (RN⁝C) on Gold Powder. *Langmuir* **1998,** *14* (7), 1684-1691.

(18) Martin, B. R.; Dermody, D. J.; Reiss, B. D.; Fang, M.; Lyon, L. A.; Natan, M. J.; Mallouk, T. E., Orthogonal Self-Assembly on Colloidal Gold-Platinum Nanorods. *Advanced Materials* **1999,** *11* (12), 1021-1025.

(19) Henderson, J. I.; Feng, S.; Bein, T.; Kubiak, C. P., Adsorption of Diisocyanides on Gold. *Langmuir* **2000,** *16* (15), 6183-6187.

(20) Bae, S. J.; Lee, C.-r.; Choi, I. S.; Hwang, C.-S.; Gong, M.-s.; Kim, K.; Joo, S.-W., Adsorption of 4-Biphenylisocyanide on Gold and Silver Nanoparticle Surfaces: Surface-Enhanced Raman Scattering Study. *The Journal of Physical Chemistry B* **2002,** *106* (28), 7076-7080.

(21) Ahn, J.; Shi, S.; Vannatter, B.; Qin, D., Comparative Study of the Adsorption of Thiol and Isocyanide Molecules on a Silver Surface by in Situ Surface-Enhanced Raman Scattering. *The Journal of Physical Chemistry C* **2019,** *123* (35), 21571-21580.

(22) Arroyave, A.; Gembicky, M.; Rheingold, A. L.; Figueroa, J. S., Aqueous Stability and Ligand Substitution of a Layered Cu(I)/Isocyanide-Based Organometallic Network Material with a Well-Defined Channel Structure. *Inorganic Chemistry* **2020,** *59* (17), 11868-11878.

(23) Balto, K. P.; Gembicky, M.; Rheingold, A. L.; Figueroa, J. S., Crystalline Hydrogen-Bonding Networks and Mixed-Metal Framework Materials Enabled by an Electronically Differentiated Heteroditopic Isocyanide/Carboxylate Linker Group. *Inorganic Chemistry* **2021,** *60* (16), 12545-12554.

(24) Yang, J.; Lee, J. Y.; Ying, J. Y., Phase transfer and its applications in nanotechnology. *Chem Soc Rev* **2011,** *40* (3), 1672-96.

(25) Bastús, N. G.; Comenge, J.; Puntes, V., Kinetically controlled seeded growth synthesis of citrate-stabilized gold nanoparticles of up to 200 nm: size focusing versus Ostwald ripening. *Langmuir* **2011,** *27* (17), 11098-11105.

(26) Kimling, J.; Maier, M.; Okenve, B.; Kotaidis, V.; Ballot, H.; Plech, A., Turkevich method for gold nanoparticle synthesis revisited. *The Journal of Physical Chemistry B* **2006,** *110* (32), 15700-15707.

(27) Shao, Y.; Gan, Z.; Epifanovsky, E.; Gilbert, A. T.; Wormit, M.; Kussmann, J.; Lange, A. W.; Behn, A.; Deng, J.; Feng, X., Advances in molecular quantum chemistry contained in the Q-Chem 4 program package. *Mol. Phys.* **2015,** *113*, 184-215.

(28) Giannozzi, P.; Baroni, S.; Bonini, N.; Calandra, M.; Car, R.; Cavazzoni, C.; Ceresoli, D.; Chiarotti, G. L.; Cococcioni, M.; Dabo, I.; Corso, A. D.; Gironcoli, S. d.; Fabris, S.; Fratesi, G.; Gebauer, R.; Gerstmann, U.; Gougoussis, C.; Kokalj, A.; Lazzeri, M.; Martin-Samos, L.; Marzari, N.; Mauri, F.; Mazzarello, R.; Paolini, S.; Pasquarello, A.; Paulatto, L.; Sbraccia, C.; Scandolo, S.; Sclauzero, G.; Seitsonen, A. P.; Smogunov, A.; Umari, P.; Wentzcovitch, R. M., QUANTUM ESPRESSO: a modular and open-source software project for quantum simulations of materials. *J. Phys.: Condens. Matter* **2009,** *21*, 395502.

(29) Giannozzi, P.; Andreussi, O.; Brumme, T.; Bunau, O.; Nardelli, M. B.; Calandra, M.; Car, R.; Cavazzoni, C.; Ceresoli, D.; Cococcioni, M.; Colonna, N.; Carnimeo, I.; Corso, A. D.; Gironcoli, S. d.; Delugas, P.; Jr, R. A. D.; Ferretti, A.; Floris, A.; Fratesi, G.; Fugallo, G.; Gebauer, R.; Gerstmann, U.; Giustino, F.; Gorni, T.; Jia, J.; Kawamura, M.; Ko, H.-Y.; Kokalj, A.; Küçükbenli, E.; Lazzeri, M.; Marsili, M.; Marzari, N.; Mauri, F.; Nguyen, N. L.; Nguyen, H.-V.; Otero-de-la-Roza, A.; Paulatto, L.; Poncé, S.; Rocca, D.; Sabatini, R.; Santra, B.; Schlipf, M.; Seitsonen, A. P.; Smogunov, A.; Timrov, I.; Thonhauser, T.; Umari, P.; Vast, N.; Wu, X.; Baroni, S., Advanced capabilities for materials modelling with Quantum ESPRESSO. *J. Phys.: Condens. Matter* **2017,** *29*, 465901.

(30) Plimpton, S., Fast Parallel Algorithms for Short-Range Molecular Dynamics. *J. Comp. Phys.* **1995,** *117*, 1-19.

(31) Ackland, G. J.; Tichy, G.; Vitek, V.; Finnis, M. W., Simple N-body potentials for the noble metals and nickel. *Philosophical Magazine A* **1987,** *56* (6), 735-756.

(32) Wang, J.; Wolf, R. M.; Caldwell, J. W.; Kollman, P. A.; Case, D. A., Development and testing of a general amber force field. *J Comput Chem* **2004,** *25* (9), 1157-74.

(33) Kaminski, G. A.; Friesner, R. A.; Tirado-Rives, J.; Jorgensen, W. L., Evaluation and reparametrization of the OPLS-AA force field for proteins via comparison with accurate quantum chemical calculations on peptides. *The Journal of Physical Chemistry B* **2001,** *105* (28), 6474-6487.

(34) Kamath, G.; Georgiev, G.; Potoff, J. J., Molecular Modeling of Phase Behavior and Microstructure of Acetone-Chloroform-Methanol Binary Mixtures. *J. Phys. Chem. B* **2005,** *109*, 19463-19473.

(35) Mark, P.; Nilsson, L., Structure and Dynamics of the TIP3P, SPC, and SPC/E Water Models at 298 K. *J. Phys. Chem. A* **2001,** *105*, 9954-9960.

(36) B. J. Fox *et al.*, Solution behavior and structural properties of Cu(I) complexes featuring m terphenyl isocyanides. *Inorganic Chemistry* **47**, 9010-9020 (2008).

(37) T. Ditri, B. Fox, C. Moore, A. Rheingold, J. Figueroa, Effective Control of Ligation and Geometric Isomerism: Direct Comparison of Steric Properties Associated with Bis-mesityl and Bis-diisopropylphenyl m-Terphenyl Isocyanides. *Inorganic Chemistry* **48**, 8362-8375 (2009).

(38) A. E. Carpenter *et al.*, Comparative Measure of the Electronic Influence of Highly Substituted Aryl Isocyanides. *Inorganic Chemistry* **54**, 2936-2944 (2015).

(39) N. G. Bastús, J. Comenge, V. Puntes, Kinetically controlled seeded growth synthesis of citrate-stabilized gold nanoparticles of up to 200 nm: size focusing versus Ostwald ripening. *Langmuir* **27**, 11098-11105 (2011).

(40) J. Kimling *et al.*, Turkevich method for gold nanoparticle synthesis revisited. *The Journal of Physical Chemistry B* **110**, 15700-15707 (2006).

(41) X. Liu, M. Atwater, J. Wang, Q. Huo, Extinction coefficient of gold nanoparticles with different sizes and different capping ligands. *Colloids and Surfaces B: Biointerfaces* **58**, 3-7 (2007).

(42) Y. Shao *et al.*, Advances in molecular quantum chemistry contained in the Q-Chem 4 program package. *Mol. Phys.* **113**, 184-215 (2015).

(43) P. Giannozzi *et al.*, QUANTUM ESPRESSO: a modular and open-source software project for quantum simulations of materials. *J. Phys.: Condens. Matter* **21**, 395502 (2009).

(44) P. Giannozzi *et al.*, Advanced capabilities for materials modelling with Quantum ESPRESSO. *J. Phys.: Condens. Matter* **29**, 465901 (2017).

(45) S. Plimpton, Fast Parallel Algorithms for Short-Range Molecular Dynamics. *J. Comp. Phys.* **117**, 1-19 (1995).

(46) G. J. Ackland, G. Tichy, V. Vitek, M. W. Finnis, Simple N-body potentials for the noble metals and nickel. *Philosophical Magazine A* **56**, 735-756 (1987).

(47) J. Wang, R. M. Wolf, J. W. Caldwell, P. A. Kollman, D. A. Case, Development and testing of a general amber force field. *J Comput Chem* **25**, 1157-1174 (2004).

(48) G. A. Kaminski, R. A. Friesner, J. Tirado-Rives, W. L. Jorgensen, Evaluation and reparametrization of the OPLS-AA force field for proteins via comparison with accurate quantum chemical calculations on peptides. *The Journal of Physical Chemistry B* **105**, 6474-6487 (2001).

(49) G. Kamath, G. Georgiev, J. J. Potoff, Molecular Modeling of Phase Behavior and Microstructure of Acetone-Chloroform-Methanol Binary Mixtures. *J. Phys. Chem. B* **109**, 19463-19473 (2005).

(50) P. Mark, L. Nilsson, Structure and Dynamics of the TIP3P, SPC, and SPC/E Water Models at 298 K. *J. Phys. Chem. A* **105**, 9954-9960 (2001).

(51) M. Karg. Versatile phase transfer of gold nanoparticles from aqueous media to different organic media. *Chemistry* **17**, 4648-4654 (2011).

(52) Hockney, Eastwood, Computer Simulation Using Particles. *Adam Hilger, NY* (1989).

(53) W. Shinoda, M. Shiga, M. Mikami, Rapid estimation of elastic constants by molecular dynamics simulation under constant stress. *Physical Review B* **69**, 134103 (2004).

(54) G. J. Martyna, D. J. Tobias, M. L. Klein, Constant pressure molecular dynamics algorithms. *The Journal of Chemical Physics* **101**, 4177-4189 (1994).

(55) M. Parrinello, A. Rahman, Polymorphic transitions in single crystals: A new molecular dynamics method. *J. Appl. Phys.* **52**, 7182-7190 (1981).

(56) M. E. Tuckerman, J. Alejandre, R. López-Rendón, A. L. Jochim, G. J. Martyna, A Liouville-operator derived measure-preserving integrator for molecular dynamics simulations in the isothermal–isobaric ensemble. *J. Phys. A: Math. Gen.* **39**, 5629 (2006).

(57) T. A. Pascal, D. Schärf, Y. Jung, T. D. Kühne, On the absolute thermodynamics of water from computer simulations: A comparison of first-principles molecular dynamics, reactive and empirical force fields. *J. Chem. Phys.* **137**, 244507 (2012).

(58) A. A. Chen, A. Do, T. A. Pascal, The Phase Diagram of Carbon Dioxide from Correlation Functions and a Many-body Potential. *J. Chem. Phys.* **155**, 024503 (2021).

(59) R. W. Zwanzig, High-Temperature Equation of State by a Perturbation Method. I. Nonpolar Gases. *The Journal of Chemical Physics* **22**, 1420 (1954).

(60) H. Liu *et al.*, Ultrahigh coulombic efficiency electrolyte enables Li||SPAN batteries with superior cycling performance. *Materials Today* **42**, 17-28 (2021).

(61) P. Mahinthichaichan, Q. N. Vo, C. R. Ellis, J. Shen, Kinetics and Mechanism of Fentanyl Dissociation from the μ-Opioid Receptor. *American Chemical Society* **1**, 2208-2215 (2021).

Chapter 6 Synthesis and characterization of *m*-terphenyl isocyanide derivatives and their use in nano-science.

6.1. Introduction.

The *m*-terphenyl ligand scaffold has been used extensively in organometallic chemistry on account of its ability to create an encumbering and protective environment around a single atom or groups of atoms. Due to its sterically encumbering nature, many examples of transition-metal complexes isolated using *m*-terphenyl-based thiolates, imidos and carboxylates have been reported.[1-3] In addition to steric protection, the *m*-terphenyl framework can be readily modified on the sigma- and central aryl rings, which in turn changes its ligation properties.[4] Our group has used the *m*-terphenyl backbone featuring an isocyanide group on the central aryl ring to isolate and characterize novel and often highly-reactive organometallic complexes.[5-8] The isolobal nature of isocyanides to the carbonyl (CO) ligand, accompanied by their similar electronic structure, allow us to study transition-metal complexes which mimic binary unsaturated metal-carbonyl complexes (e.g. $Co(CO)_4$, $Ni(CO)_3$ and $Pd(CO)_2$).[9,10] In addition, we can change the electronic properties of the *m*-terphenyl scaffold by adding more electron-donating or electron-withdrawing functional groups, effectively altering their ligation properties.

In more recent years, we have extended this isocyanide-based molecular chemistry to materials science and characterized the binding of various monotopic *m*-terphenyl isocyanides on gold and silver nanoparticles and surfaces.[11] More specifically, a novel way to achieve site-selective binding on gold nanosphere surfaces (AuNSs) was uncovered using the sterically encumbering isocyanide ligand, $CNAr^{Mes2}$ (Ar^{Mes2} = 2,6-(2,4,6-$Me_3C_6H_2)_2C_6H_2$)). Through experiment and theory, we demonstrated the mesityl flanking groups from $CNAr^{Mes2}$ generate significant steric interactions with AuNS surfaces. Size focusing experiments using $CNAr^{Mes2}$ demonstrated successful ligand exchange with AuNSs, consisting of an average diameter and distribution at 54 ± 2 nm. Evidently, the steric-surface interaction is significant enough to promote $CNAr^{Mes2}$ binding to regions of high

curvature, such as nanocrystal edges and mitigate binding to regions of low surface curvature, like nanocrystals facets. Importantly, this selective surface ligation provides a pathway for the rational design of nanocrystals with highly tailored functions.

During our studies of $CNAr^{Mes2}$ binding to AuNSs, we observed through Dynamic Light Scattering (DLS) measurements that $CNAr^{Mes2}$-capped gold nanospheres were unstable and prone to aggregation. This aggregation was likely due to a lack of Van Der Waals interactions between particles, effectively minimizing inter-particle distances.[12,13] In order to circumvent this issue, we reasoned incorporation of a phenyl group with an alkyl tail *para* to the isocyanide head group was necessary to increase inter-particle distance and minimize aggregation.[14] In addition to increased ligand length, we postulated the orientation of *m*-terphenyl ligands on AuNSs could be influenced by different alkyl tail lengths. The orientation of $CNAr^{Mes2}$ has been previously reported using both computations, surface-enhanced Raman spectroscopy (SERS) and scanning-tunneling miscopy (STM), where the ligand preferentially binds to step-edges and herringbones found on a gold surface. Herein, we report the synthesis and characterization of the *p*-phenyl functionalized $CNAr^{Mes2}$ derivatives: *p*-tolyl-$CNAr^{Mes2}$ (**1**, tolyl = $CH_3C_6H_4$), *p*-*n*-butyl-phenyl-$CNAr^{Mes2}$ (**2**, *p*-*n*-butyl-phenyl = $CH_3C_3H_6C_6H_4$), *p*-*n*-octyl-phenyl-$CNAr^{Mes2}$ (**3**, *p*-*n*-octyl-phenyl = $CH_3C_7H_{14}C_6H_4$) and *p*-*n*-dodecyl-phenyl-$CNAr^{Mes2}$ (**4**, *p*-*n*-dodecyl-phenyl = $CH_3C_{11}H_{22}C_6H_4$) and demonstrate their binding behavior to gold and silver nanospheres.

6.2. Results and Discussion.

6.2.1. Synthesis of *p*-alkyl phenyl $CNAr^{Mes2}$ derivatives.

To retain the steric encumbering properties of the *m*-terphenyl group while increasing ligand length in an attempt to prevent nanoparticle aggregation, we targeted the synthesis and isolation of four *p*-*n*-alkyl-substituted-phenyl $CNAr^{Mes2}$ ligands. These ligands feature an alkyl-substituted phenyl group appended to the *para* position of the centra aryl ring in monodentate $CNAr^{Mes2}$,

which has been well utilized for the preparation of transition-metal complexes and materials alike.[15-17] The syntheses of these four derivatives were accomplished by simple Suzuki coupling of previously reported *p*-bromo-*m*-terphenyl formamide HC(O)NH(*p*-BrAr^{Mes2}) with their respective 4-alkyl substituted phenyl boronic acids to provide the coupled formamide ligand 1-HC(O)N(H)Ar^{Mes2}-4-C_6H_4R (R= CH_3, $CH_3C_3H_6$, $CH_3C_7H_{14}$, $CH_3C_{11}H_{22}$) (Figure. 7.1).[18] As expected, an increase in alkyl chain length generates the formamide as an off-white oil (*n*-butyl, *n*-octyl, *n*-dodecyl) instead of the off-white solid observed for *p*-tolyl-CNAr^{Mes2} and CNAr^{Mes2}. Subsequent dehydration of the formamide afforded the isocyanide 1,4,-(CNAr^{Mes2})C_6H_4R, typically as a colorless oil, and all variants give rise to sharp ν_{CN} bands of ~2116 cm^{-1} as measured by attenuated-total reflectance infrared (ATR-IR) spectroscopy with $^{13}C\{^1H\}$-NMR chemical shifts of ~167-170 ppm for the isocyanide carbons (Table 7.1). These spectroscopic features agree well with previously reported monotopic and ditopic *m*-terphenyl isocyanide ligands.[4,19,20] Crystallographic structure determination of **1** and **2** reveal the alkyl-substituted phenyl groups are canted ~38° and ~41°, respectively, relative to the Ar^{Mes2} group. This is similar to the torsion angle observed in the reported phenylene-spaced ditopic *m*-terphenyl isocyanide ligand, 1,4,-(CNAr^{Mes2})$_2C_6H_4$, but differs from the directly coupled linker [CNAr^{Mes2}]$_2$.[16,17]

Notably, as alkyl chain length increases, the ability to crystallize and characterize these ligands by single crystal X-ray diffraction (sc-XRD) decreases, and this was the case for both **3** and **4**. To circumvent this problem, we reasoned reaction of **3** with a transition-metal precursor like Ni(COD)$_2$ (COD=cycloocta-1,5-diene) would enable facile crystallization of a Ni(0) organometallic complex and enable confirmation of ligand morphology. Indeed, the reaction of **3** (2 equiv.) with Ni(COD)$_2$ (1 equiv.) afforded the complex Ni(COD)(**3**)$_2$ as determined by sc-XRD. From the isolation of this complex, it is evident **3** was successfully synthesized and the *p*-phenyl

octyl group is canted ~ 50° relative to the Ar^{Mes2} group. While structural information was obtained by the reaction of **3** with $Ni(COD)_2$, no single crystals from the same reaction with **4** were able to be isolated, likely due to the length of the alkyl tail. Indeed, several attempts at crystallization of **4** upon reaction with transition-metal complexes such as $ClAu(SMe_2)$ (Me= CH_3) and $Ni(COD)_2$ were unsuccessful, affording oily products. While attempts at isolating single crystal quality material were unsuccessful, **4** was fully characterized by ^{1}H-NMR, $^{13}C\{^1H\}$-NMR, ATR-IR spectroscopy, and mass spectrometry.

Table 6.1. Spectroscopic and structural data of alkyl functionalized p-phenyl $CNAr^{Mes2}$ ligands.

Ligand	ν_{CN} (cm^{-1})	Isocyanide carbon $^{13}C\{^1H\}$-NMR chemical shift (ppm)	*p*-phenyl-R group angle relative to $CNAr^{Mes2}$ (°)
1,4,-$(CNAr^{Mes2})C_6H_4$-CH_3 (1)	2115 cm^{-1}	167 ppm	37.551
1,4,-$(CNAr^{Mes2})C_6H_4$-$C_3H_6CH_3$ (2)	2116 cm^{-1}	167.13 ppm	40.798
1,4,-$(CNAr^{Mes2})C_6H_4$-C_7H_{14} CH_3 (3)	2116 cm^{-1}	168 ppm	N/A, no sc-XRD structure isolated
1,4,-$(CNAr^{Mes2})C_6H_4$-$C_{11}H_{22}CH_3$ (4)	2115 cm^{-1}	171 ppm	N/A, no sc-XRD structure isolated

6.2.2. The binding and orientation of alkyl-derivatized *p*-phenyl $CNAr^{Mes2}$ derivatives on gold nanospheres.

To determine the ligation properties of **1-4** on nanoparticle surfaces, we first explored their binding behavior towards AuNSs. We have previously reported the binding of $CNAr^{Mes2}$ to AuNSs ranging from 10-80 nm in size and reasoned isocyanides **1-4** would exhibit similar behaviors.[11] Indeed, by using the liquid-liquid extraction technique (LLE), ligand exchange was facilitated between citrate-capped Au nanospheres of varying size (20-80 nm in diameter) and ligands **1-4** dissolved in $CHCl_3$. Despite functionalizing $CNAr^{Mes2}$ and increasing ligand length, upon transfer to chloroform ($CHCl_3$), particles appeared to aggregate and form a grey precipitate that was readily redispersed upon sonication. Inspection of transmission electron microscopy (TEM) images of the extracted isocyanide-capped Au particles indicate they maintain spherical shape, and no changes

to core nanocrystal sizes are observed (Figure 6.28.). Furthermore, displacement of citrate was confirmed by extinction measurements of the aqueous layer before and after extraction, and the binding of the isocyanides **1-4** was established using SERS, where sharp peaks are observed between ν_{CN} = 2147 and 2160 cm^{-1} (Figure 6.24). This isocyanide stretching frequency is blue-shifted relative to free isocyanide and is in good agreement with other previously reported Au-bound isocyanide SERS data (Table 6.1.).[21,22]

After confirming the binding of isocyanides **1-4** to Au NSs, the interaction of the various alkyl tails with particles was assessed. Comparison of the SERS spectra of previously reported $CNAr^{Mes2}$-capped particles with (**1**) and (**2**) capped-AuNSs suggests little interaction of alkyl tails with the Au nanocrystal surface. More specifically, in all three spectra, C-C stretching vibration modes from the phenyl ring are observed between $\nu_{C\text{-}C}$ = 1430–1625 cm^{-1}. However, despite the presence of the alkyl tails in (**1**) and (**2**), strong C−C stretching vibrations representative of alkane *gauche* ($\nu_{G(C\text{-}C)}$ = ~1085 cm^{-1}) or *trans* ($\nu_{T(C\text{-}C\ alkane)}$ = ~1070, 1121, and 1181 cm^{-1}) orientations are not observed.[23-26] This, accompanied with a lack of peaks in the C-H stretching region ($\nu_{asy(C\text{-}H)}$ = 2850 – 2930 cm^{-1}), indicate there is little interaction of the alkyl-derivatized m-terphenyl ligands (**1**) and (**2**) with 20 nm Au nanocrystal surfaces.[27-29]

While the alkyl tails of ligands (**1**) and (**2**) did not interact with Au nanocrystal surfaces, we reasoned (**3**) and (**4**) had the potential to interact due to their increased chain lengths. Indeed, inspection of the Raman spectra of a sample of (**3**)-capped AuNSs indicate the octyl tail maintains a *trans* orientation on the surface, as seen by the presence of the C-C alkane stretch at $\nu_{T(C\text{-}C\ alkane)}$ = 1183 cm^{-1}. In addition, the presence of peaks in the C-H stretching region ($\nu_{asy(C\text{-}H)}$ = 2850 – 2930 cm^{-1}) suggest the octyl chain has substantial interaction with the Au surface.

6.2.3. The binding and orientation of alkyl-derivatized *p*-phenyl $CNAr^{Mes2}$ derivatives on silver (Ag) nanospheres.

While we have studied the binding of *m*-terphenyl isocyanide derivatives on gold surfaces, little has been done with silver surfaces. Like gold particles, silver nanoparticles (AgNPs) also exhibit optical and electronic properties based on their size, shape, and surface coverage, allowing them to interact with specific wavelengths of light. This has proven particularly useful in the public health sector, as they can be used for surface plasmon resonance (SPR) biosensors.[30] Due to their wide applications, we pursued the isolation and characterization of *m*-terphenyl isocyanide-capped AgNSs using the previously reported LLE technique.

In order to determine if the *m*-terphenyl isocyanides ($CNAr^{Mes2}$, $CNAr^{Dipp2}$ and $CNAr^{Tripp2}$) exhibit similar ligand-binding properties as a function of AgNS surface curvature, LLE experiments were performed using citrate-capped AgNSs varying from 10nm – 80nm in diameter. UV-Vis measurements of the aqueous layer were recorded before and after extraction to determine the extraction efficiency of each monotopic *m*-terphenyl isocyanide ligand (Table 6.2.). Interestingly, while $CNAr^{Mes2}$ displayed selectivity for high curvature regions on AuNSs, the same trend is not observed with AgNSs. Inspection of Table 6.2 indicates $CNAr^{Mes2}$ effectively extracts all sizes of AgNSs into the organic layer. However, as nanoparticle diameter increases, the extraction efficiency of $CNAr^{Dipp2}$ decreases, indicating some selectivity of $CNAr^{Dipp2}$ to areas of higher surface curvature. Notably, this is not observed in the AuNS system, as $CNAr^{Dipp2}$ extracts all sizes. Inspection of TEM images of $CNAr^{Mes2}$ -capped particles suggest binding leads to significant shape deformation and fusion of AgNSs (Figures 6.30-6.33.). This is also observed in the TEM images of 20nm AgNSs capped with $CNAr^{Dipp2}$, however fusion is not observed in the 50nm and 80nm $CNAr^{Dipp2}$-capped samples. The AgNS fusion observed in the TEM images suggests the orientation and binding of $CNAr^{Mes2}$ on Ag nanocrystal surfaces could be strong

enough to cause significant distortion to nanocrystal cores. Additionally, the binding of isocyanide to AgNPs was confirmed using SERS, and a diagnostic peak between ν_{CN} = 2170 - 2185 cm^{-1} was observed for all ligand moieties, which is in good agreement with previously reported *m*-terphenyl isocyanide Ag(I) complexes (Figure 6.1). [31,32]

Table 6.2. Extraction efficiencies of *m*-terphenyl isocyanide ligands on AgNSs.

AgNS Size	AgNS concentration (particles/mL)	Extraction Efficiency ($CNAr^{Mes2}$)	Extraction Efficiency ($CNAr^{Dipp2}$)	Extraction Efficiency ($CNAr^{Tripp2}$)
10 nm	3.6E+12	97%	100%	24%
20 nm	3.8E+11	99%	97%	4%
50 nm	1.4E+11	92%	55%	5%
80 nm	6.8E+10	92%	59%	8%

After the binding of *m*-terphenyl isocyanides on AgNSs was established, we proceeded to examine the orientation of alkylated derivatives (**1-4**) on silver nanocrystal surfaces and compared the results to data obtained from AuNS experiments. The LLE reaction was performed to displace citrate and bind isocyanide derivatives, and the extraction efficiency was reported using UV-Vis measurements. Furthermore, the binding of **1-4** was established by SERS measurements, where the diagnostic Ag-bound isocyanide stretch is observed between ν_{CN} = 2175 and 2182 cm^{-1}, which is in good agreement with data obtained from the binding of $CNAr^{Mes2}$ to Ag molecular and nanoparticle systems.[4] Furthermore, inspection of the spectra of (**3**) reveals a sharp peak at $\nu_{T(C\text{-}C\ alkane)}$ = 1182 cm^{-1}, suggesting the octyl tail has a *trans* orientation on the Ag nanoparticle surface.[23] The same orientation of (**3**) is observed on AuNSs. There is little indication of the octyl tail in (**3**) maintaining a *gauche* orientation on the nanoparticle surface, as there are no peaks observed in the spectra at $\nu_{G(C\text{-}C)}$ = 1085 cm^{-1}. Inspection of the spectrum obtained from the binding of (**2**) on

AgNSs suggests the butyl tail maintains a *trans* orientation on the surface. This is seen by the presence of a less intense, sharp peak at 1075 cm^{-1}, and the presence of *gauche* oriented butyl chains is not observed.

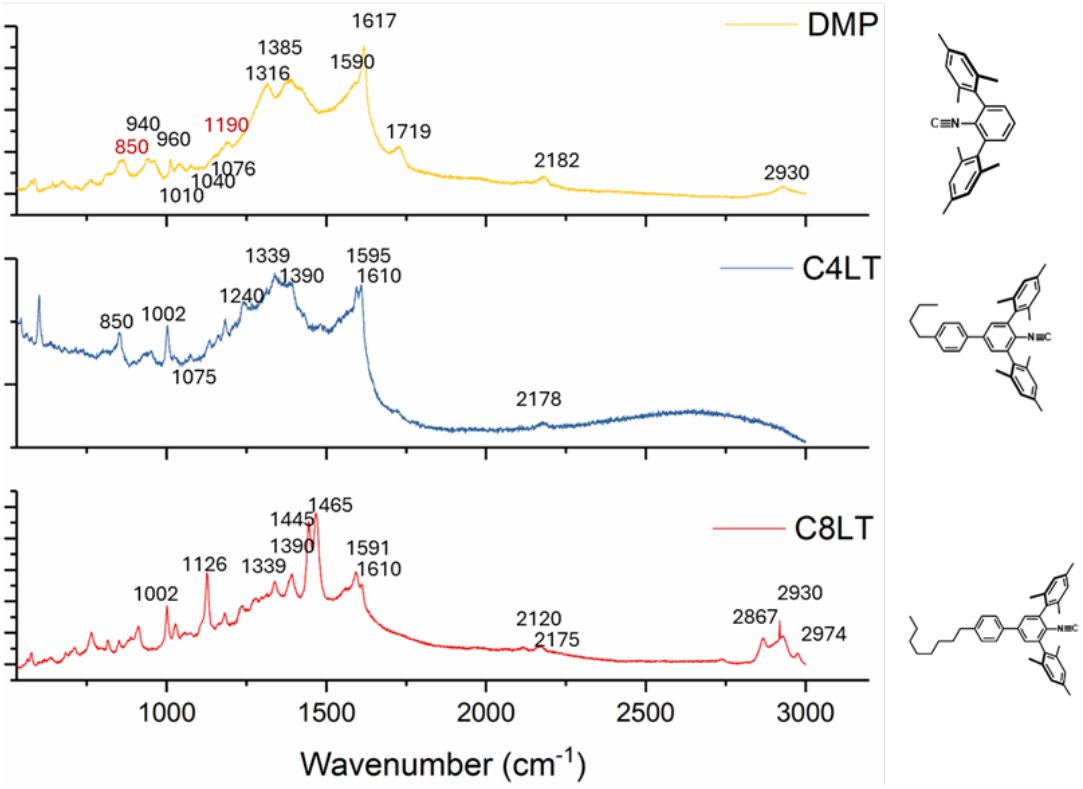

Figure 6.1. Surface-Enhanced Raman spectra of Ag-bound (top) $CNAr^{Mes2}$ (middle) (**2**) and (bottom) (**3**).

6.3. Conclusions.

The *m*-terphenyl scaffold has been modified using Suzuki coupling methods to contain alkyl chains of varying lengths. Due to this synthetic tunability, the functionalization of the gold and silver nanoparticle surfaces with alkylated ligand derivatives (**1**)-(**4**) can be studied extensively using SERS, TEM and SEM techniques. The orientation of the alkylated tails can be determined by inspection of SERS spectra, indicating a *trans* orientation for (**2**) and (**3**) is preferred on both Au and Ag nanoparticle surfaces. Notably, the alkylated ligands (**3**) and (**4**) have the ability to form a liquid crystalline material upon desolvation and form films with interesting refractive indices. In the future, we hope to form self-assembled monolayers with these two ligands when

bound to various metal centers, and study their properties using Lagmuir-Blodgett troughs, SEM and reflectance measurements.

6.4. Experimental Section.

Synthesis of (1).

I. ***Synthesis of OHCNH(p-(BPin)Ar^{Mes2}:*** A resealable ampule was charged with OHCNH(p(Br)Ar^{Mes2} (1 eq.), K_3PO_4 (4 eq.) and B_2Pin_2 (0.5 eq.). The catalyst was prepared separately, where Pd_2dba_3 (3 mol%) and PCy_3 (6 mol%) were dissolved in toluene (10mL) and stirred for 10 minutes at room temperature. ~10-20 mL of toluene were used to dissolve the solids in the resealable ampule. The reaction was stirred at 85℃ for 24 hours under an atmosphere of nitrogen. The reaction mixture was cooled and filtered over a silica plug in a fine porosity frit, while the ampule was washed with DCM (3 x 10mL) and added to the frit. The plug was rinsed with DCM and EtOAc (3x5-10mL each) and the filtered crude mixture was stripped of all volatiles. The resulting solid was washed with hexanes (~5mL) and filtered, providing OHCNH(p-(BPin)Ar^{Mes2} as a pale yellow solid. ^{1}H-NMR (402 MHz, $CDCl_3$, 20°C): δ 7.71/7.68 (d, 1H, J= 9.39 Hz) NHC(O)H), 7.54 (s, 2H, *m*-Ar), 6.92 (s, 4H, *m*-Mes), 6.73/6.70 (d, 1H, J= 10.12 Hz, NHC(O)H), 2.30 (s, 6 H, (Mes-*p*-CH3)), 2.00 (s, 12H, (Mes-*o*-CH3)), 1.32 (2, 12H, BPIN).

II. ***Synthesis of OHCNHAr$^{Mes2}C_6H_4CH_3$:*** A resealable ampule was charged with OHCNH(p-(BPin)Ar^{Mes2} (1 eq.), K_3PO_4 (4 eq.) and 4-Bromo-toluene (1.05 eq.). The catalyst was prepared separately, where Pd_2dba_3, 3 mol%), PCy_3 (6 mol%) were dissolved in toluene (10mL) and stirred for 10 minutes at room temperature. Dioxane (15mL) was used to dissolve the solids in the resealable ampule. The ampule was brought outside the glovebox and degassed DI water (0.2 mL) was added to the reaction

mixture under an atmosphere of nitrogen. The reaction was then stirred at 85℃ for 48 hours. The reaction mixture was cooled and filtered over a silica plug in a fine porosity frit, while the ampule was washed with DCM (3 x 10mL) and added to the frit. The plug was rinsed with DCM and EtOAc (3x5-10mL each) and the filtered crude mixture was stripped of all volatiles. It was redissolved into EtOAc and dried over $MgSO_4$, filtered, and the volatiles were removed by rotary evaporation. The resultant product was purified by column chromatography (silica gel) using a mixture of 2% EtOAc in hexane. The fractions were combined and concentrated under reduced pressure to provide $OHCNHAr^{Mes2}C_6H_4CH_3$ as an off-white solid. ^1H NMR (300.1 MHz, $CDCl_3$, 20°C): δ 7.68/7.64 (d, 1H, J= 11.23 Hz NHC(O)H), 7.51/7.48 (d, 2H, J =10.93 Hz) 7.40 (s, 2H, *m*-Ar), 6.97 (s, 4H, *m*-Mes), 6.93/6.95 (d, 2H, J = 8.95 Hz), 6.64/6.61 (d, 1H, J= 11.70 Hz, NHC(O)H), 2.37 (s, 3H), 2.32 (s, 6 H, (Mes-*p*-CH3)), 2.06 (s, 12H, (Mes-*o*-CH3)). *HR-MS (ESI-TOFMS, positive-ion mode*). Predicted for $[C_{32}\ H_{34}\ N\ O]^+$ *m*/*z* 448.2635. Found: *m*/*z* 448.2631 ($[M+H]^+$).

III. ***Synthesis of 1,4-(CNAr^{Mes2})C$_6$H$_4$CH$_3$ (1):*** To a stirring CH_2Cl_2 solution of 1-$HC(O)N(H)Ar^{Mes2}$-4-$C_6H_4CH_3$(0.110 g, 1 equiv) was added diisopropylamine (4 equiv) via a syringe. After stirring for 5 min, $POCl_3$(2 equiv.) was added dropwise via a syringe and the solution was stirred for 24 h. Aqueous Na_2CO_3(1.5 M, 50 mL) was added, and the resulting mixture was stirred for 5 h. The organic and aqueous layers were then separated, and the organic layer was washed with deionized water. The aqueous layers were combined and extracted with 3×25 mL of CH_2Cl_2. The organic extracts were combined, dried over $MgSO_4$, and filtered and volatiles were removed under reduced pressure. The resultant solid was washed with cold hexanes, collected

by filtration, and dried under reduced pressure. The product was recrystallized by dissolution in minimal MeCN and allowing the solution to evaporate overnight. ^{1}H -NMR (402 MHz, $CDCl_3$, 20°C): δ 7.54/7.52 (d, 2H, J = 6.68 Hz) 7.49 (s, 2H ,*m*-Ar), 7.28/7.26 (d, 2H, J = 11.70 Hz), 7.01 (s, 4H, *m*-Mes), 2.41 (s, 3H), 2.36 (s, 6 H, (Mes-*p*-CH3)), 2.10 (s, 12H, (Mes-*o*-CH3)). *HR-MS (ESI-TOFMS, positive-ion mode).* Predicted for $[C_{32}H_{32}N]^+$: *m*/*z* 430.2529. Found: *m*/*z* 430.2527 ($[M]^+$).

Synthesis of (2).

I. ***Synthesis of*** $OHCNHAr^{Mes2}C_6H_4(CH_2)_3CH_3$***:*** A resealable ampule was charged with OHCNH(*p*-Br)Ar^{Mes2} (1 eq.), K_3PO_4 (4 eq.) and $B(OH)_2$-$C_6H_4(CH_2)_3CH_3$ (1.05 eq.). The catalyst was prepared separately, where Pd_2dba_3, (3 mol%), PCy_3 (6 mol%) were dissolved in toluene (10mL) and stirred for 10 minutes at room temperature. Dioxane (15mL) was used to dissolve the solids in the resealable ampule. The ampule was brought outside the glovebox and degassed DI water (~0.1 mL) was added to the reaction mixture under an atmosphere of nitrogen. The reaction was then stirred at 85℃ for 48 hours. The reaction mixture was cooled and filtered over a silica plug in a fine porosity frit, while the ampule was washed with DCM (3 x 10mL) and added to the frit. The plug was rinsed with DCM and EtOAc (3x5-10mL each) and the filtered crude mixture was stripped of all volatiles. It was redissolved into EtOAc and dried over MgSO4, filtered, and the volatiles were removed by rotary evaporation. Crystals of the resultant product were isolated by dissolution of the product into Et_2O and slow evaporation of the solvent, giving $OHCNHAr^{Mes2}C_6H_4(CH_2)_3CH_3$ as a colorless solid. ^{1}H-NMR (400 MHz, $CDCl_3$, 20°C): δ 7.68/7.64 (d, 2H, J= 9.22 Hz), 7.53/7.43 (d, 2H, J= 9.22 Hz), 7.26/7.24 (d,1H, J= 6.45 Hz, NHC(O)H), 7.43 (s, 2H, *m*-Ar), 7.00 (s, 4H, *m*-Mes), 6.68/6.65 (d, 1H, J= 11.07 Hz,

NHC(O)H), 2.65 (t, 2H J= 16.01 Hz), 2.35 (s, 6 H, (Mes-*p*-CH3)), 2.06 (s, 12H, (Mes-*o*-CH3)), 1.60 (m, 2H), 1.35 (m, 2H), 0.92 (m, 3H). *HR-MS (ESI-TOFMS, positive-ion mode).* Predicted for m/*z* 490.3104. Found: 490.3108 *m*/*z* ($[C_{35}H_{40}NO]^+$ $[M+H]^+$).

II. ***Synthesis of 1,4-(CNAr^{Mes2}) C$_6$H$_4$(CH$_2$)$_3$CH$_3$.*** To a stirring CH_2Cl_2 solution of $OHCNHAr^{Mes2}C_6H_4(CH_2)_3CH_3$ (1 equiv) was added diisopropylamine (4 equiv) via a syringe. After stirring for 5 min, $POCl_3$(2 equiv) was added dropwise via a syringe and the solution was stirred for 24 h. Aqueous Na_2CO_3 (1.5 M, 50 mL) was added, and the resulting mixture was stirred for 5 h. The organic and aqueous layers were then separated, and the organic layer was washed with deionized water. The aqueous layers were combined and extracted with 3×25 mL of CH_2Cl_2. The organic extracts were combined, dried over $MgSO_4$, and filtered and volatiles were removed under reduced pressure. The resultant solid was washed with cold hexanes, collected by filtration, and dried under reduced pressure. The product was recrystallized by dissolution in minimal MeOH and allowing the solution to evaporate overnight. ^{1}H-NMR (402 MHz, $CDCl_3$, 20°C): δ 7.55/7.52 (d, 2H, 7.84 Hz), 7.48 (s, 2H, *m*-Ar), 7.26/7.24 (d, 2H, J = 9.37 Hz), 6.99 (s, 4H, *m*-Mes), 2.64 (t, 2H J= 6.24 Hz), 2.34 (s, 6 H, (Mes-*p*-CH3)), 2.08 (s, 12H, (Mes-*o*-CH3)), 1.60 (m, 2H), 1.35 (m, 2H), 0.93 (m, 3H). *HR-MS (ESI-TOFMS, positive-ion mode).* Predicted for: 472.299 m/*z*. Found: 472.3001 *m*/*z* ($[C_{35}H_{38}N]^+$ $[M+H]^+$).

Synthesis of (3).

I. ***Synthesis of OHCNHAr^{Mes2}C$_6$H$_4$ (C$_7$H$_{14}$CH$_3$):*** A resealable ampule was charged with OHCNH(*p*-Br)Ar^{Mes2} (1 eq.), K_3PO_4 (4 eq.) and 1,4-B(OH)$_2$-C_6H_4 ($C_7H_{14}CH_3$) (1.05 eq.). The catalyst was prepared separately, where Pd_2dba_3, 3 mol%), PCy_3 (6 mol%) were dissolved in toluene (10mL) and stirred for 10 minutes at room temperature.

Dioxane (15mL) was used to dissolve the solids in the resealable ampule. The ampule was brought outside the glovebox and degassed DI water (0.2 mL) was added to the reaction mixture under an atmosphere of nitrogen. The reaction was then stirred at 85℃ for 48 hours. The reaction mixture was cooled and filtered over a silica plug in a fine porosity frit, while the ampule was washed with DCM (3 x 10mL) and added to the frit. The plug was rinsed with DCM and EtOAc (3x5-10mL each) and the filtered crude mixture was stripped of all volatiles. It was redissolved into EtOAc and dried over MgSO4, filtered, and the volatiles were removed by rotary evaporation, giving $OHCNHAr^{Mes2}C_6H_4(CH_2)_3CH_3$ as a colorless solid. *This compound is often in between two states: a liquid and a solid--- liquid crystalline*. ^{1}H-NMR (402 MHz, $CDCl_3$, 20°C): δ 7.68/7.64 (d, 1H, J = 10.73 Hz, NHC(O)H), 7.54/7.51 (d, 2H, J = 7.66 Hz), 7.46/7.43 (d, 1H, J= X Hz), NHC(O)H), 7.42 (s, 2H, *m*-Ar), 6.98 (s, 4H, *m*-Mes), 7.24/ 7.22 (d, 2H, J=7.84 Hz) 6.62/6.59 (d, 1H, J= 10.22 Hz Hz, NHC(O)H), 2.63 (t, 2H, J = 8.12 Hz) 2.33 (s, 6 H, (Mes-*p*-CH_3)), 2.06 (s, 12H, (Mes-*o*-CH_3)), 1.62 (m, 3H), 1.26 (m, 12H). *HR-MS (ACPI-TOFMS, positive-ion mode).* Predicted for m/*z* 546.3730. Found: 546.3730 *m*/*z* ($[C_{39}H_{48}NO]^+$ $[M+H]^+$).

II. ***Synthesis of $CNAr^{Mes2}C_6H_4(C_7H_{14}CH_3)$:*** To a stirring CH_2Cl_2 solution of $OHCNHAr^{Mes2}C_6H_4(C_7H_{14}CH_3)$ (1 equiv) was added diisopropylamine (4 equiv) via a syringe. After stirring for 5 min, $POCl_3$ (2 equiv) was added dropwise via a syringe and the solution was stirred for 24 h. Aqueous Na_2CO_3 (1.5 M, 50 mL) was added, and the resulting mixture was stirred for 5 h. The organic and aqueous layers were then separated, and the organic layer was washed with deionized water. The aqueous layers were combined and extracted with 3×25 mL of CH_2Cl_2. The organic extracts were

combined, dried over $MgSO_4$, and filtered and volatiles were removed under reduced pressure. ^{1}H-NMR (402 MHz, $CDCl_3$, 20°C): δ 7.55/7.53 (s, 2H, J = 7.89 Hz), 7.48 (s, 2H), 7.25 (s, 2H), 6.99 (s, 4H), 2.64 (t, 2H, J= 6.63 Hz), 2.34 (s, 2H (Mes-*p*-CH_3)), 2.08 (s, 12H (Mes-*o*-CH_3), 1.62 (m, 5H), 1.25 (m, 8H), 0.86 (m, 4H). *HR-MS (ECI-TOFMS, positive-ion mode).* Predicted for m/*z* 528.3625. Found: 528.3619 *m*/*z* ([$C_{39}H_{46}N]^+$ $[M+H]^+$).

Synthesis of (4).

I. ***Synthesis of OHCNH(Ar^{Mes2})C$_6$H$_4$-C$_{11}$H$_{22}$CH$_3$***: A resealable ampule was charged with OHCNH(p-(BPin)Ar^{Mes2} (1 eq.), K_3PO_4 (4 eq.) and 4-dodecylbenzene (1.05 eq.). The catalyst was prepared separately, where Pd_2dba_3, 3 mol%), PCy_3 (6 mol%) were dissolved in toluene (10mL) and stirred for 10 minutes at room temperature. Dioxane (15mL) was used to dissolve the solids in the resealable ampule. The ampule was brought outside the glovebox and degassed DI water (0.2 mL) was added to the reaction mixture under an atmosphere of nitrogen. The reaction was then stirred at 85℃ for 48 hours. The reaction mixture was cooled and filtered over a silica plug in a fine porosity frit, while the ampule was washed with DCM (3 x 10mL) and added to the frit. The plug was rinsed with DCM and EtOAc (3x5-10mL each) and the filtered crude mixture was stripped of all volatiles. It was redissolved into EtOAc and dried over $MgSO_4$, filtered, and the volatiles were removed by rotary evaporation. The resultant product was purified by column chromatography (silica gel) using a mixture of 2% EtOAc in hexane. The fractions were combined and concentrated under reduced pressure to provide OHCNH(Ar^{Mes2})C_6H_4-$C_{11}C_{22}CH_3$ as an off-white oil. ^{1}H-NMR (402 MHz, $CDCl_3$, 20°C): δ 7.67/7.65 (s, 2H, J = 12.41 Hz), 7.53/7.51 (d, 2H, J = 8.00) 7.41 (s,

2H), 7.24/7.22 (s, 2H, J= 7.60 Hz), 6.97 (s, 4H), 6.61/6.59 (d, 1H, J =11.18 Hz) 2.62 (t, 2H, J= 6.36 Hz), 2.33 (s, 2H (Mes-*p*-CH_3)), 2.05 (s, 12H (Mes-*o*-CH_3), 1.58 (m, 2H), 1.25 (m, 20H), 0.86 (m, 3H).

II. ***Synthesis of 1,4-CN(Ar^{Mes2})C$_6$H$_4$-C$_{11}$H$_{22}$CH$_3$ (4)***: To a stirring CH_2Cl_2 solution of OHCNH(Ar^{Mes2})C_6H_4-$C_{11}C_{22}CH_3$ (1 equiv.) was added diisopropylamine (4 equiv.) via a syringe. After stirring for 5 min, $POCl_3$(2 equiv.) was added dropwise via a syringe and the solution was stirred for 24 h. Aqueous Na_2CO_3(1.5 M, 50 mL) was added, and the resulting mixture was stirred for 5 h. The organic and aqueous layers were then separated, and the organic layer was washed with deionized water. The aqueous layers were combined and extracted with 3×25 mL of CH_2Cl_2. The organic extracts were combined, dried over $MgSO_4$, and filtered and volatiles were removed under reduced pressure. ^{1}H-NMR (500 MHz, C_6D_6, 20°C): δ 7.40 (s, 2H), 7.33/7.32 (s, 2H, J= 8.13 Hz), 7.11/7.10 (d, 2H, J = 7.62 Hz), 6.89 (s, 4H), 2.62 (t, 2H, J= 6.36 Hz), 2.54(t, 2H, J= 9.57 Hz), 2.19 (s, 2H (Mes-*p*-CH_3)), 2.13 (s, 12H (Mes-*o*-CH_3), 1.60 (m, 2H), 1.31 (m, 20H), 0.91 (m, 3H). *HR-MS (ECI-TOFMS, positive-ion mode).* Predicted for m/*z* 584.4251. Found: 584.4245 *m*/*z* ([$C_{43}H_{54}N$]$^+$ [M+H]$^+$).

Nuclear Magnetic Resonance (NMR) Spectroscopic Data.

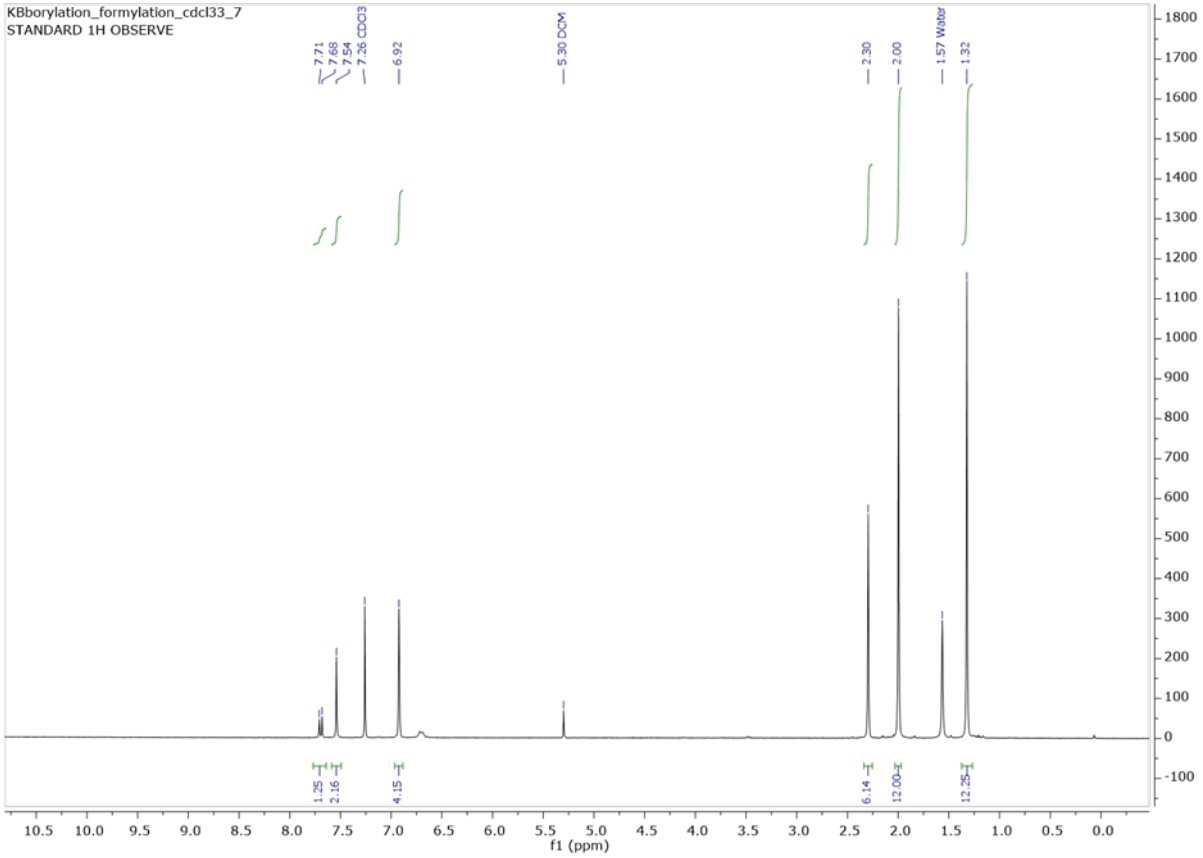

Figure 6.2. ^{1}H-NMR spectrum of OHCNH(*p*-(BPin)Ar^{Mes2} in $CDCl_3$.

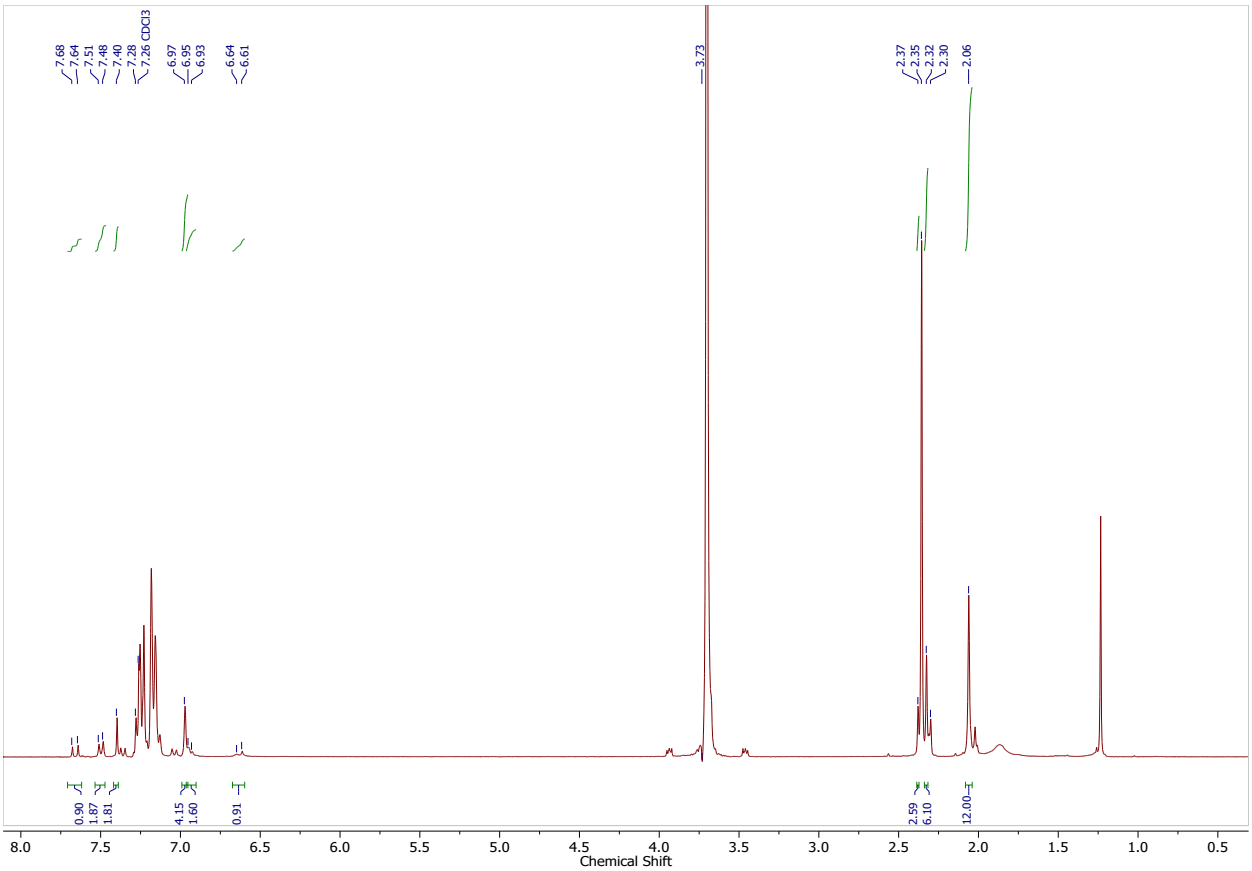

Figure 6.3. ^{1}H NMR of OHCNHAr^{Mes2}C$_6$H$_4$CH$_3$ in CDCl$_3$.

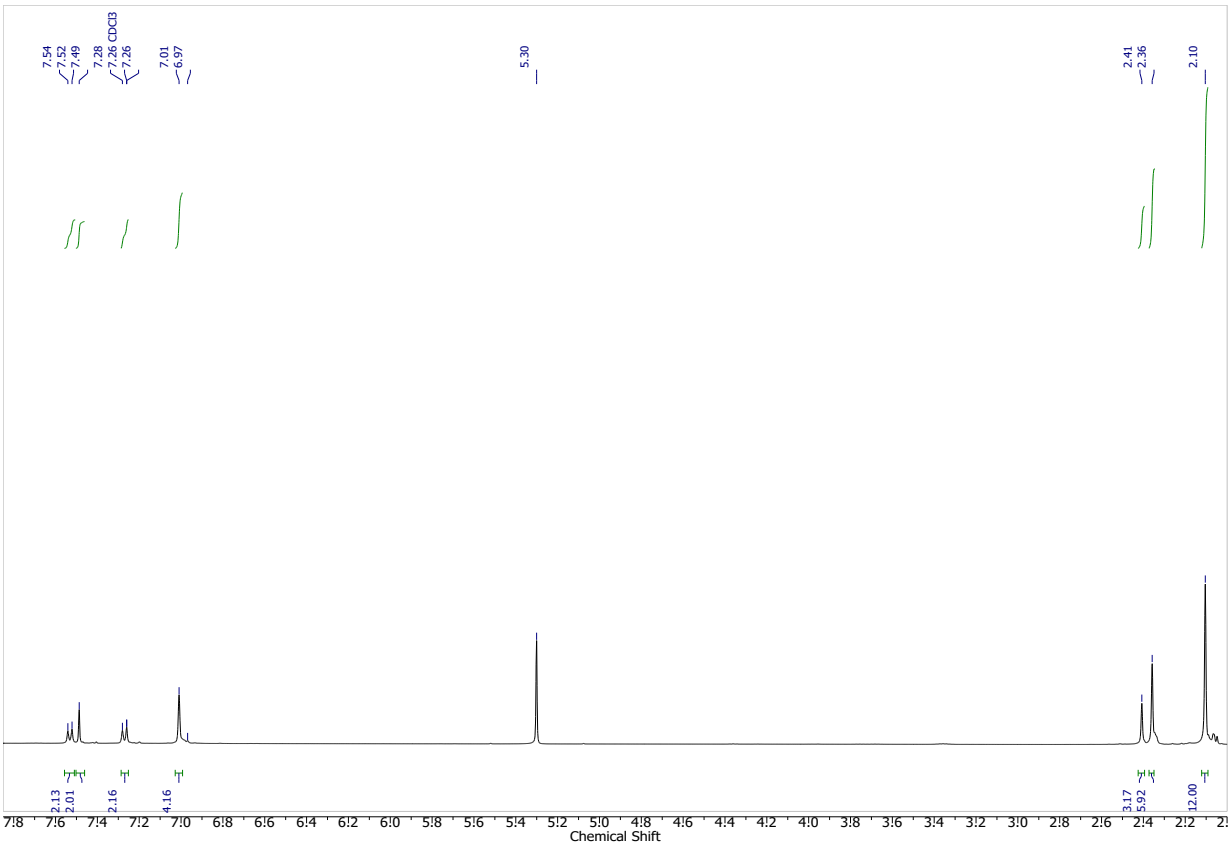

Figure 6.4. ^{1}H-NMR of 1,4-(CNAr^{Mes2})$C_6H_4CH_3$ (**1**) in $CDCl_3$.

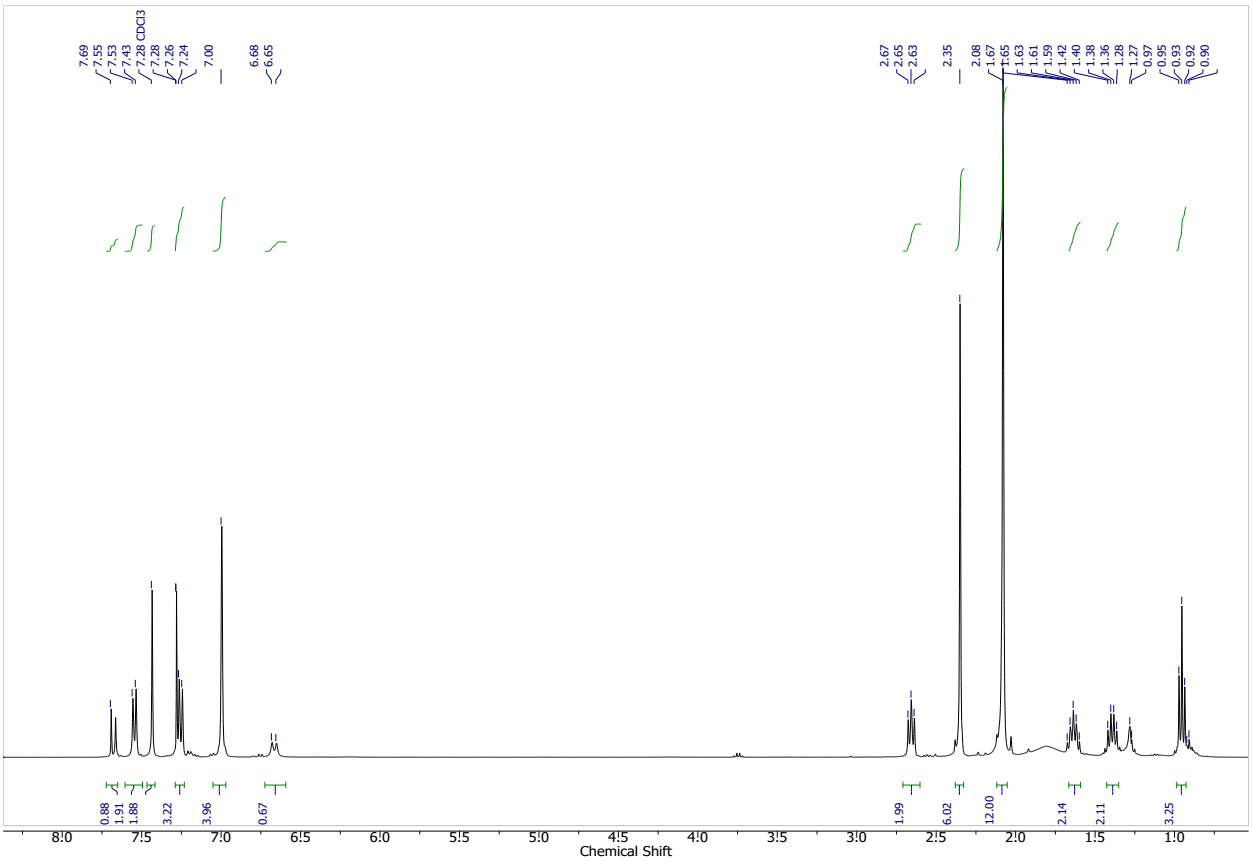

Figure 6.5. ^{1}H-NMR of OHCNHAr^{Mes2}C$_6$H$_4$(CH$_2$)$_3$CH$_3$ in CDCl$_3$.

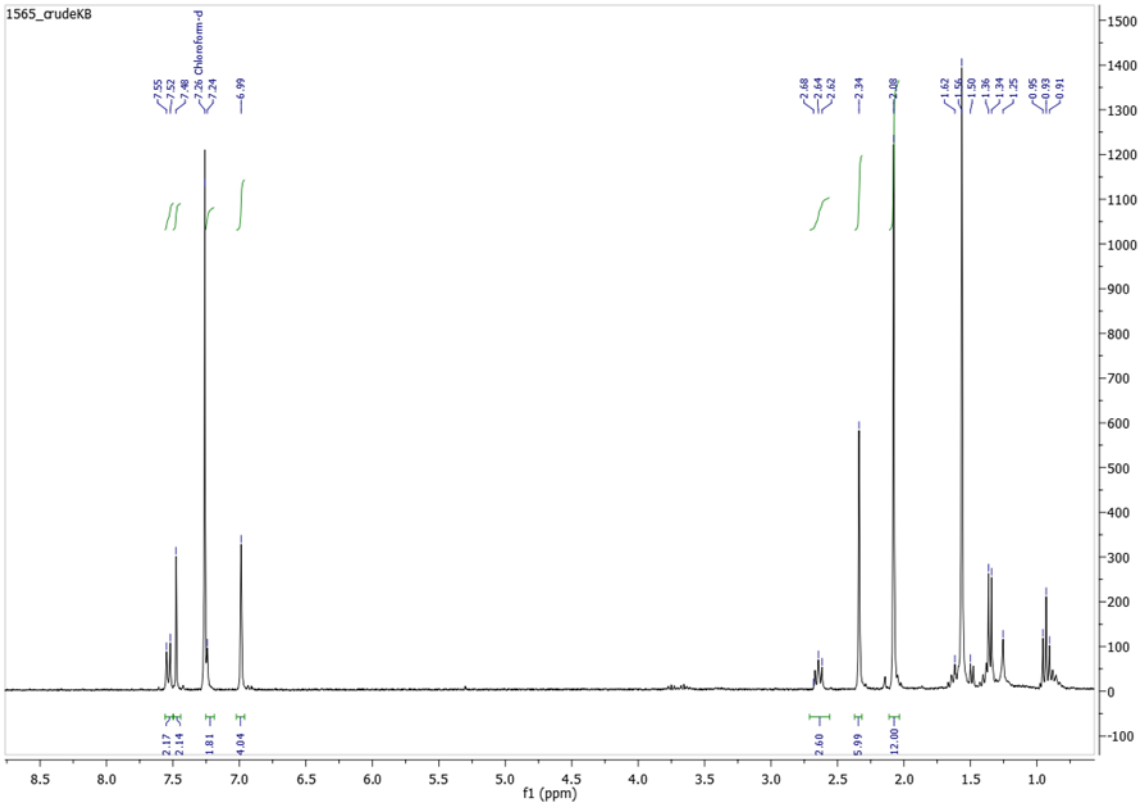

Figure 6.6. ^{1}H-NMR of CNAr^{Mes2}C$_6$H$_4$(CH$_2$)$_3$CH$_3$ (**2**) in CDCl$_3$.

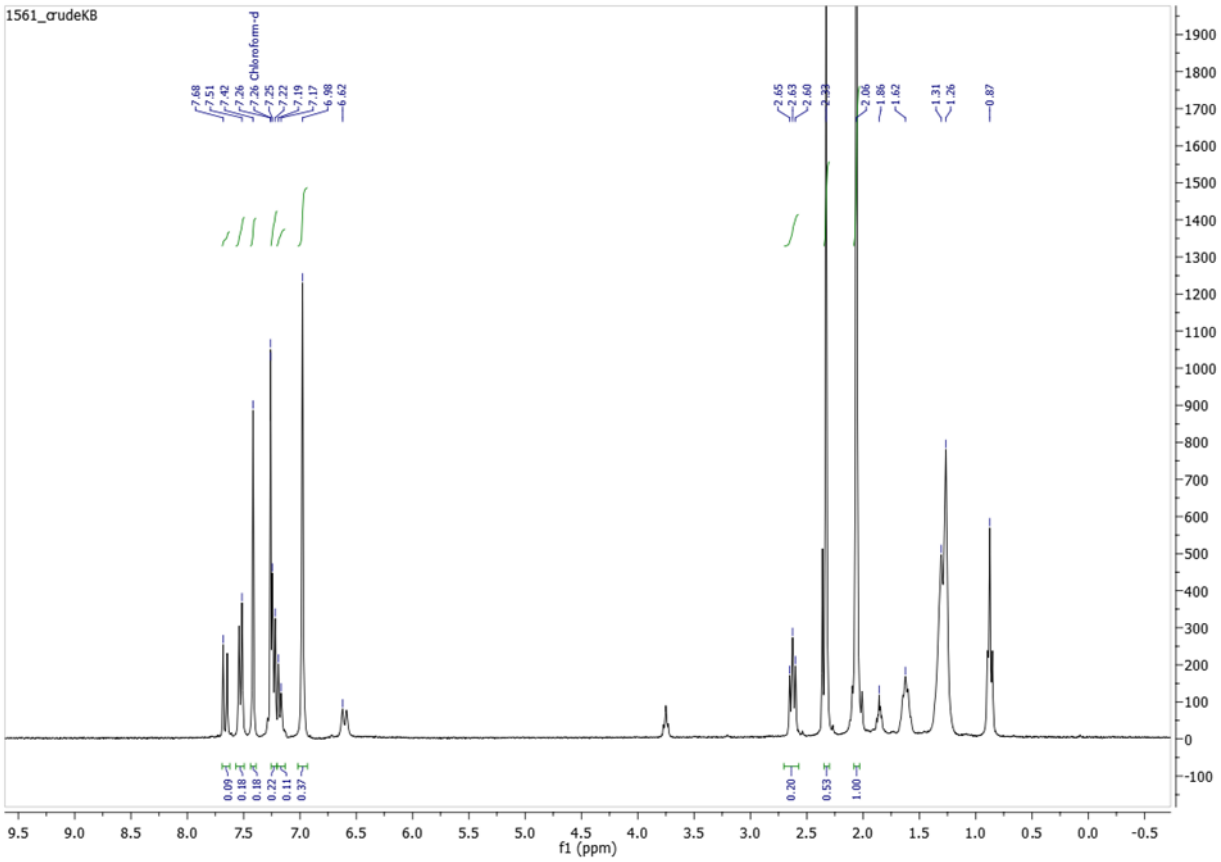

Figure 6.7. ^{1}H-NMR of OHCNHAr^{Mes2}C$_6$H$_4$ ($C_7H_{14}CH_3$) in $CDCl_3$.

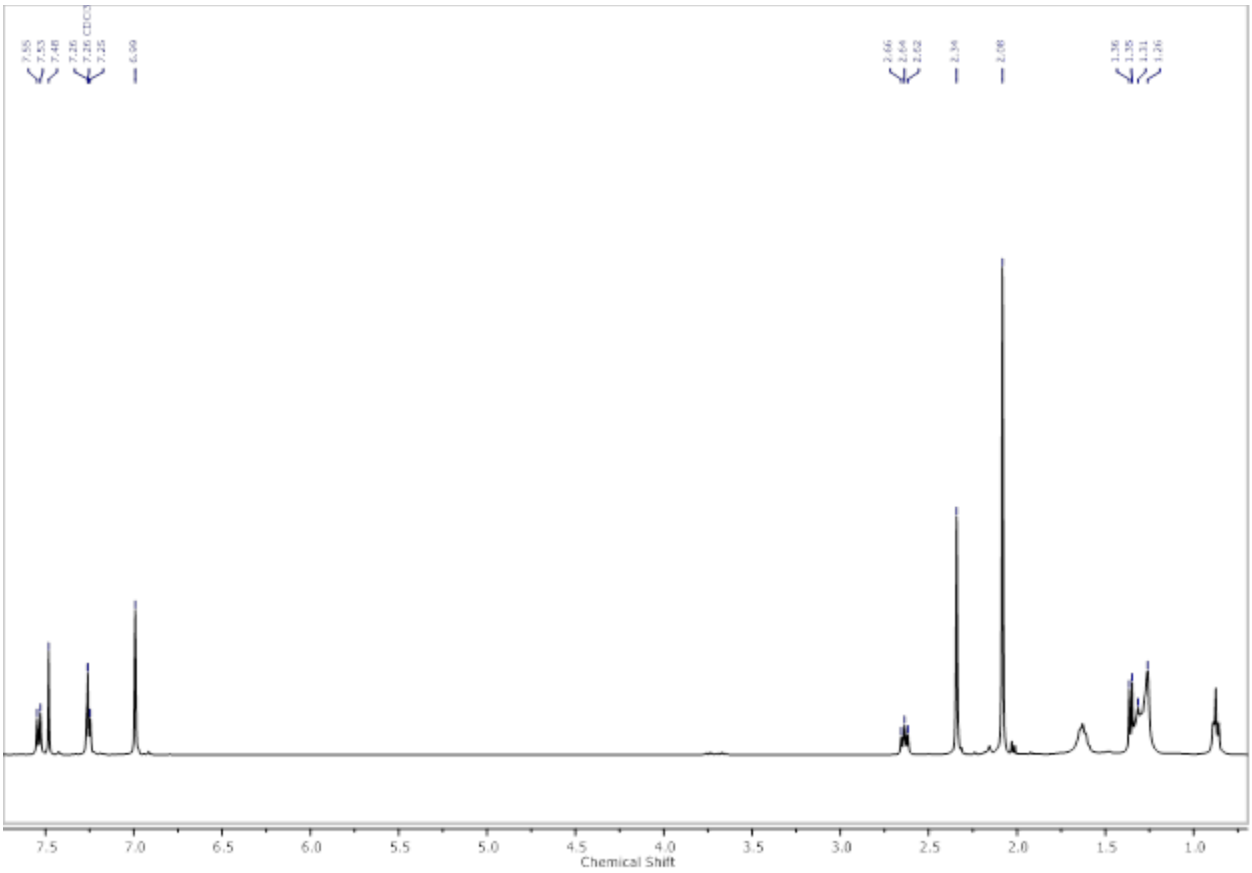

Figure 6.8. ^{1}H-NMR of (**3**) in $CDCl_3$.

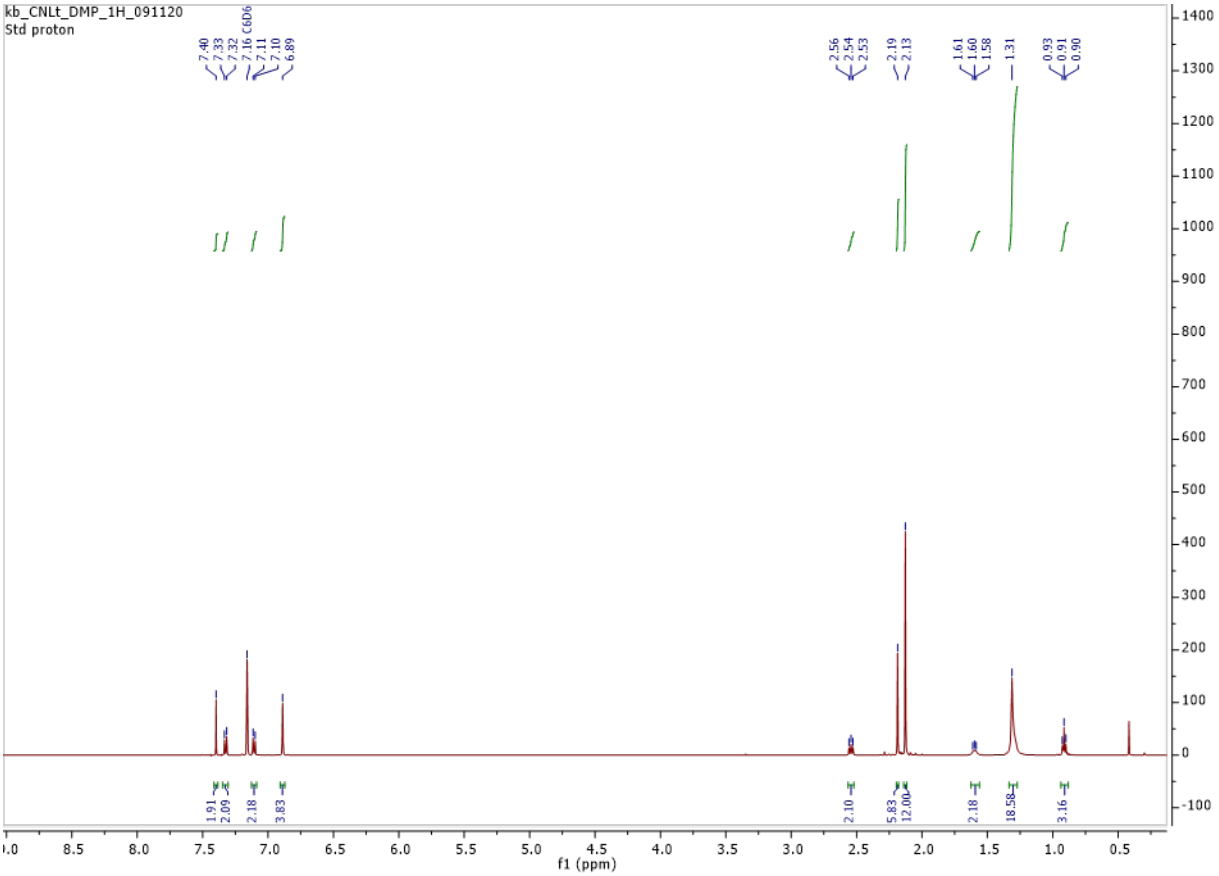

Figure 6.9. ^{1}H-NMR of (**4**) in C_6D_6.

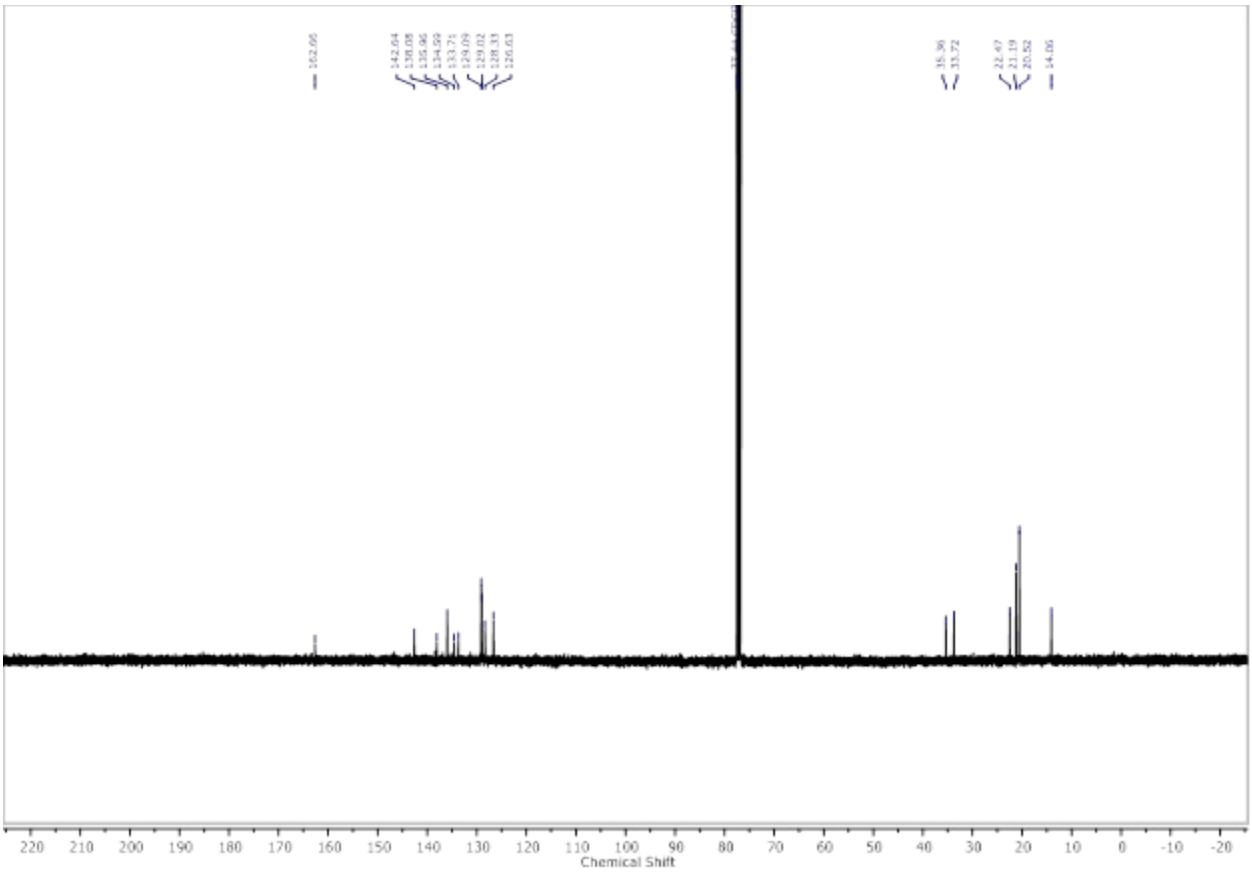

Figure 6.10. ^{13}C-NMR of OHCNHAr^{Mes2}C$_6$H$_4$(CH$_2$)$_3$CH$_3$ in CDCl$_3$.

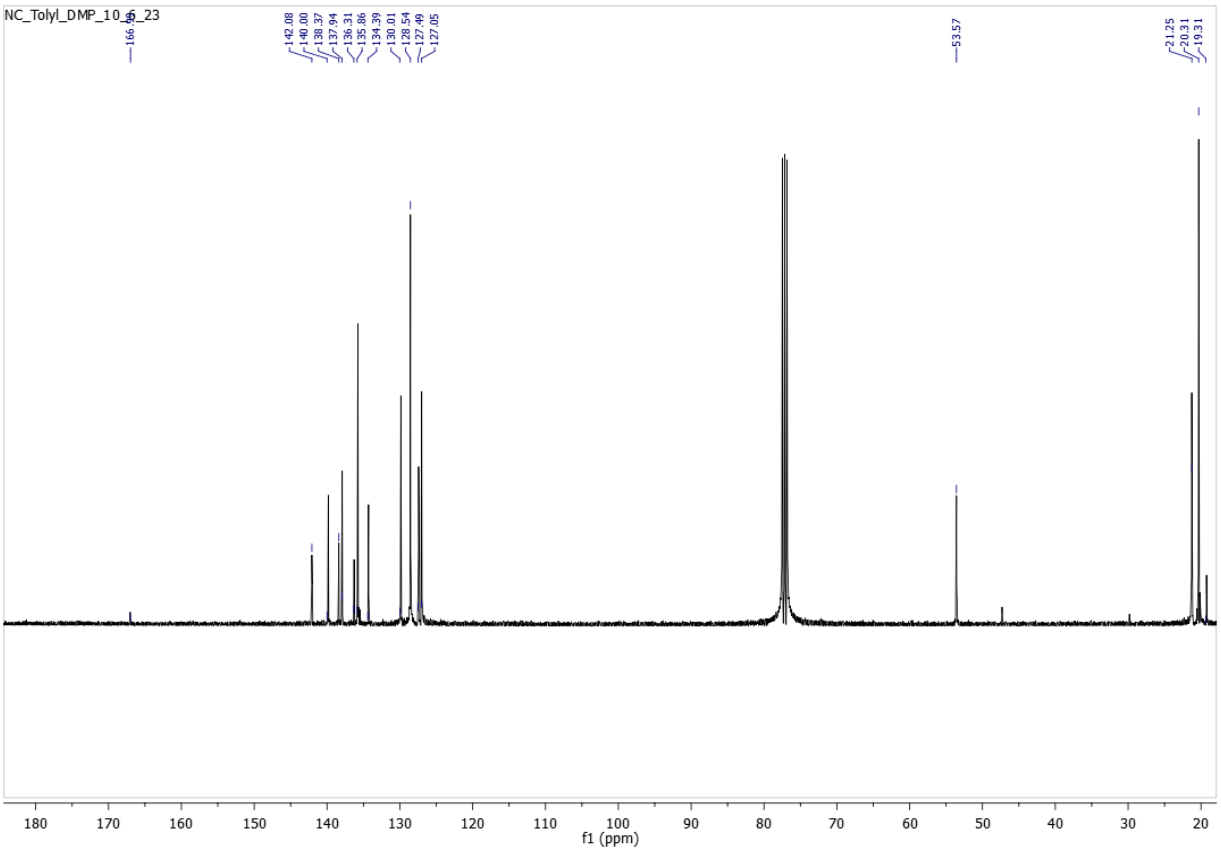

Figure 6.11. ^{13}C-NMR of 1,4-(CNAr^{Mes2})$C_6H_4CH_3$ (**1**) in $CDCl_3$.

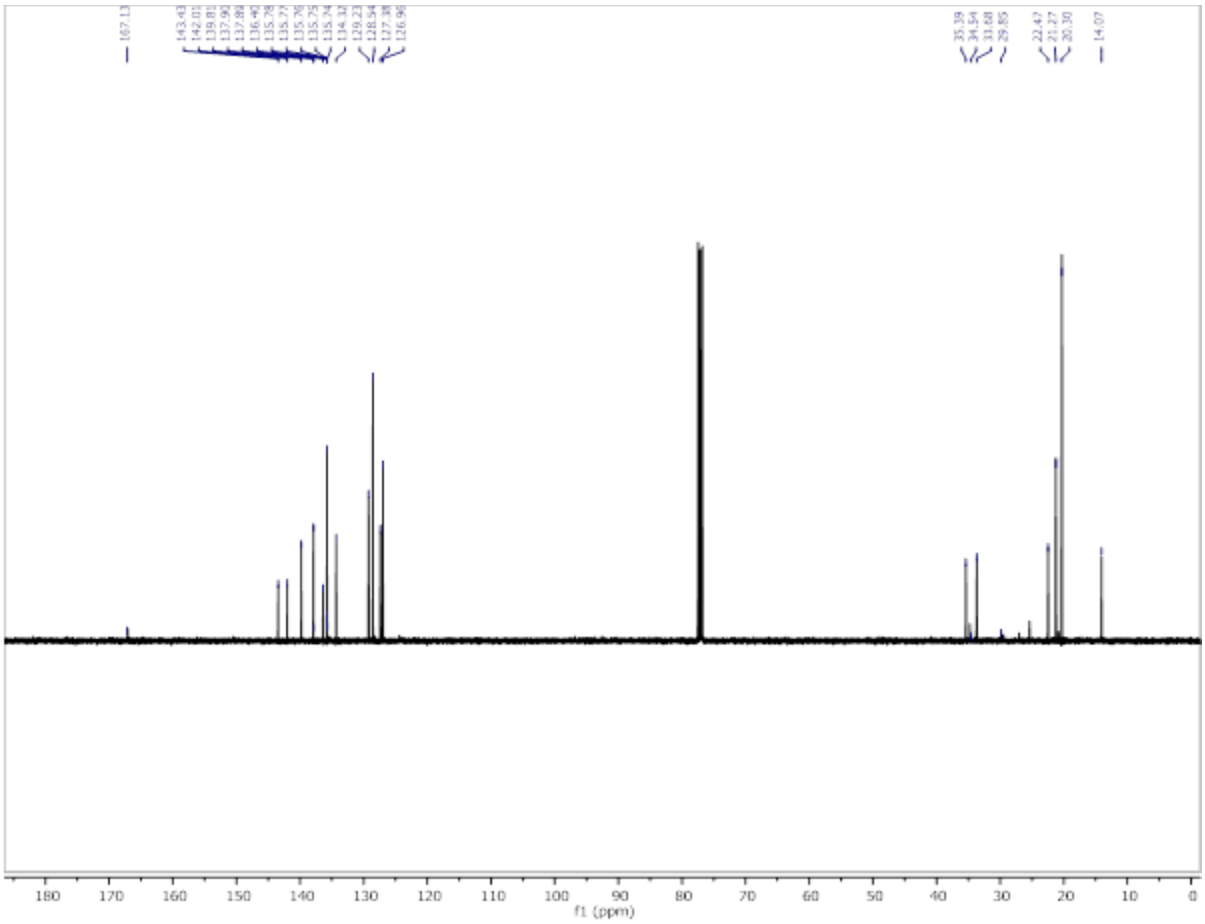

Figure 6.12. ^{13}C-NMR of CNAr^{Mes2}C$_6$H$_4$(CH$_2$)$_3$CH$_3$ (**2**) in CDCl$_3$.

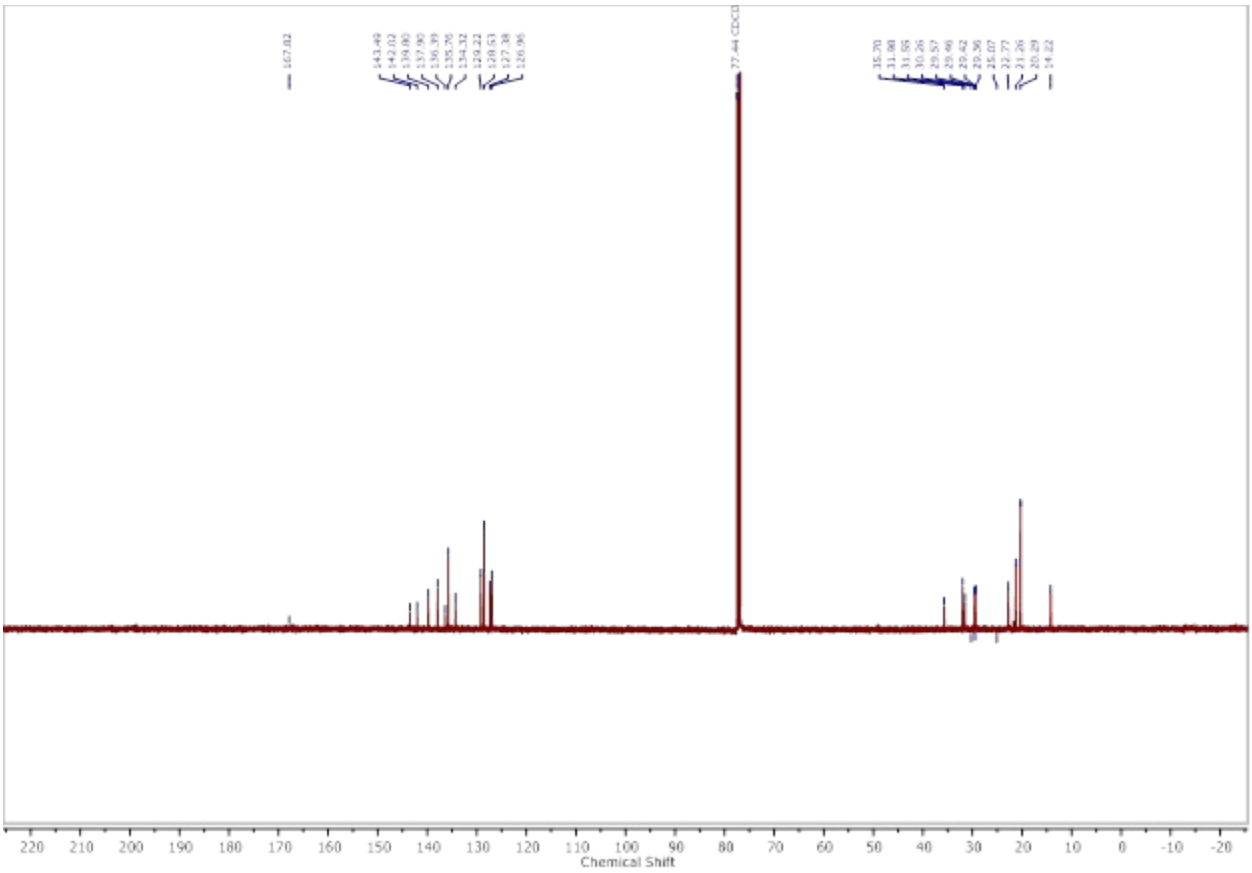

Figure 6.13. ^{13}C-NMR of (**3**) in $CDCl_3$.

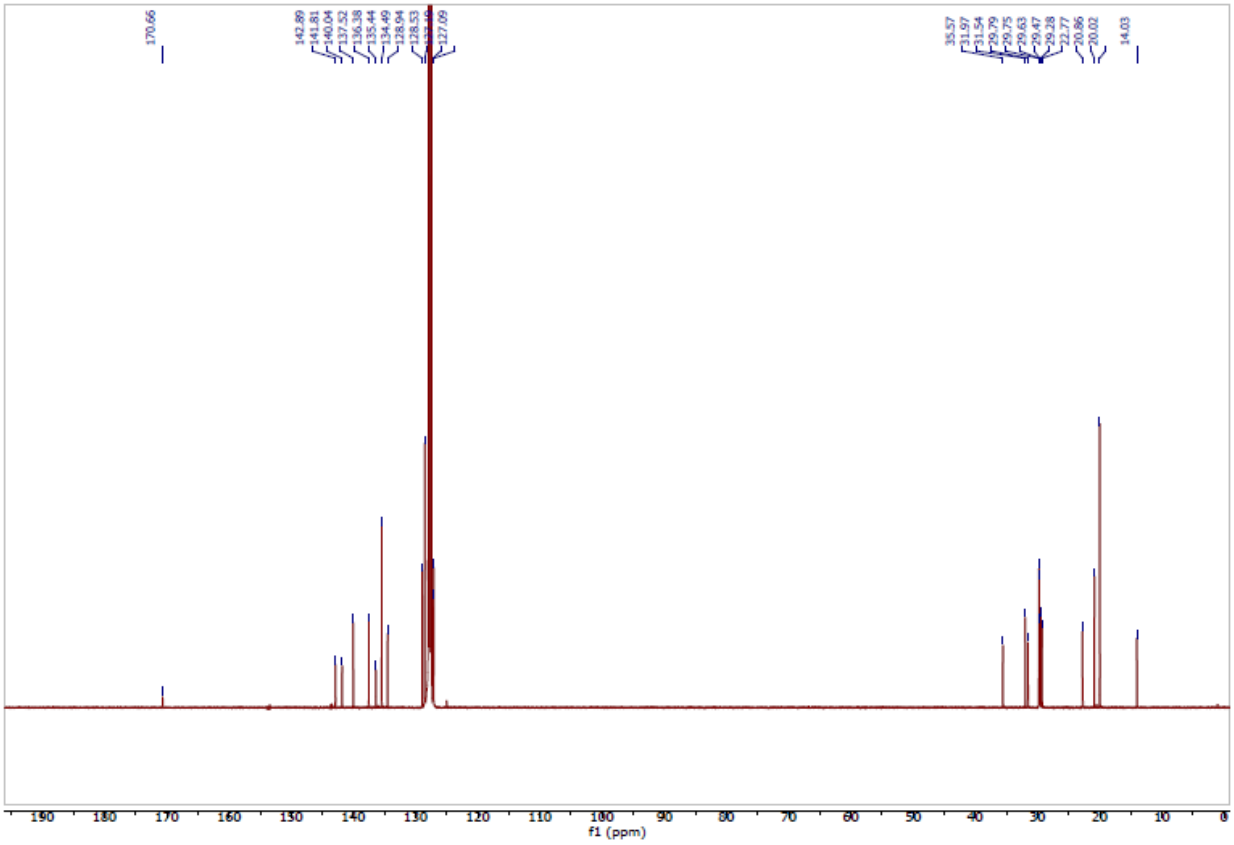

Figure 6.14. ^{13}C-NMR of **2** in $CDCl_3$.

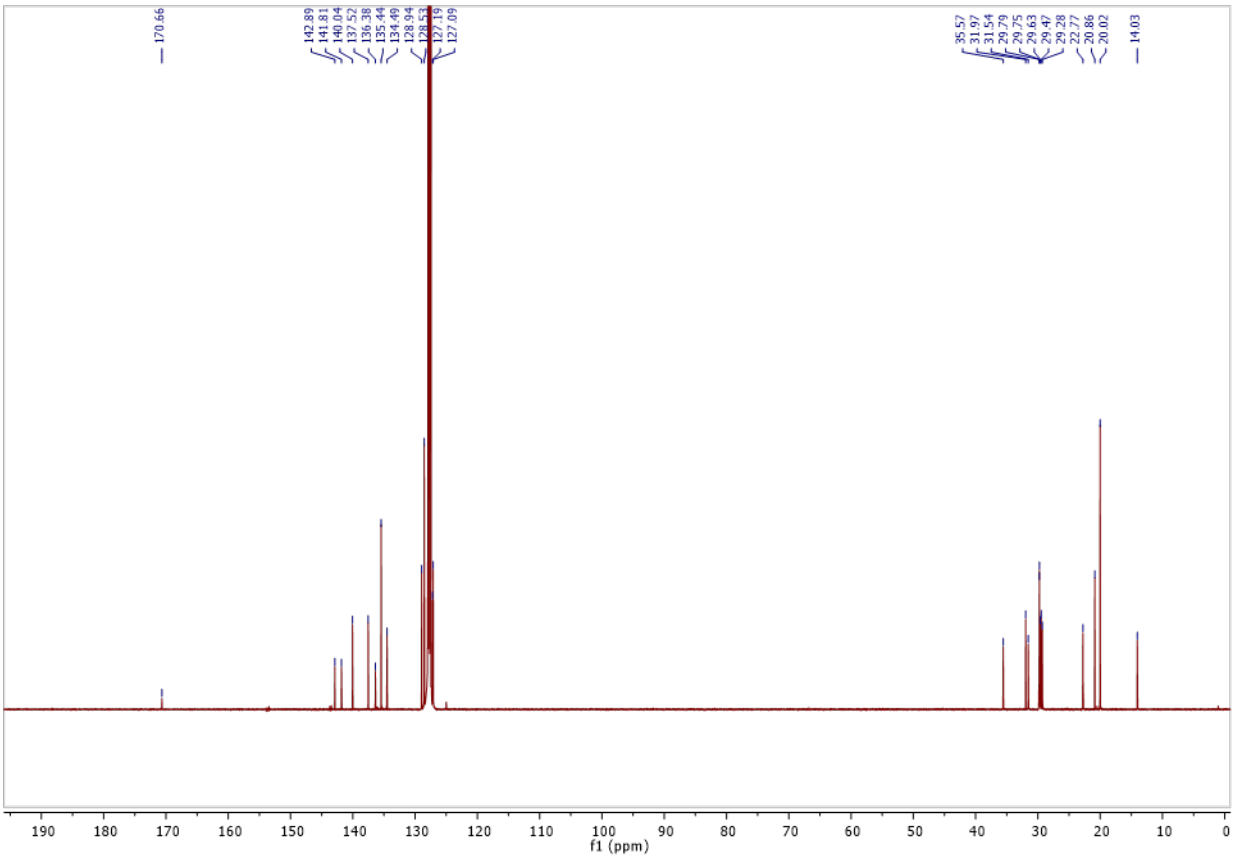

Figure 6.15. ^{13}C-NMR of **4** in C_6D_6.

IR Spectroscopic Data

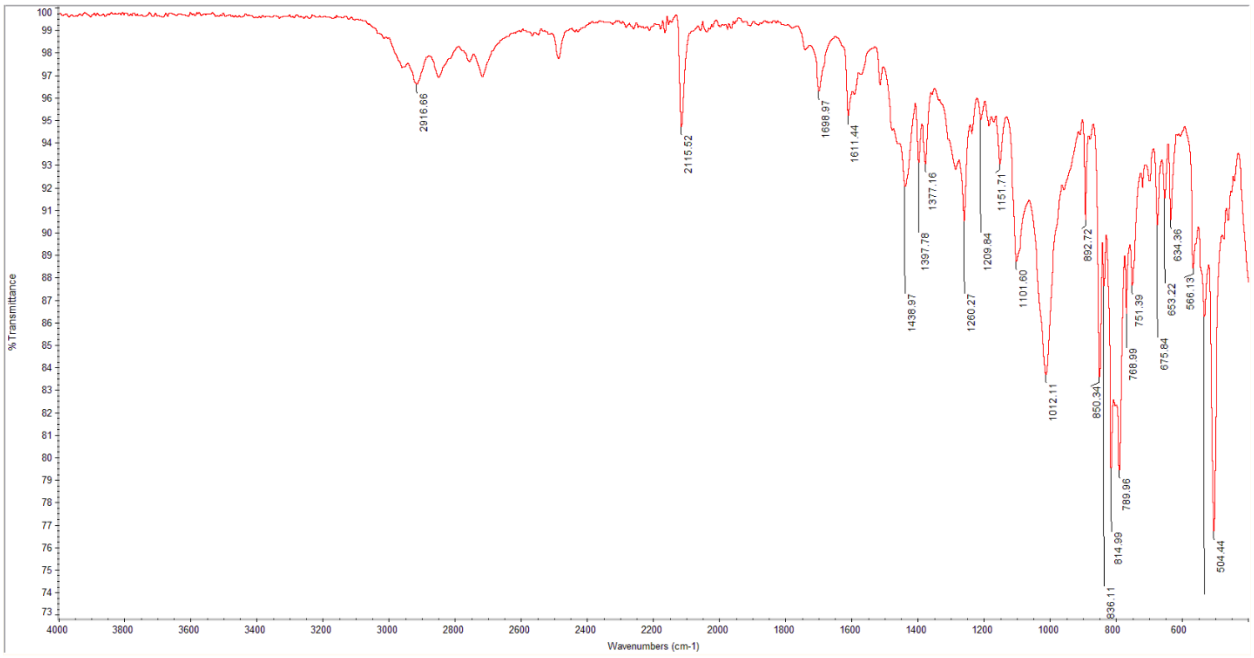

Figure 6.16. ATR-IR of 1,4-(CNAr^{Mes2})$C_6H_4CH_3$ (**1**). Free isocyanide stretching frequency (ν_{CN}) appears at 2116 cm^{-1}.

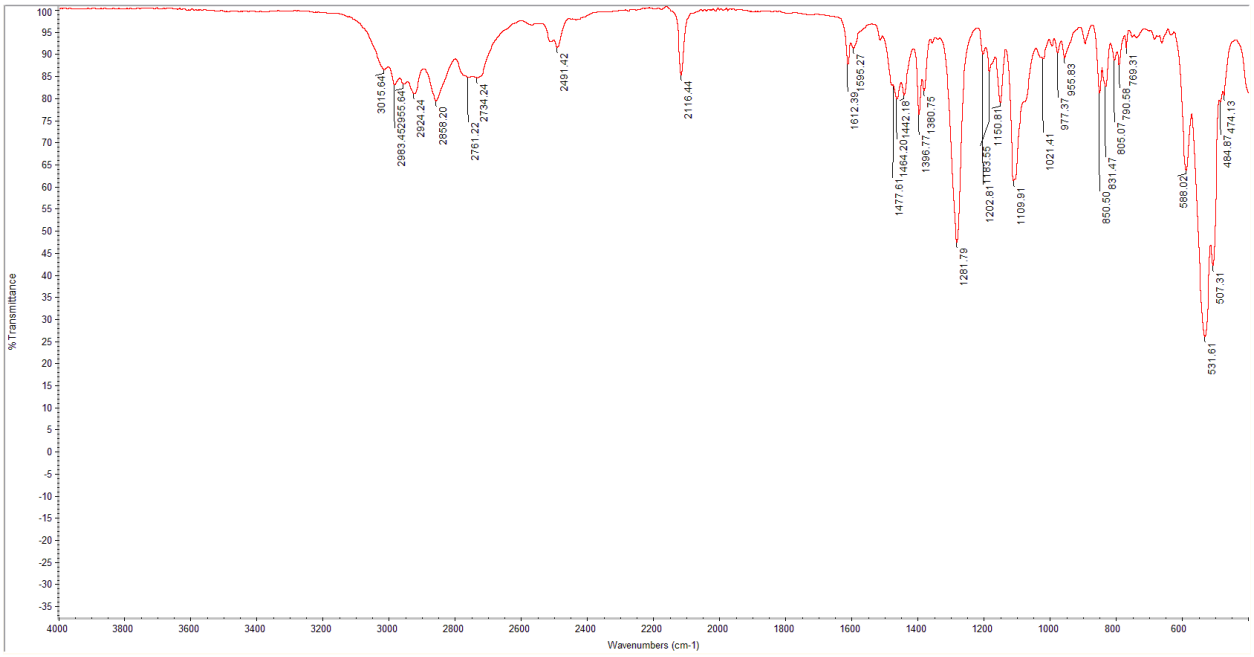

Figure 6.17. ATR-IR spectra of solid CNAr$^{Mes2}C_6H_4(CH_2)_3CH_3$ (**2**).

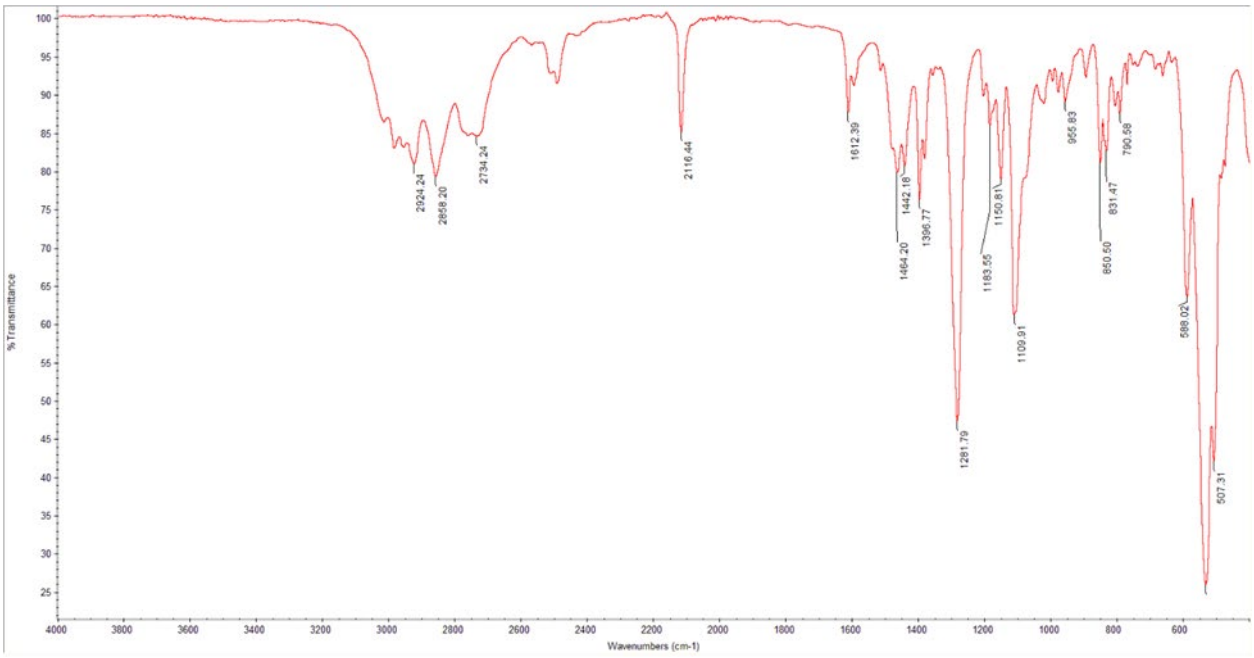

Figure 6.18. ATR-IR of solid $CNAr^{Mes2}C_6H_4(CH_2)_7CH_3$ (**3**). The free isocyanide stretching frequency(n_{CN}) is seen as a sharp peak at 2116 cm^{-1}.

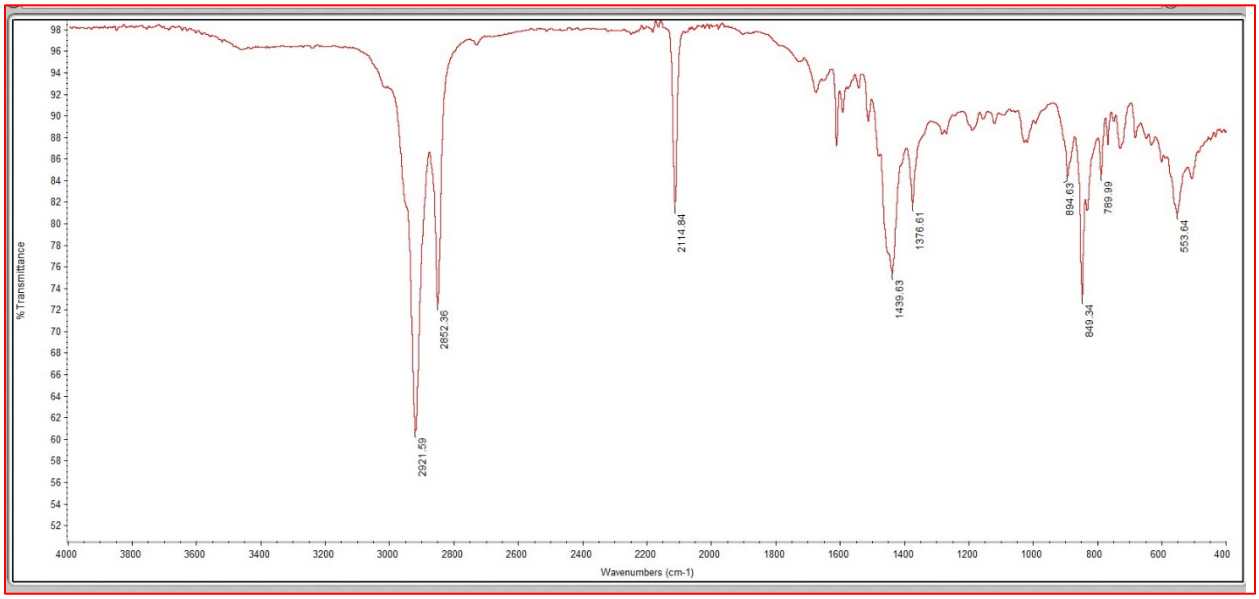

Figure 6.19. ATR-IR of (**4**). The free isocyanide stretching frequency(ν_{CN}) is seen as a sharp peak at 2115 cm^{-1}.

Crystallographic Structure Determination.

Table 6.3. X-Ray crystallographic data collection and refinement information for (**1**).

Name	$OHCNHAr^{Mes2}C_6H_4CH_3$	$CNAr^{Mes2}C_6H_4CH_3$
Formula	$C_{32}H_{33}NO$	$C_{32}H_{32}N$
Crystal System	Orthorhombic	Trigonal
Space Group	Fdd2	R-3
***a*, Å**	27.1064(9)	41.5293(4)
***b*, Å**	42.0117(13)	41.5293(4)
***c*, Å**	17.8973(5)	7.69920(10)
α, deg	90	90
β, deg	90	90
γ, deg	90	120
V, Å^3	20381.2(11)	11499.7(3)
Z	32	18
Radiation (λ, Å)	Cu-Kα, 1.54178	Cu-Kα, 1.54178
ρ (calcd.), g/cm^3	1.167	1.117
μ (Mo Ka), mm^{-1}	0.530	0.481
Temp, K	100	100.15
θ max, deg	70.090	70.098
data/parameters	667	4849/3/281
***R*$_1$**	0.0343(8818)	0.0565
***wR*$_2$**	0.0869(9429)	0.1421
GOF	1.038	1.041

Table 6.4. X-Ray crystallographic data collection and refinement information for (**2**).

Name	$CNAr^{Mes2}C_6H_4(CH_2)_3CH_3$
Formula	$C_{35}H_{37}N$
Crystal System	tetragonal
Space Group	$I4_1/a$
***a*, Å**	25.4647(13)
***b*, Å**	25.4647(13)
***c*, Å**	17.9631(15)
α, deg	90
β, deg	90
γ, deg	90
V, Å^3	11647.2(15)
Z	16
Radiation (l, Å)	MoKα (λ = 0.71073)
r (calcd.), g/cm^3	1.099
m (Mo Ka), mm^{-1}	0.063
Temp, K	100.15
q max, deg	24.797
data/parameters	5000/4/373
R_1	0.0787
wR_2	0.2134
GOF	1.042

Table 6.5. X-Ray crystallographic data collection and refinement information for $Ni(COD)L_2$, L = (**3**).

Name	$Ni(COD)L_2$, L = (**3**)
Formula	$C_{86}H_{102}N_2Ni$
Crystal System	triclinic
Space Group	P-1
***a*, Å**	14.2089(6)
***b*, Å**	15.6653(6)
***c*, Å**	17.0710(7)
α, deg	92.194(1)
β, deg	111.709(2)
γ, deg	91.338(2)
V, Å^3	3524.8(3)
Z	2
Radiation (l, Å)	CuKα (λ = 1.54178)
ρ (calcd.), g/cm^3	1.152
μ (Mo Ka), mm^{-1}	00.732
Temp, K	100.15
θ max, deg	66.640
data/parameters	12101/0/848
***R*$_1$**	0.0445
***wR*$_2$**	0.1123
GOF	1.034

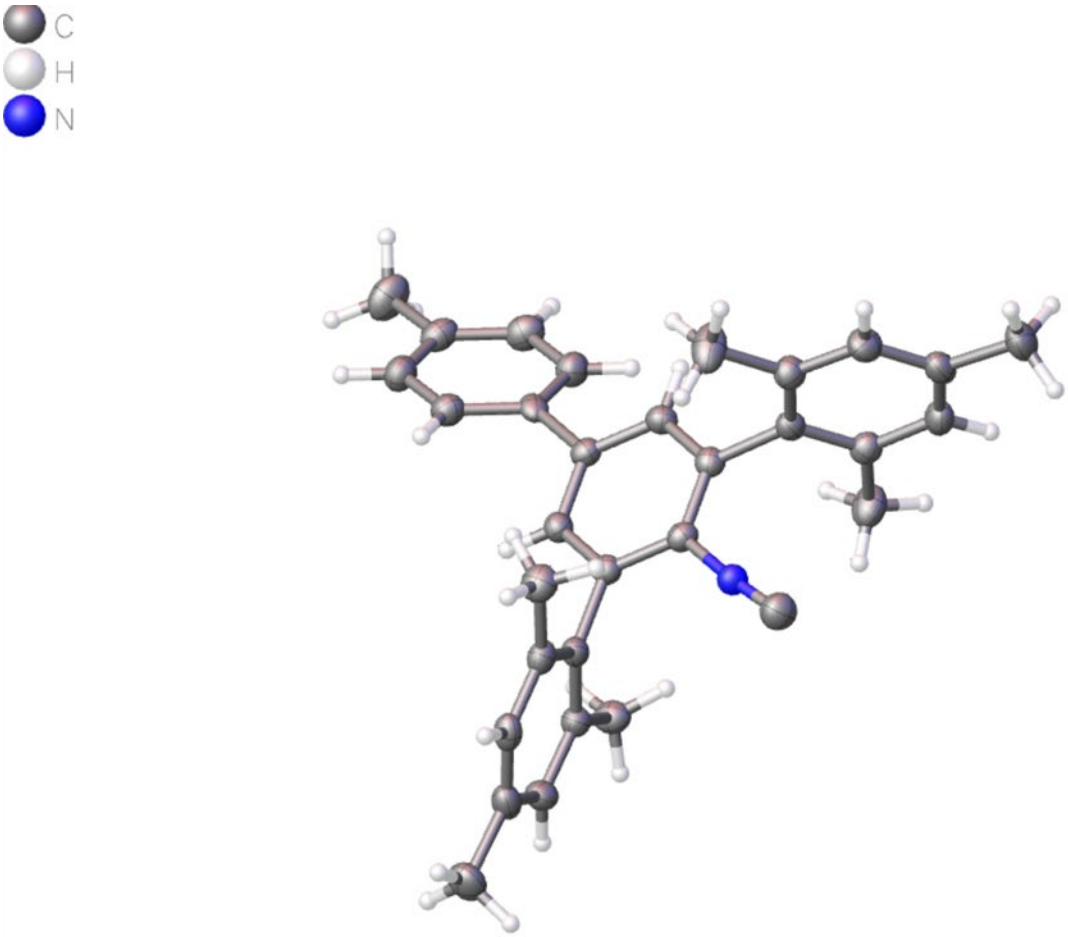

Figure 6.20. X-ray crystal structure of $CNAr^{Mes2}C_6H_4CH_3$ (**1**).

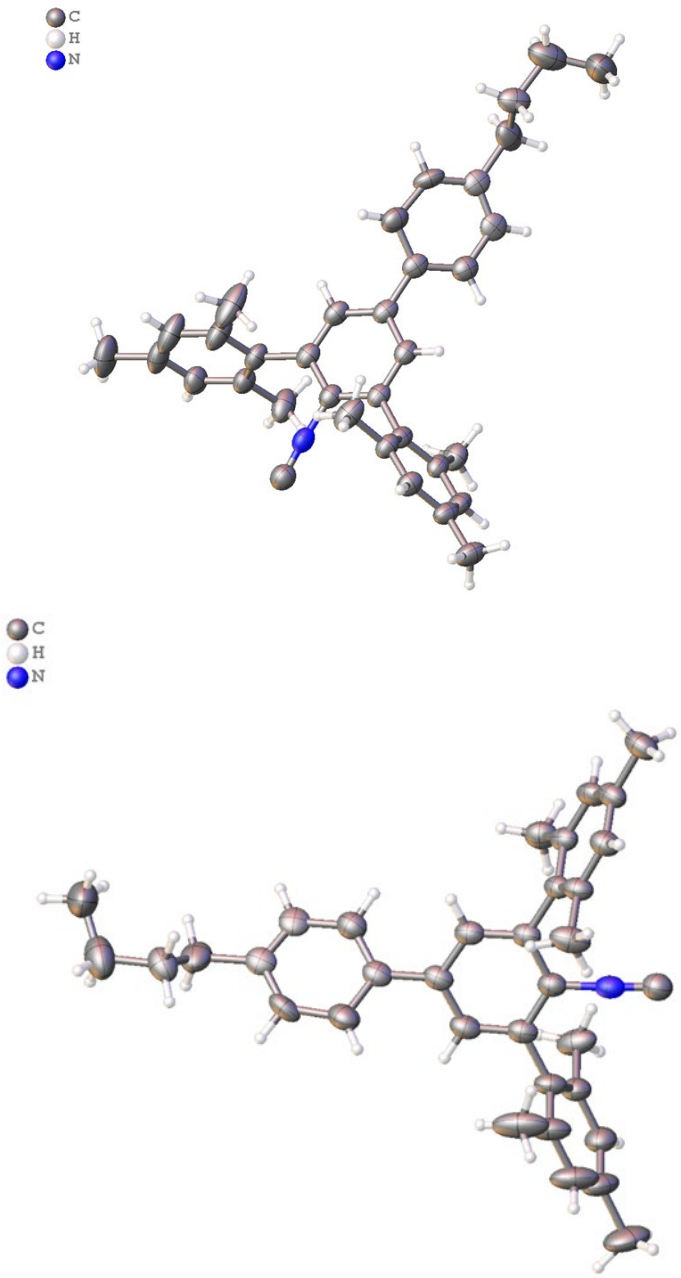

Figure 6.21. X-Ray crystal structure of $CNAr^{Mes2}C_6H_4(CH_2)_3CH_3$ (**2**) from two different views.

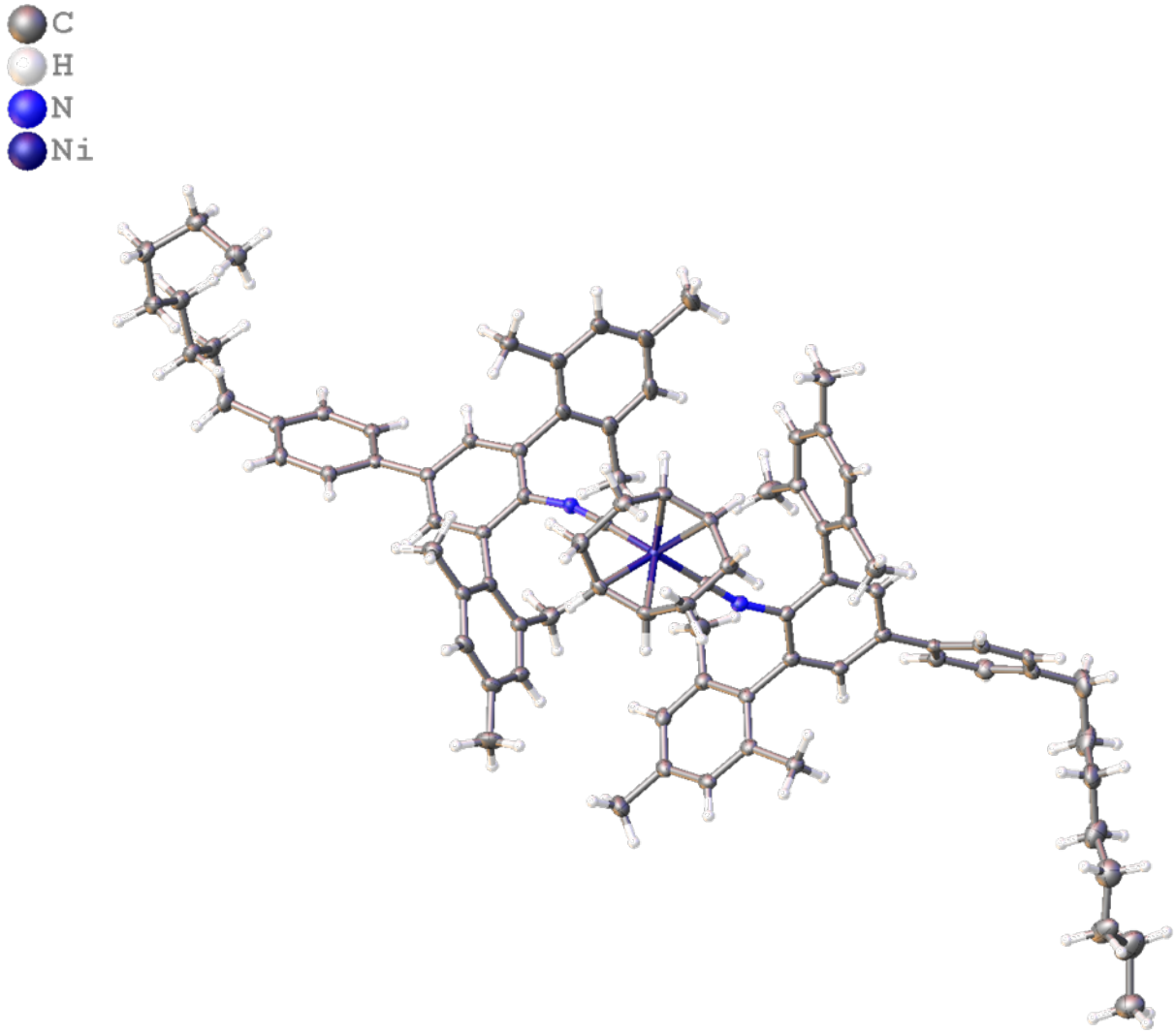

Figure 6.22. X-Ray crystal structure of Ni(COD)L_2, L = (**3**). While (3) was not isolated as a free isocyanide molecule, reaction with a transition-metal allowed for structural confirmation and characterization of (**3**). It is worth mentioning the bond lengths in metal-bound (**3**) are likely not the same as free (**3**).

Nanocrystal Characterization

Transmission electron microscopy (TEM) images were collected using a ThermoFisher Talos 200X TEM with an operation voltage of 200 kV. Samples were prepared by drop-casting AuNP solutions on copper grids and allowed to settle overnight in closed vials. UV–visible absorption measurements were performed on Cary 50/60 UV-Vis spectrophotometer. Raman measurements were performed on Renishaw 25 micro-Raman spectrometer (Renishaw Invia) coupled with a Leica microscope with 50× objective (Leica N-plan) in the range of 800−2400 cm−1 . A

wavelength of 532 nm was used as an excitation source generated by 50 mW Ar-Ion LASER. Zeta potential values were measured using a Malvern NANO-ZS90 Zetasizer.

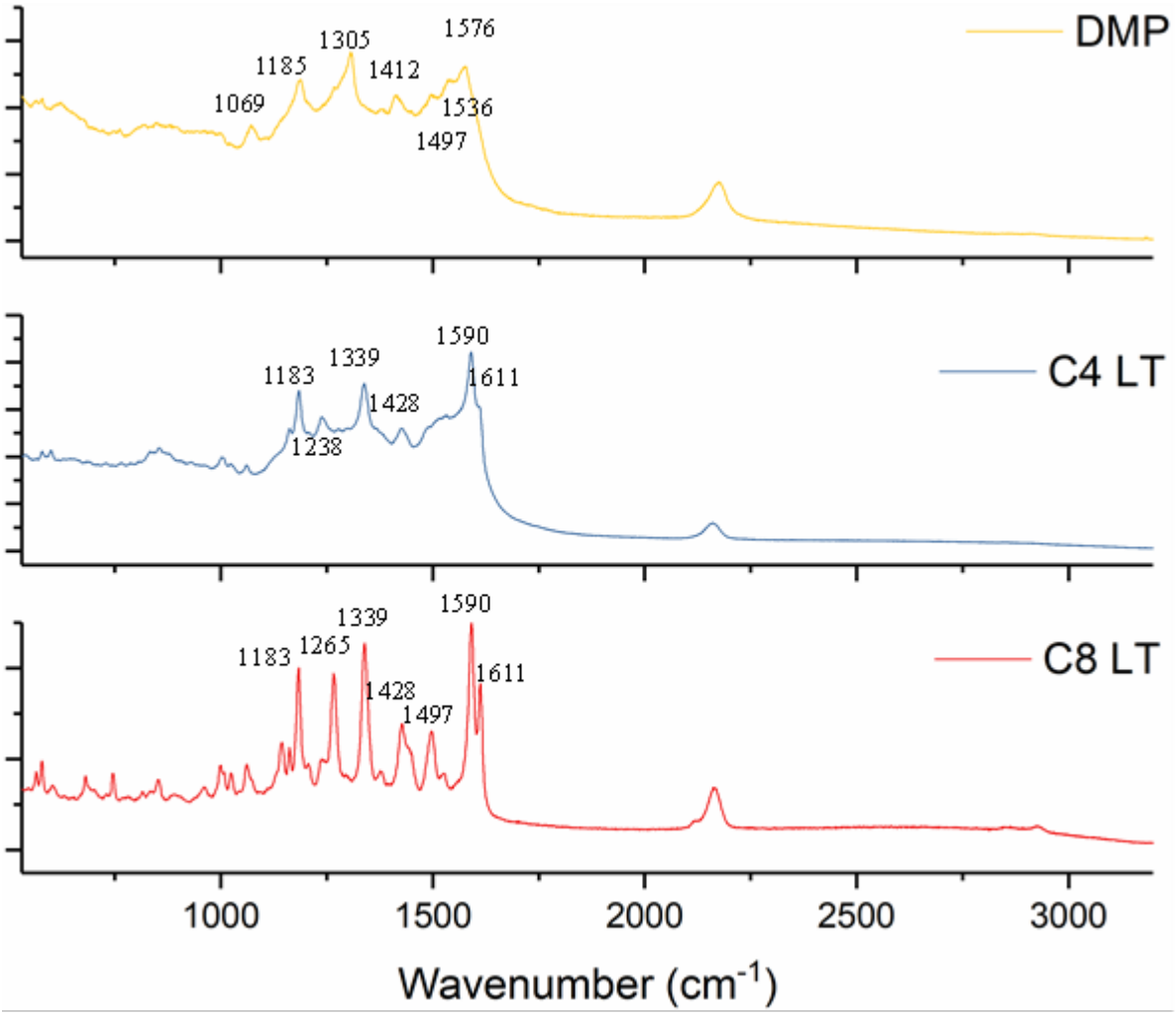

Figure 6.23. SERS (532nm) taken on a sample of 20 nm AuNSs capped with (top) $CNAr^{Mes2}$, (middle) (**2**) and (bottom) (3) after LLE. The blue-shifted isocyanide stretching frequency (relative to free ν_{CN} = 2116 cm^{-1}) observed between ν_{CN} = 2147 and 2160 cm^{-1} is indicative of the ligand binding to gold.

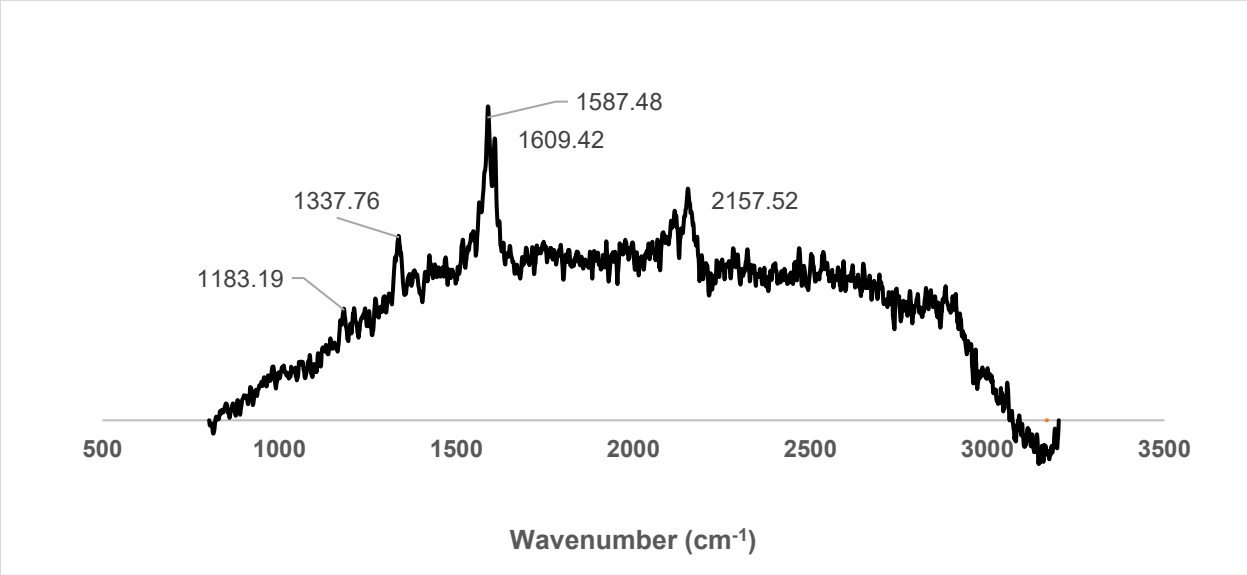

Figure 6.24. SERS (532 nm) taken on a sample of 20 nm AuNSs capped with (**1**) after LLE. Binding of the isocyanide is confirmed by the isocyanide stretching frequency observed at ν_{CN} = 2157 cm^{-1}. Some free (**3**) is observed at ν_{CN} = 2116 cm^{-1} in this spectrum.

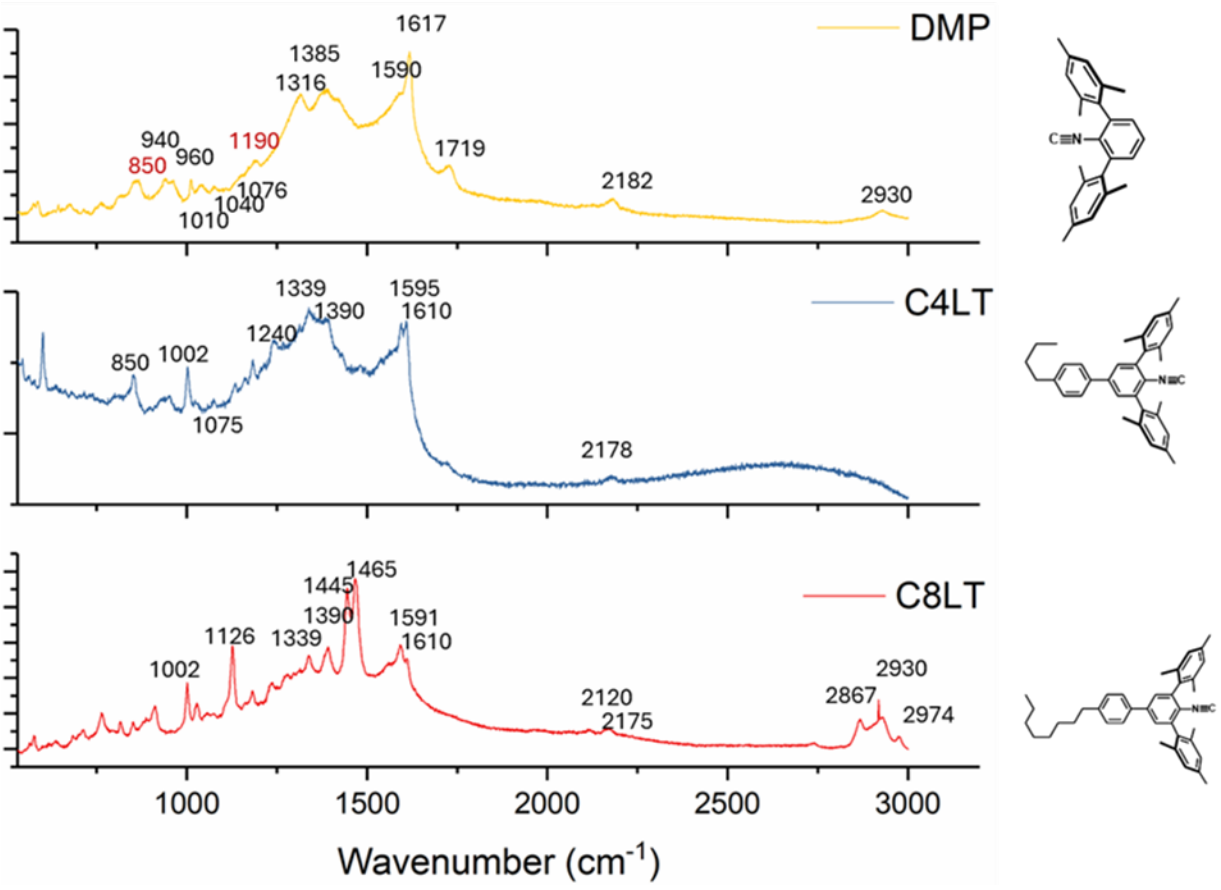

Figure 6.25. SERS spectra of 50 nm AgNSs capped with ligands (**2**) and (**3**) after LLE. The isocyanide stretching frequency observed at ν_{CN} = 2175 cm^{-1} is indicative of isocyanide binding to Ag(I).

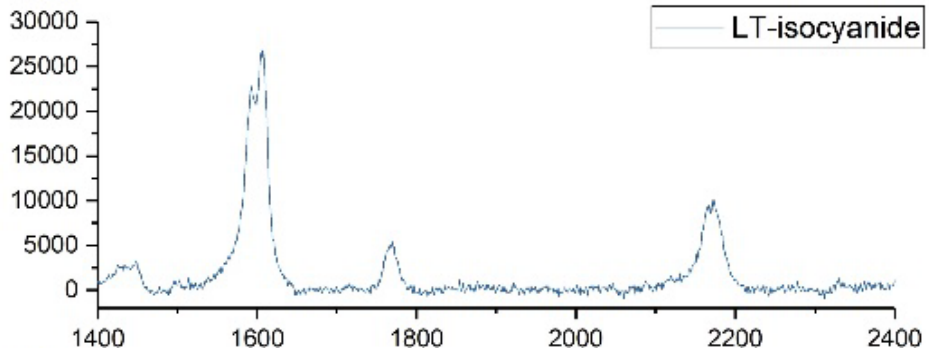

Figure 6.26. SERS (532 nm) taken on a sample of 20 nm AgNSs capped with (**4**) after LLE. Binding of the isocyanide is confirmed by the isocyanide stretching frequency observed at ν_{CN} = 2190 cm^{-1}.

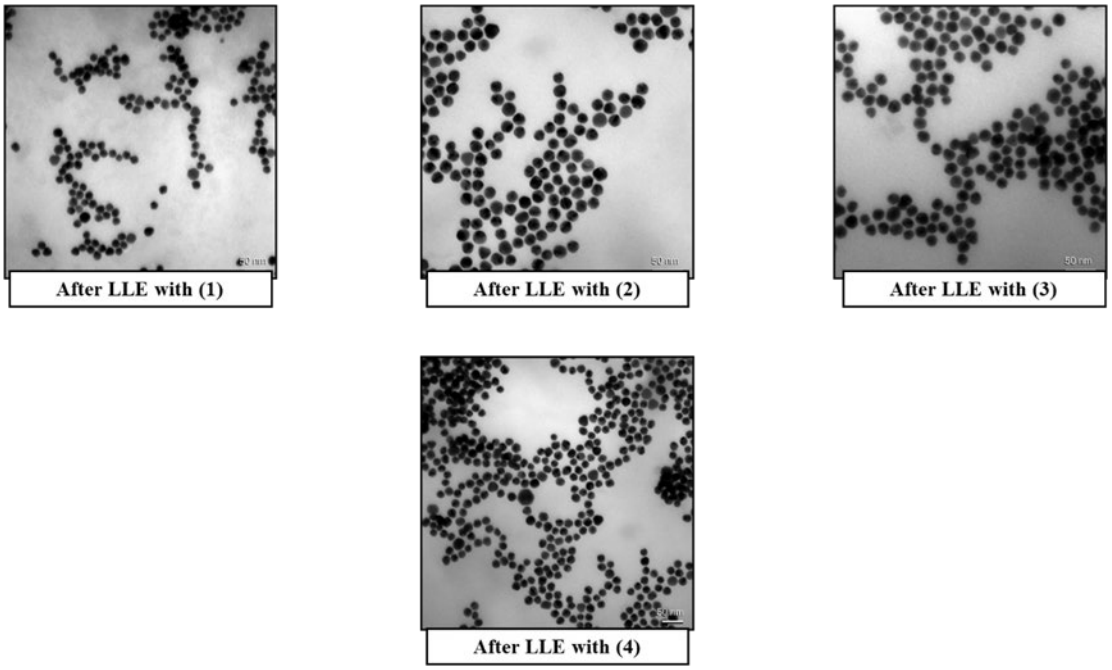

Figure 6.27. TEM images of 20nm AuNSs after LLE with isocyanide ligands **1-4**.

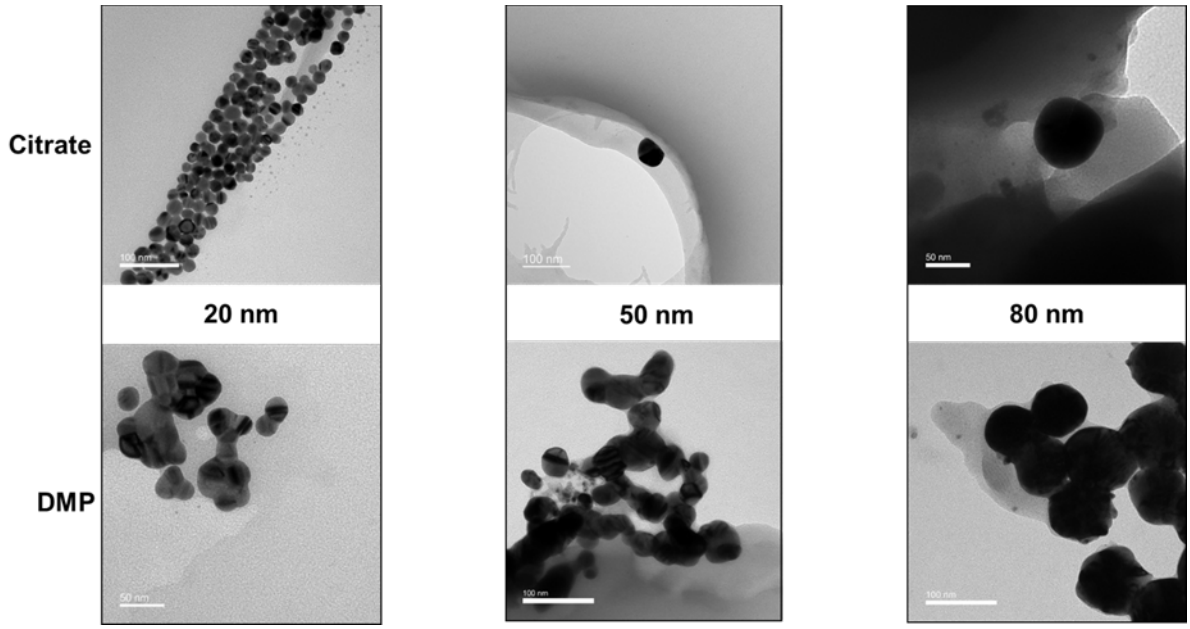

Figure 6.28. TEM images of AgNSs before (top) and after (bottom) LLE with $CNAr^{Mes2}$.

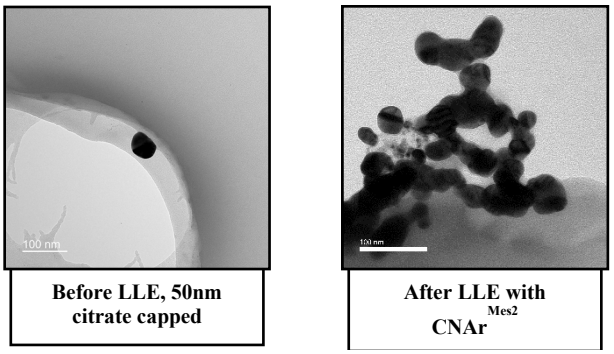

Figure 6.29. TEM Images of 50nm AgNSs after LLE with isocyanide ligands **1-4.** Some fusion of AgNSs is occurring based on TEM images after LLE with *m*-terphenyl isocyanide ligands.

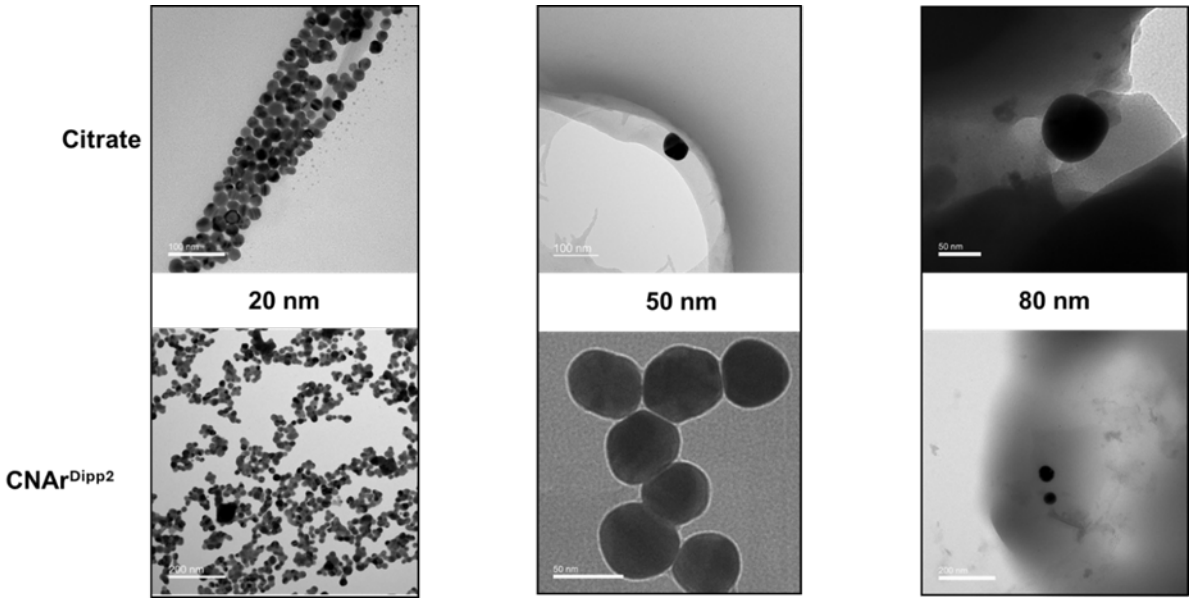

Figure 6.30. TEM images of AgNSs before (top) and after (bottom) LLE with $CNAr^{Dipp2}$.

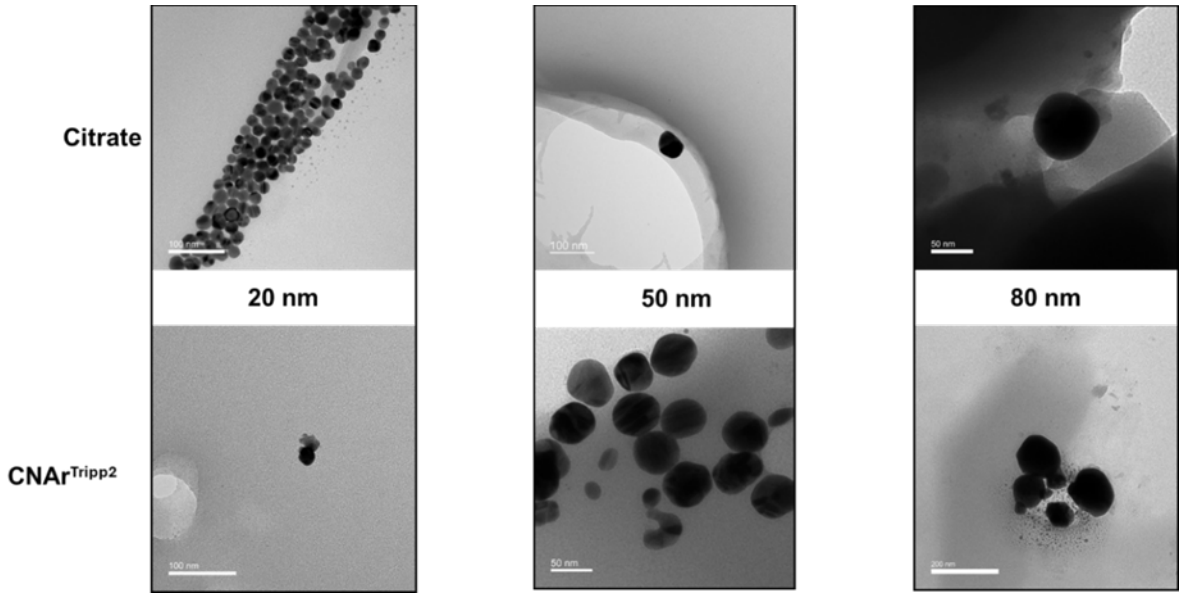

Figure 6.31. TEM images of AgNSs before (top) and after (bottom) LLE with CNAr^{Tripp2}.

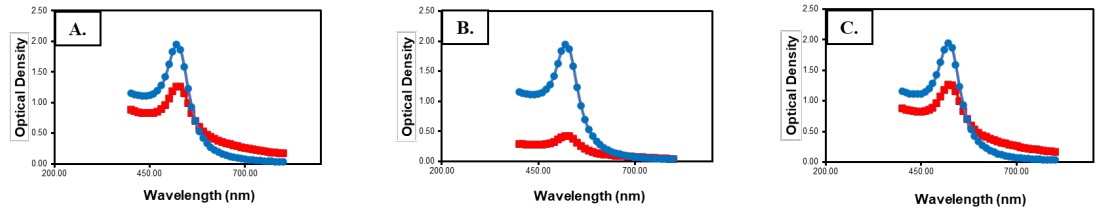

Figure 6.32. UV-Vis measurements taken of aqueous layer before (blue) and after (red) LLE on 20nm AuNSs for (left) (**1**), (middle) (**2**), and (right) (**3**) capping ligands.

6.5. References.

(1) Gavenonis, J.; Tilley, T. D. "Tantalum alkyl and silyl complexes of the bulky (terphenyl)imido ligand [2,6-(2,4,6-MeCH)CHN=]([Ar*N=]).: Generation and reactivity of [(Ar*N=)(Ar*NH)Ta(H)(OSOCF)], which reversibly transfers hydride to an aromatic ring of the arylamide ligand" *Organometallics* **2002**, *21*, 5549.

(2) Clyburne, J. A. C.; McMullen, N. "Unusual structures of main group organometallic compounds containing -terphenyl ligands" *Coordin Chem Rev* **2000**, *210*, 73.

(3) Dickie, D. A.; MacIntosh, I. S.; Ino, D. D.; He, Q.; Labeodan, J. A.; Jennings, M. C.; Schatte, G.; Walsby, C. J.; Clyburne, J. A. C. "Synthesis of the bulky -terphenyl phenol Ar*OH (Ar* =CH-2,6-Mes, Mes=2,4,6-trimethylphenyl) and the preparation and structural characterization of several of its metal complexes" *Can J Chem* **2008**, *86*, 20.

(4) Ditri, T. B.; Fox, B. J.; Moore, C. E.; Rheingold, A. L.; Figueroa, J. S. "Effective Control of Ligation and Geometric Isomerism: Direct Comparison of Steric Properties Associated with Bis-mesityl and Bis-diisopropylphenyl -Terphenyl Isocyanides" *Inorg Chem* **2009**, *48*, 8362.

(5) Emerich, B. M.; Moore, C. E.; Fox, B. J.; Rheingold, A. L.; Figueroa, J. S. "Protecting-Group-Free Access to a Three-Coordinate Nickel(0) Tris-isocyanide" *Organometallics* **2011**, *30*, 2598.

(6) Margulieux, G. W.; Weidemann, N.; Lacy, D. C.; Moore, C. E.; Rheingold, A. L.; Figueroa, J. S. "Isocyano Analogues of [Co(CO)]: A Tetraisocyanide of Cobalt Isolated in Three States of Charge" *J Am Chem Soc* **2010**, *132*, 5033.

(7) Wang, S.; Figueroa, J. "Synthesis, structure, and reactivity of bulky isocyanides supported unsaturated chromium dianion species" *Abstr Pap Am Chem S* **2019**, *258*.

(8) Molchtarzadeh, C. C.; Margulieux, G. W.; Carpenter, A. E.; Weidemann, N.; Moore, C. E.; Rheingold, A. L.; Figueroa, J. S. "Synthesis and Protonation of an Encumbered Iron Tetraisocyanide Dianion" *Inorg Chem* **2015**, *54*, 5579.

(9) Cotton, F. A.; Zingales, F. "Donor-Acceptor Properties of Isonitriles as Estimated by Infrared Study" *J Am Chem Soc* **1961**, *83*, 351.

(10) Yamamoto, Y. "Zerovalent Transition-Metal Complexes of Organic Isocyanides" *Coordin Chem Rev* **1980**, *32*, 193.

(11) Wang, Y. F.; Chen, A. A.; Balto, K. P.; Xie, Y.; Figueroa, J. S.; Pascal, T. A.; Tao, A. R. "Curvature-Selective Nanocrystal Surface Ligation Using Sterically-Encumbered Metal-Coordinating Ligands" *Acs Nano* **2022**.

(12) Xiong, H. L.; Yuan, Y. Z.; Li, H.; Zhu, H. L.; Jiang, X. J. "Computer simulation of colloidal aggregation induced by directionalism of long range van der Waals forces" *Acta Phys-Chim Sin* **2007**, *23*, 1241.

(13) Xiong, Y.; Liu, X. M.; Xiong, H. L. "Aggregation modeling of the influence of pH on the aggregation of variably charged nanoparticles" *Sci Rep-Uk* **2021**, *11*.

(14) Heuer-Jungemann, A.; Feliu, N.; Bakaimi, I.; Hamaly, M.; Alkilany, A.; Chakraborty, I.; Masood, A.; Casula, M. F.; Kostopoulou, A.; Oh, E.; Susumu, K.; Stewart, M. H.; Medintz, I. L.; Stratakis, E.; Parak, W. J.; Kanaras, A. G. "The Role of Ligands in the Chemical Synthesis and Applications of Inorganic Nanoparticles" *Chem Rev* **2019**, *119*, 4819.

(15) Agnew, D. W.; DiMucci, I. M.; Arroyave, A.; Gembicky, M.; Moore, C. E.; MacMillan, S. N.; Rheingold, A. L.; Lancaster, K. M.; Figueroa, J. S. "Crystalline Coordination Networks of Zero-Valent Metal Centers: Formation of a 3-Dimensional Ni(0) Framework with -Terphenyl Diisocyanides" *J Am Chem Soc* **2017**, *139*, 17257.

(16) Agnew, D. W.; Gembicky, M.; Moore, C. E.; Rheingold, A. L.; Figueroa, J. S. "Robust, Transformable, and Crystalline Single-Node Organometallic Networks Constructed from Ditopic -Terphenyl Isocyanides" *J Am Chem Soc* **2016**, *138*, 15138.

(17) Arroyave, A.; Gembicky, M.; Rheingold, A. L.; Figueroa, J. S. "Aqueous Stability and Ligand Substitution of a Layered Cu(I)/Isocyanide-Based Organometallic Network Material with a Well-Defined Channel Structure" *Inorg Chem* **2020**, *59*, 11868.

(18) Balto, K. P.; Gembicky, M.; Rheingold, A. L.; Figueroa, J. S. "Crystalline Hydrogen-Bonding Networks and Mixed-Metal Framework Materials Enabled by an Electronically Differentiated Heteroditopic Isocyanide/Carboxylate Linker Group" *Inorg Chem* **2021**, *60*, 12545.

(19) Fox, B. J.; Sun, Q. Y.; DiPasquale, A. G.; Fox, A. R.; Rheingold, A. L.; Figueroa, J. S. "Solution behavior and structural properties of Cu(I) complexes featuring -terphenyl isocyanides" *Inorg Chem* **2008**, *47*, 9010.

(20) Efraty, A.; Feinstein, I.; Frolow, F.; Goldman, A. "Coordination Polymers of Rhodium(1+) with Di-Isocyanonaphthalene (1,4 and 1,5) Linkages" *J Chem Soc Chem Comm* **1980**, 864.

(21) Kim, N. H.; Kim, K. "Adsorption characteristics of arylisocyanide on Au and Pt electrode surfaces: Surface-enhanced Raman scattering study" *J Phys Chem B* **2006**, *110*, 1837.

(22) Kim, S.; Ihm, K.; Kang, T. H.; Hwang, S.; Joo, S. W. "Binding property and structure of aromatic isocyanide self-assembly monolayers on Ag and Au surfaces" *Surf Interface Anal* **2005**, *37*, 294.

(23) Foucault, R.; Birke, R. L.; Lombardi, J. R. "SERS of surfactants in monolayer and multibilayer forms on an electrified Ag surface" *Langmuir* **2003**, *19*, 8818.

(24) Kudelski, A. "Structures of monolayers formed from different HS-(CH)-X thiols on gold, silver and copper:: comparitive studies by surface-enhanced Raman scattering" *J Raman Spectrosc* **2003**, *34*, 853.

(25) Ansar, S. M.; Gadogbe, M.; Siriwardana, K.; Howe, J. Y.; Dogel, S.; Hosseinkhannazer, H.; Collier, W. E.; Rodriguez, J.; Zou, S. L.; Zhang, D. M. "Dispersion Stability, Ligand Structure and Conformation, and SERS Activities of 1-Alkanethiol Functionalized Gold and Silver Nanoparticles" *J Phys Chem C* **2014**, *118*, 24925.

(26) Bantz, K. C.; Nelson, H. D.; Haynes, C. L. "Plasmon-Enabled Study of Self-Assembled Alkanethiol Ordering on Roughened Ag Substrates" *J Phys Chem C* **2012**, *116*, 3585.

(27) Sebek, J.; Knaanie, R.; Albee, B.; Potma, E. O.; Gerber, R. B. "Spectroscopy of the C-H Stretching Vibrational Band in Selected Organic Molecules" *J Phys Chem A* **2013**, *117*, 7442.

(28) Kubackova, J.; Izquierdo-Lorenzo, I.; Jancura, D.; Miskovsky, P.; Sanchez-Cortes, S. "Adsorption of linear aliphatic α, ω-dithiols on plasmonic metal nanoparticles: a structural study based on surface-enhanced Raman spectra" *Phys Chem Chem Phys* **2014**, *16*, 11461.

(29) Knoll, W.; Philpott, M. R.; Golden, W. G. "Surface Infrared and Surface Enhanced Raman Vibrational-Spectra of Monolayer Assemblies in Contact with Rough Metal-Surfaces" *J Chem Phys* **1982**, *77*, 219.

(30) Talarska, P.; Boruczkowski, M.; Zurawski, J. "Current Knowledge of Silver and Gold Nanoparticles in Laboratory Research-Application, Toxicity, Cellular Uptake" *Nanomaterials-Basel* **2021**, *11*.

(31) Ahn, J.; Shi, S.; Vannatter, B.; Qin, D. "Comparative Study of the Adsorption of Thiol and Isocyanide Molecules on a Silver Surface by in Situ Surface-Enhanced Raman Scattering" *J Phys Chem C* **2019**, *123*, 21571.

(32) Barnett, B. R.; Moore, C. E.; Chandrasekaran, P.; Sproules, S.; Rheingold, A. L.; DeBeer, S.; Figueroa, J. S. "Metal-only Lewis pairs between group 10 metals and Tl(I) or Ag(I): insights into the electronic consequences of Z-type ligand binding" *Chem Sci* **2015**, *6*, 7169.